12-16-1994

Impact of Nuclear Rocket Engine Design on Control Strategies

John A. Lambright

The University of New Mexico

OFFICE OF GRADUATE STUDIES
107 Humanities Building
Albuquerque, NM 87131-1041
Telephone (505) 277-2711
FAX (505) 277-7405

THE UNIVERSITY OF NEW MEXICO
ALBUQUERQUE, NEW MEXICO 87131

POLICY ON USE OF THESES AND DISSERTATIONS

Unpublished theses and dissertations accepted for master's and doctor's degrees and deposited in the University of New Mexico Library are open to the public for inspection and reference work. *They are to be used only with due regard to the rights of the authors.* The work of other authors should always be given full credit. Avoid quoting in amounts, over and beyond scholarly needs, such as might impair or destroy the property rights and financial benefits of another author.

To afford reasonable safeguards to authors, and consistent with the above principles, anyone quoting from theses and dissertations must observe the following conditions:

1. Direct quotations during the first two years after completion may be made only with the written permission of the author.
2. After a lapse of two years, theses and dissertations may be quoted without specific prior permission in works of original scholarship provided appropriate credit is given in the case of each quotation.
3. Quotations that are complete units in themselves (e.g., complete chapters or sections) in whatever form they may be reproduced and quotations of whatever length presented as primary material for their own sake (as in anthologies or books of reading) ALWAYS require consent of the authors.
4. The quoting author is responsible for determining "fair use" of material he uses.

This thesis/dissertation by John A. Lambright has been used by the following persons whose signatures attest their acceptance of the above conditions. (A library which borrows this thesis/dissertation for use by its patrons is expected to secure the signature of each user.)

NAME AND ADDRESS DATE

John A. Lambright

Candidate

Chemical & Nuclear Engineering

Department

This dissertation is approved, and it is acceptable in quality and form for publication on microfilm:

Approved by the Dissertation Committee:

, Chairperson

Patrick J McDaniel

J. Eric Haskin

Accepted:

Dean, Graduate School

Dec 16, 94

Date

IMPACT OF NUCLEAR ROCKET ENGINE DESIGN ON CONTROL STRATEGIES

BY

JOHN A. LAMBRIGHT

B.S., University of Illinois, 1984
M.S., University of Illinois, 1985

DISSERTATION

Submitted in Partial Fulfillment of the
Requirements for the Degree of

Doctor of Philosophy in Nuclear Engineering

The University of New Mexico
Albuquerque, New Mexico

December 1994

Dedicated to my wife and children

ACKNOWLEDGMENTS

There are many to whom I owe a great debt in achieving this milestone in my education. First, I give special thanks to Dr. Pat McDaniel, for his guidance and counseling throughout my graduate career at the University of New Mexico. I would also like to give special thanks to my advisor, Dr. Norm Roderick. I express appreciation to Prof. Mohamed El-Genk and Prof. Eric Haskin of the Chemical and Nuclear Engineering Department, and Prof. Arzi Razani of the Mechanical Engineering Department for serving on the committee and for their time and effort reviewing this work.

IMPACT OF NUCLEAR ROCKET ENGINE DESIGN ON CONTROL STRATEGIES

BY

JOHN A. LAMBRIGHT

ABSTRACT OF DISSERTATION

Submitted in Partial Fulfillment of the
Requirements for the Degree of

Doctor of Philosophy in Nuclear Engineering

The University of New Mexico
Albuquerque, New Mexico

December 1994

IMPACT OF NUCLEAR ROCKET ENGINE DESIGN ON CONTROL STRATEGIES

John A. Lambright
B.S., University of Illinois, 1984
M.S., University of Illinois, 1985
Ph.D., University of New Mexico, 1994

ABSTRACT

In a nuclear thermal rocket engine, the propellant gas can be varied independent of the peak chamber temperature. Startup and shutdown times can be varied over a wide range due to this uncoupling of the energy source from the working fluid. Therefore, in the early stages of nuclear rocket engine development, a study of the impact of the engine design on control strategies and systems was conducted. In order to define what is required in terms of engine thrusting times, this study focused on the thrust requirements for a Reusable Orbital Transfer Vehicle (ROTV).

Three nuclear rocket designs were used to compare startup control strategies. The three designs were the NERVA (nuclear engine for rocket vehicle application) small engine, wire core, and particle bed reactors. These three reactors were chosen to represent the spectrum of possible solid core reactor types which had been considered by NASA (National Air and Space Administration) for the Space Exploration Initiative.

Models exist in the literature for both the NERVA small engine and particle bed reactors. A comparable model of the wire core reactor was unavailable. Therefore, prior to assessing the impact of nuclear rocket engine design on control strategies, modeling of the wire core reactor was performed.

Development of a computer code that modeled the physical phenomena of a nuclear rocket engine startup was required to compare startup strategies for the three reactor types. The STRTUP computer code which was developed, modeled the important time-dependent effects that occur in a fission reactor as a result of the physics of fission.

Also modeled by the code were the core heat transfer process, a turbopump, and reactivity feedback effects.

In the derivation of the non-dimensional Smith-Stenning equations which were coded into the STRTUP computer code, response time constants were defined for reactor power, delayed neutron precursor density, core outlet temperature, and core inlet pressure. The reactor power and core outlet temperature response time constants exhibited the greatest variance between the three reactors.

When comparing the startup simulation results between the three reactor models, it was found that the following parameters varied significantly as a result of differences in engine design and control strategies:

a. Startup response time for power level, reactor outlet temperature, and turbopump outlet pressure
b. Propellant reactivity feedback effects
c. Temperature reactivity feedback effects
d. Control drum span startup requirement
e. Control drum reactivity insertion and removal rate requirement.

However, from a reactor kinetics and engine controllability standpoint there was only a small difference found between the NERVA and particle bed reactors. The wire core exhibited a substantial difference with the other two designs primarily due to variance in the startup response time for power level and propellant reactivity feedback effects.

TABLE OF CONTENTS

TABLE OF CONTENTS (continued)

TABLE OF CONTENTS (concluded)

Section Page

FIGURES

Figure Page

FIGURES (concluded)

TABLES

TABLES (concluded)

1.0 INTRODUCTION

An inherent advantage of nuclear rocket propulsion is the virtually unlimited energy supply available from a reactor (Refs. 1, 2, 3). The heat from a reactor can provide sufficient energy to exhaust a low molecular weight propellant such as hydrogen at much higher velocities than are possible in chemical rockets operating at the same temperature. The higher exhaust velocities lead directly to superior rocket performance. The best of all possible chemical propellants (excluding free-radical systems) is liquid hydrogen-oxygen which produces an exhaust velocity of 4,459 m/s (Ref. 4). A nuclear rocket operating at 2700°K using hydrogen as the propellant produces an exhaust velocity of 8,575 m/s (Ref. 5). Therefore, when a hydrogen-propelled nuclear rocket is compared with a liquid oxygen-hydrogen-propelled chemical rocket, the exhaust velocity is found to be approximately 87 percent higher.

The primary function of any rocket is to accelerate a payload to some prescribed velocity (Refs. 6, 7). To appreciate what the extra exhaust velocity of nuclear rockets would mean, Table 1 gives velocities required for typical missions. Chemical rockets (single stage) are hard pressed to reach the goals of either the escape or satellite missions.

Table 1

Burnout Velocities by Mission

Mission	Burnout velocity (m/s)
Escape	10,668
Satellite	8,235
ICBM (8050 km)	6,710
IRBM (2415km)	4,575
V-2 (322km)	1,678

Another excellent measure of rocket performance is burnout velocity (V_e). For a single stage rocket:

$$V_e = V_c \ln(M_o/M_e) - g\, t_b \cos\theta + V_o \qquad (1.1)$$

where,

V_c = propellant exhaust velocity
M_o = initial mass
M_e = burnout mass
g = acceleration of gravity
$\cos\theta$ = cosine of the angle that the thrust vector makes with the vertical
t_b = time to burnout
V_o = initial velocity at takeoff.

Equation (1.1) is applicable as long as rocket engine burn time is short in comparison to the time required to change orbital altitude which will be the case when considering a reusable orbital transfer mission.

To optimize burnout velocity, the mass ratio (M_o/M_e) should be made as large as possible. However, practical engineering considerations dictate that the amount of propellant be no more than almost 90 percent of the total weight (Ref. 4). The ratio of maximum propellant weight to total vehicle weight for large rockets is relatively independent of whether a chemical or nuclear rocket is employed. Therefore, when comparing the ratio of maximum propellant weight to total vehicle weight (M_o/M_e), neither type of rocket system offers a significant performance advantage.

If initial velocity is assumed to be zero, Equation (1.1) reduces to:

$$V_e = 2.3\, V_c - g\, t_b \cos\theta \quad . \qquad (1.2)$$

To a close approximation (Ref. 4):

$$V_c = k\,(T_c/M)^{1/2} \qquad (1.3)$$

where,

k = constant
T_c = mean combustion chamber temperature

M = mean molecular weight of the propellant gas

and all other terms have been previously defined.

As can be seen from Equation (1.3), the higher the ratio of (T_c/M) the larger the burnout velocity will become. The performance advantage of nuclear rockets is gained primarily by employing lower molecular weight propellants (such as hydrogen) as compared with chemical rockets, since chemical rockets can operate at higher chamber temperatures.

Finally, assuming a given maximum allowable chamber temperature and choosing the propellant, Equation (1.3) can be expressed as:

$$V_e = k_1 - g\, t_b \cos\theta \qquad (1.4)$$

where,

$k_1 = k\,(T_c/M)^{1/2}$

and all other terms have been previously defined.

Equation (1.4) illustrates that another means of maximizing rocket performance is to insure thrust duration is as short as possible. In the case of the Reusable Orbital Transfer Vehicle (ROTV) the thrust times are defined by weight of the payload and rocket system and the difference in altitude of the orbits transited. Refer to Section 1.5 for a more detailed discussion on thrust time requirements.

1.1 Missions Which Require a Nuclear Rocket

Lower performance chemical rockets will probably be favored for most military near earth missions except for those requiring extremely large payloads (Refs. 1, 3, 4). For use as a ROTV and for extraterrestrial missions, the nuclear rocket has significant advantages since higher burnout velocities are available (Ref. 8).

For all space systems, the cost of placing the system mass in low earth orbit (LEO) is a major portion of the overall system cost (Ref. 8). In fact for many systems, it is the dominant cost. Therefore, the total system cost can be minimized by minimizing the mass lifted to LEO.

Unlike the one way orbital transfer vehicle, the ROTV must carry the propellant required to return to LEO on its trip to geosynchronous orbit (GEO). This is not an insignificant mass increase that must be placed in LEO for the ROTV above that required for the one way transfer vehicle (Ref. 8). Therefore for low performance engines, it may be more economical to not attempt a reusable vehicle.

Propellant utilization will be the major economic issue in deciding between a reusable vehicle or an expendable one. There exists a break-even specific impulse for a given transfer mission that can serve as the criteria for whether or not a ROTV makes sense. If the engine can achieve this break-even specific impulse or greater, then a reusable vehicle makes sense. This break-even specific impulse will be a function of the difference in levels within the Earth's gravity well in which the transfer vehicle operates (Refs. 4, 8).

For small orbital altitude increases most types of rocket propulsion systems are adequate. For transfers to one-half GEO and above, specific impulses exceeding 600 seconds are required to reach break-even (Ref. 8). Transfers in the GEO to lunar range require a specific impulse exceeding 800 seconds to break-even (Ref. 8). Therefore, a hydrogen-propelled nuclear rocket offers a considerable performance advantage over a liquid hydrogen-oxygen-propelled chemical rocket for use as a ROTV.

1.2 Research Objective

The objective of this research is to investigate the impact of nuclear rocket engine design on control strategies for rocket engine startup. This objective will be pursued by investigating three nuclear rocket designs typical of solid core rockets which had been considered by the National Air and Space Administration (NASA) for the Space Exploration Initiative. The three designs are the NERVA (nuclear engine for rocket vehicle application) small engine, wire core, and particle bed reactors. The NERVA design is fairly well defined and has been extensively documented in the literature. The particle bed and wire core reactors are folded flow type cores and could potentially offer some significant performance advantages in roles where light weight is important.

These three reactors were chosen to represent the spectrum of possible solid core reactor types which were considered by NASA for the Space Exploration Initiative. The only major design issue not addressed is the low pressure concept. This has been left out due to a lack of design information on which to build credible models.

Table 2 compares these three reactor types. Engine startup response time may be significantly altered by design differences between the three reactors. As illustrated in Table 2, the wire core has a fast neutronics spectrum while the NERVA and particle bed reactors have an epi-thermal and thermal neutronics spectrum, respectively. The neutronics spectrum and moderation type primarily effect the response time for shifts in power level and delayed neutron precursor densities. A substantial variance in fuel surface area is exhibited by the three reactor designs. The particle bed, wire core, and NERVA reactors have a very high, high, and medium fuel surface area, respectively. The fuel form, surface area, and type alter the response time for increases of chamber and outlet temperatures. Refer to Sections 1.3, 4.1, and 4.2 for a more detailed comparison of the design differences between the three reactor types.

To investigate the impact of nuclear rocket engine design on startup control strategies this research will:

Table 2

Solid Core Designs

Design Choice	NERVA	Particle Bed	Wire Core
Neutronics	Epi-thermal	Thermal	Fast
Fuel Form	Prismatic	Particle	Wire Cermet
Fuel Surface Area	Medium	Very High	High
Fuel Type	UC_2	UC_2	UN
Moderation	Integral	Separate	None

a. Develop a wire core reactor rocket engine model to a consistent level of detail with the NERVA small engine and particle bed models.

b. Perform a deterministic comparison of key rocket engine parameters for the NERVA small engine, particle bed, and wire core rocket engine designs.

c. Quantify rocket engine response time constants for a low thrust (72 kN) engine for each of the three reactors.

d. Develop a nuclear rocket engine modeling code which incorporates models for (1) the time-dependent effects in a fission reactor which result from the physics of fission, (2) delayed neutrons with six delayed groups, (3) delayed beta and gamma heating, (4) the core heat transfer process, (5) a turbopump, (6) reactivity feedback effects, and (7) a time optimal control law.

e. Define a quantitative basis for the impact of solid core nuclear design on usable startup control strategies.

f. Define a quantitative basis for the impact of reactivity feedback effects on control and safety margins.

g. Determine whether or not one common optimal startup control strategy can be employed despite substantial variance in neutronics, fuel surface area and form between the three rocket engine designs.

1.3 Description of a Solid Core Nuclear Rocket

One design option for a nuclear rocket is to utilize a solid fuel element reactor to heat a single liquid propellant. Figure 1 gives a simplified drawing of a solid core nuclear rocket. Liquid hydrogen is stored in insulated tanks from which it is forced through a propellant pump. The hydrogen then flows at high pressure to the exit end of the nozzle. At the end of this nozzle, the propellant enters a distribution plenum regeneratively cooling the walls of the nozzle and reactor chamber. From there it passes into the entry plenum of the reactor core. Most of the coolant then flows through the end reflector and reactor core where its temperature is raised to approximately 2600°K.

During this process the hydrogen pressure also drops. The hydrogen is ejected through a convergent-divergent nozzle where the thermal energy of the gas is converted into kinetic energy for rocket thrust. A small percentage of coolant flows into passages in the reflector which initially bypasses the core. Orificing occurs in these passages which not only determines flow but also outlet temperature of the hydrogen. This gas can be ducted to the drive turbine of a turbopump. Also, a very small amount of hydrogen can be used to cool the structural columns of the reactor core.

Reflector control is one means that can be adopted to control power level. These reflectors could extend the entire length of the reactor core. Coolant holes would run through the reflector in the axial direction with hydrogen gas being used to maintain tolerable temperatures and temperature gradients. Typical values found in the literature for the NERVA small engine hydrogen gas reflector exit conditions are 294.9°K and 4.21 MPa (Ref. 5). As was previously mentioned, the gas exiting the reflector can be used to power a turbopump. Since the main gas flow is at substantially different pressure and temperature conditions, separation must occur between the reflector and the core. Graphite walls can be used for this purpose.

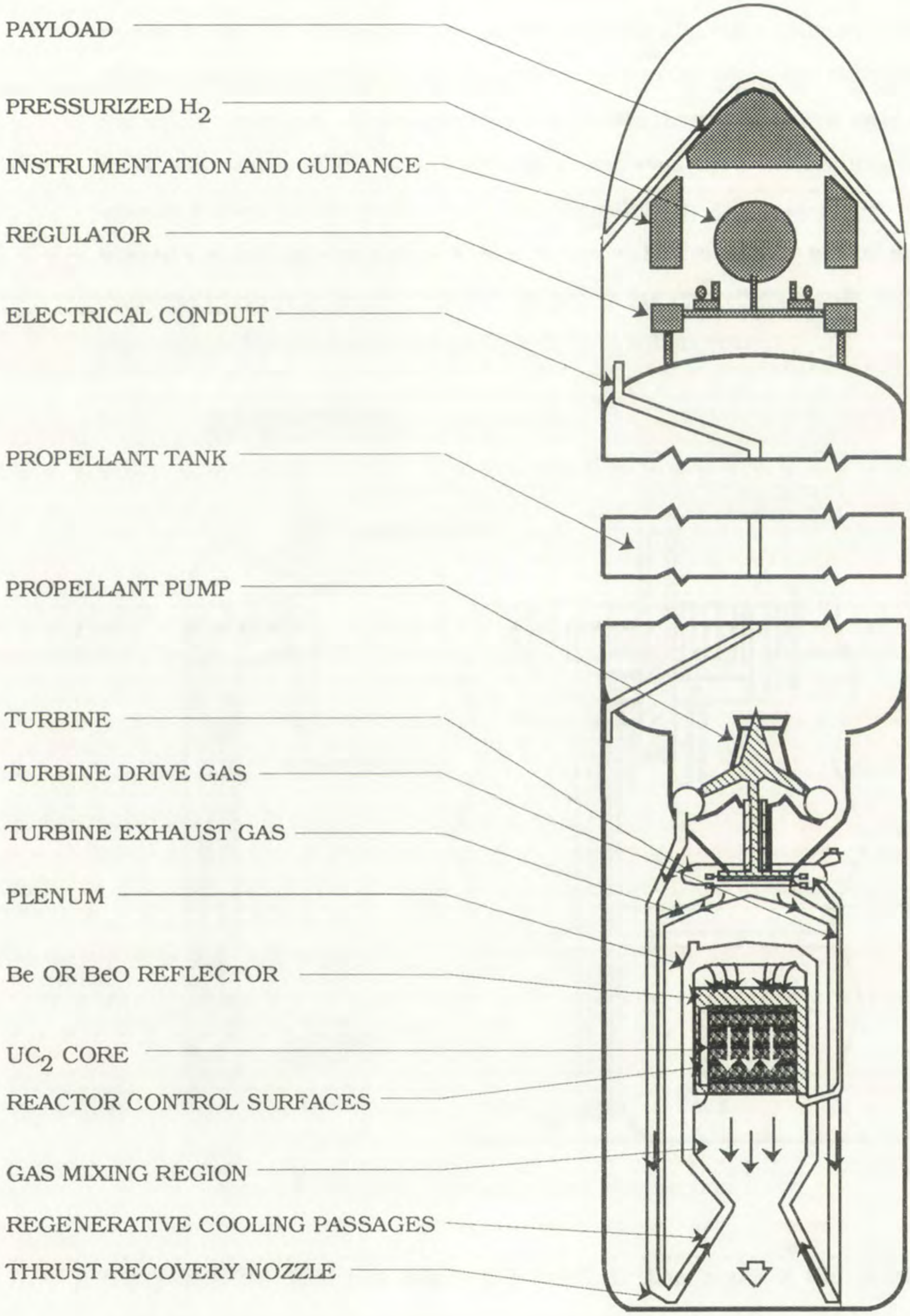

Figure 1 Schematic Diagram of a Nuclear Rocket

Control of reactor power can be accomplished by assemblies as shown in Figure 2 (Ref. 9). The plates are curved portions of a right cylinder. These plates must be cooled due to neutron capture within the boron and subsequent α-particle admission. Hydrogen coolant is passed through a hollow shaft and down both sides of the plate. Control is achieved by a mechanical drive system geared to the shaft. When an individual or group of plates faces inward towards the core, part of the reflector will be effectively cut off and a decrease in neutron level will occur. As plates are rotated outwards more of the reflector becomes available and power level will increase.

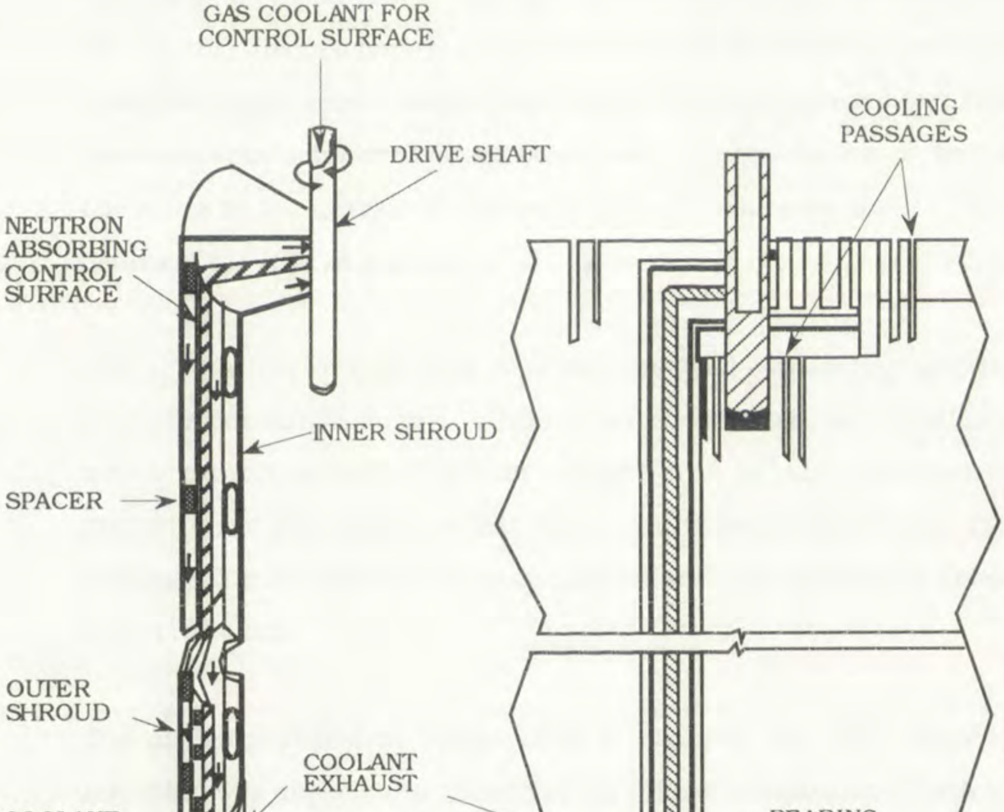

Figure 2 Control Plate Assembly Cross Section

Because of the relatively short operational lifetime, some of the problems typically encountered in commercial reactor operation such as shielding and radiation damage as well as afterheat removal are less severe. Shielding of personnel and sensitive components may require an additional weight penalty. However, utilizing the liquid hydrogen within its tank as a neutron shield for most of the thrust duration can significantly reduce this weight penalty.

1.3.1 NERVA Reactor

The primary performance requirement of the NERVA reactor was to act as a source to transmit thermal energy to the hydrogen propellant at a rate to maintain the thrust chamber gas temperature at 2500°K with a pressure of 3.10 MPa and a flow rate of 40.3 kg/s (including 0.5 kg/s hot bleed) (Refs. 10, 11, 12, 13). The reactor was designed to have an endurance capability of 3000 seconds of operation at design conditions. However, ground test endurance was to be 4500 seconds at design conditions. The reactor was to be capable of ten starts to the design conditions. Figure 3 illustrates many of the design details of the NERVA reactor.

The NERVA reactor discussed here was designed considering system weight tradeoffs for single engine, single module operation to shielding criteria which protect sensitive reactor, engine and vehicle components from excessive radiation levels and to meet requirements for limiting propellant heating. The shields were to be compatible with the addition of shielding for crew protection.

The nuclear subsystem design criteria reliability was 99.7 percent. This reliability was apportioned to each of the critical components which made up the reactor assembly.

The reactor was designed to withstand a steady acceleration of +6 g and −4 g along the thrust axis and +3 g in the lateral direction. Positive accelerations were in the flight direction. The design goal for the nuclear subsystem was to maintain the as delivered weight, excluding shielding, at less than 3860 kg.

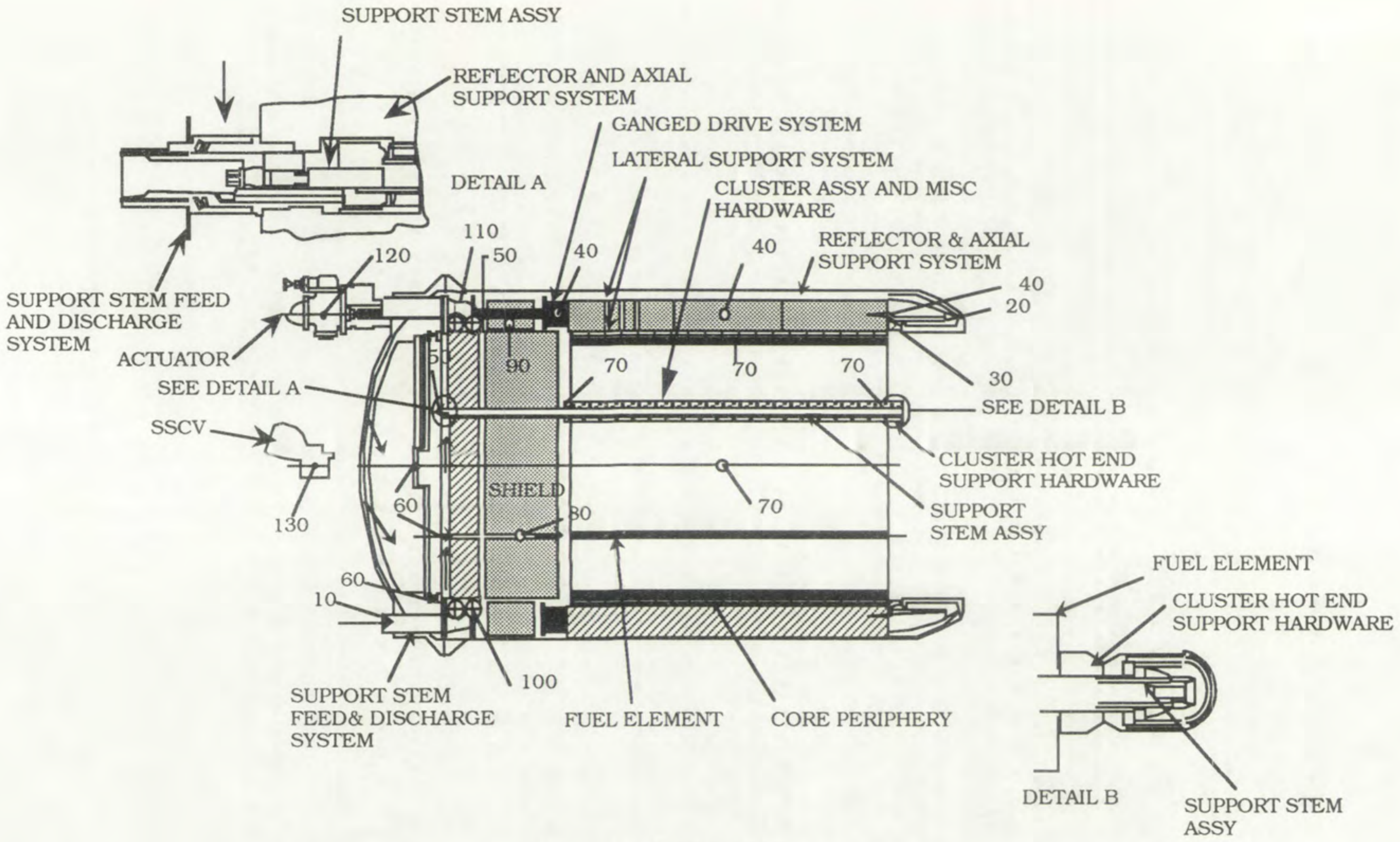

Figure 3 NERVA Reactor

The NERVA reactor was a hydrogen cooled, graphite moderated, intermediate neutron energy reactor designed to operate at a nominal 1575 MW thermal power. The major components of the reactor consisted of the core, reflector, structural support and shield. Reactivity control devices consisted of neutron absorbing vanes assembled in the control drums with a ganged drum drive.

The design of the NERVA reactor was based on the design features of the KIWI, NRX and PHOEBUS technology reactors (Refs. 11, 12). Major modifications from the designs previous to the NRX-A6 reactor configuration (NRX-A2 through NRX-A5) and XE engines were the elimination of the graphite inner reflector and the use of a modified stacked beryllium ring reflector rather than beryllium sectors, the use of counterflow support stems in lieu of tie rods, and aft end reactor support rather than forward support. The ganged drum drive mechanism was incorporated and provided rotational control to the eighteen drums through use of six actuators in order to meet the actuation system flight reliability requirements.

The basic configuration and features of the NERVA reactor can be described as follows (Ref. 10):

a. The core assembly consisted of clustered graphite-uranium fuel elements supported axially from the dome end support plate by cooled metal support stems and bundled radially by a distributed lateral support structure.

   The core consisted of 1878 fueled elements and 349 unfueled elements. There were no partial fueled elements as in previous reactors. The elements were collected into 253 regular and 48 irregular clusters (see Figure 4).

b. The reflector assembly consisted of axially stacked modified beryllium rings housing eighteen control drums and providing longitudinal cooling holes and lateral support spring pockets. The

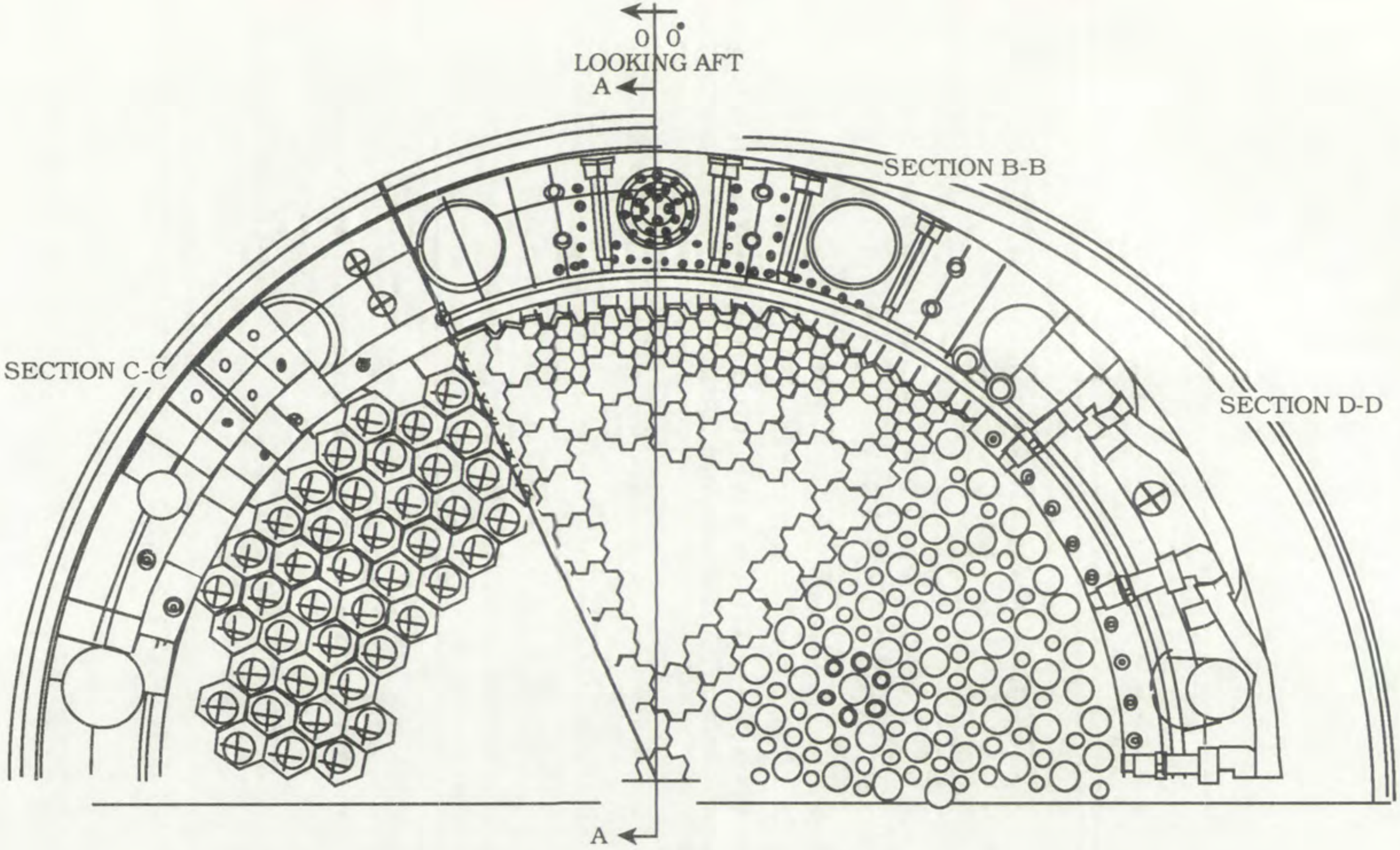

Figure 4 NERVA Reactor Cross Section

spring pockets enclosed coiled Inconel lateral support springs. The control drum design was similar to the NRX-A6 design, but was smaller in diameter.

c. The reactor support structure consisted of a core support plate, dome end support cone, nozzle end support ring, and locating cone.

d. For the NERVA reactor a light weight shield, made of neutron and gamma attenuating material, was located below the core support plate as a central shield and above the reflector as an extension shield. The prime purpose of this shield was to reduce heating of propellant in the flight tank and protect sensitive components.

e. The structural support stem flow system consisted of a flow control valve, valve actuator, control system, orifices, inlet plenum and mixing chamber. Flow control was to be used for initial reactivity trimming and to compensate for the loss of reactivity due to core corrosion during steady state power operation.

f. The seals consisted of the axial distributed seal system at the core periphery, the nozzle reflector interface seal, and the seals at various component interfaces to maintain proper separation and distribution of coolant flow.

g. The flight anti-criticality poison wire system consisted of flexible wires containing enriched B^{10} inserted into the fuel element flow channels and attached to an actuator and control system providing for their withdrawal prior to engine startup.

The nuclear subsystem had two coolant inlet flow paths. The main feedline supplied coolant to the nozzle. The major portion of the hydrogen, as on previous reactors, entered the reactor from the nozzle tubes at the reflector inlet plenum. This flow then passed through the reflector and control drum coolant passages as well as through the annulus between the periphery of the reflector and the pressure vessel. The flow from these passages passed into the reflector outlet plenum and through the extension shield.

The flow then mixed with the structural support stem and bypass effluent. From the extension shield plenum, the flow went radially inward between the baffle and the forward pressure vessel closure. The flow was distributed by the baffle to the forward plenum.

From this forward plenum, the gas passed though multiple hollow spools and into holes in the support plate. A plenum between the support plate and the central shield distributed the flow from the holes in the support plate into holes and passages in the shield. The flow then entered the core inlet plenum. There a small portion of the flow entered the lateral support system. The major portion of the flow entered the fuel elements through screens mounted on cluster plates prior to being metered by orifices in the individual element coolant passages. Both flows were discharged into the thrust chamber and were expelled through the nozzle.

The second feedline from the pump discharge supplied coolant to the support stem feed and discharge system. A constant flow from the support stem control valve (SSCV) entered the reactor via pipes passing through two of the 18 ports located on the forward closure.

Due to the variation in the reactivity flow requirements to the structural support stem assemblies, a bypass diverted flow from the main stem flow into the center of the support stem mixing chamber. The rest of the flow was distributed to the support stem assemblies.

The support stem inlet piping was manifolded at the periphery forward of the extension shield, where the gas flow entered multiple small tubes. These tubes provided a structurally flexible passage into the structural support system inlet plenum. This plenum was located between the support plate forward face and the structural support mixing chamber. The gas flow was then distributed to each of the structural support stems where it flowed through the stems to the aft end of the cluster, and then reversed to flow forward between a pressure tight liner and the support stem. Orifices installed in each stem distributed the flow.

This flow from the support stem assembly was then discharged into the support stem mixing chamber. From this chamber the support stem feed and discharge flow entered the extension shield outlet plenum and joined the propellant from the reflector system. All the coolant then passed through the flow baffles, support plate and central shield and flowed into the core.

The fuel element design was a 19 channel low-expansion carbonaceous matrix containing uniformly dispersed fuel particles, a graphite-carbide composite aft-end tip, and a niobium-carbide channel and aft-end coating. The fuel element was a 1.91 cm nominal hexagon with 19 flow channels sized to produce a 27 percent void fraction after coating. The overall element length of 132 cm including a 2.5 cm tip, represented the same basic element geometry that had been used in the NRX technology program. The fueled portion of the element consisted of pyrolytic coated uranium carbide fuel beads uniformly dispersed in a graphitized cabonaceous matrix. This matrix was made from graphite flour, carbon black and a catalyzed binder. The radial thermal expansion of this element matrix was controlled so as not to cause a solid core expansion, during reactor operation, of greater than 1.3 percent of the as-assembled core dimensions.

The element channels accommodated orifice jets brazed at the inlet end of the channel to control individual channel flow. This resulted in flat radial temperature profiles at the design orifice angle. Orificing also minimized temperature variations in an element and between elements. The element flow channels were coated for corrosion protection.

The outside surface of all the fuel elements at the aft end were coated for 6.35 cm for corrosion protection. The 6.35 cm coating length permitted an element hexagon envelope tolerance of ± 0.0017 cm across the flats over the major portion of the element length. Full length coating of the elements would have produced a ± 0.0025 cm envelope tolerance leading to larger interstitial gaps upon stacking of the elements. The uncoated fuel elements also minimized axial tensile stresses produced by differential thermal expansions between elements because they had a low friction interface for slippage. The aft end tip was to consist of (a) an approximately 1.42 cm long transition section of unfueled graphite and (b) a 2.5 cm long carbide-graphite section with a reduced thermal expansion coefficient.

The optimum combination of transition and composite section lengths and materials was to be selected for the tip design based on cluster support design and material properties. The interface between the transition and composite sections had high residual stresses due to differences in thermal expansion between the two materials. These stresses were minimized by the 2.5 cm long carbide-graphite section.

The thrust requirements for a ROTV are more closely matched by the 72 kN thrust NERVA small engine design than by the 337 kN thrust NERVA engine which has just been described (Refs. 8, 14). Therefore, the NERVA small engine model will be utilized as an appropriate basis for comparison with the particle bed and wire core reactors which will be described in Sections 1.3.2 and 1.3.3, respectively.

The small engine design represented an accumulation of all the knowledge gained in the NERVA rocket program. It is important to note that the small engine was never built but was the result of a design study performed near the end of the NERVA project. The NERVA 337 kN thrust engine and small engine designs are very similar. Both the NERVA high thrust level engine and small engine designs took advantage of the full flow cycle idea. The hydrogen propellant flow path previously described for the NERVA high thrust level engine was virtually identical to the conceptional flow path for the small engine and the structural designs were similar. Therefore, a detailed description of the conceptionalized physical construction of the small engine will not be discussed further since the physical construction of the NERVA 337 kN thrust level engine has already been described.

The major design differences between the NERVA high thrust level engine and small engine model were as follows:

a. Number of fuel and support elements
b. Reactor power level
c. Engine thrust.

The reactor power level for the small engine model was 367 MWth. The NERVA small engine design included 564 hexagonally shaped, (UC_2 - ZrC) C composite fuel elements containing a total of 52.4 kg of uranium with a 93.15 percent enrichment. The NERVA small engine model also consisted of 241 support elements, containing zirconium hydride as a neutron moderator. Table 3 gives a listing of the major NERVA small engine design characteristics.

Table 4 provides a weight breakdown of the major constructural parameters for the NERVA small engine model.

In Table 5, the propellant flow rate, pressure, and temperature for the NERVA small engine model are given for various points within the engine.

1.3.2 Particle Bed Reactor

The particle bed reactor is a thermal reactor, fueled with 93.5 percent enriched uranium and moderated by beryllium (Refs. 15, 16, 17). Particle bed reactor designs based on zirconium hydride and lithium hydride moderators are also feasible.

Table 3

NERVA Small Engine Design Characteristics

Design Characteristic	Parametric Value
Thrust (kN)	72.0
Specific Impulse (s)	875
Thermal Power (MW)	367
Turbopump Power (MW)	0.93
Turbopump Speed (rpm)	46,950
Pump Discharge Pressure (MPa)	6.03
Engine Flow Rate (kg/s)	8.5
Chamber Temperature (°K)	2695
Chamber Pressure (MPa)	3.10
Core Diameter (m)	0.89
Core Length (m)	1.32
Be Reflector, o.d. (m)	1.25
Be Reflector Thickness (mm)	117
Pressure Vessel, o.d. (m)	1.3
Pressure Vessel Length (m)	1.9
Pressure Vessel Thickness (mm)	21

Table 4

NERVA Small Engine Mass Estimates

Constructural Parameter	Mass Estimate (kg)
Reactor Core and Hardware	868
Reflector and Hardware	569
Internal Shield	239
Pressure Vessel	150
Turbopump	41
Nozzle and Skirt Assembly	224
Propellant Lines	15
Thrust Structure and Gimbal	28
Valves and Actuators	207
Instrumentation and Electronics	159
Contingency	50
Total	**2550**

Table 5

Propellant Flow Rate, Pressure, and Temperature for the NERVA Small Engine

State Point Description	Flow Rate (kg/s)	Pressure (MPa)	Temperature (°K)
Pump Inlet	8.51	0.12	17.0
Pump Exit	8.51	6.03	19.8
Tie Tube Manifold Inlet	4.05	5.72	20.3
Tie Tube First Pass Exit	4.05	5.38	56.9
Tie Tube Exit	4.05	5.02	428.9
Slat Manifold Inlet	0.64	5.72	20.3
Slat First Pass Exit	0.64	5.24	167.1
Slat Exit	0.64	5.02	431.5
Turbine Inlet	4.13	4.86	428.6
Turbine Exit Mixed	4.69	4.13	415.6
Turbine Bypass Inlet	0.55	4.86	428.6
Nozzle Inlet	3.83	4.63	21.4
Nozzle Exit	3.83	4.21	240.4
Reflector Exit	3.83	4.21	294.9
Shield Inlet	8.51	4.06	361.0
Core Inlet	8.51	3.96	370.1
Fuel Element Exit	8.33	3.10	2728.0
Core Bypass Exit	0.18	3.10	370.1
Chamber	8.51	3.10	2695.8

The principal features of the particle bed reactor design when utilized as a ROTV are shown in Figure 5 (Ref. 18). The beryllium moderated core contains channels for 19 fuel elements, each 6.4 cm in diameter (Refs. 19, 20). Six additional channels contain launch poison safety chains. These remain in place until orbit is achieved, and are withdrawn just before reactor startup.

Coolant enters the core through the launch poison guide tubes in the beryllium moderator. It then flows through distribution holes in the

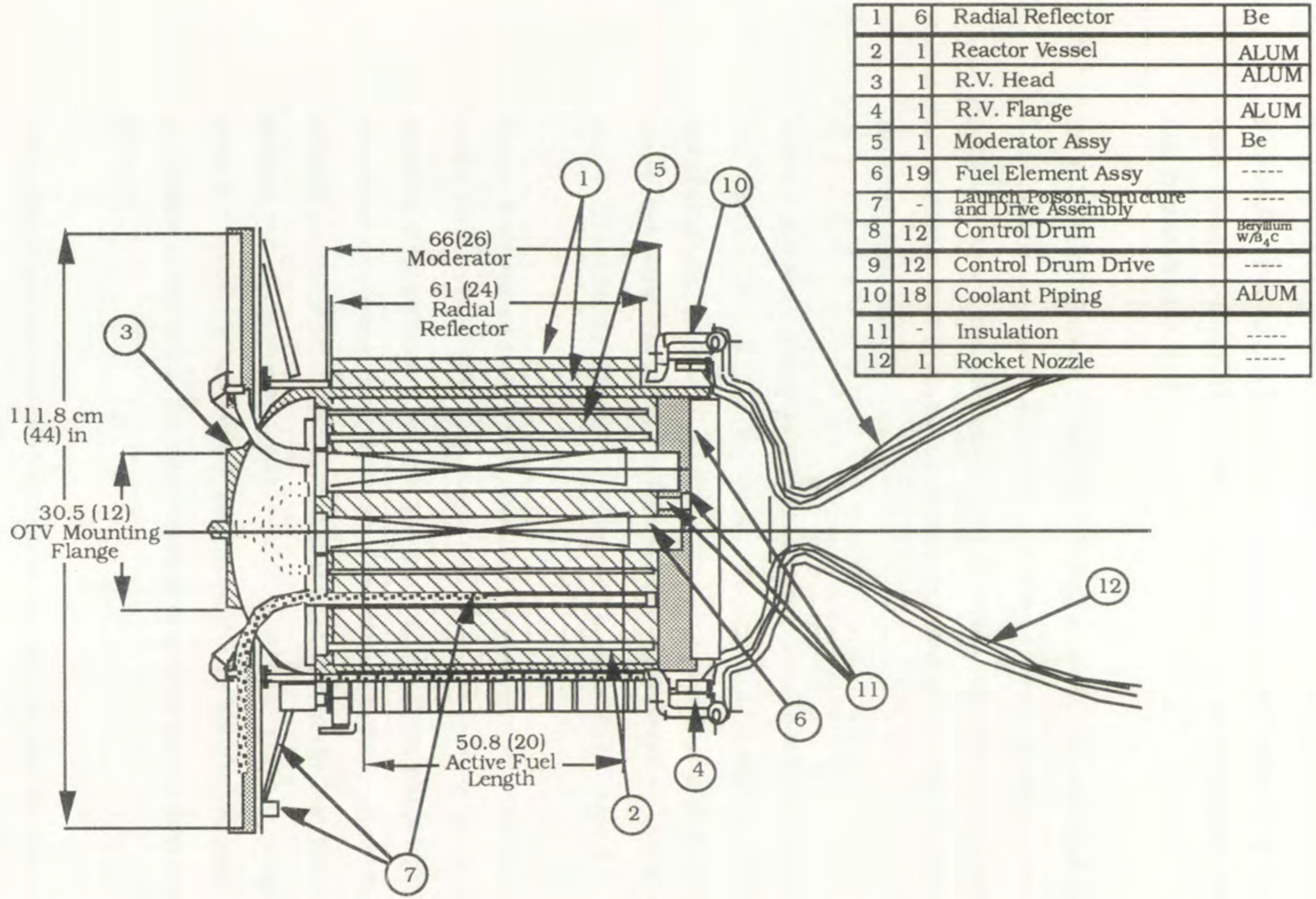

1	6	Radial Reflector	Be
2	1	Reactor Vessel	ALUM
3	1	R.V. Head	ALUM
4	1	R.V. Flange	ALUM
5	1	Moderator Assy	Be
6	19	Fuel Element Assy	-----
7	-	Launch Poison, Structure and Drive Assembly	-----
8	12	Control Drum	Beryllium W/B_4C
9	12	Control Drum Drive	-----
10	18	Coolant Piping	ALUM
11	-	Insulation	-----
12	1	Rocket Nozzle	-----

Figure 5 OTV Particle Bed Reactor Assembly Elevation View

beryllium moderator to a thin annular plenum around each fuel element. From there the coolant flows radially inward through the outer cool frit, the packed fuel particle bed, and the hot inner frit (see Figure 6). Hot coolant then exits along the central channels of each element to a common outlet plenum and nozzle (see Figure 7).

An aluminum pressure vessel is located between the core and the reflector. This design approach allows the rotating control drums to be outside the pressure vessel, eliminating the need for seals. The aluminum pressure vessel is relatively transparent to neutrons, and has only a small effect on reactivity (Ref. 20).

Table 6 gives the principal overall constructural parameters for the particle bed reactor (Ref. 21). The mass estimates and constructural parameter dimensions for the particle bed reactor which are illustrated in Table 6 can be compared with the NERVA small engine parameters provided in Tables 3 and 4. This comparison will be discussed in detail in Chapter 4.

Figure 8 shows an end view of a typical fuel element and the transition to the outlet plenum (Ref. 22). At the core boundary, the particle bed is replaced by a graphite plug between the inner and outer frits. These plugs together with the beryllium moderator extensions form the end reflectors. Not shown is a zone of inert particles (i.e., particles without uranium) in the last centimeter of the packed bed. This inert zone thermally isolates the graphite plugs and avoids local hot spots. Coolant flow rate through this zone is reduced. A similar inert zone is located at the core reflector boundary at the inlet end of the fuel element.

Mechanical pressure on the bed is provided by the combination of a rhenium compression donut, graphite support block, washer and gusset structure, and four rhenium bolts. Load pressure is approximately 62.1 MPa, which is comparable to that used in the electrical heating experiments on packed beds.

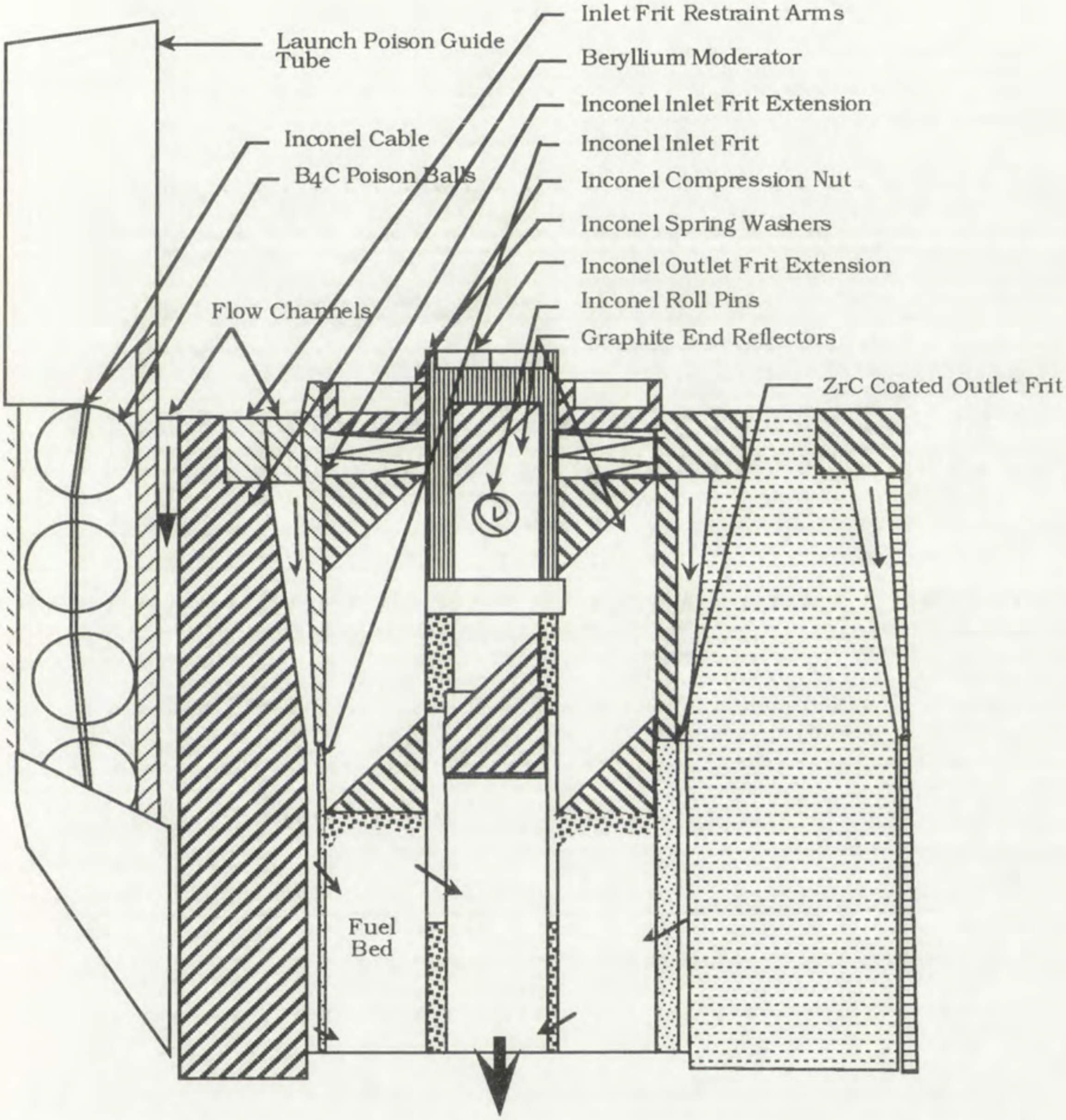

Figure 6 Particle Bed Reactor Cross Section of Fuel Element and Moderator Inlet

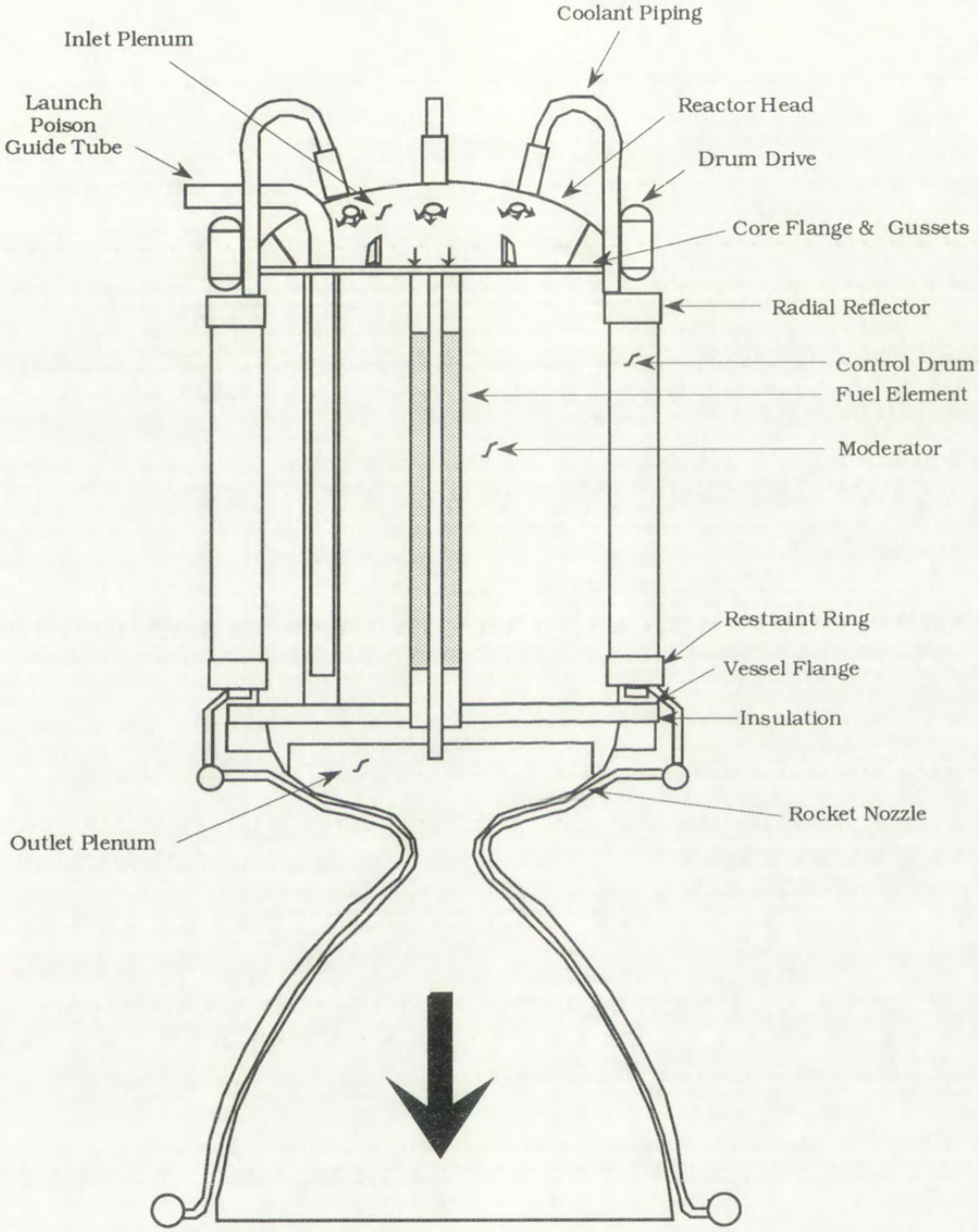

Figure 7 Particle Bed Reactor Assembly

Table 6

Principal Constructural Parameters of the Particle Bed Reactor Orbital Transfer Vehicle

Constructural Parameter	Parametric Value
Core Diameter/Length	50/50 cm
Number of Fuel Elements	19
Fuel Element OD/ID/Length	6.5/1.9/71 cm
Hot Frit Composition/Thickness	ZrC Coated Carbon-Carbon/3.0 mm
Cold Frit Composition/Thickness	Stainless Steel/1.5 mm
Fuel Particle OD/Coating Composition	500 micron/ZrC
Fuel Particle Kernel OD/Composition	200 micron/UC-ZrC
Fuel Particle Buffer Layer Thickness/ Composition	75 micron/PyC (50% D.F.)
Fuel Particle Sealer Layer Thickness/ Composition	35 micron/PyC
Be Moderator OD/Length	50.8/66 cm
Fuel Bed Volume	15 Liters
Axial Element Reflector Composition/ Thickness	Graphite/7.6 cm
Reactor Vessel Composition/Thickness	Aluminum/1.6 cm
Number/Composition/ID of Launch Poison Tubes	6/Aluminum/2.3 cm
Launch Poison Composition	B_4C Beads on String
Radial Reflector Composition/Thickness	Beryllium/5.2 cm
Number/Diameter of Control Drums	12/6.0 cm
Control Drum Composition	Beryllium/B_4C (120° Segment)
Fuel Element Weight (19)	125 kg
Beryllium Moderator Weight (inc. Axial Reflector)	145 kg
Beryllium Radial Reflector Weight	70 kg
Reactor Vessel Weight	110 kg
Control Drum Weight (inc. Drive)	95 kg
Launch Poison Weight	15 kg
Miscellaneous	40 kg
Total Reactor Assembly Weight	**600 kg**

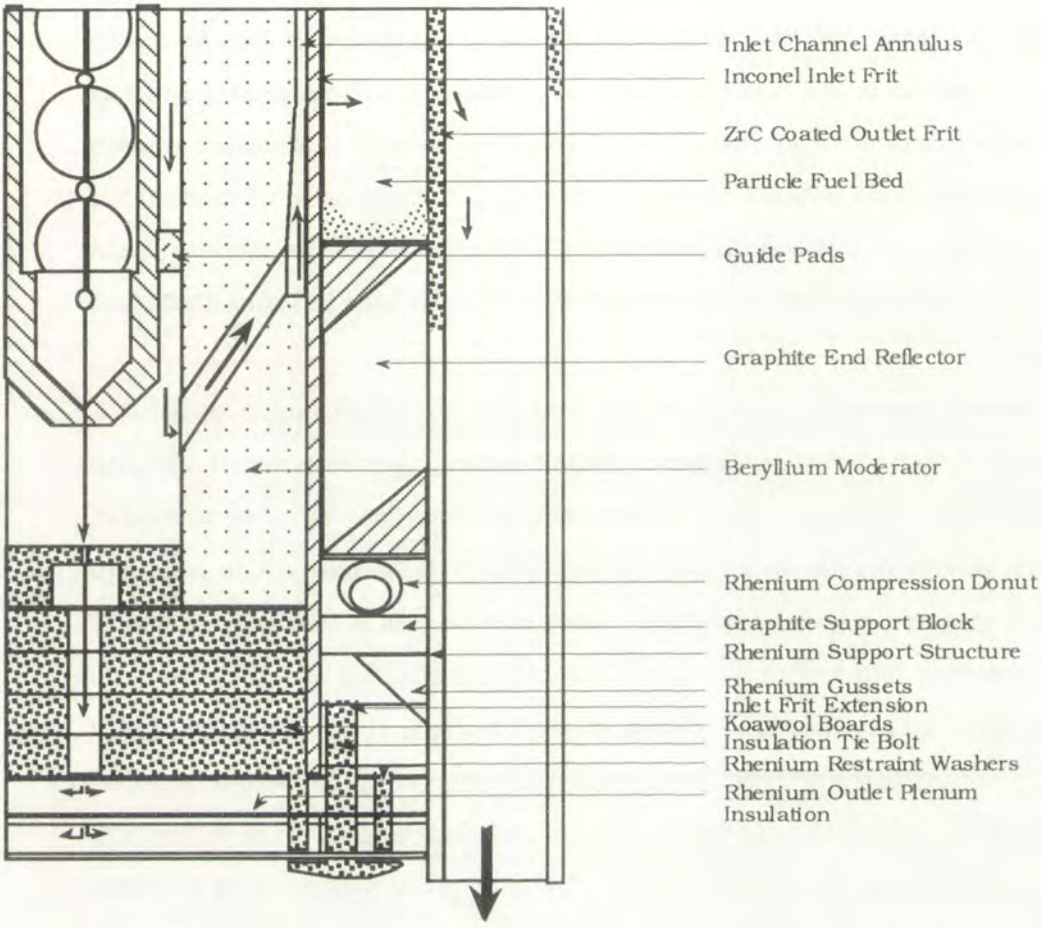

Figure 8 Particle Bed Fuel Element Outlet to Plenum

These end members are maintained at approximately 2000°K by a bleed stream from the inlet coolant channel. At the inlet end of the fuel element a stainless steel spring washer and compression nut maintain load on the bed. These members are kept at coolant inlet temperature.

A principal feature of the particle bed reactor is the low operating temperature throughout most of the reactor (Refs. 23, 24, 25, 26). The only portions at high temperature are the hot frits and part of the fuel particle bed. If a hot end design approach is used, the graphite plugs and rhenium load members at the outlet of the fuel elements are above 2000°K.

Another principal feature of the particle bed reactor is the low core pressure drop and coolant velocity. For the NERVA reactor, the core pressure drop and exit Mach number in the coolant channels were high (approximately 3.0 MPa pressure drop and Mach number of 0.25). In the particle bed reactor, core pressure drop is an order of magnitude less than the NERVA reactor, and the Mach number at the end of the hot frit channel is only 0.2. Low pressure drop and Mach number ease structural design and increase reliability.

A third principal feature of the particle bed reactor is simple construction and low thermal stress. In the NERVA design, the solid graphite elements experienced large temperature differences. The inlet end of the element operated at approximately 200°K and the outlet at approximately 2700°K. Thermal expansions and stresses were large, requiring a complex support structure. In the particle bed reactor, the same differential temperature is taken across a thin packed bed of small particles. The bed readily accommodates high temperature gradients and rapid changes in temperature. The hot frit is the only structural element at high temperatures. It operates at constant temperature along its length. The hot frit is not constrained axially, and readily expands and contracts when its temperature changes, i.e., startup and shutdown. Particle bed reactor elements subjected to rapid heating and cooling, up to approximately 500°K/s, have shown no damage, even after dozens of cycles (Refs. 27, 28). This rate of temperature change is an order of magnitude higher than NERVA.

A fourth principal feature of the particle bed reactor is very low radiation damage and fuel burnup. This contrasts with continuous power reactor systems for nuclear electric propulsion, where radiation damage and burnup are orders of magnitude higher. A typical particle bed reactor orbital transfer mission burns only 0.1 percent of the reactor fuel, and the total neutron fluence is only 10^{18} n/cm^2 (Ref. 21). The particle bed reactor materials and fuel particles need not demonstrate high radiation damage resistance, only the ability to operate at the temperature and pressure of the coolant.

An allied feature is the low radiation dose to the payloads. The propellant, tankage, and other structure already present in the particle bed reactor provide good shielding, and extra shielding is not required because of the short operating time (fluence at the payload is below 10^{12} n/cm^2, and gamma dose below 10^4 rad, compared to the allowable values of 10^{13}n/cm^2 and 5x10^5 rad for SP-100 payloads) (Ref. 21).

1.3.3 Wire Core Reactor

The wire core reactor is based on results of developmental studies of nuclear rocket propulsion systems. The reactor core is made up of annular fuel assemblies of continuous clad fuel wires (Ref. 29). Between subsequent layers of fuel wires, unfueled spacer wires maintain wire spacing and allow coolant flow through void spaces. The spacers are held in place by wire tension. Figures 9 and 10 show the fuel assembly construction sequence and the final fuel geometry and coolant flow through it. The fuel annuli are stacked side by side and smaller annuli nest inside larger annuli to form the core.

The wire core reactor shown in Figures 11 and 12 has a fast neutron spectrum. Coolant flows into the reactor axially from either or both ends and radially outward through the fuel. The central void region can be occupied by a single rod with two sections, one of beryllium and one of poison. Axial motion of the rod controls the amount of reflector (beryllium) or poison in the reactor and, with it, the reactor power level. One of the alternate methods of reactor control, which is the model employed in this dissertation, utilizes control drums in the reflector region and eliminates the central control rod. Beryllium reflectors surround the core, and the entire core is encased in a pressure vessel.

The fuel wires have a uranium mononitride (UN) core, clad with either pure tungsten or tungsten-5 weight percent rhenium (W-5Re), with an outer diameter of 0.5 to 2.5 mm. The spacer wires are thinner than the fuel wires

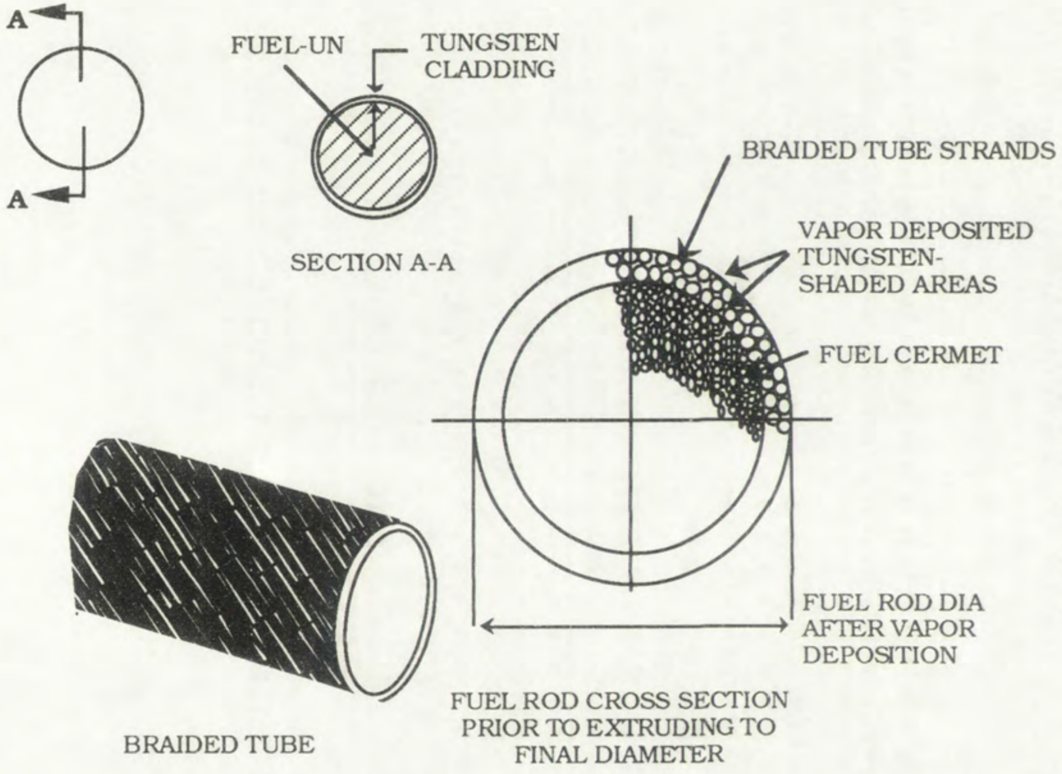

MAKING FUELED WIRE

- Obtain 8 mil Tungsten Wire
- Braid Wires Into 125 mil diameter Tube
- Obtain 4 mil Size UN Fuel Particles
- Fill Braided Tube With Coated Fuel
- Vapor Deposit Tungsten on Filled Tube
- Swage Tube From 125 to 75 mils
- Draw to 35 mil diameter Finished Wire

Figure 9 Wire Fuel Fabrication

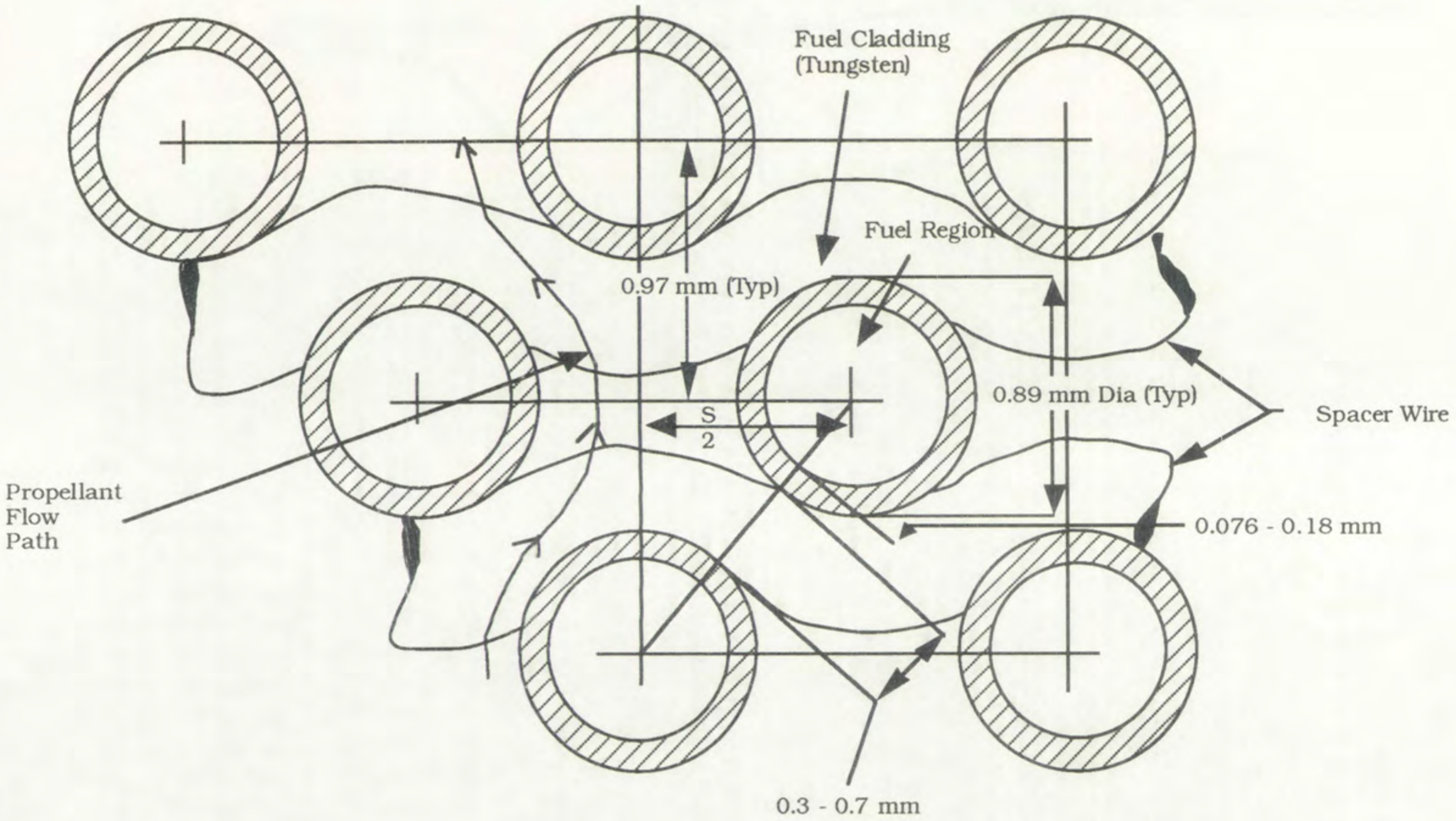

Figure 10 Wire Core Reactor Fuel Matrix

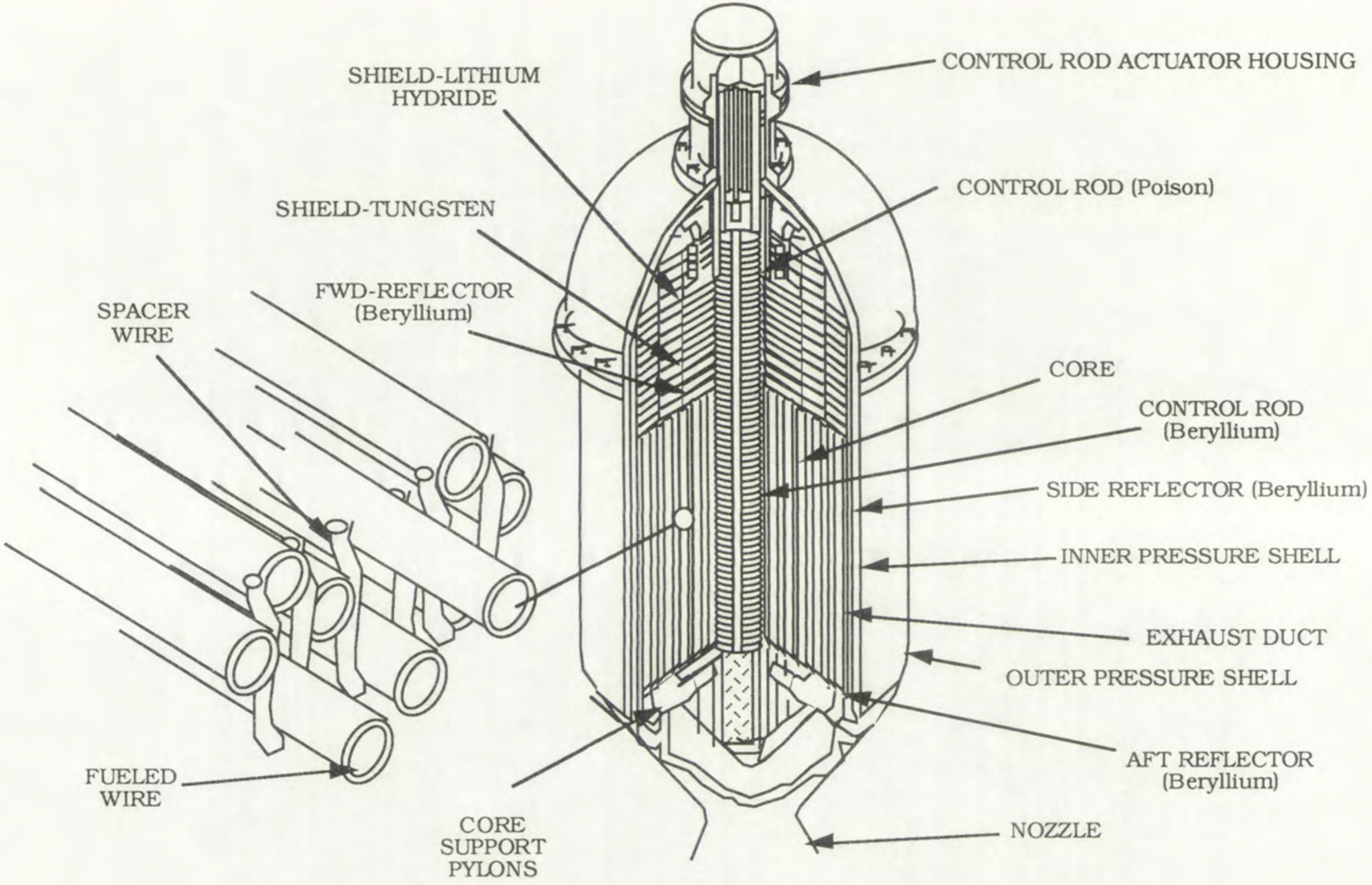

Figure 11 Wire Core Reactor

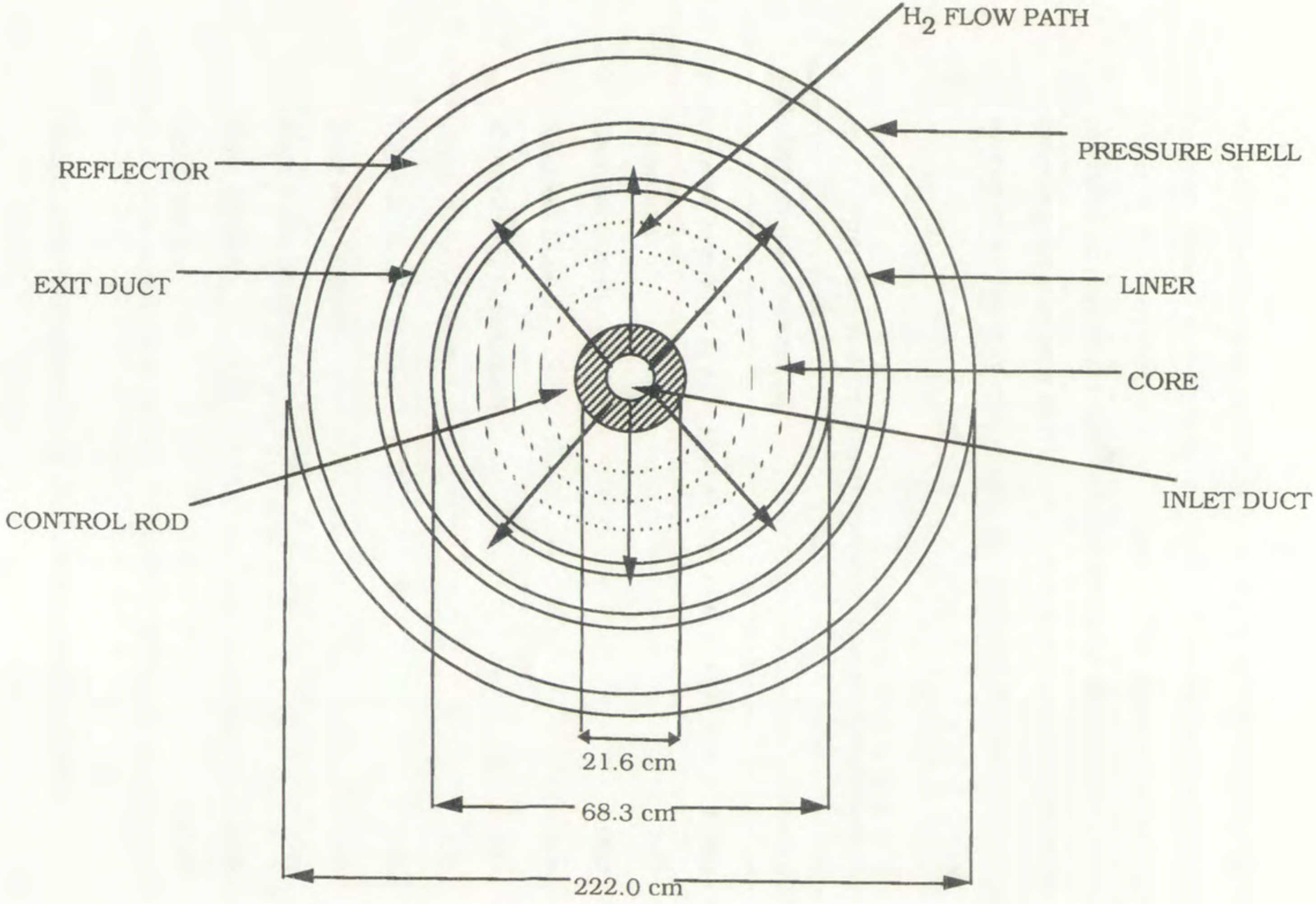

Figure 12 Wire Core Reactor Cross Section

and are assumed to be either pure tungsten or W-5Re. The small diameter of the wire helps keep the peak fuel temperature down.

Table 7 gives the reactor/shield assembly weight breakdown for the wire core reactor. Table 7 can be compared with Table 6 for the particle bed reactor and Table 4 for the NERVA small engine. The mass estimates from Table 7 provided an initial starting configuration for the detailed wire core reactor modeling for use as a ROTV which is described in Appendix B. Final mass estimates for the wire core reactor are provided in Table B12 in Appendix B.

Table 7

Wire Core Reactor Shield Assembly Weight Breakdown

Constructural Parameter	Mass (kg)
Active Core	1,560
Reflectors	910
Gamma Shield	1,060
Neutron Shield	245
Control and Actuators	190
Outer Pressure Shell	425
Inner Pressure Shell	255
Core Rear Support	115
Core Front Support	160
Core Sheath	165
Total Weight	**5,085**

1.4 Safety Issues Pertaining to the Design of a Nuclear Rocket

Rapid and accurate control of both thrust and temperature are critical to a nuclear rocket successfully completing its mission. Control of these two parameters as well as engine component characteristics establish the method of propulsion system control. Some of the more important safety requirements and engine characteristics are as follows (Ref. 9):

a. Maximum core temperature which imposes a limitation on maximum propellant temperature and engine specific impulse

b. Maximum core temperature change rates which must be limited due to core thermal stress considerations

c. Turbopump performance characteristics which generally influence the selection of operational techniques and require consideration of turbine power and maximum turbine inlet temperatures

d. Reactor nucleonics which play an important role in establishing control system requirements

e. Reactor criticality and reactivity contributions, which are a function of operating power level, duration, and thermodynamic-hydrodynamic interactions

f. Nuclear safety considerations which add an additional burden to safety and reliability problems already common to chemical rocket engines.

Nuclear rocket engine design requires optimization of three coupled stages within the startup, power operation, and shutdown processes. These stages are increase/decrease in reactor power, temperature increase within the core, and increase/decrease in hydrogen flow. Increasing reactor power in a time optimal fashion without exceeding any safety limits is the most critical aspect of the overall rocket startup (Refs. 30, 31, 32). The possibility of prompt criticality in an optimum startup demands that a nuclear rocket have a built-in control system. The power level desired for heatup may be below the ultimate maximum power level when full hydrogen flow conditions are reached.

To minimize coolant consumption during a reactor power increase at least some minimum coolant flow will be necessary to insulate the reactor from its outside pressure shell (Ref. 33). An outside shell is required to hold a high-pressure reactor together but cannot withstand extremely high temperature. Minimizing coolant consumption during this phase will allow more payload and increase the advantages of nuclear rockets when compared to chemical rockets. The desired power level for heatup must be reached as quickly as possible with little or no overshoot to prevent exceeding any stress limits (Ref. 34).

The second coupled phase of the engine startup is reactor heatup. Since temperature is increased most rapidly by low coolant flow and high reactor power, thermal stress minimization is of vital concern during an optimal heatup. These stresses can be roughly minimized by utilization of a linear increase in average core temperature. These thermal stresses, however, necessitate a limit on the rate of change of temperature at low flow rates. This constraint can probably be best approximated by a constraint of reactor power. As was previously mentioned, this constraint may very well be less than the rated design power. The temperature response phase is potentially the slowest phase on a time duration basis when compared to power and coolant flow rate increases.

During the coolant flow increase phase, the introduction of hydrogen coolant adds a significant amount of positive reactivity. Even though a highly enriched uranium cores possess a prompt negative temperature coefficient, some sort of mechanical device will probably be required. The coupling between the three phases of engine startup is due to the negative temperature coefficient of reactivity for the heatup phase and the positive density coefficient of reactivity during the hydrogen coolant increase phase. Both short-term and long-term control can be accomplished by a combination of these three sources of reactivity (Ref. 35). The following equation represents this relationship:

$$\rho = \rho_{CR} + \alpha_H (P_H/T_H) + \alpha_T (T_C)^{1/2} \tag{1.5}$$

where,

ρ = reactivity
ρ_{CR} = control device reactivity
α_H = hydrogen density reactivity coefficient
P_H = hydrogen pressure
T_H = hydrogen temperature
α_T = bare core temperature reactivity coefficient
T_C = core temperature.

For safety considerations there should be sufficient control device reactivity to overcome any positive or negative reactivity swings due to hydrogen density or core temperature.

The hydrogen density effect is the result mainly of the moderating ability of hydrogen. Increased hydrogen density decreases the fast leakage of neutrons and increases the reactivity. The negative temperature coefficient arises from the decrease in neutron absorption in the fuel with increased temperature. This results in an increase in the neutron diffusion length and a resultant decrease in reactivity. Control device reactivity either increases or decreases neutron density by the relative position of the neutron absorbing constituents within the rods or drums (described in more detail in Section 1.3).

The desire to keep the propellant exhaust temperature at its highest possible value requires that steady state thermal stresses be kept near limiting values. The steady state thermal stresses were proportional to the power density for a given NERVA core geometry. Since transients such as flow increases can cause transient thermal stresses which are considerably higher than steady state stresses, some limitation must be imposed on transients (Refs. 36, 37). However, to accomplish an optimum startup the coolant flow level must be changed from one level to another in minimum allowable time. Therefore, one critical safety concern in an optimum startup is increasing coolant flow to its desired level in minimum time without exceeding the maximum tolerable thermal stress.

For the simplified NERVA example, where a constant reactor power level is assumed in the axial direction, maximum stress remains at the channel exit for the complete transient. However, when the power level is a function of axial position and maximum power is not at the channel exit, the maximum stress point may no longer be at the exit.

For the case when power level is a function of axial position:

a. The maximum steady state stress will occur at the position of maximum power level
b. The time required to increase hydrogen flow to its desired level is decreased by greater curvature in the axial power distribution
c. The position of maximum thermal stress shifts during the flow increase.

In Reference 36 three different power distributions as shown in Figure 13 are assumed to illustrate the above points. The optimal time to complete a 20 percent increase in flow is shown in Figure 14. It can be seen that the time almost doubles for the flattest power distribution as compared to the one with the most curvature.

In Figure 15 the position of maximum thermal stress (combination of both steady state and transient stress) is plotted versus time during this transient. For the power distribution with the most curvature, the maximum stress

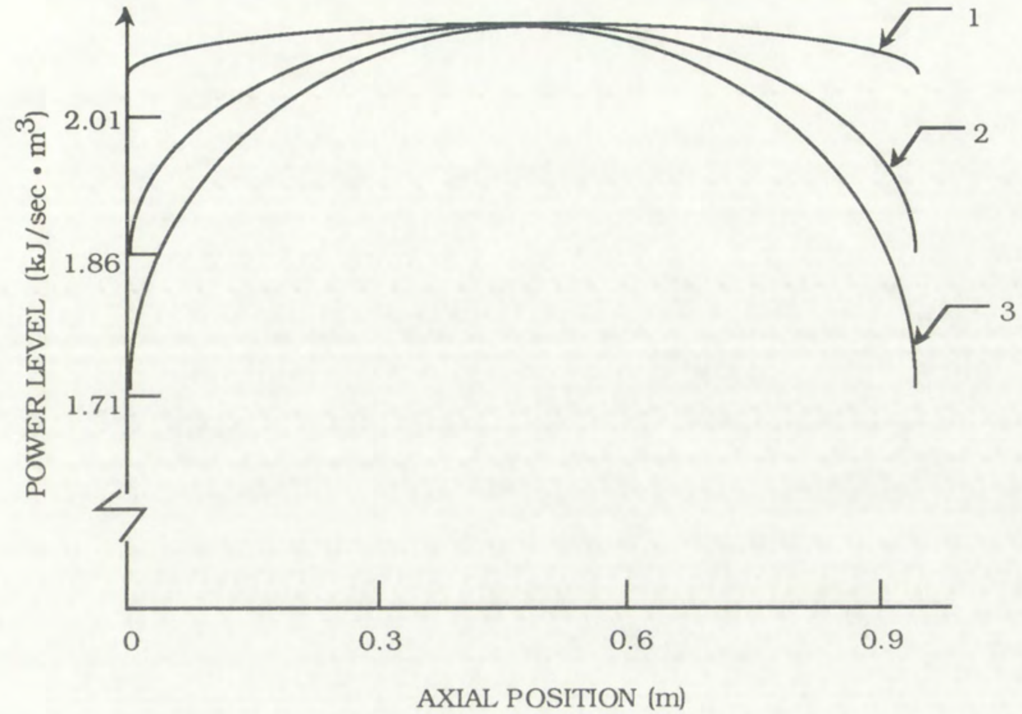

Figure 13 Power Level as a Function of Axial Position - Three Distributions

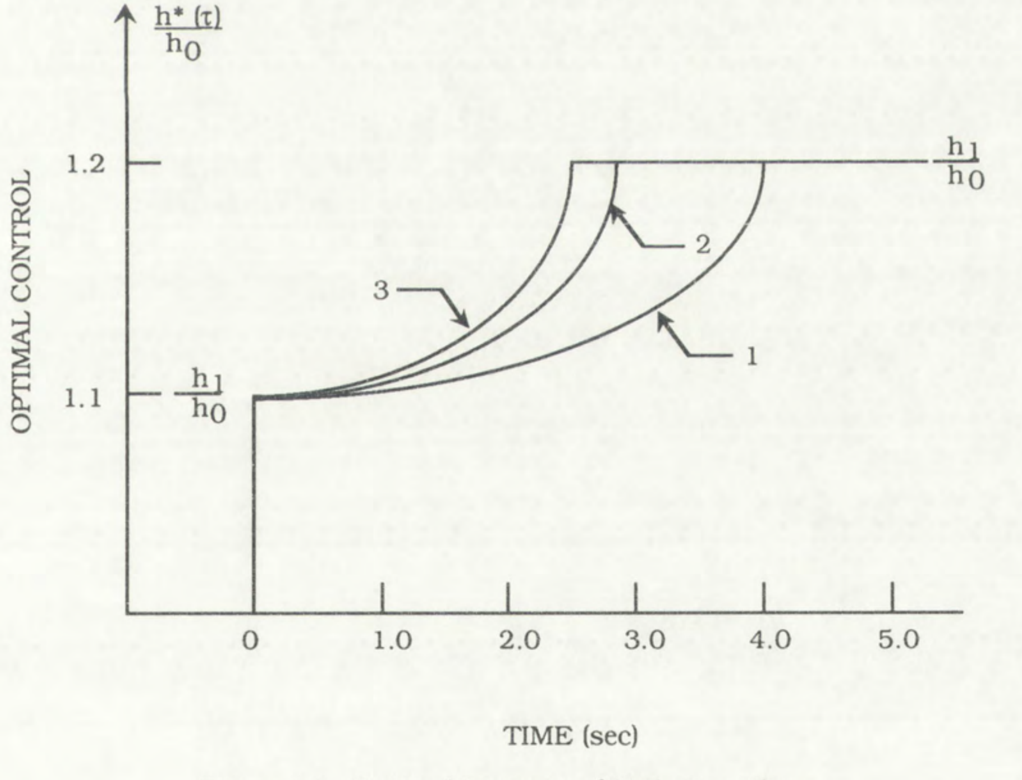

Figure 14 Optimal Increase of Hydrogen Flow

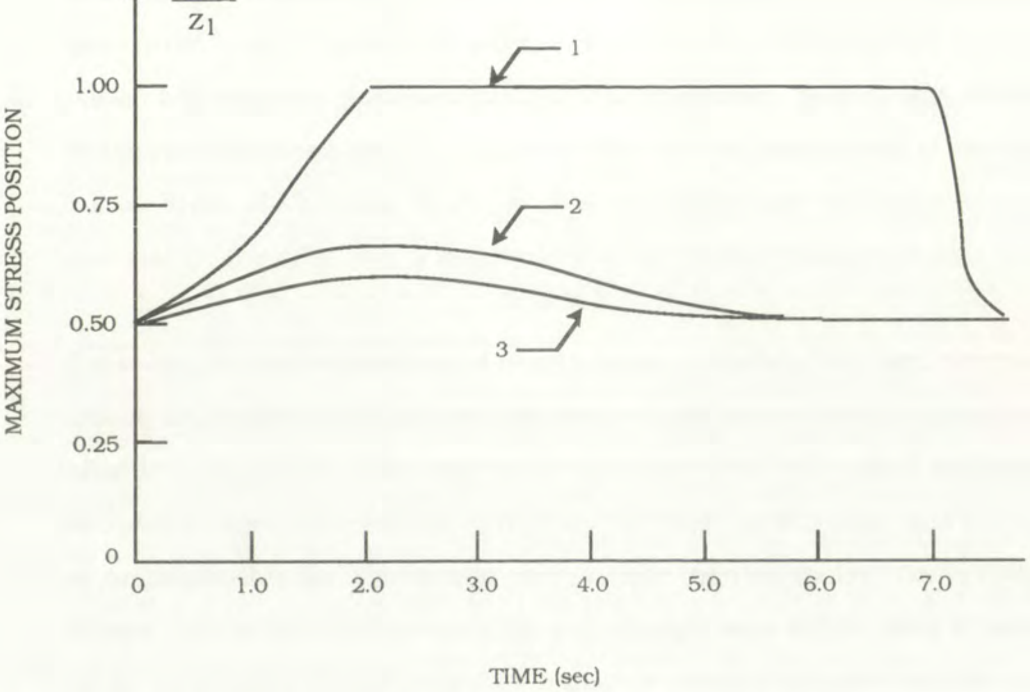

Figure 15 Position of Maximum Thermal Stress During Optimal Transient

point shifts only slightly away from the position of maximum steady state stress. For the flattest distribution, the point of maximum stress reaches the channel exit and remains there for most of the transient.

From this example it can be seen that a time optimal solution, regardless of the assumed axial power curvature, requires that maximum stress be kept at its limit somewhere within the channel and should not exceed a stress limit anywhere within the channel. Also, from a thermal stress limit standpoint, the time for this third phase of the engine startup can be minimized by increasing the axial flux curvature.

1.5 Discussion of a Reusable Orbital Transfer Rocket

Conventional chemical rockets are a very tightly coupled system compared to nuclear thermal rockets. The energy release from the chemical reaction determines the peak temperature that can be obtained in the combustion chamber. The nature of the chemical reaction also determines the startup and shutdown times for the engine. Also, the engine sizing is optimized for one thrust level. In a nuclear thermal rocket engine, the propellant gas can be varied independent of the peak chamber temperature. Startup and shutdown times can be varied over a wide range due to this uncoupling of the energy source from the working fluid. It appears at this time that nuclear rockets can also be throttled over a much wider range than chemical rockets.

Therefore, in the early stages of development, a study of the impact of engine design on control strategies and systems should prove useful. Based on the chemical experience base, one might conclude that very short startup and shutdown times are essential. This may not really be the case, and it appears to be impossible for a prismatic core nuclear thermal rocket like the NERVA design. Nominal startup times for that design were in the tens of seconds range (approximately 80 seconds). It may be possible to speed up the startup sequence used for that engine, but it is not clear how much. The major problem with slow startup sequences is the ineffective use of coolant (hence a mass penalty) during the low power portion of the transient. If the required burn at full thrust is of the order of 10 seconds, then an 80 second startup sequence may well be very inefficient.

In order to define what is required, in terms of engine thrusting times, this study will focus on the thrust requirements for a Reusable Orbital Transfer Vehicle. A ROTV has been proposed by both NASA and DoD (the Department of Defense) as being useful for their national missions. This is a near term mission, not quite in the category of the NASA manned trip to Mars. However, in order to safely go to Mars with a nuclear powered vehicle, near earth testing will have to be performed, and the ROTV is one potential operational testing mission. The national plan to develop a nuclear thermal rocket engine is based on the manned Mars mission, however, and this complicates the development of a ROTV. For the Mars mission, a high thrust engine is required (~333.6 kN). This engine may be overkill for the level of payloads likely to be ferried from low earth orbit to high earth orbit by a

ROTV. At that thrust level some burn times will be very short and a propellent penalty will have to be paid for long startup times.

Consider the following scenario. A ROTV designed to move nominal payloads from low earth orbit to geosynchronous earth orbit must burn four times to complete a circuit (Ref. 8). Its first, and longest burn, departs the low earth, nearly circular orbit and injects the vehicle on a Hohmann transfer elipse. When the vehicle reaches apogee and geosychronous altitude, a second burn is required to circularize its orbit there. After the payload is unloaded, a third burn puts the transfer vehicle on a return Hohmann elipse to low earth orbit. A fourth burn is required to circularize the low earth orbit. The fuel required to return the vehicle for reuse will be a significant fraction of the payload for near term payloads. Therefore, this fuel should be used as efficiently as possible. The third and fourth burns are the shortest ones. Thus inefficiencies in using the propellant on these burns will have the largest mass penalties.

Table 8 presents nominal burn times for a ROTV hauling various payloads from LEO to GEO (Refs. 8, 14). It is based on a 333.6 kN thrust engine using a particle bed reactor design, rather than a NERVA-like design. The particle bed design appears to be considerably lighter than the NERVA design and therefore better suited for this mission. Three payloads are considered; 1 MT, 5 MT, and 10 MT. (Current payloads required in GEO are in the 2 MT class.) The required tankage has been estimated based on a structure mass factor of 15 percent of initial propellant mass contained.

Table 8

ROTV Burn Times (sec)

Payload	Burn 1	Burn 2	Burn 3	Burn 4
1 MT	50	35	12	9
5 MT	200	140	48	36
10 MT	350	245	84	63

The nominal engine weight for the ROTV is 2 MT. If a heavier engine is developed, like the NERVA engine, then the run times will not be as short nor will the ROTV be as cost effective, assuming the engine lifetimes are similar.

One solution to the above short run times is to develop a lower thrust engine. If the thrust is reduced by a factor of three to about 111.2 kN, the engine weight can be reduced slightly to about 1.5 MT (Ref. 8). The run times will be approximately three times as long. This may add additional gravity losses during the long burns, that were not considered in the above analysis, but they should not be very significant. However, by changing the size of the engine, a different development and manufacturing effort may be required. This could add significantly to development costs. For all rocket engine models considered in this dissertation, a reference thrust level of 72 kN was chosen based on the NERVA small engine design.

1.6 Research Approach

To determine the impact of engine design on control strategies, a range of designs must be considered. To base all of the analysis on a NERVA design may give the wrong answer. NASA had considered no less than 10 designs for solid core nuclear thermal rockets. These designs have many similarities and some significant differences. In order to cover the main differences, three representative concepts have been chosen for this study. These concepts are listed in Table 2 with a short summary of their major differences. They were chosen to represent the spectrum of possible solid core reactor types which had been considered by NASA for the Space Exploration Initiative. The tools developed in this study can be applied to this and other concepts in the future if the need arises.

This research will investigate the impact on control strategies of three solid core nuclear rocket designs. Control strategies, as discussed in Chapters 2 and 5 and in detail in Appendix A, are defined in terms of control and safety margins, and startup algorithms.

Control and safety margins which are essential in coping with external events will be analyzed by using a nuclear rocket engine modeling code (STRTUP computer code) which will be discussed in Section 4.4. Startup algorithms will be implemented in the nuclear rocket engine modeling code to demonstrate efficient and safe operational procedures for each of the three types of reactors. Efficiency will be defined in terms of the effective specific impulse obtainable as compared with the propellant consumed during engine startup.

The research approach will consist of:

a. Developing parametric static design models for each of three engine types as a function of thrust level

b. Calculating dynamic neutronics, heat transfer, and turbopump parameters for each of the three designs

c. Developing and running a modeling code to analyze startup sequences for each design.

This approach will aid in defining a quantitative basis for the impact of solid core nuclear rocket engine design on usable control strategies. The emphasis here will be on startup concerns. There is more flexibility in control of the startup process than there is in the shutdown sequence due to the presence of the delayed neutron tail during shutdown. The penalties paid by a nuclear thermal ROTV for the shutdown sequence may be a characteristic of all such vehicles. At any rate the shutdown optimization part of the analysis has been left for future work.

2.0 SUMMARY OF NUCLEAR ROCKET STARTUP MODELING EQUATIONS, CONTROL TECHNIQUES, AND SAFETY IMPLICATIONS

In Appendix A, a derivation of the Smith-Stenning equations (Refs. 38, 39, 40, 41) as they apply to nuclear rocket control is provided. These equations were coded into the STRTUP computer program which is described in Chapter 4. The open loop dynamic performance of a nuclear rocket engine with either a bleed turbine or topping turbine drive can be accurately described by a system of ordinary, nonlinear differential equations (Refs. 38, 39, 40, 41). These equations, which model neutron kinetics, delayed neutron precursor density, core hear transfer, and a turbopump, are given in Equations (2.1) through (2.4), respectively:

$$\tau_m \frac{dp'}{dt} = \left(\frac{\rho}{\beta} - 1\right)p' + z' \tag{2.1}$$

$$\tau_D \frac{dz'}{dt} = p' - z' \tag{2.2}$$

$$\tau_c \frac{dT'_2}{dt} = P' - P'_1\sqrt{T'_2} \tag{2.3}$$

$$\tau_p \frac{dP'_1}{dt} = P'_1\sqrt{T'_2} - P'^2_1 / \sqrt{T'_2} \quad . \tag{2.4}$$

where,

τ_m = neutron kinetics response time constant

P' = ratio of reactor power to its design value

ρ = reactivity

β = effective delayed neutron fraction

z' = ratio of neutron precursor density to its design value

τ_D = delayed neutron precursor response time constant

τ_c = outlet temperature response time constant

T'_2 = ratio of outlet temperature to its design value

P'_1 = ratio of inlet pressure to its design value

τ_p = turbopump response time constant.

NERVA controller design was an ongoing and evolving process from the late 1950s until the program was terminated in the early 1970s. Appendix A gives a description of the control design that was in place just prior to program termination. Also provided in Appendix A is a detailed description of current control methodology for accomplishing a time optimal startup and the safety issues pertaining to a time optimal startup.

3.0 SUMMARY OF WIRE CORE REACTOR MODELING

Models exist in the literature for both the NERVA small engine and particle bed reactors, therefore no additional modeling development for these reactor types was performed. In the case of the wire core reactor, a comparable model to the other reactor types was unavailable. Therefore, prior to assessing the impact of nuclear rocket engine design on control strategies, modeling of the wire core reactor was performed. Appendix B describes this modeling process.

Table 9 gives the final dimensions and masses by region for the wire core model. These dimensions and masses will be utilized in the startup strategy comparison analysis which is described in Chapters 4 and 5.

Table 9

Wire Core Regions – Material Constituents, Masses, and Dimensions

Region	Outer Radius (cm)	Material	Mass (kg)
Inlet Hole	4.5	Hydrogen	
Inlet Frit	5.0	Aluminum	9.14
Fuel	26.63	UN	375.03
		Tungsten	580.96
Exit Duct	28.31	Hydrogen	
Liner	29.31	Carbon Steel	26.83
Reflector	44.31	Beryllium	570.72
		Control Drums (B_4C)	32.54
Pressure Vessel (within cylinder)	46.31	Stainless Steel	422.76
		Aluminum	142.63
Pressure Vessel (hemispherical ends)		Stainless Steel	211.00
		Aluminum	71.19
	Total	**Stainless Steel**	**2,228.98**
		Aluminum	**1,809.04**

4.0 MODELING OF STARTUP PROBLEMS FOR THE WIRE CORE, PARTICLE BED, AND NERVA REACTORS

A Reusable Orbital Transfer Vehicle which is designed to move nominal payloads from low earth orbit to geosynchronous earth orbit must burn four times to complete a circuit. The burn times versus payload were given previously in Table 8. The fuel required to return the vehicle for reuse will be a significant fraction of the payload for near term payloads. Therefore, this fuel should be used as efficiently as possible. Inefficiencies in using the propellant on the third and fourth burns (returning to LEO) will have the largest mass penalties. As can be seen from Table 8, the smaller the payload the shorter the required burn time, and also the greater the potential mass penalty. Therefore, optimizing reactor startups is an important component in maximizing the efficient use of a ROTV.

This chapter will discuss the modeling process for reactor startups for the wire core, particle bed, and NERVA reactors. In Section 4.1, a comparison of key reactor parameters is discussed. Section 4.2 describes the response time constants associated with the nuclear rocket model. Also, the response time constant parametric value assignment for each of three reactor types will be given. In Section 4.3, the key equations for the nuclear rocket model will be summarized. Finally, Section 4.4 discusses the computer code which was developed for this dissertation to model the startup of a nuclear rocket engine.

4.1 Comparison of Rocket Engine Parameters

Before the modeling process commenced a list of key rocket engine parameters for the particle bed reactor was compiled (Refs. 15 through 28). Some of these parameters were applicable to the wire core and NERVA small engine reactors while others were not. Table 10 presents the results of this literature search. In the case of the wire core reactor, very little information was available in the literature, therefore most of the parametric values listed were derived from the model which was constructed as part of this dissertation. The NERVA reactor has a substantial amount of description in the literature. In its case, References 10 through 13 as well as Reference 5 were primarily utilized in the development of Table 10.

Table 10

Comparison of Rocket Engine Parameters

Parameter	Wire Core	Particle Bed	NERVA
Nozzle Density (g/cm^3)	2.7E+0	2.7E+0	2.7E+0
Vessel Yield Strength (Pa)	2.5E+8	2.5E+8	2.5E+8
Top Reflector Thickness (cm)	5.0E+0	5.0E+0	5.0E+0
Inner Radial Reflector Thickness (cm)	1.5E+1	6.0E+0	1.17E+1
Bottom Reflector Thickness (cm)	5.0E+0	5.0E+0	5.0E+0
Fuel-to-Moderator Volume Ratio		7.0E–1	
Core Height-to-Radius Ratio	2.0E+0	2.0E+0	2.78E+0
Power Shape Factor	1.0E+0	1.0E+0	1.0E+0
Pump Pressure Ratio	3.0E+1	3.0E+1	5.025E+1
Pump Efficiency	6.5E–1	6.5E–1	6.5E–1
Turbine Inlet Temperature (°K)	4.28E+2	4.28E+2	4.28E+2
Turbine Efficiency	9.0E–1	9.0E–1	9.0E–1
Chamber Pressure (Pa)	3.1E+6	3.1E+6	3.1E+6
Chamber Temperature (°K)	2.7E+3	2.7E+3	2.7E+3
Nozzle Exit Pressure (Pa)	1.0E+4	1.0E+4	1.0E+4
Nozzle Divergence Angle (°)	1.5E+1	1.5E+1	1.5E+1
Nozzle Material Yield Strength (Pa)	6.0E+8	6.0E+8	6.0E+8
Core Inlet Temperature (°K)	2.0E+2	2.0E+2	2.0E+2

Table 10

Comparison of Rocket Engine Parameters (continued)

Parameter	Wire Core	Particle Bed	NERVA
Core Moderator Coolant Volume Fraction	Moderator - 56.9% Spacer Wires - 10% Cladding - 5.2% Fuel - 27.9%	1.0E–1	
Outer Frit Thickness (cm)		1.5E–1	
Outer Frit Density (g/cm^3)		2.7E+0	
Outer Frit Volume Fraction		7.5E–1	
Inner Frit Thickness (cm)	5.0E–1	5.0E–1	
Inner Frit Density (g/cm^3)	2.69E+0	2.69E+0	
Inner Frit Volume Fraction	6.7E–1	6.7E–1	
Relative Frit-to-Bed Pressure Drop	1.0E+1	1.0E+1	Core Pressure Drop 2.97 MPa
Number of Fuel Elements		1.9E+1	5.64E+2 - fuel elements 2.41E+2 - support elements
Fuel Element Exit Mach Number	2.5E–1	2.5E–1	2.5E–1
Peak MW/L	5.0E+0	1.0E+1	1.0E+0
Fuel Kernel Radius (cm)	Wire diameter - 3.69E–2 Core diameter - 97.88 cm	1.4E–2	Core diameter - 57.0 cm
Fuel Kernel Density (g/cm^3)	1.30E+1	1.11E+1	
Low Density Carbon Radius (cm)	Tungsten Clad Tungsten radius - 4.45E–2	1.7E–2	Elements 0.89 cm - long 1.91 cm flat-to-flat

Table 10

Comparison of Rocket Engine Parameters (concluded)

Parameter	Wire Core	Particle Bed	NERVA
Low Density Carbon Density (g/cm^3)	Tungsten density - 19.2	9.5E–1	Fuel element contains 19 coolant channels
Pyrolytic Carbon Radius (cm)		2.1E–2	52.4 kg of uranium
Pyrolytic Carbon Density (g/cm^3)		1.9E+0	
Zirconium Carbide Radius (cm)		2.5E–2	
Zirconium Carbide Density (g/cm^3)		6.44E+0	

The first set of parametric values given in Table 10 are associated with the turbopump. As was previously discussed in Chapter 1, a turbopump will be modeled to minimize the overall vehicle structural weight. Either a topping or a bleed cycle can be employed to power the turbine. In a chamber bleed system, gases are bled off directly from the main combustion chamber. In a topping cycle, the heated hydrogen gas emerging from the thrust chamber cooling jacket is used as the turbine working fluid before being injected into the main combustion chamber. Topping gas turbine drives render the highest possible theoretical cycle efficiency.

Most chemical rocket turbopumps have employed either single or multistage centrifugal pumps. However, when hydrogen is utilized as the rocket monopropellant, multistage axial pumps have typically been constructed. This design is well-suited to liquid hydrogen service which entails the problems of extremely low fluid temperature and density. Low fluid density results in high volume flow and in high pressure head requirements. For applications at either flow rates higher than 27 kg/s or pressure head rises above 9.65 MPa, a multistage axial pump is generally superior with respect to construction and performance (Ref. 42).

Since both the flow rates and pressure heads developed for the NERVA XE' and small engines were less than the design values where an axial pump has significant performance advantages, the pump which was constructed for the XE' engine and proposed for the small engine was a single-stage, radial exit flow type with an aluminum impeller. A single-stage turbine with stainless steel rotors was coupled to the pump. Also, a full flow topping cycle was employed.

The particle bed and wire core reactor models will have propellant flow rates and thrust levels matched to the NERVA small engine design. Also, both reactors will utilize hydrogen as the propellant. Therefore, one turbopump design will be initially chosen for all three rocket engine models, and the following turbopump design parameters will be standardized:

a. Pump efficiency
b. Turbine inlet temperature
c. Turbine efficiency.

The turbine and pump efficiencies listed in Table 10 were chosen based on typical parametric values for single-stage centrifugal pumps and single-stage impulse turbines (Ref. 42). Also, a comparison was made with the NERVA XE' engine turbopump turbine and pump efficiencies (Ref. 5). A design value for topping cycle turbine inlet temperature was chosen from Reference 5.

The pump pressure ratio will vary between the three designs. The pressure drop across the NERVA small engine design is substantially greater than either of the two folded flow core designs. From Reference 5 the typical pressure drop across the NERVA small engine core was from 6.03 to 3.10 MPa, approximately a factor of two. Pressure drops for the folded flow core particle bed and wire core designs can be expected to be approximately ten percent (Ref. 20). Therefore, when a fixed chamber pressure is employed for all three reactor models, the design outlet pressure of the turbopump for the NERVA model will be almost a factor of two greater than the other two reactors.

The next rocket engine design parameters to be discussed will be those associated with the rocket nozzle. The design values chosen for nozzle parameters will be standardized for the three rocket engine designs since the propellant type, core exit Mach number, and thrust levels are identical.

The nozzle divergence angle is defined as the half angle made by the divergence cone with respect to the rocket axis. Optimum divergence cone half angles are generally between 12 and 18 degrees (Ref. 4). The divergence angle given in Figures 42 and 47 for the NERVA small engine (Ref. 5) is approximately 15 degrees. Therefore, the parametric value chosen for the nozzle conical half angle with respect to the rocket axis is 15 degrees.

The nozzle material yield strength and density are a function of the nozzle construction material(s). Aluminum will be utilized due to its relatively light weight and high material yield strength. Aluminum has also been proposed in many instances in the literature for use as the nozzle construction material (Refs. 4, 5, 18, 21). Therefore, the nozzle density is 2.7 g/cm^3 with a yield strength of 600 MPa.

The vessel shape was extensively documented for both the particle bed and NERVA designs. Typical values given for height-to-radius ratios were factors of two to three. For high strength, low weight applications, aluminum pressure vessels were discussed in the literature and in fact proposed for use for both the NERVA small engine and particle bed reactors. Therefore, an aluminum pressure vessel is the standardized choice for all three designs. Once the pressure vessel constituent material and dimensions are chosen, then the vessel yield strength is also known.

A number of constructional parameters given in Table 10 apply only to the particle bed reactor. These parameters are associated with the relative dimensions and material densities of the fuel particles themselves. Also, an outer frit is only applicable to the particle bed design. The following is a list of the parameters which had no ready comparison between the three designs:

a. Outer frit thickness

b. Outer frit density

c. Outer frit volume fraction

d. Low density carbon radius

e. Low density carbon density

f. Pyrolitic carbon radius

g. Pyrolitic carbon density

h. Zirconium carbide radius

i. Zirconium carbide density.

Where these constructional parametric values which only apply to the particle bed reactor are given in Table 10, a listing of similar constructional features for the wire core and NERVA designs is provided. For more details on wire core construction refer to Appendix B and Section 1.3.3. The NERVA small engine reactor physical construction is described in Section 1.3.1.

Both a top and bottom reflector were modeled for the three designs. In the case of the NERVA reactor, dimensions and constituent materials were matched with those from the small engine design (Ref. 5).

References 18 and 24 provided the basis for top and bottom reflector parametric value assignments for the particle bed reactor. No information existed in the literature for the wire core reactor. Also, the criticality and dimension analysis described in Appendix B did not consider the axial thickness or material constituents of the top and bottom reflectors. Therefore, assignment of values for the wire core was based on similar parametric values from the NERVA and particle bed designs.

An inner radial reflector is modeled for all three reactors. The reflector thickness for the NERVA reactor was taken from the small engine design (Ref. 5). The wire core inner reflector thickness was found during the criticality and dimension analysis performed as part of this dissertation. Finally, the particle bed inner reflector dimensions were taken from References 18 and 21.

A number of the comparison parameters are properties associated with the hydrogen propellant. To compare startup strategies between the three reactor models, these propellant properties were standardized. Therefore, the chamber temperature and pressure, core exit Mach number, and core inlet temperature parametric values were assigned consistently between the engines, even though other values were found in some of the references.

The number of fuel elements varied between the models. Also, the number of fuel elements for the particle bed reactor varied between References 15 through 28. Nineteen fuel elements were the most common number found in the literature for the particle bed reactor when the power level was similar to the 367 MWth small engine design. The number of fuel elements and support elements for the NERVA reactor was taken from Reference 5. The wire core reactor is composed of numerous fuel wires separated by spacer wires and as such does not have fuel elements which readily compare with either of the other two designs.

Power densities are much higher for the folded flow cores (particle bed and wire core reactors) than for the NERVA design (Refs. 20, 29). Reference 5 provided the power density for the NERVA small engine reactor. The folded core designs have power densities of approximately ten to fifty times greater than the small engine.

The final parameter compared in Table 10 is the fuel-to-moderator volume ratio. This parameter directly relates to the physical configuration and the desired neutron energy spectrum of the core. As was shown in Table 2, both the moderation and neutronics spectrum vary between the three reactor models. In the case of the wire core reactor, no moderation is required, therefore, this ratio is essentially infinite. The particle bed reactor has separate moderation and a thermal neutron spectrum. Therefore the particle bed design has the lowest ratio of fuel-to-moderator volume. References 18 and 21 provided the basis for the parametric value chosen for the particle bed. The NERVA reactor has an epi-thermal neutron spectrum with integral moderation. Therefore, the small engine design exhibits an intermediate value of fuel-to moderator volume ratio as compared with the two folded flow core designs.

As can be seen from the discussion in this section, the engine and reactor parameters which were listed in Table 10 fall into the following four general categories of comparison:

a. Due to physical differences in construction no comparison can be made
b. Parametric value requires standardization between engine models to compare startup strategies
c. Parametric value varies between models but this variance is not significant
d. Parametric value varies between models and this variance is significant.

Table 11 gives a categorization of each of the key rocket engine parameters listed in Table 10 based on the comparison scheme which has just been discussed.

In the following section, some of the parametric values given in Tables 10 and 11 will be utilized to assign design values for the neutronics, delayed neutron precursor density, core outlet temperature, and core inlet pressure response time constants for the three nuclear rocket engine models.

Table 11

Categorization of Key Rocket Engine Parameters

Parameter	Categorization
Nozzle Density	b
Vessel Yield Strength	b
Top Reflector Thickness	b
Inner Radial Reflector Thickness	d
Bottom Reflector Thickness	b
Fuel-to-Moderator Volume Ratio	d
Core Height-to-Radius Ratio	c
Power Shape Factor	b
Pump Pressure Ratio	d
Pump Efficiency	b
Turbine Inlet Temperature	b
Turbine Efficiency	b
Chamber Pressure	b
Chamber Temperature	b
Nozzle Exit Pressure	b
Nozzle Divergence Angle	b
Nozzle Material Yield Strength	b
Core Inlet Temperature	b
Core Moderator Coolant Volume Fraction	a
Outer Frit Thickness	a
Outer Frit Density	a
Outer Frit Volume Fraction	a
Inner Frit Thickness	a

Table 11

Categorization of Key Rocket Engine Parameters (concluded)

Parameter	Categorization
Inner Frit Density	a
Inner Frit Volume Fraction	a
Relative Frit-to-Bed Pressure Drop	a
Number of Fuel Elements	a
Fuel Element Exit Mach Number	b
Peak MW/L	d
Fuel Kernel Radius	a
Fuel Kernel Density	a
Low Density Carbon Radius	a
Pyrolytic Carbon Radius	a
Pyrolytic Carbon Density	a
Zirconium Carbide Radius	a
Zirconium Carbide Density	a

4.2 Description of the Rocket Engine Response Time Constants and Derivation of Associated Parametric Values

A description of the rocket engine response time constant equations will be presented here. For further detail on derivation of these equations refer to Appendix A and References 38 through 41. Also presented in this section will be a derivation of the parametric values for the neutronics, delayed neutron precursor density, core outlet temperature, and core inlet pressure response time constants.

The response time constant equations can be derived directly from the Smith-Stenning equations which describe the open loop dynamic performance of a nuclear rocket engine with either a bleed turbine or topping turbine drive. The Smith-Stenning equations will be summarized in Section 4.3.

4.2.1 Temperature Response Time Constant

The first of the response time constants described here was derived from the core heat transfer process model. The core heat transfer response time constant is as follows:

$$\tau_c = \frac{M_c \; C_{p_c} \; T_c}{\dot{m}_d \; C_p \; T_2} \tag{4.1}$$

where,

τ_c = core heat transfer response time constant
M_c = fuel mass
$\dot{m}_d$ = propellant mass flow rate at the design point
C_{p_c} = reactor specific heat capacity
C_p = propellant specific heat capacity
T_c = mean core temperature
T_2 = propellant outlet temperature.

Equation (4.1) illustrates that the temperature response time constant is a ratio of thermal energy buildup in the fuel to the energy removal rate of the propellant. The temperature response time constant (τ_c) was found to vary between the three modeled reactors. In this case some of the variables were fixed (i.e., identical parametric values for all three reactor models) when engine parameters such as thrust level and propellant type were standardized to insure consistency of comparison between startup results. Therefore, the following parameters were set to consistent values for the three reactor types:

a. Mean core temperature
b. Propellant mass flow rate

c. Propellant specific heat capacity

d. Core outlet temperature.

The variance in the temperature response time was, therefore, dependent upon only the fuel mass and the reactor specific heat capacity. The fuel mass for the wire core was taken from the criticality and dimension analysis which is described in Appendix B. For the NERVA small engine, the fuel mass estimate accounted for not only the uranium dicarbide fuel mass but also the moderator mass since the fuel was imbedded in the graphite moderator. Reference 5 provided the reactor mass value for the NERVA small engine. In Reference 21 design details for use of the particle bed reactor as a ROTV are given. A weight breakdown for the particle bed reactor and its fuel mass is given in Table 3 in Section 1.3.2. Fuel mass was solely used for determination of the particle bed temperature response time constant because its design employs separate moderation.

Fuel specific heat capacity depends upon the fuel type as well as the temperature of the fuel. If a constant mean core temperature of 1400°K is assumed, then fuel specific heat capacity will vary between the reactor models based upon only the material constituents of the fuel. In the NERVA model the fuel specific heat capacity is a weighted average of the fuel and moderator specific heat capacities. As is given in Table 2, the NERVA and particle bed reactors employ uranium dicarbide (UC_2) fuel while the wire core utilizes uranium mononitride fuel.

The specific heat capacity for both the UN and UC_2 fuel was taken from Reference 43. In the case of the UN fuel, the specific heat capacity was directly available from Figure 344 of Reference 43 (Volume 4). Two sets of tests provided data for the UN fuel ranging from 6°K to 1422°K. The specific heat capacity for UN fuel at 1400°K was found to be 247.4 J/kg·°K.

Two sets of tests were reported in Reference 43 for uranium dicarbide fuel. These tests are plotted on Figure 142 of Reference 43 (Volume 4). The data for

UC_2 fuel extends from 10°K to 673°K. Therefore, an extrapolation of the reported data was required to determine specific heat capacity at 1400°K. References 44 through 46 provided the theoretical basis for the extrapolation to a temperature above the range of the plotted data of Figure 142 in Reference 43. The specific heat capacity of UC_2 fuel at 1400°K was determined to be 292.2 J/kg·°K.

A summary of the values chosen for all variables associated with the temperature response time constant is provided in Table 12.

Table 12

Temperature Response Time Constant Variables for the Three Reactor Models

Variable	NERVA	Wire Core	Particle Bed
Fuel Mass (kg)	868	375	125
Reactor Specific Heat Capacity (kJ/kg·°K)	0.461	0.247	0.292
Propellant Mass Flow Rate (kg/s)	8.5	8.5	8.5
Propellant Specific Heat Capacity (kJ/kg·°K)	15.81	15.81	15.81
Mean Core Temperature (°K)	1400	1400	1400
Propellant Outlet Temperature (°K)	2700	2700	2700

4.2.2 Pressure Response Time Constant

The second of the response time constants is obtained from the model for the turbopump. It is derived from the turbopump speed equation. The turbopump response time constant is as follows:

$$\tau_p = \frac{I \; P_{1_d}}{2\phi_p K_p} \qquad (4.2)$$

where,

τ_p = turbopump response time constant
I = rotational moment of inertia
P_{1_d} = core inlet pressure at the design point
ϕ_p = turbine power at the design point
K_p = known constant.

To determine the turbopump response time constant, a specific pump and turbine design must be chosen. As can be seen from Equation (4.2), most of the variables associated with this time constant are independent of the reactor type being modeled. The only critical variable associated with reactor model is the pump design outlet pressure.

For any given pump design, the relation between fluid flow rate (Q), developed fluid head (ΔH), required driving power (hp), and rotating speed (N) can be defined by three expressions called the affinity laws of a pump. These laws state:

a. Pump volume flow rate varies directly with speed

$$\frac{Q_1}{Q_2} = \frac{N_1}{N_2} \tag{4.3}$$

b. Pump developed head varies directly as the square of speed

$$\frac{\Delta H_1}{\Delta H_2} = \frac{N_1^2}{N_2^2} \tag{4.4}$$

c. Pump driving power varies directly as the cube of speed

$$\frac{hp_1}{hp_2} = \frac{N_1^3}{N_2^3} \quad . \tag{4.5}$$

The affinity laws are based on the assumption that the pump efficiency is independent of the rotating speed. Actual pump operation has shown, however, that pump efficiency does change with speed. The degree depends upon the individual pump design, but is usually not more than two to three percent within a reasonable range from the rated design point (Refs. 4, 42).

As is shown in Equation (4.4), the pressure rise for an ideal pump is equal to the square of shaft speed. The known constant (K_p) from Equation (4.2) is a pump efficiency factor which relates conversion of shaft speed into pressure rise for a real pump. Equation (4.6) expresses this relationship as follows:

$$P_1 - P_p = K_p w^2 \qquad (4.6)$$

where,

P_1 = pump outlet pressure
P_p = pump inlet pressure
w = shaft speed in radians/sec.

Several types of energy losses occur during pump operation which affect efficiency. These losses are as follows:

a. Hydraulic losses - These include friction losses in the passages and flow turbulence losses. The friction losses are a function of the "wetted areas" in the passages and the roughness of their surfaces. The turbulence losses are caused by disturbances in certain regions of the pump, such as at the inlet and outlet edge of the vanes of both the impeller and diffuser and in the return guide vanes.

b. Disk friction losses - The energy required to rotate a disk, such as an impeller or inducer, is known as disk friction loss. The disk friction losses are due to two actions; (1) the actual fluid friction of the fluid on the disk and (2) a pumping action on the fluid in contact with the disk.

c. Mechanical losses - These are losses in the bearings and seals caused by mechanical friction.

d. Leakage losses - To prevent the pumped fluid from leaking back to the suction side after it has passed the impeller and is at outlet pressure levels, close-clearance labyrinth-type seals or wearing rings are typically employed. Leakback lowers the flow capacity of a pump and thus increases the required pumping power.

In practice, (K_p) is determined experimentally once a pump has already been constructed. For this work, (K_p) for NERVA small engine will be derived, and will be assumed to be constant for different pressure rises and shaft speeds. As was discussed in Section 4.1, one turbopump model will initially be employed for all three nuclear rocket engine designs, and this model will be based on the proposed NERVA small engine turbopump design. By manipulating Equation (4.6), the relationship for the known pump constant (K_p) can be expressed as:

$$K_p = \frac{P_1 - P_p}{w^2} \quad . \tag{4.7}$$

In Reference 5, the values for the variables in Equation (4.7) are as follows:

a. Pump outlet pressure - 6.03 MPa
b. Pump inlet pressure - 0.12 MPa
c. Shaft speed - 46,950 rev/min.

Therefore, the pump constant (K_p) was determined to be 0.244 kg/m.

The next variable in Equation (4.2) to be discussed is the rotational moment of inertia (I). The rotational moment of inertia describes how the mass of a rotating body is distributed about its axis of rotation. Equation (4.8) expresses this relationship:

$$I = \sum_{i} m_i \; r_i^2 \tag{4.8}$$

where,

m_i = mass of the i^{th} particle

r_i = radial distance from the center of rotation for the i^{th} particle

and all other terms have been previously defined.

The physical configuration of the impeller primarily determines the rotational moment of inertia for a pump. Many complicated operational considerations affect impeller geometry. Refer to Reference 42 for more detail on impeller design.

By assuming that the rate of change of the square of shaft speed is linear over the time interval during rocket engine turbopump startup, the rotational moment of inertia can be determined by:

$$I = \frac{2 \;\; hp}{w^2} \quad . \tag{4.9}$$

In Reference 5, the values for the variables in Equation (4.9) are as follows:

a. Shaft power - 0.93 MW
b. Shaft speed - 46,950 rev/min.

Therefore, the pump rotational moment of inertia (I) was determined to be 0.0768 kg·m^2.

Once all variables for the turbopump response time constant (τ_p) were determined for the NERVA small engine design, Equation (4.2) was utilized to calculate its parametric value. For the NERVA model, (τ_p) was found to be 1.02 seconds.

Next, the calculation of (τ_p) for the wire core and particle bed reactors will be discussed. The pressure drop across either of these folded flow core designs is substantially less than the NERVA reactor. Therefore, when chamber pressures are standardized between the three engines, the design outlet pressure for the turbopump for the wire core and particle bed reactors will be approximately a factor of two less than for the NERVA reactor. Pump inlet pressure is assumed to be constant for all three engines. The rotational moment of inertia and pump constant are also standardized for all three engines since the same single-stage radial flow pump is assumed in each engine design. Turbine power at the design point (ϕ_p) will vary between the NERVA design and the folded flow core designs because the pressure rise requirements across the pump differ. By combining Equations (4.4) and (4.5), the relationship between pump power (hp) and pump head developed (ΔH) can be expressed as:

$$\frac{hp_1}{hp_2} = \left(\frac{\Delta H_1}{\Delta H_2}\right)^{3/2} \quad . \tag{4.10}$$

Therefore, if the pressure head requirement decreases by a factor of two, the pump power requirement will be reduced by a factor of 2.83. This reduction factor for the pump power requirement can directly be equated to a reduction in the turbine power at the design point. With all turbopump response time constant variables known for the wire core and particle bed engines, (τ_p) was found to be 0.721 seconds.

A summary of the values chosen for all variables associated with the turbopump response time constant is provided in Table 13.

Table 13

Turbopump Response Time Constant Variables
for the Three Reactor Models

Variable	NERVA	Wire Core	Particle Bed
Rotational Moment of Inertia ($kg \cdot m^2$)	0.0768	0.0768	0.0768
Turbopump Outlet Pressure (MPa)	6.03	3.41	3.41
Turbine Design Power (MW)	0.93	0.33	0.33
Pump Constant (kg/m)	0.244	0.244	0.244

4.2.3 Neutron Kinetics and Delayed Neutron Precursor Density Response Time Constants

The other two response time constants are related to the standard lumped parameter neutron kinetics and precursor equations. The neutron kinetics response time constant is as follows:

$$\tau_m = \frac{\ell}{\beta} \tag{4.11}$$

where,

τ_m = neutron kinetics response time constant
ℓ = neutron generation time
β = effective delayed neutron fraction.

The neutron kinetics response time constant (τ_M) differs for each of the three reactor types because both the neutron generation time and effective delayed neutron fraction depend upon the physical configuration of the reactor model. In regards to the neutron generation time, Table 14 illustrates the variance between the three models. To summarize, the wire core has a fast neutron spectrum while the NERVA exhibits an epi-thermal spectrum, and the particle bed is a thermal reactor. Also, differences occur in effective delayed neutron fraction. The effective delayed neutron fraction is defined as that percentage of neutrons available for fission which were borne delayed (i.e., not directly from fission itself). Again differences in the parametric value for the effective delayed neutron fraction arise because of variance in the neutronics spectrum. Reference 47 was utilized in determination of both the neutron generation time and the effective delayed neutron fraction for the particle bed reactor. In the case of the NERVA reactor, References 11 through 14 as well as Reference 5 provided information utilized in assignment of values for both variables. Finally, information in the literature did not exist for the wire core reactor, therefore, values for (ℓ) and ($\bar{\beta}$) were chosen based upon other similar fast neutron spectrum reactor types. Table 14 presents the values chosen for both the neutron generation time and effective delayed neutron fraction for each of the three reactor types.

Table 14

Neutron Generation Time and Effective Delayed Neutron Fraction for the Three Reactor Models

Variable	NERVA	Wire Core	Particle Bed
ℓ (sec)	1.0E–4	1.0E–7	3.9E–5
β	7.0E–3	6.5E–3	7.6E–3

The delayed neutron precursor response time constant is as follows:

$$\tau_{D_i} = 1/\lambda_i \tag{4.12}$$

where,

τ_{D_i} = delayed neutron precursor time constant for the i^{th} family

λ_i = precursor decay constant for the i^{th} family.

In Reference 48 values are given for the precursor decay constants for the six delayed neutron families. The response time constants for delayed neutron precursor density are independent of the reactor type modeled. Therefore, (τ_{D_1}) through (τ_{D_6}) have the identical values for the NERVA, wire core, and particle bed reactors.

The STRTUP nuclear rocket modeling code which was developed for this dissertation employs six delayed neutron group families. Therefore, each of the nuclear rocket designs is characterized by nine response time constants which are directly related to physical phenomenon of a nuclear rocket engine startup. It should also be noted that these response time constants could also be utilized if modeling during at power operations or shutdown was required with only minor variations. Table 15 provides a listing of the parametric values for the response time constants for the NERVA small engine, wire core, and particle bed reactors.

Table 15

Nuclear Rocket Response Time Constants (sec)

Time Constant	NERVA	Wire Core	Particle Bed
τ_c	1.54	0.357	0.141
τ_p	1.02	0.721	0.721
τ_m	1.43E-2	1.54E-5	5.17E-3
τ_{D_1}	80.65	80.65	80.65
τ_{D_2}	32.79	32.79	32.79
τ_{D_3}	9.01	9.01	9.01
τ_{D_4}	3.32	3.32	3.32
τ_{D_5}	0.88	0.88	0.88
τ_{D_6}	0.33	0.33	0.33

4.3 Summary of Key Equations for the Nuclear Rocket Model

A summary of the equations which will be utilized in the STRTUP computer code to model the process of nuclear rocket startup will now be given. For more detail on the derivation of these equations refer to Appendix A and References 38 through 41.

A lumped parameter model was used. The standard lumped parameter neutron kinetics and precursor equations are as follows:

$$\frac{dP}{dt} = \frac{\rho - \beta}{\ell} P + \lambda z \tag{4.13}$$

and,

$$\frac{dz}{dt} = \frac{\beta}{\ell} P - \lambda z \tag{4.14}$$

where,

P = reactor power

z = neutron precursor density

ρ = reactivity

β = effective delayed neutron fraction

ℓ = neutron generation time

λ = precursor decay constant.

From these two equations the following equations were derived which were implemented in the computer model:

$$\tau_m \frac{dp'}{dt} = \left(\frac{\rho}{\beta} - 1\right) p' + z' \tag{4.15}$$

and,

$$\tau_D \frac{dz'}{dt} = p' - z' \tag{4.16}$$

where,

$$P' = \frac{P}{P_D} \tag{4.17}$$

$$z' = \frac{\ell\lambda}{\beta} \frac{z}{z_D} \tag{4.18}$$

and all other terms have been previously defined.

The core heat transfer process is modeled by:

$$M_c C_{P_c} \frac{T_c}{T_2} \frac{dT_2}{dt} = P - \dot{m} C_p (T_2 - T_1) \tag{4.19}$$

where,

M_c = fuel mass
C_{P_c} = fuel specific heat
T_c = mean core temperature
T_2 = propellant outlet temperature
$\dot{m}$ = propellant mass flow rate
C_p = propellant specific heat capacity
T_1 = propellant inlet temperature.

From Equation (4.19) the following equation was derived which was implemented in the computer model:

$$\tau_c \frac{dT_2'}{dt} = P' - P_1' \sqrt{T_2'} \tag{4.20}$$

where,

$$T'_2 = \frac{T_2}{T_{2_D}} \tag{4.21}$$

$$P'_1 = \frac{P_1}{P_{1_D}} \tag{4.22}$$

and all other terms have been previously defined.

The speed of the turbopump unit is obtained from the following equation:

$$\frac{d}{dt}\left[Iw^2\right] = \eta_T C_p T_2 \dot{m}_T \left\{ 1 - \left(\frac{1}{PR}\right)^{\frac{\gamma-1}{\gamma}} \right\} - \dot{m}\left(P_1 - P_p\right) / \eta_p \rho_{HL} \tag{4.23}$$

where,

I = rotational moment of inertia

w = shaft speed in radians/sec

η_T = turbine efficiency

$\dot{m}_T$ = turbine mass flow rate

PR = turbine pressure ratio

γ = ratio of specific heats

P_p = pump inlet pressure

η_p = pump efficiency

ρ_{HL} = propellant density in the pump

and all other terms have been previously defined.

From Equation (4.23) the following equation was derived which was implemented in the computer model:

$$\tau_p \frac{dP'_1}{dt} = P'_1 \sqrt{T'_2} - P'^{2}_1 / \sqrt{T'_2} \quad . \tag{4.24}$$

The reactivity equation for the nuclear rocket reactor is as follows:

$$\rho = \rho_o + \alpha_F \sqrt{T'_2} + \alpha_c \rho_c \tag{4.25}$$

where,

ρ = total reactivity

ρ_o = control device reactivity

α_F = negative fuel temperature coefficient

α_c = positive propellant density coefficient

ρ_c = propellant density

and all other terms have been previously defined.

From Equation (4.25) the last modeled equation was derived:

$$\rho = \rho_o + \alpha_F \sqrt{T'_2} + \alpha_H P'_1/T'_2 \quad , \tag{4.26}$$

Equations (4.15), (4.16), (4.20), (4.24), and (4.26) form a set of ten coupled, non-linear ordinary differential equations. Ten equations are required because six groups of delayed neutron precursors are modeled.

4.4 STRTUP Computer Code

The STRTUP computer code is a FORTRAN based code which calculates the time-dependent effects that occur in a fission reactor as a result of the physics of fission. It is a point kinetics code as it is currently configured. However, it could easily be modified into a nodal kinetics code if extra detail in spatial resolution is required. It models the delayed neutrons with the standard set of six delayed groups. But it also models delayed beta heating and delayed gamma heating. It does this by using a set of exponential decay functions similar to the exponential decay families used for delayed neutrons. Both of these delayed heating effects are important for transients lasting tens of seconds if an accurate measure of total power is required based on an estimate of prompt power or the neutron flux level. Also, modeled by the code are the core heat transfer process, a turbopump, and reactivity feedback effects. These are considered as described in Sections 4.3, 5.2, and Appendix A.

The STRTUP code is also set up in a mode that allows easy expansion of the number of differential equations modeled in an organized fashion. It currently uses a Runge–Kutta–Fehlberg third and fourth order integrator, but the integration model can be easily swapped out for a higher or lower order module. Both higher and lower order Runge–Kutta-Fehlberg modules are available as subroutines within the program.

The Runge–Kutta–Fehlberg numerical method is a standard technique for solution of first–order differential equations. As was discussed in Section 4.3, ten coupled, nonlinear ordinary differential equations have been coded to model prompt power, delayed neutron density, outlet temperature, and inlet pressure for the three nuclear rocket engine models. This coupled set of equations can be written in the following general form:

$$y' = f\,(x,y) \tag{4.27}$$

where,

$$y\,(x_o) = y_o \quad . \tag{4.28}$$

This initial value problem consists of ten differential equations and a condition which the solution for each must satisfy. The assumption here is that f(x,y) has a unique solution on some interval x_o. It can be shown that the truncation error per step is on the order (h^5), where (h) is the step length (Ref. 49). Therefore, the solution method employed in the STRTUP computer code is a fourth–order method.

The STRTUP code is also flexible in the printouts that it will produce so that different types of problems can be easily investigated. The code is written in such a way that it is obvious that the main problem solved is the solution of a set of coupled, ordinary nonlinear differential equations. Additional physics and spatially dependent models can easily be added by deriving the appropriate differential equations and coding them. The code does require a FORTRAN programmer to modify and does not have its own simulation language comparable to many modeling code systems. In short the STRTUP code models the time-dependent physics of a fission core, heat transfer, a turbopump, and reactivity feedback effects and provides a basis for reactor control simulation studies with the appropriate integration routines.

4.4.1 Discussion of Program Structure and Subroutines

The STRTUP computer program as currently configured is written in a modular format. A brief discussion of the various program modules will follow. A listing and description of the most important program variables is given in the comment section which precedes the main program. Also, listed are the input parameters required. For a complete listing of the STRTUP computer code and a sample input deck refer to Appendices C and D, respectively.

The main program is used to establish common variables and to set up the flow path between the subroutines. The following are the most important subroutines with a brief description of their function:

a. Subroutine Input - allows all input variables to be read into the program and establishes the solution matrix dimensions.

b. Subroutine Solver - provides equations to solve for prompt power, decay beta power, decay gamma power, total power, energy level, outlet temperature, inlet pressure, temperature reactivity feedback and propellant reactivity feedback for each integration time step.

c. Subroutine Init - initializes the state variables and calculates the first derivates.

d. Subroutine Syseq - contains the differential equations which model the nuclear rocket engine and reactivity feedback effects.

e. Subroutine Default - resets all major variables to their default values and provides data blocks which input decay constant information for the beta, gamma, and delayed neutron groups.

f. Function Rhof - provides the control function for reactor startup.

g. Subroutines ET2M, RKF12M, RKF23M, RKF34M, RKF45M - these are the integration subroutines which can be used to solve the first-order differential equations. As currently configured only the RKF34M subroutine is being utilized.

All other subroutines have appropriate comment blocks which describe their function in the program listing in Appendix C.

5.0 STARTUP SIMULATION RESULTS

This chapter will discuss the startup simulations which were performed for the NERVA small engine, particle bed, and wire core reactors. Before startup simulations incorporating temperature and pressure feedback effects were performed, initial base case configurations were established for all three reactor models. Section 5.1 describes the base case configurations utilized for the startup simulations. The incorporation of temperature and propellant feedback effects into the nuclear rocket models is discussed in Section 5.2. In Sections 5.3 through 5.5 the startup simulation results for NERVA small engine, particle bed, and wire core reactors are summarized, respectively. Finally, Section 5.6 compares the startup simulation results for the three reactor models and discusses the effect of differences in the key rocket engine parameters.

5.1 Establishment of Base Case Configurations for the NERVA Small Engine, Particle Bed, and Wire Core Reactor Models

As was discussed in Section 1.5, two potential design options for a ROTV are using a lower thrust engine such as the NERVA small engine or throttling a higher thrust engine which may be developed for a manned Mars mission to lower thrust levels. Because of the weight penalty of a higher thrust engine as compared to a lower thrust engine, the reactor startup simulation studies described in Chapter 5 will model a standardized 72 kN lower thrust engine.

Establishing a standardized thrust requirement implies that reactor outlet temperature, chamber pressure, and propellant weight flow rate must also be approximately the same when comparing the three nuclear rocket engine models. Therefore, reactor outlet temperature, chamber pressure, and propellant weight flow rate were not allowed to vary by more than two percent between the designs. No more than two percent variance between standardized parameters was chosen so that the overall uncertainty in the results would not be affected by thrust variance. In actuality the variance between reactor outlet temperature and chamber pressure was less than two percent for the three reactor models while propellant weight flow rates were identical.

As an initial approximation, reactor power level was taken to be 367 MW based on the design study described in Reference 5 for the NERVA small engine. Also, the turbopump design was initially standardized even though the pump outlet pressure requirement for the NERVA small engine is approximately twice that of the folded flow reactors. For a more detailed description of the basis for the turbopump design choice refer to Section 4.2.2.

Startup simulations were performed for all three reactor models to establish key reactor design parameter base case values and to standardize core outlet temperature and chamber pressure. These startup simulations employed a step change reactivity insertion of 0.9 β. As design power level was approached, reactivity was gradually removed to minimize any potential overshoot. Temperature and propellant reactivity feedback effects were not incorporated into these startup simulations. Also, the rates of increase of pump outlet pressure and reactor outlet temperature were not constrained. Pump operational constraint limits (discussed in Appendix A) and transient thermal stress limits (discussed in Section 1.4) were not considered since the purpose of these startup simulations was to establish design parametric values only, not allowable power level increase rates. The following standardized initial conditions were employed for the startup simulations for all three models:

a. Initial power level - 1.0 kW

b. Initial core inlet temperature - 200°K

c. Initial chamber temperature - 200°K

d. Propellant weight flow rate - 8.5 kg/s

e. Propellant specific heat capacity - 15.8 kJ/kg ·°K.

The first set of startup simulations to be discussed was for the NERVA small engine model. With the rocket engine response time constants set at the values given in Table 15 and the design power level set at 367 MW, a core outlet temperature of 2865°K and a pump outlet pressure of 6.12 MPa were obtained. As a comparison, the design values for the NERVA small engine from Reference 5 are a core outlet temperature of 2695°K and pump outlet pressure of 6.03 MPa.

To reduce core outlet temperature to approximate the design value from Reference 5 required adjustment of design power level as will be shown in the discussion which follows.

The core heat transfer process was modeled by:

$$M_c C_{P_c} \frac{T_c}{T_2} \frac{dT_2}{dt} = P - \dot{m} C_p (T_2 - T_1) \tag{5.1}$$

where,

M_c = fuel mass

C_{Pc} = fuel specific heat capacity

T_c = mean core temperature

T_2 = propellant outlet temperature

P = reactor power
$\dot{m}$ = propellant mass flow rate
C_p = propellant specific heat capacity
T_1 = propellant inlet temperature.

When steady state outlet temperature, propellant flow rate, and reactor power level conditions are reached Equation (5.1) simplifies to :

$$P = \dot{m}C_p(T_2 - T_1) \quad . \tag{5.2}$$

Considering that the propellant flow rate, mean propellant specific heat capacity, and core inlet temperature are fixed, only core outlet temperature will vary with reactor power level. As can be seen from Equation (5.2), a reduction in reactor power will also reduce core outlet temperature.

A sensitivity analysis was performed which varied the design power level for the NERVA small engine model until the core outlet temperature was approximately 2695°K. The results of this sensitivity study are given in Table 16. Also, shown in Table 16 is the variance of pump outlet pressure with design power level. As is detailed in the development of the Smith-Stenning equations described in Appendix A, pump outlet pressure varies with the square root of outlet temperature and therefore is also dependent upon design power level.

As is illustrated by Table 16, once the design power level was reduced to 345 MW to obtain a core outlet temperature of 2705°K, it also reduced pump outlet pressure to below the design value required to maintain chamber pressure at 3.10 MPa. Therefore, another sensitivity study was performed

Table 16

Sensitivity Analysis - NERVA Small Engine Outlet Temperature and Inlet Pressure Variation With Design Power Level

Power Level (MW)	Outlet Temperature (°K)	Inlet Pressure (MPa)
367	2865	6.12
350	2741	5.86
335	2632	5.62
345	2705	5.80

which varied the pump response time constant to increase pump outlet pressure to 6.03 MPa. Equation (4.2) will be restated here for convenience of the discussion which follows:

$$\tau_p = \frac{I\,P_{1_d}}{2\phi_p K_p} \tag{5.3}$$

where,

τ_p = turbopump response time constant
I = rotational moment of inertia
P_{1_d} = core inlet pressure at the design point
ϕ_p = turbine power at the design point
K_p = known constant.

A detailed description of each of the parameters in Equation (5.3) is given in Section 4.2.2. Since the core inlet pressure design parametric value is fixed because of a fixed pressure drop across the core and the design requirement of a standardized chamber pressure, other pump parameters must be varied to increase pump outlet pressure to approximately 6.03 MPa. Variance of the rotational moment of inertia or the pump constant implies alteration of the physical configuration of the pump. As is described in more detail in Reference 42, these physical alterations based on preliminary design studies are a standard design practice. Table 17 provides the results of the sensitivity study which varied the turbopump response time constant to obtain a pump outlet pressure of approximately 6.03 MPa.

Table 17

Sensitivity Analysis - NERVA Small Engine Pump Outlet Pressure Variation
With the Turbopump Response Time Constant

Turbopump Response Time Constant (sec)	Pump Outlet Pressure (MPa)
0.9	7.42
0.95	6.66
0.98	6.26
1.0	6.01

As can be seen from Table 17, the overall reduction of turbopump response time constant was less than two percent of the design value derived from Reference 5.

From the results of the two sensitivity studies for the NERVA small engine design, reactor power level was reduced from 367 MW to 345 MW and the pump response time constant was reduced by approximately two percent to establish standardized core outlet temperature and chamber pressure parametric values.

The next startup simulations to be discussed were for the particle bed reactor. As was the case for the NERVA small engine design, the initial startup simulation utilized the rocket engine response time constants from Table 15 and a design power level of 367 MW. Also employed were the standardized initial conditions previously discussed for the NERVA startup simulations. A core outlet temperature of 2869°K and a pump outlet pressure of 6.34 MPa were obtained from the initial startup simulation. Once again design power level required adjustment to reduce the reactor outlet temperature. A reactor power level of 345 MW was chosen for the next startup simulation. The core outlet temperature obtained with a design power of 345 MW was 2709°K.

With the outlet temperature within two percent of the standardized value, the pump outlet pressure obtained was almost twice the required design pressure. Recall from the discussion in Section 4.2.2, the pressure drop across both the particle bed and wire core designs is approximately ten percent of the design pump outlet pressure. Therefore, a pump outlet pressure of approximately 3.41 MPa is required to obtain a chamber pressure of 3.10 MPa. A sensitivity study was performed which varied the turbopump response time constant to reduce the pump outlet pressure to approximately its design value. As was the case for the NERVA turbopump response time constant sensitivity study, a reduction in pump outlet pressure necessitated an increase in the time constant. Also, an increase in the turbopump response time constant implied that a physical alteration of the turbopump design was required. Therefore, a single turbopump model which only varied in its outlet pressure requirement was no longer a viable design option for the three nuclear rocket models. Table 18 details the pump outlet pressure reduction sensitivity study for the particle bed reactor model.

From the results of the outlet temperature reduction and the turbopump response time constant sensitivity studies for the particle bed reactor design, reactor power level was reduced from 367 MW to 345 MW and the pump response time constant was increased from 0.72 to 1.0 second. Also, it was found that a single turbopump design for all three reactor models could not be employed.

Table 18

Sensitivity Analysis - Particle Bed Pump Outlet Pressure Variation With the Turbopump Response Time Constant

Turbopump Response Time Constant (sec)	Pump Outlet Pressure (MPa)
0.9	4.22
0.95	3.79
1.0	3.42

The final startup simulations to be discussed were for the wire core reactor. Considering the results from the startup simulations for both of the other two reactor models, the initial startup simulation for the wire core reactor set design power at 345 MW and the turbopump response time constant at 1.0 second. Also, as was the case for the startup simulations for the other two reactor designs, the response time constants other than the turbopump response time constant were set to the values given in Table 15. Other standardized initial conditions as previously specified for the NERVA startup simulations were also utilized. The initial startup simulation resulted in a reactor outlet temperature of 2672°K and a pump outlet pressure of 2.94 MPa. When comparing the three reactor models, the outlet temperature was within the two percent variation specification for the standardized parametric design values. Therefore, no further adjustment of design power level was required. However, the pump outlet pressure was approximately 14 percent below the design value. Therefore, a sensitivity study reducing the turbopump response time constant to increase the pump outlet pressure was required. This turbopump response time constant variation implied that each reactor model required an individually designed turbopump. Table 19 provides the results of the turbopump time constant variation sensitivity analysis for the wire core reactor model. As shown in Table 19, the pump response time constant was decreased from 1.0 to 0.93 seconds to increase pump outlet pressure to 3.43 MPa.

Table 19

Sensitivity Analysis - Wire Core Pump Outlet Pressure Variation
With the Turbopump Response Time Constant

Turbopump Response Time Constant (sec)	Pump Outlet Pressure (MPa)
1.0	2.94
0.9	3.67
0.93	3.43

Even though thermal and propellant reactivity feedback effects had not been incorporated into the startup simulations to this point, a comparison of core outlet temperature, pump outlet pressure and reactor power level time rate of increase between the three models is useful. Figures 16 through 18 provide this comparison for a step change reactivity insertion of 0.9 β followed by a gradual removal of reactivity as the design power level was approached.

Figure 16 illustrates that relatively rapid increases in core outlet temperature are possible with reactor power level at or near its design value. The temperature response for the wire core and particle bed reactors were similar

Figure 16

Core Outlet Temperature Response to a Step Reactivity Insertion of 0.9 β

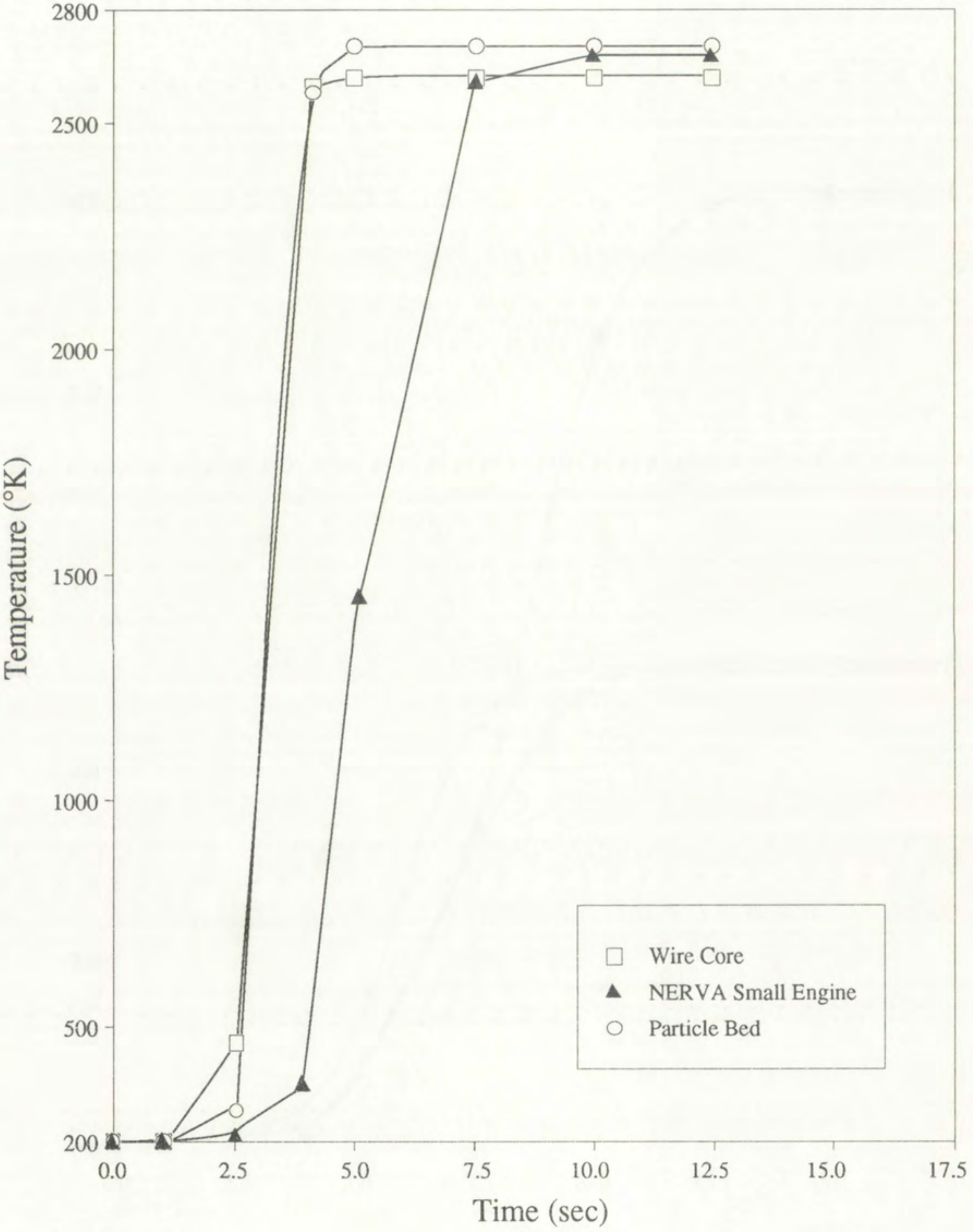

Figure 17

Pump Outlet Pressure Response to a Step Reactivity Insertion of 0.9 β

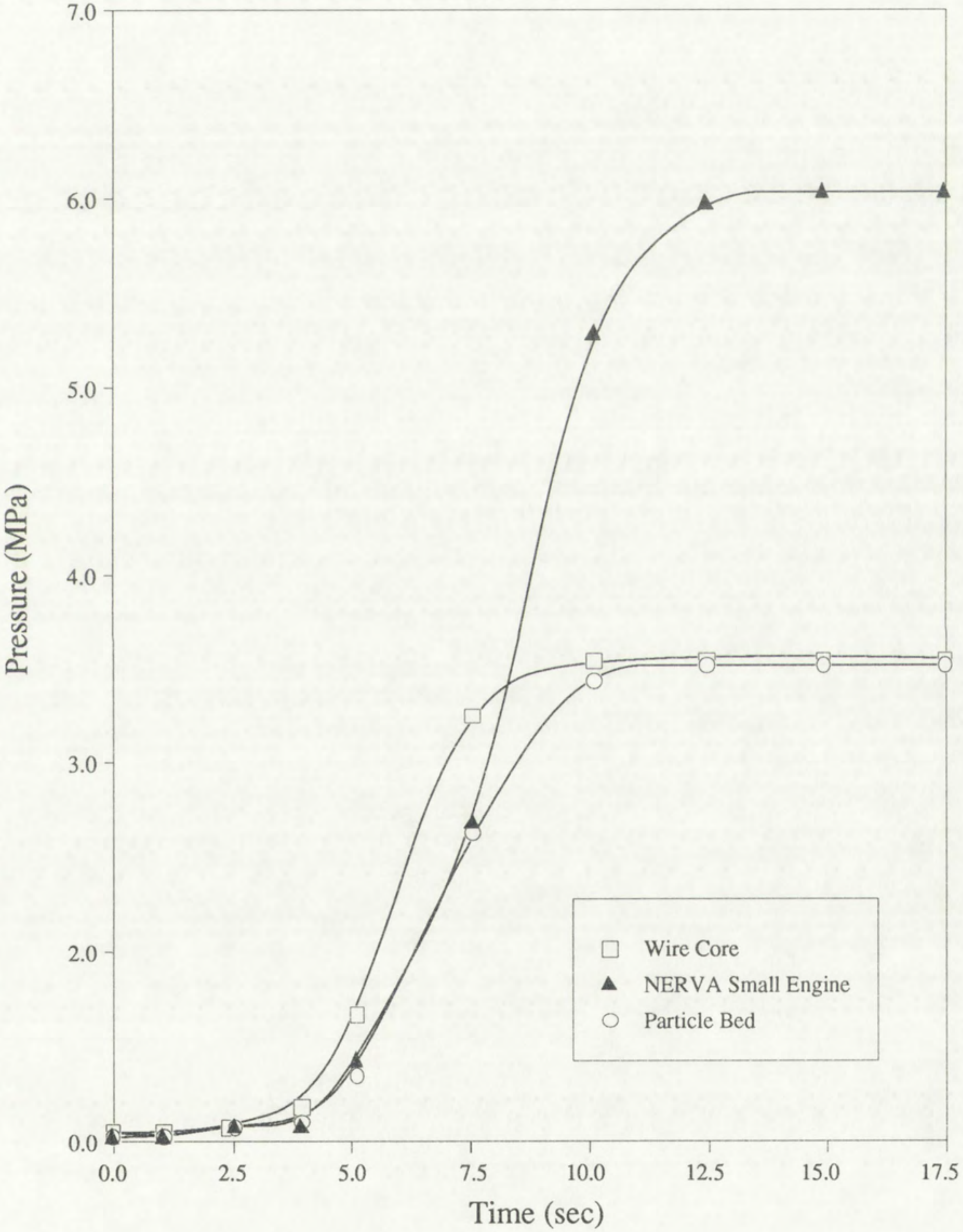

Figure 18

Reactor Power Level Response to a Step Reactivity Insertion of 0.9 β

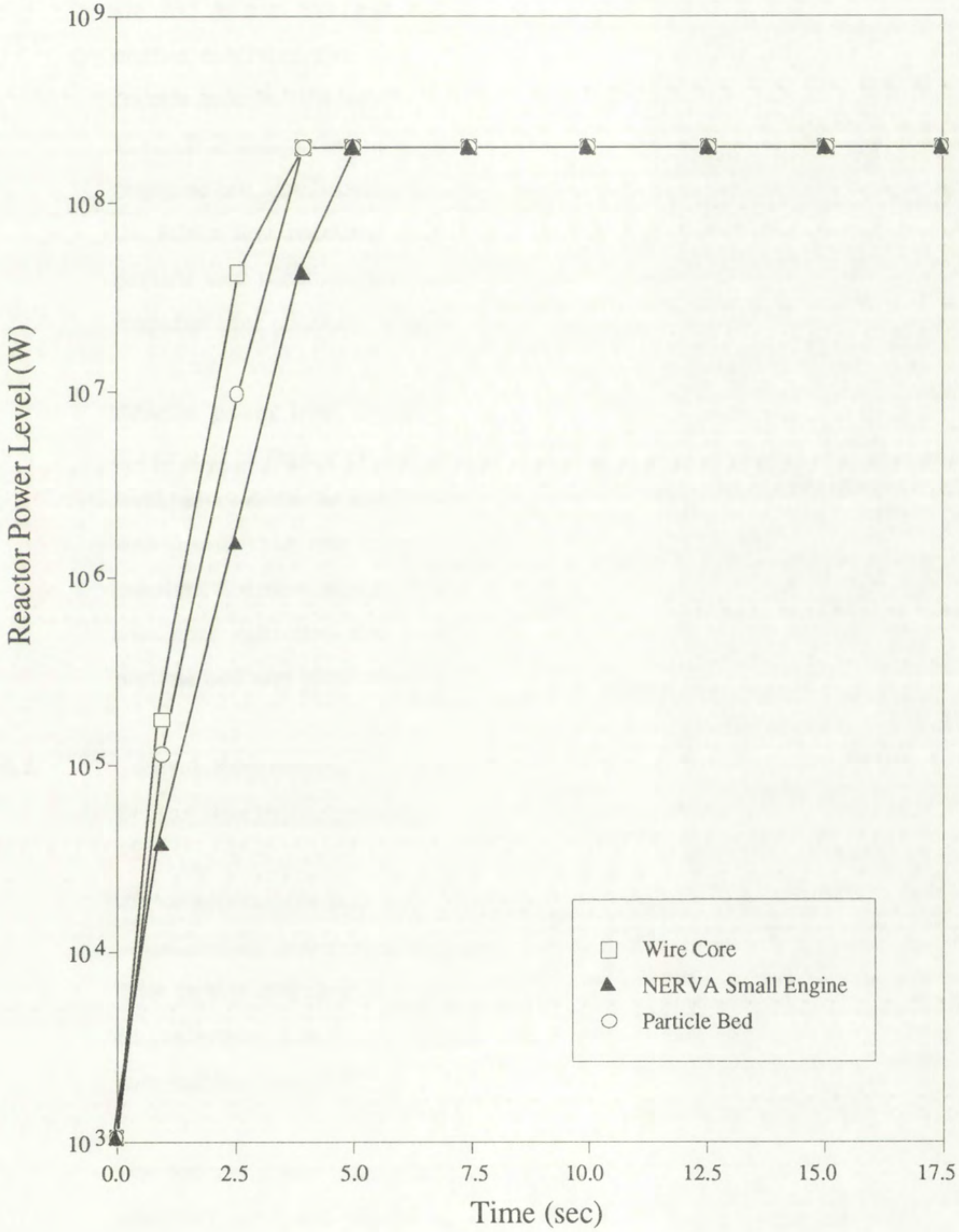

while the NERVA reactor took approximately twice as long to reach design outlet temperature.

In Figure 17 turbopump outlet pressure increase during engine "bootstrap" is shown. As was the case for engine temperature response, the NERVA small engine exhibited the most sluggish outlet pressure increase of the three reactor models. It took the NERVA engine model approximately twice as long to reach design turbopump outlet pressure. This was due not only to a slower response but also because its design value was 2.62 MPa greater than either of the folded flow reactors. The wire core had a more rapid response than the particle bed reactor. This was as expected since the wire core turbopump response time constant is seven percent less than that of the particle bed.

Reactor power level increase due to a step reactivity insertion of 0.9 β is illustrated in Figure 18 for the three reactor models. When comparing power level response to the neutronics response time constants given in Table 15, it was found that the smaller the value for the neutronics response time constant the more rapid the power level change would become. Therefore, the wire core exhibited the most rapid power level response followed by the particle bed and NERVA small engine reactors.

5.2 Control Requirements Associated With Propellant Initiation and Reactor Heatup Reactivity Feedback

In this section, the reactivity feedback effects due to temperature increase and propellant initiation during a nuclear rocket engine startup will be discussed. Prior to this discussion, a brief overview of NERVA control requirements will be presented. Finally, the control law implemented in the STRTUP computer code will be described.

The control drum span and speed of rotation is primarily a function of the reactivity feedback effects as well as the requirement to provide adequate shutdown margin and rapid startup capability throughout the operational lifetime of the ROTV. The control drum span represents the change in feedback reactivity of the reflector caused by the rotation of the control drums over their travel range.

Table 20 provides a summary of the static requirements for the NERVA reactor control drum span (Ref. 50). The NERVA engine basic drum span without maneuvering is further illustrated by Figure 19. By combining the parameters in Table 20, the NERVA designers developed a set of drum spans which also accounted for a failed or a stuck drum.

Table 20

Summary of the Static Requirements for the NERVA Reactor Control Drum Span

Requirement	Magnitude ($)
Corrosion Allowance	+1.00
Cold Critical Uncertainty	±0.15 (3σ)
Hot Critical Uncertainty	±0.30 (3σ)
Effect of Xenon Buildup on Startup	+0.30 (3σ)
Required Shutdown Margin for Non-Operating Conditions	−1.50
Required Shutdown Margins for Operating Conditions	−0.25
Cold Flow Test and Bootstrap	−1.00 (3σ)

In addition to the NERVA engine static requirements, a control drum dynamic requirement of $ 0.7 was necessary for the power period required during autostart (Ref. 50). Preliminary autostart studies identified deviations around cold critical of +$0.9 and −$0.6 during chilldown and bootstrap. NERVA control designers believed that some optimization of the problem would result in a value close to the $0.7 used in the drum span development (Ref. 50). The NERVA control drums were designed for a drum span of $6.0. Also, provided for NERVA engine control was a $3.0 structural support

Figure 19

NERVA Basic Drum Span Requirement Without Maneuvering

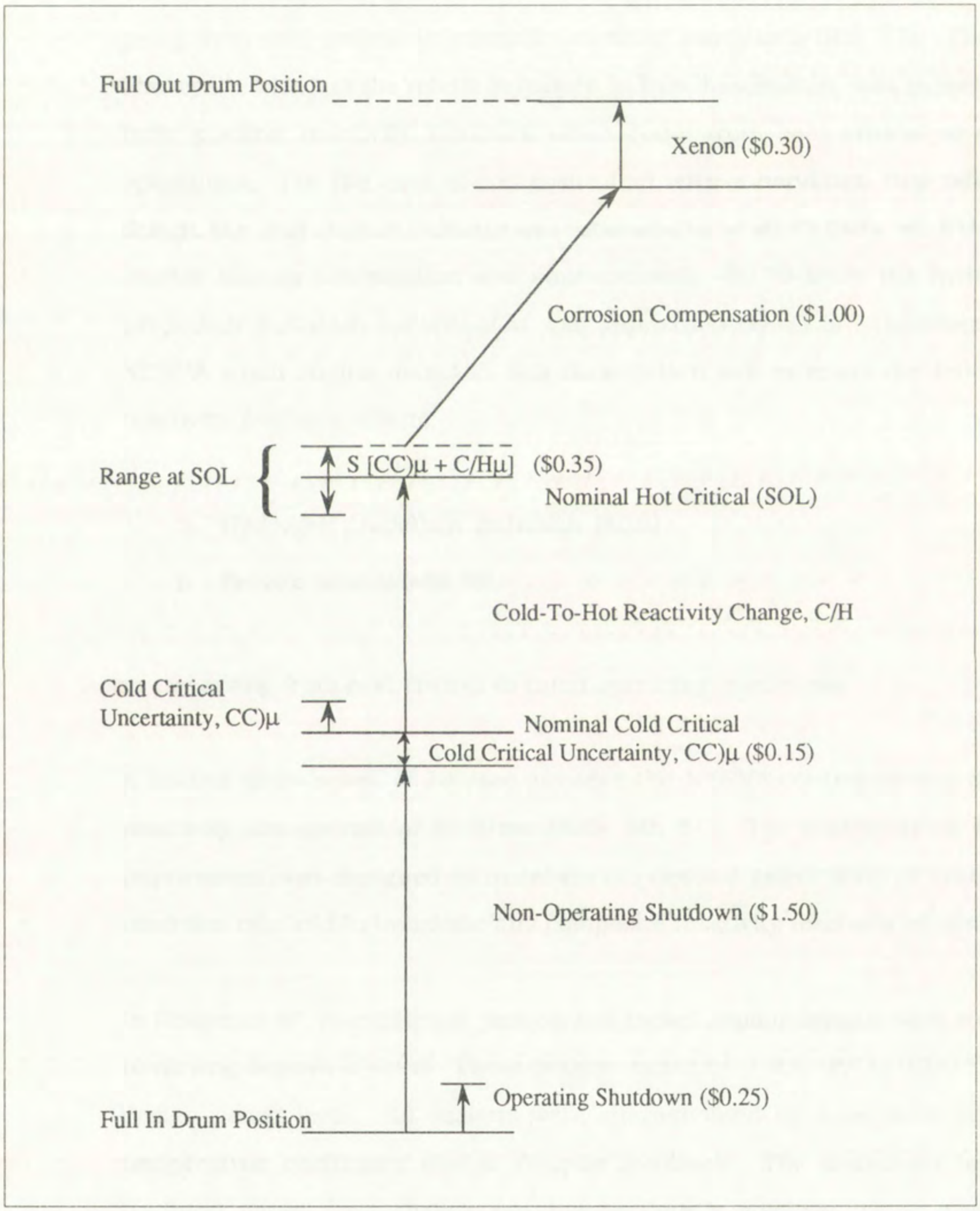

assembly span for rated condition operation (Ref. 51). The support assembly controlled reactivity by modifying propellant bleed flow as described in Section 1.3.1.

The NERVA hot bleed cycle had an $0.8 negative reactivity feedback change in going from cold critical to criticality at rated conditions (Ref. 51). The full flow cycle, which is the model employed in this dissertation, was expected to have positive reactivity feedback when going from cold critical to rated operations. For the case of composite fuel with a beryllium ring reflector design, the total reactivity change was estimated to be $0.75 (Refs. 50, 51). The reactor heatup contribution was approximately –$0.75 while the hydrogen propellant initiation contribution was approximately $1.5. Therefore, the NERVA small engine model in this dissertation will estimate the following reactivity feedback effects:

a. Hydrogen propellant initiation ($1.5)

b. Reactor heatup (–$0.75)

in traversing from cold critical to rated operating conditions.

A control drum speed of 10°/sec provided the NERVA control system with a reactivity change rate of $0.6/sec (Refs. 50, 51). The control drum speed requirement was designed to maintain the desired power level or reactivity insertion rate and to overcome any composite reactivity feedback effects.

In Reference 47, four different particle bed rocket reactor designs were studied to varying degrees of detail. These designs varied from 400 MW to 2000 MW in design power level. All designs were characterized by a negative prompt temperature coefficient due to Doppler feedback. The moderator heatup feedback varied from slightly negative to slightly positive. In all practical cases, the propellant worth was positive, although core configurations with negative coolant worth could be designed.

Many sensitivity studies were performed to assess the variance of reactivity feedback effects with design alterations. The feedback coefficients due to moderator temperature changes, coolant density variations, and control shutter position were assessed for different moderator compositions and values of fuel element pitch. To select representative values for the feedback coefficients utilized in this analysis, a median value of fuel element pitch and a beryllium moderator were chosen. Therefore, the particle bed engine model in this dissertation will estimate the following reactivity feedback effects:

a. Hydrogen propellant initiation ($1.33)

b. Reactor heatup (–$1.21)

in traversing from cold critical to rated operating conditions.

Another particle bed reactor sensitivity study described in Reference 47 varied fuel element pitch to determine the effect of this variance on control shutter worth. The results of this sensitivity study indicated that shutter worth did not vary greatly with fuel element pitch and that the worth varied monotonically with angle. Also, a total control worth of $11.0 was estimated.

No value for the reactivity insertion rate for particle bed reactor control drums could be found in the literature review. Therefore, as an initial approximation the particle bed model will assume a control system reactivity change rate of $0.6/sec to be consistent with the NERVA small engine design.

In the case of the wire core reactor, no control system information was available in the literature. Therefore, propellant feedback effects were estimated from the hydrogen density reduction sensitivity studies described in Appendix B. These sensitivity studies indicated that propellant initiation feedback could range from approximately $1.0 to $4.0. In Section 5.5, reactor startup simulation sensitivity studies will be described which varied propellant feedback worth to determine its effect on wire core reactor control strategies. As an initial approximation reactor heatup feedback will be estimated to be $1.0 to be consistent with other fast spectrum reactors. The tungsten cladding negative Doppler feedback is the primary contributor to the negative temperature coefficient. To be consistent with the other two designs, the wire core reactor control system reactivity change rate will be initially set to $0.6/sec. In comparison to the NERVA and particle bed reactors, a greater reactivity removal rate may well be required to compensate for the potentially greater positive reactivity addition rate from propellant initiation.

The control law implemented in the STRTUP computer code and the modeling of reactivity feedback effects will now be discussed. To model reactivity feedback requires measurement of pump outlet pressure as well as either a direct or indirect measurement of core outlet temperature. Measurement of pump outlet pressure is straightforward and many different measurement techniques are available (Ref. 42). Therefore, it will not be discussed further here.

Reactor outlet temperature measurement is more complicated to obtain than inlet pressure measurement due to the high operating temperature environment of the rocket engine chamber. Both direct temperature measurement and indirect estimation methods are available to determine reactor outlet temperature.

To directly measure core outlet temperature tungsten-rhenium thermocouples have been proposed. Thermocouples composed of tungsten with either six or 20 weight percent rhenium have temperature measurement ranges of up to 3300°K. However, nonlinearities at the upper end of the temperature measurement range can occur. Either of the two proposed thermocouples require thicker thermocouple junction wires than are employed in other thermocouples with lower upper end temperature measurement ranges. Thicker thermocouple junction wires increase temperature response lag times. When engine startup times are very short (less than ten seconds) temperature response lag times pose another difficulty in the use of direct temperature measurement.

Different methods of indirect outlet temperature estimation are available. The controller utilized for the particle bed models in Reference 47 estimated outlet temperature from measurements of throat pressure and propellant mass flow rate. Another potential method of indirect outlet temperature determination is based solely on the measurement of throat pressure. In either of these indirect estimation techniques chocked flow conditions at the nozzle throat must exist. With chocked flow conditions present at the nozzle throat:

$$\frac{\dot{m}}{A_{th}} = \frac{P}{RT} \, Ma \sqrt{\gamma \; RT} \tag{5.4}$$

where,

$\dot{m}$ = mass flow rate

A_{th} = area of the nozzle throat

P = propellant pressure at the throat

R = gas constant

T = propellant temperature at the throat

Ma = Mach number = 1.0

γ = ratio of specific heat.

The particle bed outlet temperature estimation method employed in Reference 47 utilized Equation (5.4) directly. The ratio of throat temperature and pressure to the design operating point can be derived directly from Equation (5.4). Equation (5.5) expresses this relationship as follows:

$$T = T_D \left(\frac{P}{P_D} \right)^2 \tag{5.5}$$

where,

T_D = design temperature
P_D = design pressure
and all other terms have been previously defined.

As shown in Equation (5.5), temperature at the rocket throat as well as any other point in the rocket system can be determined indirectly from a pressure measurement if chocked flow conditions exist at the nozzle throat.

Other methods of indirect outlet temperature estimation such as temperature ratioing have been proposed in the literature. The reactivity feedback control input in the STRTUP computer code assumes that either an indirect or direct measurement of core outlet temperature is available. Also, a pump outlet pressure measurement is determined for the computation of propellant feedback.

Equations which modeled the time dependent change of reactivity due to reactor heatup and propellant density differences were derived directly from the Smith-Stenning equations. Equations (5.6) and (5.7) which were implemented into the STRTUP computer code are as follows:

$$\frac{d\rho_T}{dt} = \frac{\alpha_F}{T_2^{1/2}} \frac{dT_2}{dt} \tag{5.6}$$

where,

$\frac{d\rho_T}{dt}$ = time rate of reactivity change due to reactor heatup
α_F = negative temperature coefficient of reactivity
T_2 = core outlet temperature

and,

$$\frac{d\rho_H}{dt} = \frac{\alpha_H}{T_2^{2}} \left[T_2 \frac{dP_1}{dt} - P_1 \frac{dT_2}{dt} \right] \tag{5.7}$$

where,

$\frac{d\rho_H}{dt}$ = time rate of reactivity change due to propellant density differences

α_H = propellant coefficient of reactivity

P_1 = core inlet pressure

and all other terms have been previously defined.

Equation (5.6) illustrates that reactivity feedback due to temperature change varies inversely with a given temperature change since (α_F) is always negative. Therefore, during reactor heatup negative reactivity feedback will occur in going from cold critical to rated design conditions.

The time rate of reactivity change due to propellant density differences is not only dependent upon the current operating point (i.e., propellant density) but also upon the relative time rates of change of core inlet pressure and outlet temperature. Even though the net effect of traversing from cold critical to rated design conditions is a positive reactivity addition, at some points during this transient the time rate of reactivity change due to propellant density differences may well be negative. Also net negative reactivity feedback is possible at some point in the transient if time rate of change of outlet temperature is sufficiently greater than the time rate of change of inlet pressure.

The control law model incorporated into the STRTUP computer code not only accounts for reactivity feedback effects but also determines the reactivity demand by comparing measured power level and design power level. If measured power level is below a prescribed percentage of design power level, then the demand reactivity during startup will be at a constant reactivity insertion rate determined by input parameter assignment. Demand reactivity is that value of reactivity which is necessary to maintain a constant positive reactor period until measured power is within a prescribed fraction of design power. Also, the power level at which demand reactivity removal commences is set by input parameters and is also a function of the previous constant reactivity insertion rate. To minimize potential undesirable power overshoots, the control law will commence demand reactivity removal at a lower relative power level when the previous constant reactivity insertion rate is higher. The control law employed in the STRTUP computer code is similar to that utilized for the KIWI-A reactors. For further description of the KIWI-A control law refer to Appendix A. Finally, demand reactivity and reactivity feedback estimation determine the required control drum position. Control drum position alteration rate and the correspondent reactivity change rate have initially been set to 10°/sec and \$0.6/sec, respectively, as was previously discussed in this section. In the next three sections of Chapter 5, reactor startup simulations for the three reactor models utilizing the control law which has just been described will be discussed.

5.3 Startup Simulation Results for the NERVA Small Engine Model

Prior to discussing the startup simulation results for the NERVA small engine model, the commonalities in methodological approach in the startup simulations for the three rocket engine models will be described.

Five demand reactivity insertions were analyzed to bound the range of potential rocket engine startup times for each of the three reactor types. The prompt jump approximation was used to estimate the demand reactivity requirement for 5, 10, 20, 40, and 80 second reactor startups. This approximation can be expressed as follows:

$$\frac{\rho}{\beta} = \frac{1}{1 + \lambda\ t / \ln\left(P_f/P_o\right)} \tag{5.8}$$

where,

ρ = reactivity

β = effective delayed neutron fraction

λ = precursor decay constant
t = time
P_f = final power
P_o = initial power.

To provide a basis for comparison of engine startup results attributable only to the variance in the reactor response time constants and reactivity feedback effects required that demand reactivity should be a constant. Therefore, as is illustrated by Equation (5.8), the effective delayed neutron fraction must also be set to a constant. In the calculation of the five standardized demand reactivities, the effective delayed neutron fraction for the NERVA small engine was utilized. As is described in more detail in Section 5.2, a constant demand reactivity also implied that the measured power level where reactivity removal commenced was also standardized.

A common set of initial conditions was established for the startup simulations. These initial conditions were as follows:

a. Reactor critical
b. Power level - 1.0 kW
c. Chamber temperature - 200°K
d. Inlet temperature - 200°K
e. Inlet pressure - 0.12 MPa
f. Engine chilldown completed.

Figures 16 through 18 in Section 5.1 illustrate reactor power level, core outlet temperature, and pump outlet pressure response, respectively, to a 0.9 β step reactivity insertion for each of the three reactor models. In each case design conditions were rapidly approached. A plateau occurred when each of the parameters was within one percent of design conditions. Since the basis for comparison between the three rocket engine models was that portion of the startup where rapid transient response occured, time to within one percent of design conditions will be employed as a standardized comparison parameter. Table 21 and Figure 20 illustrate the startup time to within one percent of design conditions as a function of demand reactivity for the NERVA small engine model. As can be observed in Figure 20; reactor power level, reactor outlet temperature, and pump outlet pressure all exhibited a similar variance as demand reactivity was altered. In each case power level responded the most rapidly followed by outlet temperature and then inlet pressure. The response time differential to within one percent of design conditions for the three parameters decreased as the reactor startup time increased.

Table 21

NERVA Startup Time to Within One Percent of Design Conditions

ρ_D(¢)	Power (sec)	Temperature (sec)	Pressure (sec)
86.4	6.2	8.5	12.7
76.1	10.0	12.3	15.9
61.4	22.1	24.5	27.4
44.3	56.1	58.1	60.5
28.5	129.2	130.7	132.9

Table 22 lists reactivity feedback effects and required control drum span as a function of demand reactivity. The control drum span startup requirement was at its maximum for the most rapid startup transient because the propellant feedback reactivity differential was also at its maximum. As demand reactivity decreased, the control drum span startup requirement reached its minimum for the 27.4 second startup and then gradually increased (by approximately seven percent) as startup time was increased to 132.9 seconds. As can be seen in Tables 21 and 22, the control drum span startup requirement was not only a function of the reactivity feedback levels but also the time differential between outlet temperature and inlet pressure response. Also illustrated was that the control drum span startup

Figure 20

NERVA Startup Time to Within One Percent of Design Conditions

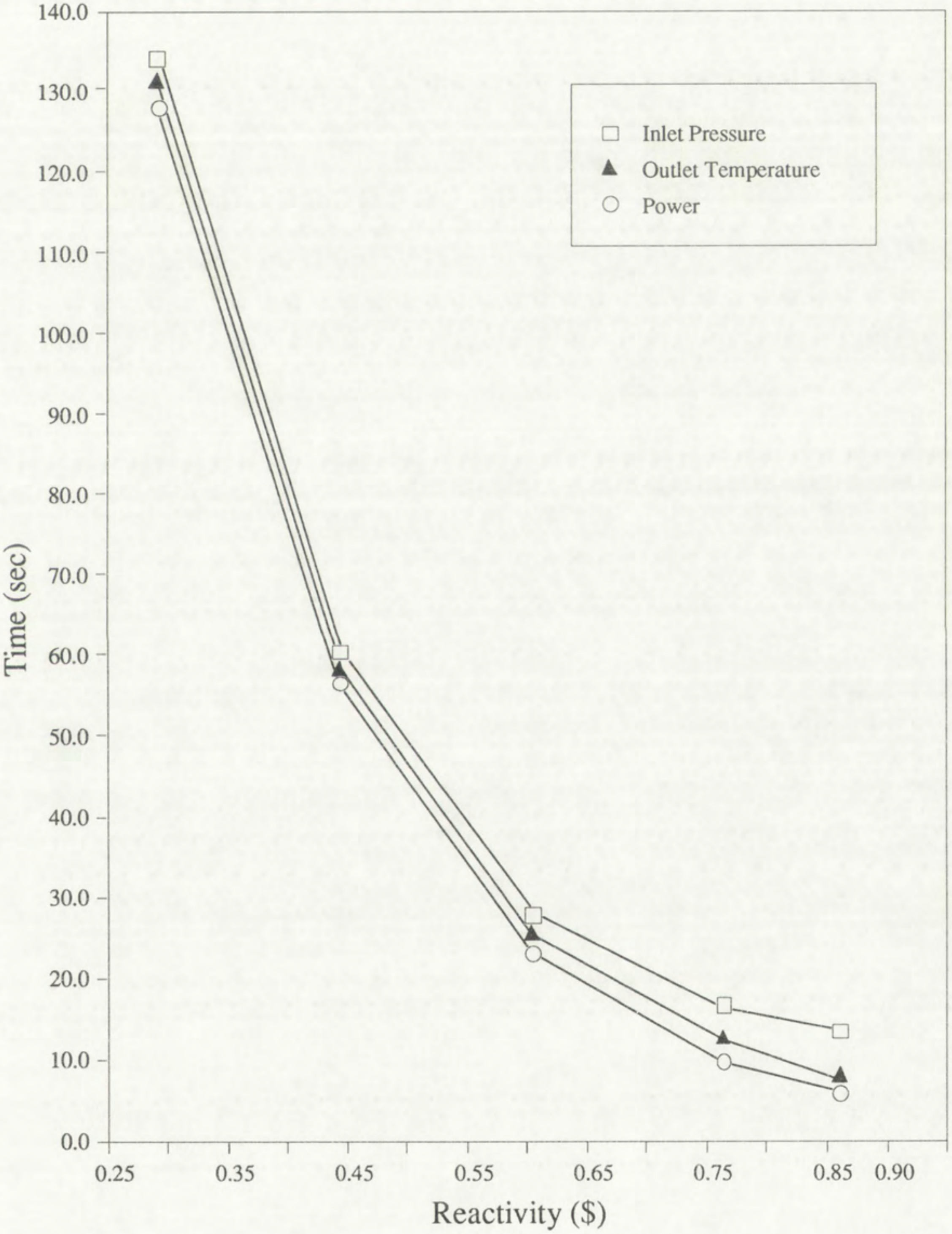

Table 22

NERVA Reactivity Feedback Effects and Control Drum Span Startup Requirement ($)

ρ_D	$\Delta\rho_{CD}$	$\Delta\rho_{prop}$	$\dot{\rho}_{max_p}$(/s)	$\Delta\rho_{temp}$	$\dot{\rho}_{max_t}$(/s)
0.864	2.27	1.80	0.57	–0.75	–0.34
0.761	2.03	1.57	0.33	–0.75	–0.31
0.614	1.32	1.50	0.15	–0.75	–0.15
0.443	1.36	1.50	0.12	–0.75	–0.08
0.285	1.42	1.50	0.10	–0.75	–0.03

requirement reached a practical minimum level as a function of the propellant reactivity feedback level.

For each of the five startup simulations, the maximum reactivity rate of change is given in Table 22 for both propellant and temperature feedback effects. The rate of reactivity change for both feedback effects decreased with increasing startup time to design conditions. Recall from the discussion in Section 5.2, the control drum reactivity change rate was set to $0.6/sec. For the most rapid startup, the control mechanism could minimally overcome the maximum propellant reactivity insertion rate.

Temperature reactivity feedback did not vary as a function of demand reactivity. However, the maximum rate of negative temperature feedback decreased by an order magnitude as the temperature response time to within one percent of design conditions increased from 8.5 to 130.7 seconds.

Figures 21 through 23 illustrate the reactivity feedback profiles and control drum response to 0.864, 0.614, and 0.285 β demand reactivity insertions, respectively. For the 0.864 β demand reactivity startup, the control drums initially inserted reactivity since both propellant and temperature feedback effects were minimal. From approximately 2.5 to 6.0 seconds after startup initiation both the temperature and propellant feedback was negative due to

Figure 21

NERVA Reactivity Feedback Profile
(0.864 β Insertion)

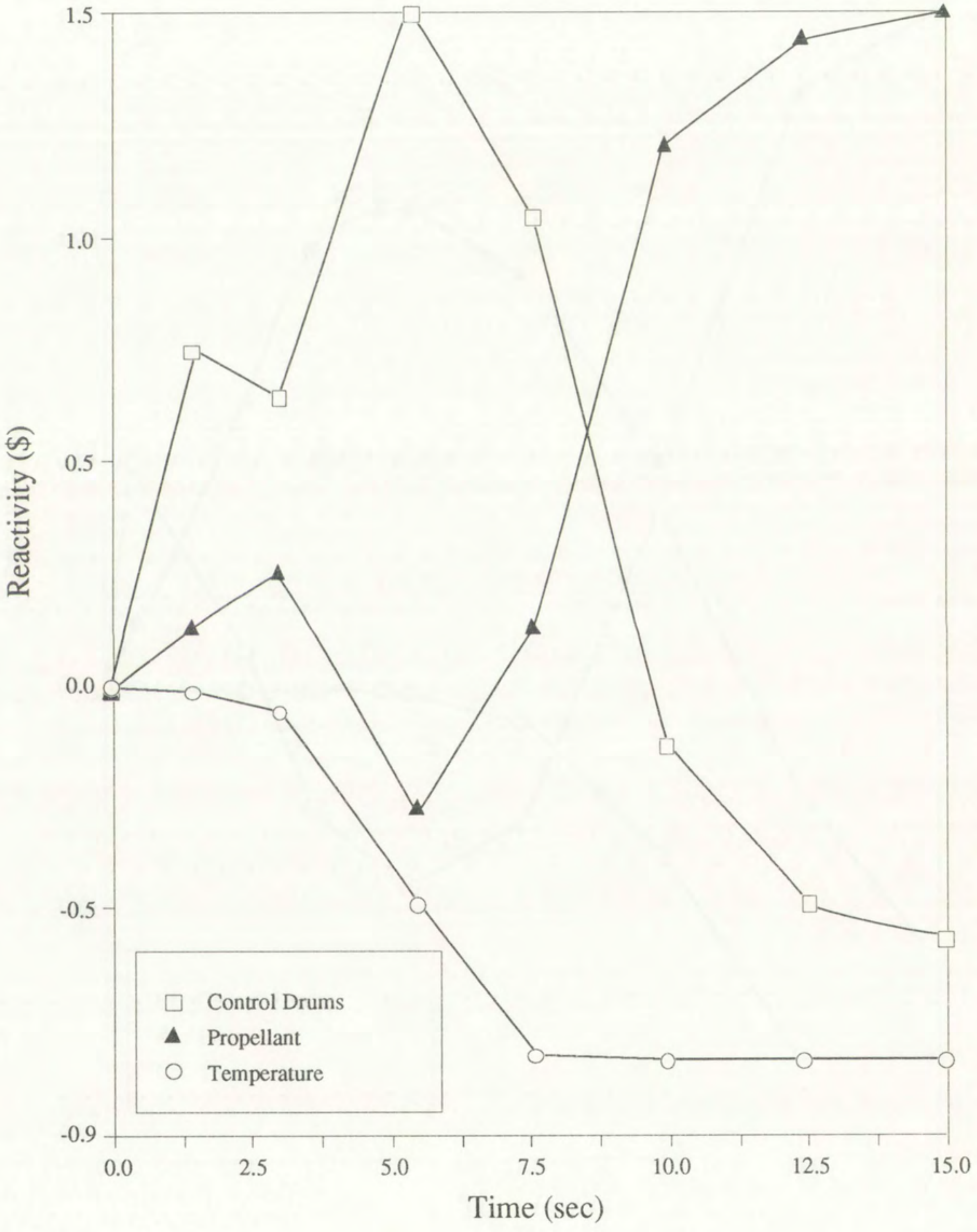

Figure 22

NERVA Reactivity Feedback Profile
(0.614 β Insertion)

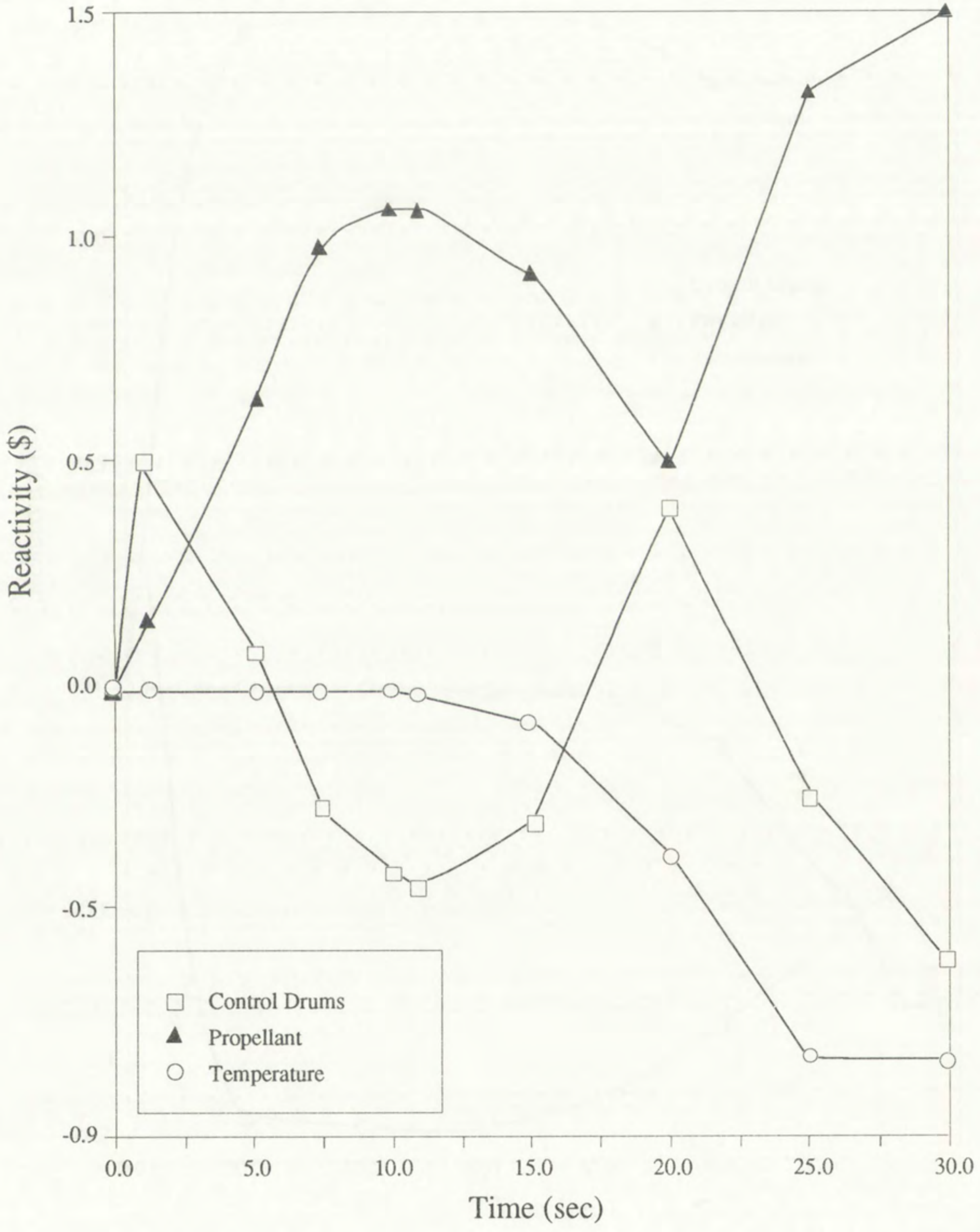

Figure 23

NERVA Reactivity Feedback Profile
(0.285 β Insertion)

increasing core temperature and decreasing propellant density, respectively. The control drums responded during this portion of engine startup by a reactivity insertion of approximately \$0.9. Once core outlet temperature approached its design value, propellant feedback inserted reactivity at or near its maximum rate given in Table 22 from 7.5 to 10.0 seconds after startup initiation. The control drums responded to this positive propellant feedback by removing reactivity at the maximum rate of \$0.6/sec. Equilibrium of feedback effects and control drum position occurred at approximately 15.0 seconds.

In the 0.614 β demand reactivity insertion illustrated in Figure 22, propellant feedback was positive throughout the startup transient. This was due to the increased temperature response time as well as the decreased differential between the temperature and pressure response times. The practical implication of having only positive propellant feedback was a reduction of the required control drum span. Also, by increasing the startup time the maximum propellant reactivity feedback insertion rate decreased. Therefore, the control safety margin increased without having to also increase the control drum speed. Temperature feedback exhibited a slower response as compared with the 0.864 β startup but had a similar profile shape.

In the 0.285 β demand reactivity insertion illustrated in Figure 23, temperature response was delayed substantially further still. Very little temperature feedback occurred until 100.0 seconds after the startup was commenced. Between 100.0 and 130.0 seconds after startup initiation, temperature reactivity feedback was –\$0.75. Positive propellant feedback increased to near its maximum level in the first 20.0 seconds of the startup and varied by approximately \$0.25 throughout the remainder of the transient. The rate of change of reactivity feedback effects was much slower than in all other startups allowing more control margin without increasing the control drum speed.

From a control standpoint alone, all five startups were feasible. However, neither transient thermal stress limits nor turbopump operational constraints were considered for the purpose of this analysis. These additional considerations would increase the NERVA small engine design startup time to values greater than those obtainable if only control system constraints are considered.

5.4 Startup Simulation Results for the Particle Bed Model

As was the case for the NERVA small engine model, five standardized demand reactivity startup simulations were performed. Table 23 and Figure 24 illustrate the startup time to within one percent of design conditions for the particle bed model. As can be observed in Figure 24; reactor power level, reactor outlet temperature, and pump outlet pressure all exhibited a similar variance as demand reactivity was altered. In each case power level and outlet temperature responded similarly while inlet pressure response lagged. The response time differential to within one percent of design conditions between inlet pressure and the other two parameters decreased as the reactor startup time increased.

Table 23

Particle Bed Startup Time to Within One Percent of Design Conditions

ρ_D(¢)	Power (sec)	Temperature (sec)	Pressure (sec)
86.4	6.3	6.3	10.4
76.1	9.4	9.4	13.0
61.4	22.3	22.4	26.1
44.3	58.2	58.2	60.7
28.5	132.2	132.2	134.1

Table 24 lists reactivity feedback effects and required control drum span as a function of demand reactivity. The control drum span startup requirement

Figure 24

Particle Bed Startup Time to Within One Percent of Design Conditions

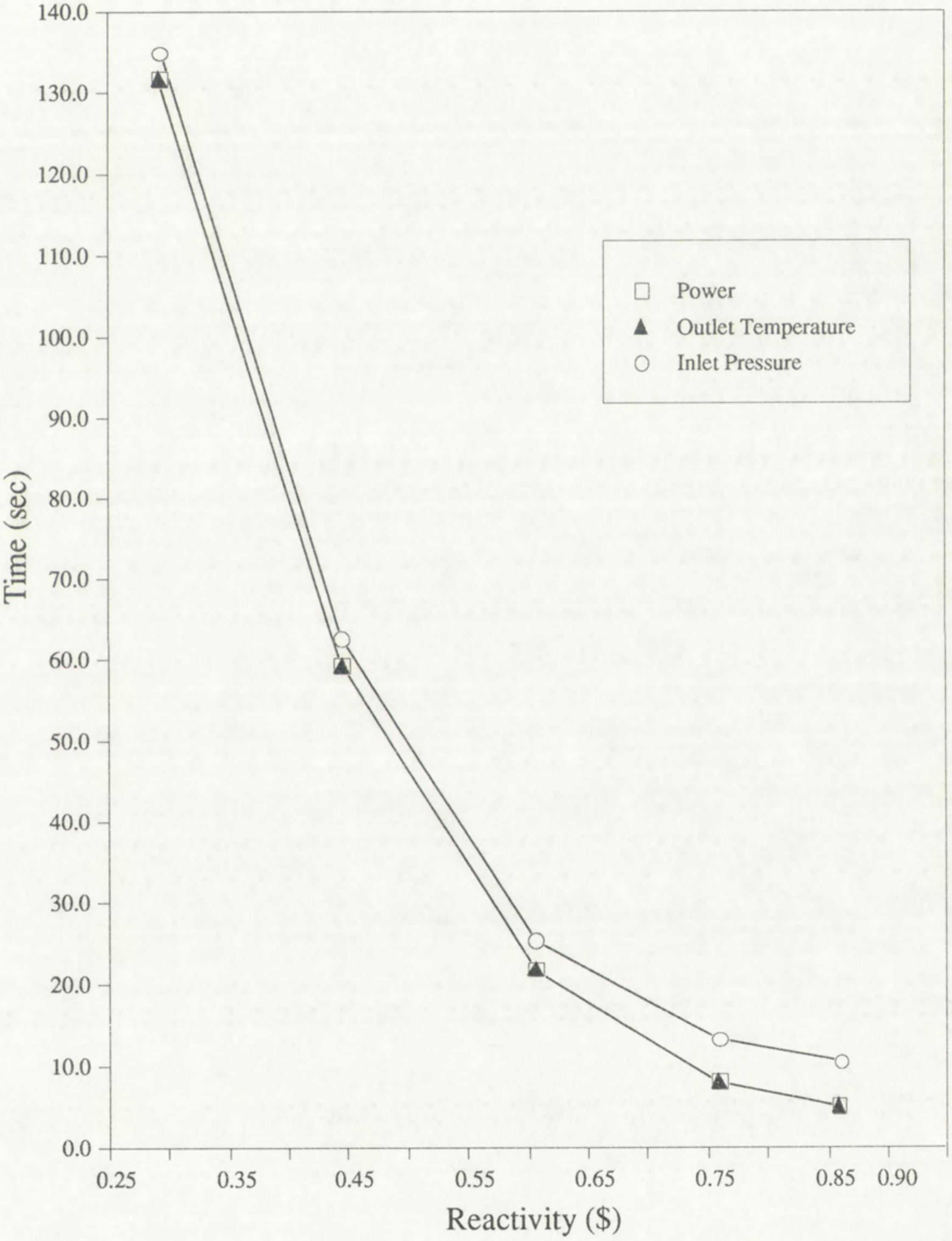

Table 24

Particle Bed Reactivity Feedback Effects and Control Drum Span Startup Requirement ($)

ρ_D	$\Delta\rho_{CD}$	$\Delta\rho_{prop}$	$\dot{\rho}_{max_p}$(/s)	$\Delta\rho_{temp}$	$\dot{\rho}_{max_t}$(/s)
0.864	2.69	2.06	0.56	−1.21	−0.60
0.761	2.53	1.91	0.56	−1.21	−0.58
0.614	1.78	1.35	0.48	−1.21	−0.20
0.443	1.47	1.33	0.25	−1.21	−0.11
0.285	1.30	1.33	0.17	−1.21	−0.05

was at its maximum for the most rapid startup transient because the propellant feedback reactivity differential was also at its maximum. As demand reactivity decreased, the control drum span startup requirement also decreased. The control drum span startup requirement was reduced by approximately 50 percent as startup time increased from 10.4 to 134.1 seconds. As can be seen in Tables 23 and 24, the control drum span startup requirement was not only a function of the reactivity feedback levels but also the time differential between outlet temperature and inlet pressure response. Also illustrated was that the control drum span startup requirement reached a practical minimum level as a function of the propellant reactivity feedback level.

For each of the five startup simulations, the maximum reactivity rate of change is given in Table 24 for both propellant and temperature feedback effects. The rate of reactivity change for both feedback effects decreased with increasing startup time to design conditions. Recall from the discussion in Section 5.2, the control drum reactivity change rate was set to $0.6/sec. For the most rapid startups, the control mechanism could minimally overcome the maximum propellant reactivity insertion rate. Temperature reactivity feedback did not vary as a function of demand reactivity. However, the maximum rate of negative temperature feedback decreased by a factor of 12 as the temperature response time to within one percent of design conditions increased from 6.3 to 132.2 seconds.

Figures 25 through 27 illustrate the reactivity feedback profiles and the control drum response to 0.864, 0.614, and 0.285 β demand reactivity insertions, respectively. For the 0.864 β demand reactivity startup, the control drums initially inserted reactivity since both the propellant and temperature feedback effects were minimal. From approximately 3.5 to 6.5 seconds after startup initiation both the temperature and propellant feedback was negative due to increasing core temperature and decreasing propellant density, respectively. The control drums responded during this portion of the engine startup by a reactivity insertion of approximately $1.75. Once core outlet temperature approached its design value, propellant feedback inserted reactivity at or near its maximum rate given in Table 24 from 6.0 to 10.0 seconds after startup initiation. The control drums responded to this positive propellant feedback by removing reactivity at the maximum rate of $0.6/sec. Equilibrium of feedback effects and control drum position occurred at approximately 12.5 seconds.

In the 0.614 β demand reactivity insertion illustrated in Figure 26, propellant feedback was positive throughout the startup transient. This was due to the increased temperature response time as well as the decreased differential between the temperature and pressure response times. The practical implication of having only positive propellant feedback was a reduction of the required control drum span. Also, by increasing the startup time the maximum propellant reactivity feedback insertion rate decreased. Therefore, the control safety margin increased without having to also increase the control drum speed. Temperature feedback exhibited a slower response as compared with the 0.864 β startup but had a similar profile shape.

In the 0.285 β demand reactivity insertion illustrated in Figure 27, temperature response was delayed substantially further still. Very little temperature feedback occurred until 100.0 seconds after the startup was

Figure 25

Particle Bed Reactivity Feedback Profile
(0.864 β Insertion)

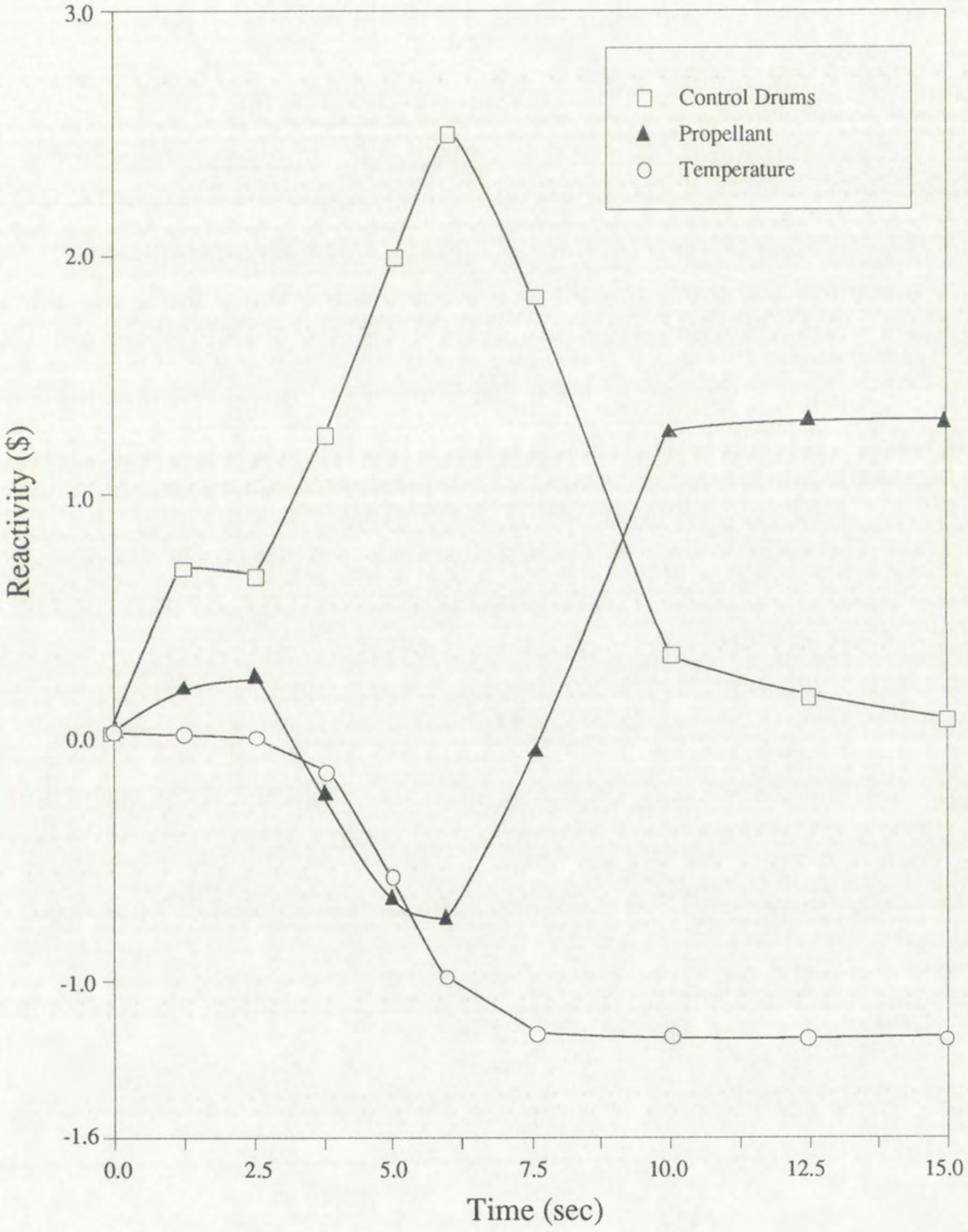

Figure 26

Particle Bed Reactivity Feedback Profile
(0.614 β Insertion)

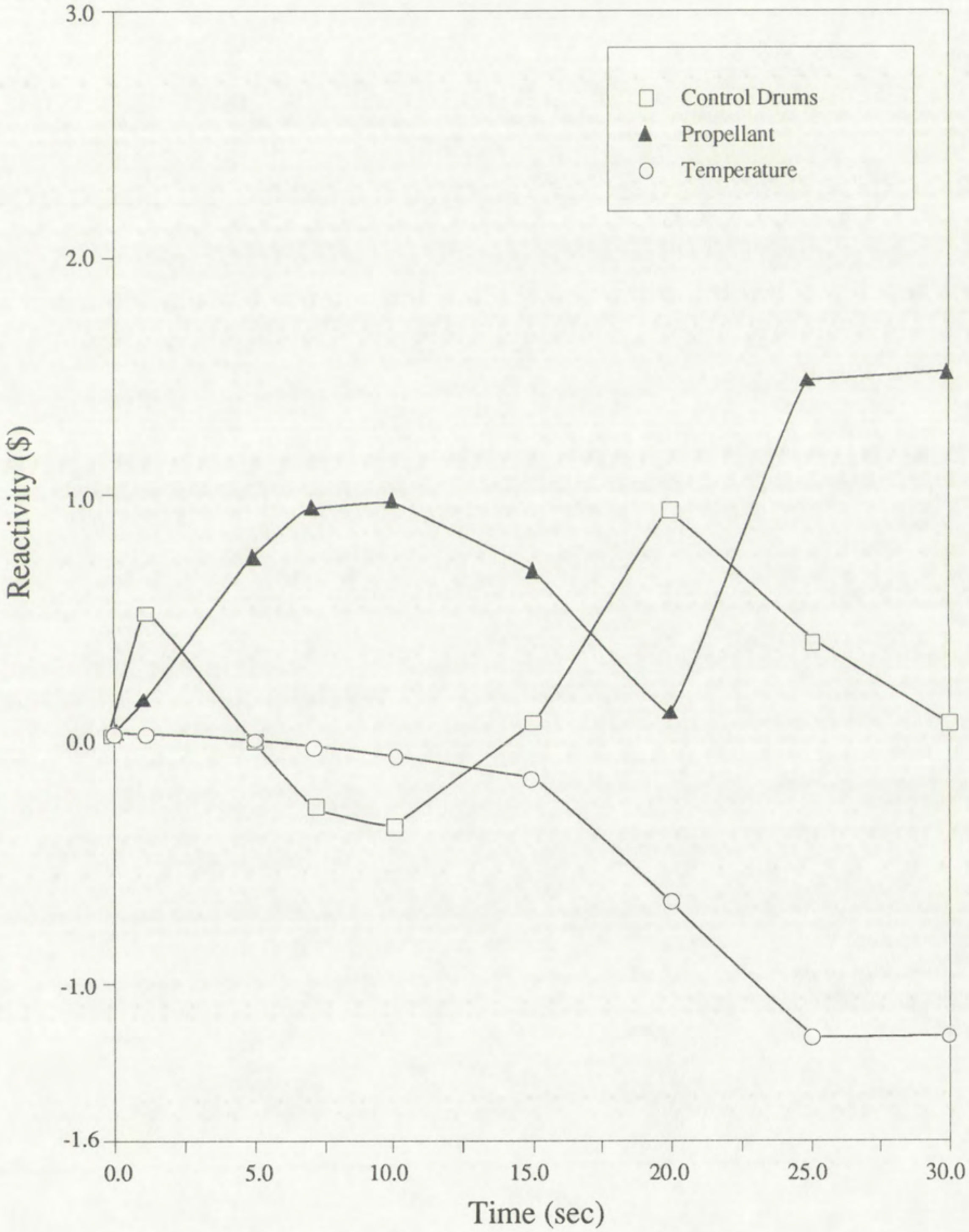

Figure 27

Particle Bed Reactivity Feedback Profile
(0.285 β Insertion)

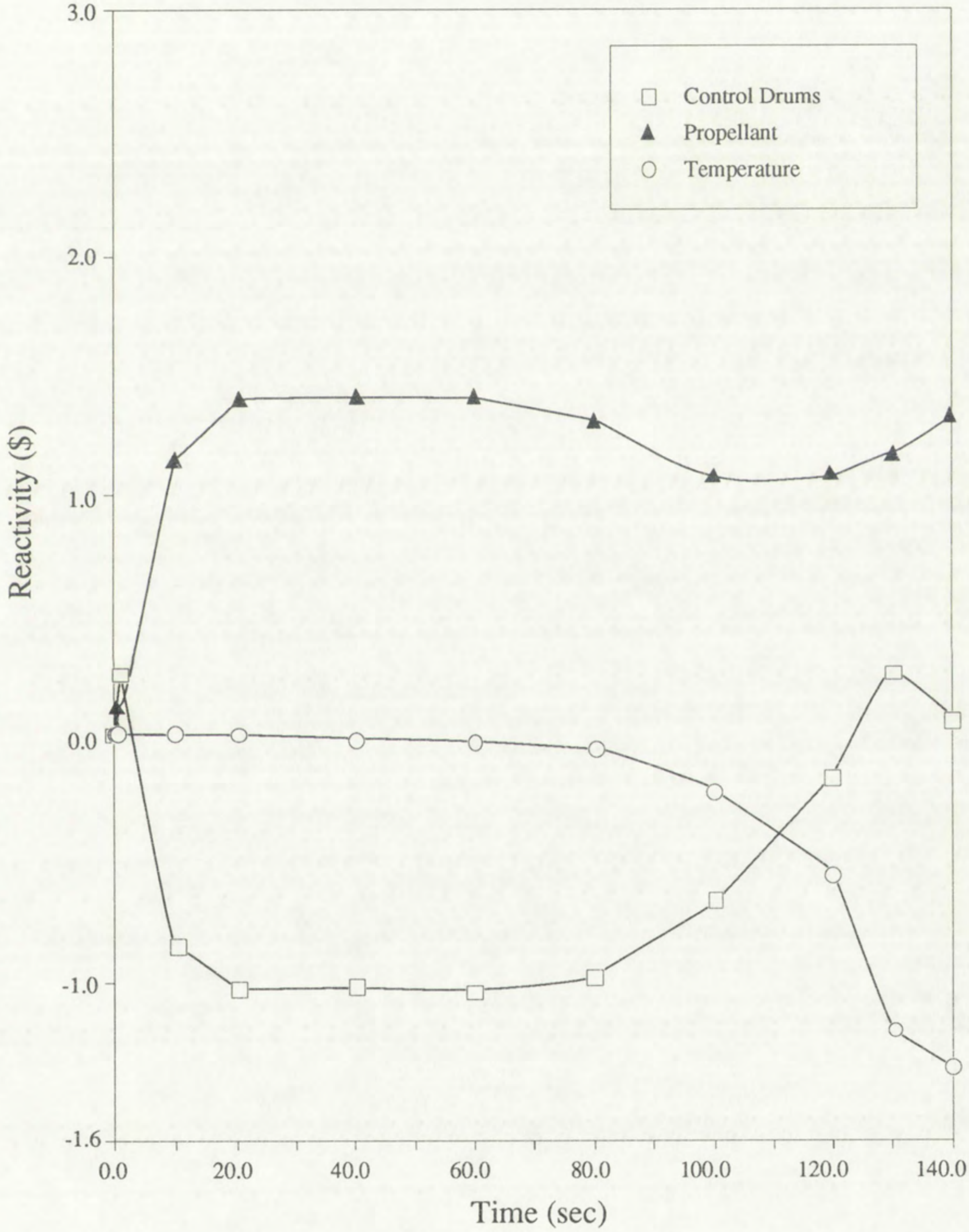

commenced. Between 100.0 and 135.0 seconds after startup initiation, temperature reactivity feedback was –$1.21. Positive propellant feedback increased to near its maximum level in the first 20.0 seconds of the startup and varied by approximately $0.3 throughout the remainder of the transient. The rate of change of reactivity feedback effects was much slower than in all other startups allowing more control margin without increasing the control drum speed.

From a control standpoint alone, all five startups were feasible. However, neither transient thermal stress limits nor turbopump operational constraints were considered for the purpose of this analysis. These additional considerations would increase the particle bed rocket engine design startup time to values greater than those obtainable if only control system constraints are considered.

5.5 Startup Simulation Results for the Wire Core Model

As was the case for the other two reactor models, five standardized demand reactivity startup simulations were performed. However, due to the greater uncertainty in the magnitude of propellant reactivity feedback as compared with the particle bed and NERVA small engine designs, a sensitivity analysis was conducted which varied propellant feedback worth from $1.0 to $4.16. With propellant feedback worth set to $1.0 and the control drum reactivity change rate at $0.6/sec, demand reactivity was varied from 0.864 to 0.285 β. In all five startup simulations unstable power oscillations were observed because the propellant reactivity insertion rate exceeded the control system reactivity removal rate. Due to this instability the control drum reactivity change rate was increased to $1.5/sec.

With the control drum reactivity change rate set to $1.5/sec, propellant feedback worth was varied from $1.0 to $4.16. In this sensitivity analysis, stable startup simulations were observed until propellant feedback worth exceeded $2.5. When propellant feedback worth was greater than $2.5, the propellant reactivity insertion rate exceeded the control system reactivity removal rate.

Therefore, an additional sensitivity study was performed which increased the control system reactivity removal rate until a stable startup simulation result could be obtained with demand reactivity at 0.864 β and propellant feedback worth at approximately \$4.16. When the control system reactivity removal rate reached \$2.5/sec, a stable startup simulation occurred. At this magnitude of reactivity control rate, the reactivity feedback effects of propellant density changes could be controlled. To illustrate the potentially greatest variation between the three reactor models, a propellant feedback worth of \$4.16 was chosen for the wire core reactor base case analysis.

Table 25 and Figure 28 illustrate the startup time to within one percent of design conditions with propellant feedback worth set to \$4.16 and the control system reactivity change rate at \$2.5/sec. As can be observed in Figure 28; reactor power level, reactor outlet temperature, and pump outlet pressure all exhibited a similar variance as demand reactivity was altered. In each case power level responded the most rapidly followed by outlet temperature and then inlet pressure. The response time differential to within one percent of design conditions for the three parameters decreased as the reactor startup time increased.

Table 25

Wire Core Startup Time to Within One Percent of Design Conditions

ρ_D(¢)	Power (sec)	Temperature (sec)	Pressure (sec)
86.4	2.2	3.0	7.2
76.1	3.1	3.8	7.9
61.4	6.5	7.2	10.3
44.3	17.5	18.6	22.2
28.5	50.0	50.4	57.5

Figure 28

Wire Core Startup Time to Within One Percent of Design Conditions

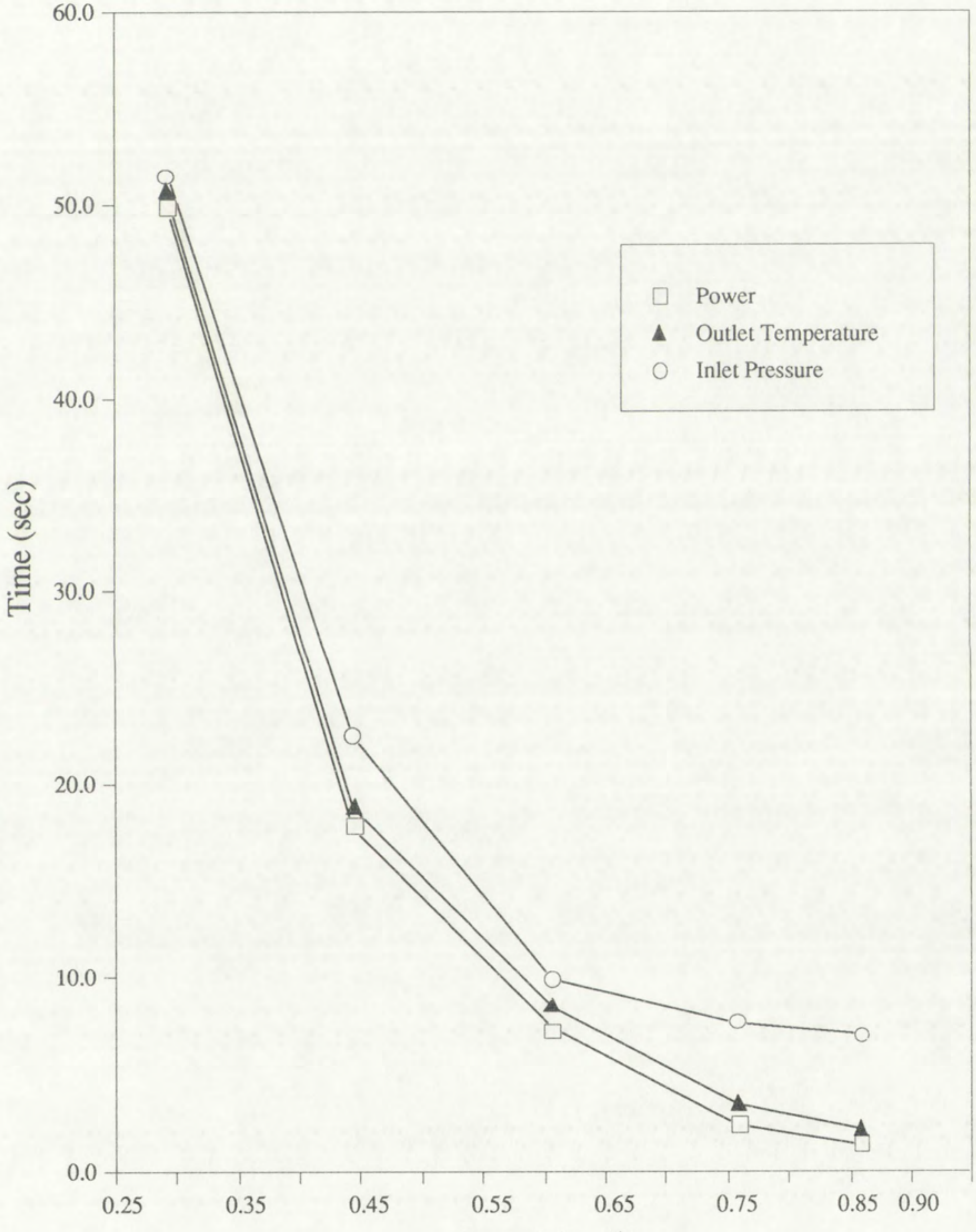

Table 26 lists reactivity feedback effects and required control drum span as a function of demand reactivity. The control drum span startup requirement was at its maximum for the most rapid startup transient because the propellant feedback reactivity differential was also at a maximum. As demand reactivity decreased, the control drum span startup requirement reached its minimum for the 22.2 second startup and then increased (by approximately 30 percent) as startup time was increased to 51.5 seconds. As can be seen in Tables 25 and 26, the control drum span startup requirement was not only a function of the reactivity feedback levels but also the time differential between outlet temperature and inlet pressure response. Also illustrated was that the control drum span startup requirement reached a practical minimum level as a function of the propellant reactivity feedback level.

Table 26

Wire Core Reactivity Feedback Effects and Control Drum Span Startup Requirement ($)

ρ_D	$\Delta\rho_{CD}$	$\Delta\rho_{prop}$	$\dot{\rho}\,\max_p$ (/s)	$\Delta\rho_{temp}$	$\dot{\rho}\,\max_t$ (/s)
0.864	7.90	7.73	2.49	–1.00	–0.91
0.761	7.81	7.60	2.49	–1.00	–0.88
0.614	6.41	6.06	2.49	–1.00	–0.38
0.443	3.35	4.16	0.94	–1.00	–0.19
0.285	4.40	4.16	0.94	–1.00	–0.10

For each of the five startup simulations, the maximum reactivity rate of change is given in Table 26 for both propellant and temperature feedback effects. The rate of reactivity change for both feedback effects decreased with increasing startup time to design conditions. For the three most rapid startups, the control mechanism could minimally overcome the maximum propellant reactivity insertion rate. Temperature reactivity feedback did not vary as a function of demand reactivity. However, the maximum rate of negative temperature feedback decreased by a factor of nine as the temperature response time to within one percent of design conditions increased from 3.0 to 50.4 seconds.

Figures 29 through 31 illustrate the reactivity feedback profiles and control drum response to 0.864, 0.614, and 0.285 β demand reactivity insertions, respectively. For the 0.864 β demand reactivity startup, control drums initially inserted reactivity since the temperature feedback was minimal and propellant feedback was slightly negative. From approximately 1.2 to 2.5 seconds after startup initiation both the temperature and propellant feedback was negative due to increasing core temperature and decreasing propellant density, respectively. The control drums responded during this portion of the engine startup by a reactivity insertion of approximately $2.0. Once core outlet temperature approached its design value, propellant feedback inserted reactivity at or near its maximum rate given in Table 26 from 2.5 to 7.0 seconds after startup initiation. The control drums responded to this positive propellant feedback by removing reactivity at the maximum rate of $2.5/sec. Equilibrium of feedback effects and control drum position occurred at approximately 7.5 seconds.

In the 0.614 β demand reactivity insertion illustrated in Figure 30, propellant feedback was both negative and positive during the startup transient. However, the maximum differential of propellant reactivity feedback decreased by approximately 22 percent as startup time to within one percent of design conditions increased from 7.2 to 10.3 seconds. The practical implication of this reduction of the maximum propellant reactivity feedback differential was a reduction of the required control drum span. When comparing the 0.864 and 0.614 β demand reactivity startups, the maximum propellant feedback reactivity insertion rate remained essentially constant. Therefore, the control safety margin did not increase. Temperature feedback exhibited a slower response as compared with the 0.864 β startup but had a similar profile shape.

Figure 29

Wire Core Reactivity Feedback Profile
(0.864 β Insertion)

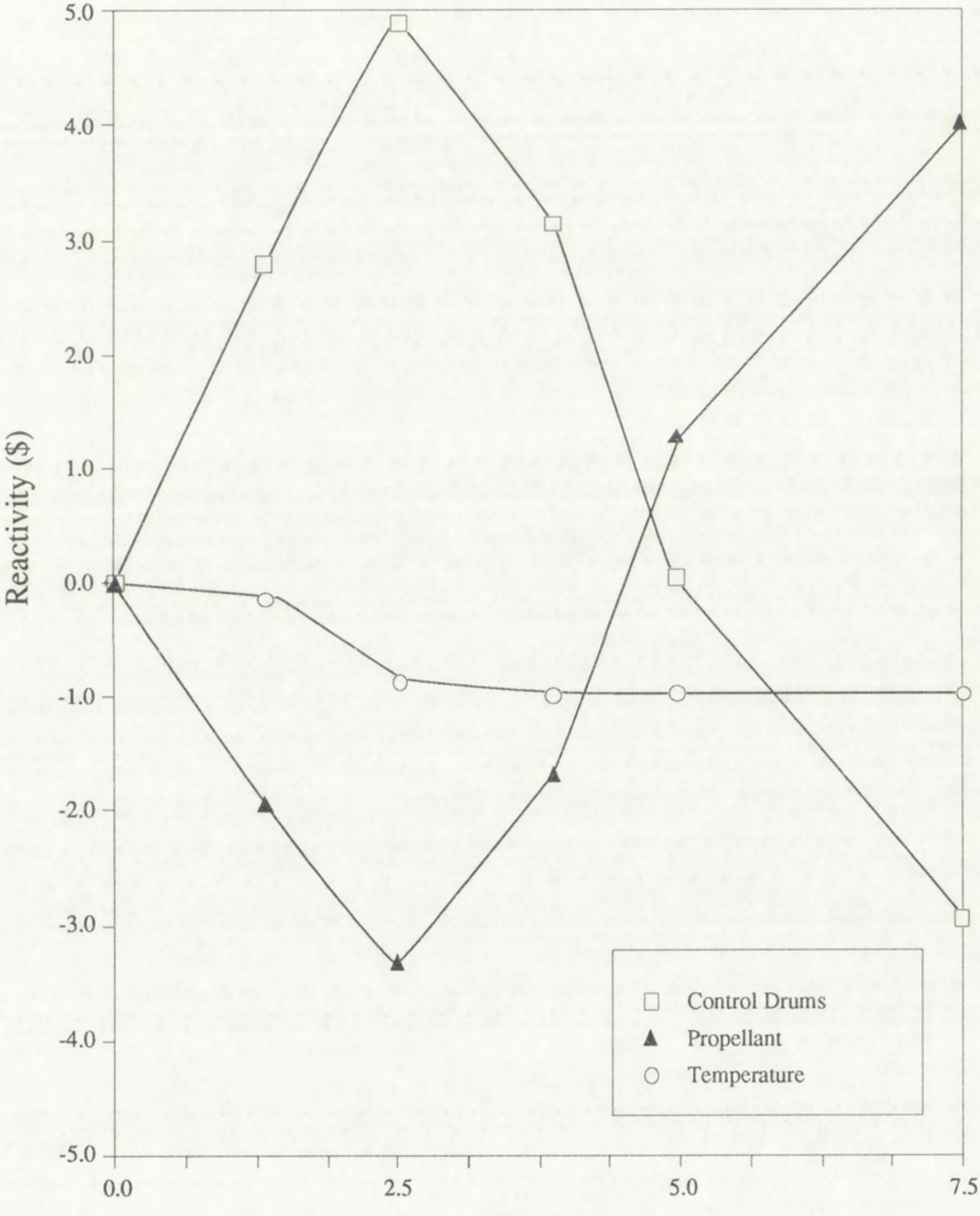

Figure 30

Wire Core Reactivity Feedback Profile
(0.614 β Insertion)

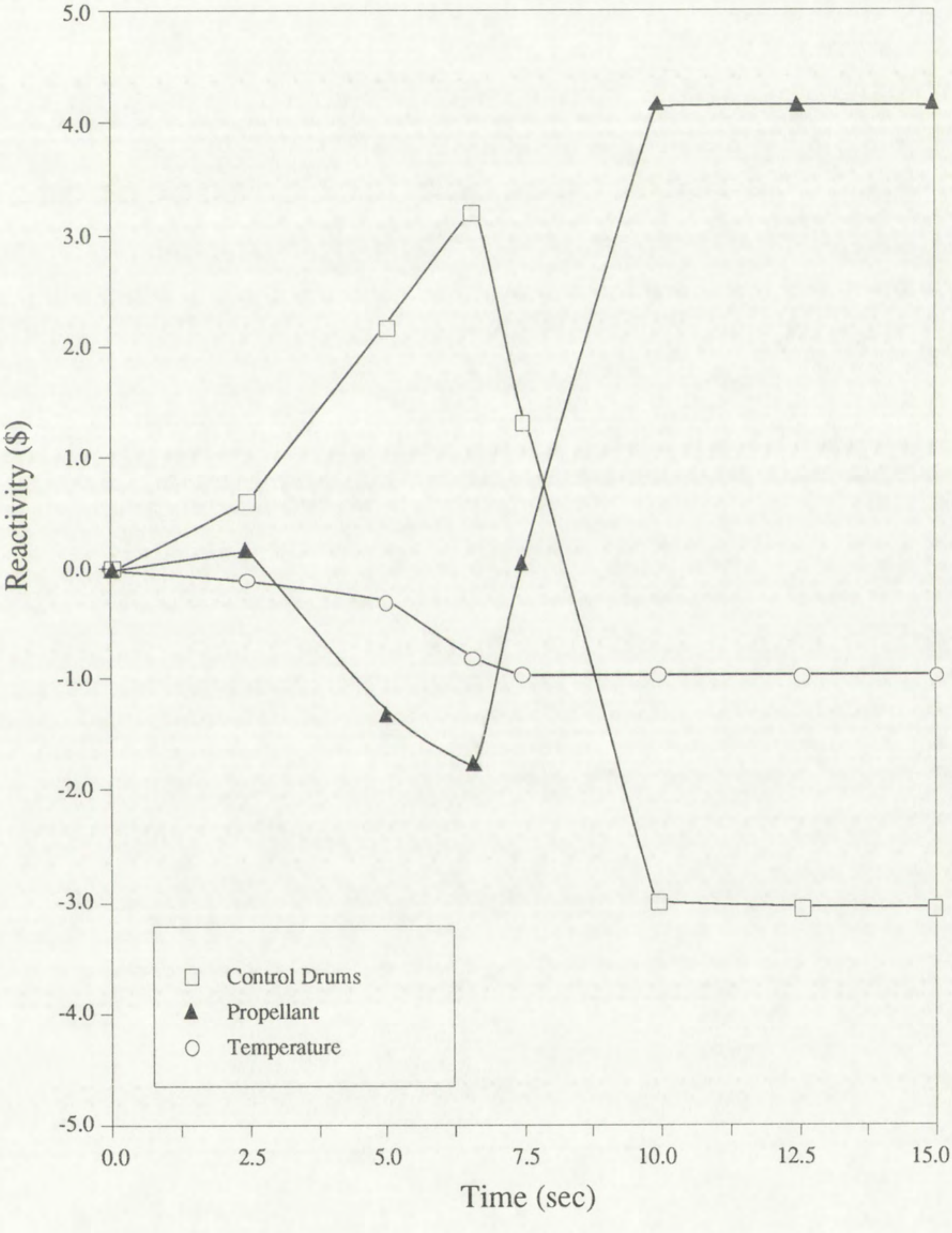

Figure 31

Wire Core Reactivity Feedback Profile
(0.285 β Insertion)

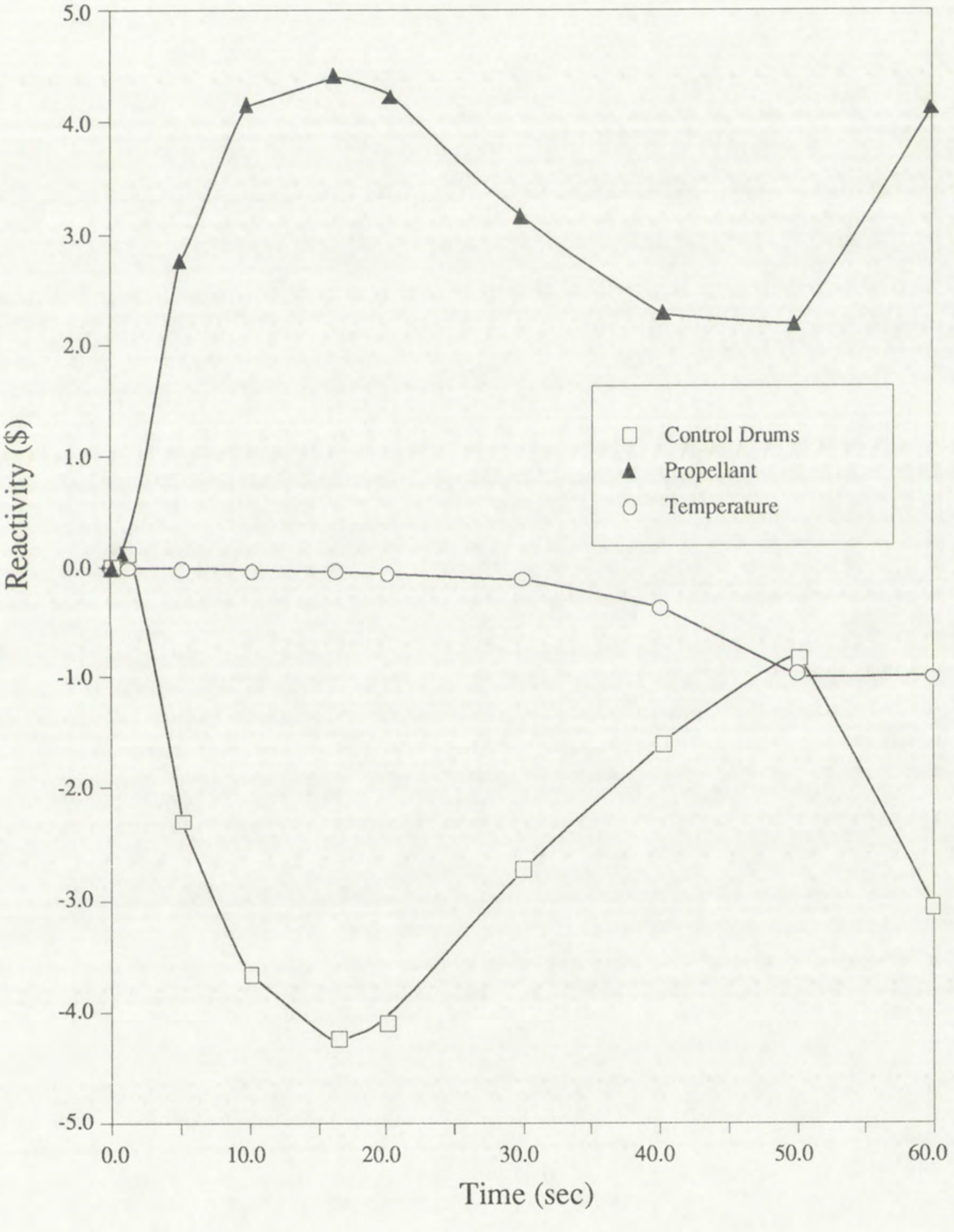

In the 0.285 β demand reactivity insertion illustrated in Figure 31, temperature response was delayed substantially further still. Very little temperature feedback occurred until 25.0 seconds after the startup was commenced. Between 25.0 and 50.0 seconds after startup initiation, temperature reactivity feedback was –$1.0. Positive propellant feedback increased to near its maximum level in the first 16.0 seconds of the startup and varied by approximately $2.0 throughout the remainder of the transient. The rate of change of reactivity feedback effects was much slower than in all other startups allowing more control margin without increasing the control drum speed.

Two other values of propellant feedback worth ($1.0 and $2.5) were analyzed for the five demand reactivity startups. In these two sensitivity studies, the control system reactivity removal rate was set to $1.5/sec. The essential shape of the reactivity feedback profiles as illustrated in Figures 29 through 31 was not affected; however, the magnitude of the propellant reactivity feedback differential decreased. Also, the demand reactivity level where propellant reactivity feedback remained positive throughout the startup transient increased. The reduction of control drum speed resulted in a slight increase in engine startup times. With the exception of the three aforementioned differences in the startup profiles which occurred when propellant feedback was varied, no other significant characteristics of the feedback effects or startup profiles were altered.

From a control standpoint alone, all five startups for each of the three values of propellant reactivity feedback were feasible. However, neither transient thermal stress limits nor turbopump operational constraints were considered for the purpose of this analysis. These additional considerations would increase the wire core rocket engine design startup time to values greater than those obtainable if only control system constraints are considered.

5.6 Comparison of Startup Simulation Results Between the Three Nuclear Rocket Engine Models

In this section the startup simulation results which were discussed in Sections 5.3, 5.4, and 5.5 for the NERVA small engine, particle bed, and wire core reactors, respectively, will be compared. Also compared will be the effect of the variance of engine design and engine startup time on controllability and safety margins. The following parameters will form the basis of this comparison:

a. Startup response time for power level, reactor outlet temperature, and turbopump outlet pressure
b. Propellant reactivity feedback effects
c. Temperature reactivity feedback effects
d. Control drum span startup requirement
e. Control drum speed (reactivity insertion and removal rate) requirement.

It was found that the variance of the neutronics, heat transfer, and turbopump response time constants between the three rocket engine models altered engine response time. Figure 32 illustrates the reactor power level startup time from cold critical to within one percent of design conditions as a function of demand reactivity for each of the three reactor designs. Recall from the discussion in Section 4.2.3 that the wire core neutronics response time constant was approximately three orders of magnitude less than the NERVA small engine design and a factor of 500 less than the particle bed design. This three order of magnitude difference in the neutronics response time constant between the three models effectively bounds the variance which would be expected for any of the ten design options which had been considered by NASA for the Space Exploration Initiative. When comparing the thermal particle bed reactor and the epithermal NERVA small engine reactor, the power level startup time varied by no more than six percent for any of the startup simulations. As expected, the wire core reactor exhibited

Figure 32

Reactor Power Level Response Time Comparison for the Three Reactor Models

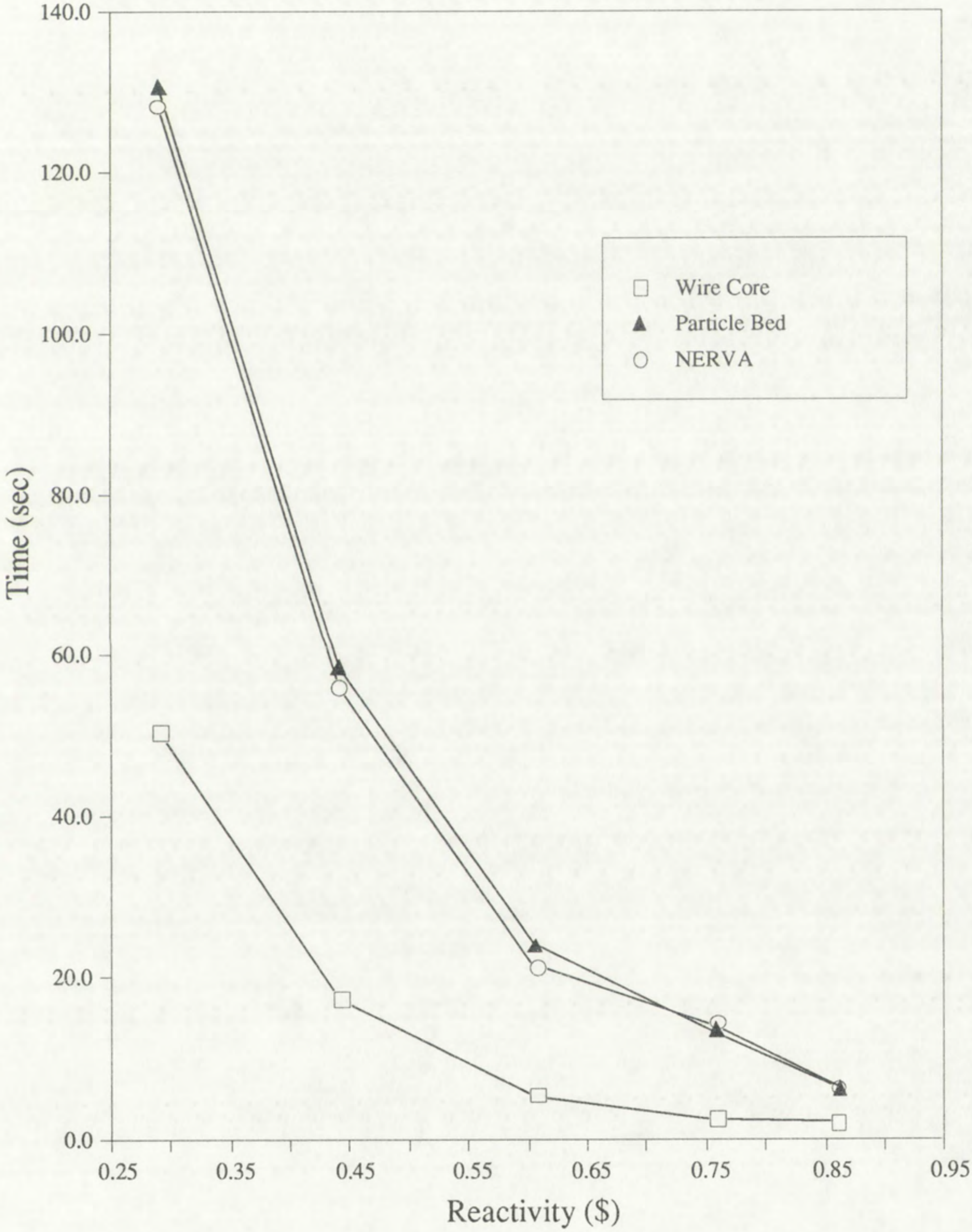

the most rapid power level increase of any of the three models. For the five startup simulations, the power level transit time from cold critical (1.0 kW) to within one percent of design power level (341.5 MW) for the wire core reactor was from a factor of 3.5 to 2.6 faster. The power level response time differential between the wire core and the other two reactors increased as demand reactivity was reduced. Based on control considerations alone, engine transients from cold critical to design power level within five seconds are clearly attainable for each of the three reactor models. Startup time can be further reduced (to approximately two seconds) if a fast neutron spectrum reactor such as the wire core design is employed.

Figure 33 illustrates the core outlet temperature response time from cold critical (200°K) to within one percent of design conditions (2673°K) as a function of demand reactivity for each of the three reactor models. Recall from the discussion in Section 4.2.1 that the particle bed reactor heat transfer response time constant was approximately a factor of 11 less than the NERVA small engine design and a factor of 2.5 less than the wire core reactor design. As was the case for the neutronics response time constant, this range of difference in the heat transfer response time constant between the three models effectively bounds the variance which would be expected for any of the ten design options which had been considered by NASA for the Space Exploration Initiative. It was found that the outlet temperature response time was not only a function of the heat transfer response time constant but more importantly a function of the neutronics response time constant. Therefore, even through the particle bed reactor exhibited the least time differential between power level and outlet temperature response, the outlet temperature transit time from cold critical to within one percent of design conditions for the wire core design was more rapid. When comparing the outlet temperature response time for the wire core and particle bed models, the wire core reactor was at a minimum twice as fast for all five startup simulations.

Figure 33

Outlet Temperature Response Time Comparison for the Three Reactor Models

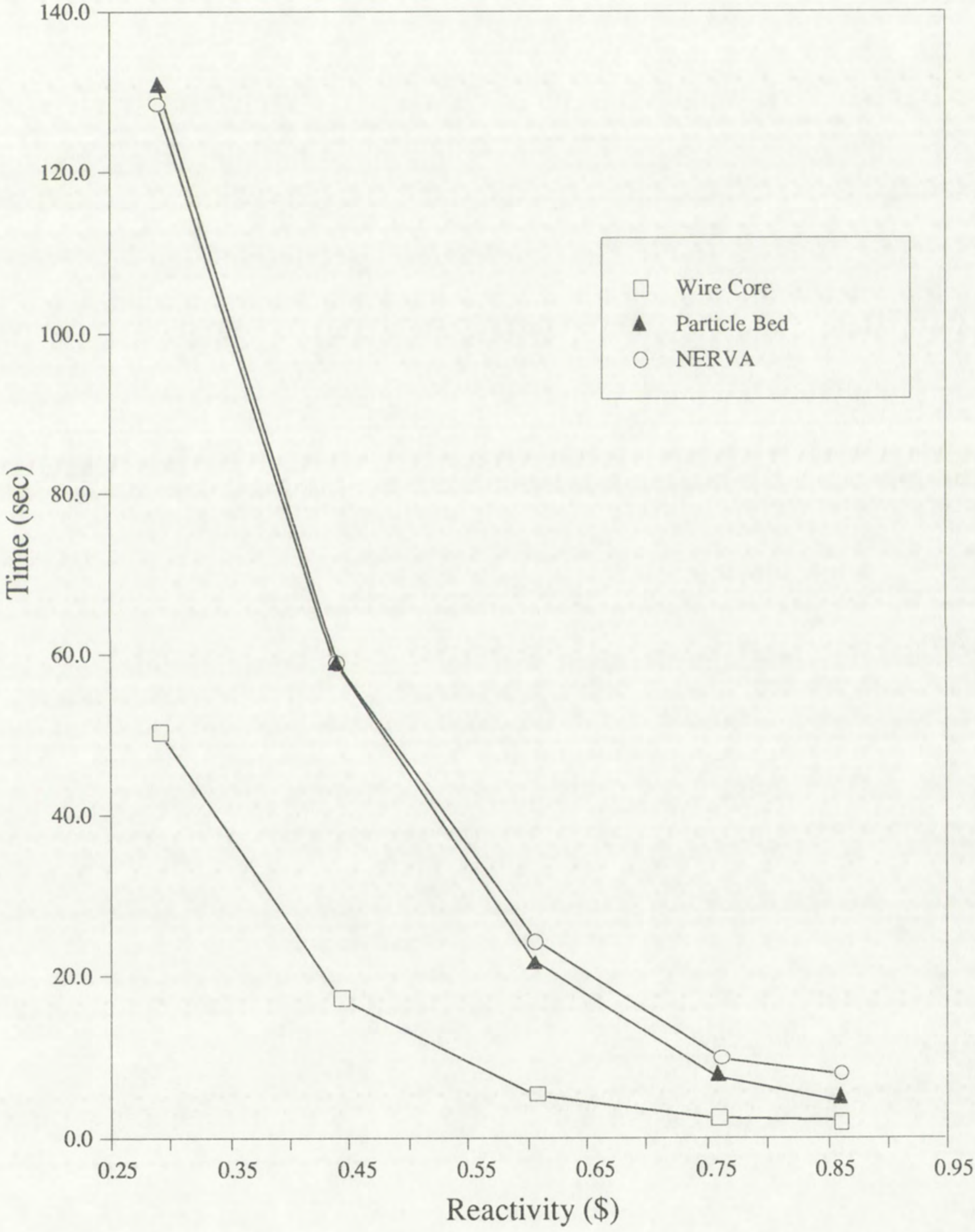

The NERVA small engine and particle bed models provide a basis for comparison which can be utilized to isolate and examine the dependence of the engine heatup time upon the heat transfer response time constant. First, the power level transit time to design conditions for the two models is nearly identical. Second, there is a factor of 11 differential in the heat transfer response time constant between the particle bed and NERVA small engine models which effectively bounds the variance if any other design option would be considered. This is due to the heat transfer response time constant variance being primarily a function of fuel mass when the thrust requirement is standardized. To propose a design with substantially greater reactor mass than the NERVA small engine would decrease ROTV efficiency. Also, to propose a design with less fuel mass than the particle bed reactor would further increase power density which would necessitate design changes to further increase heat transfer efficiency and impose an additional safety burden. As compared with the particle bed reactor, the NERVA small engine model exhibited an approximately two second temperature response lag time until engine startup time approached 60 seconds.

Outlet temperature response time is also constrained by transient thermal stress limits. For the purpose of this control strategy analysis, the transient thermal stress limit and correspondent heatup rate limit for the wire core reactor will be assumed to be bounded by those of the particle bed and NERVA small engine designs since no detailed stress analysis for the wire core engine was available in the literature. The maximum rate of temperature increase based upon transient thermal stress limits for the particle bed and NERVA small engine designs are as follows:

a. Particle bed - 500°K/sec (Refs. 27, 28)

b. NERVA small engine - 83°K/sec (Ref. 5).

Therefore, over a 2500°K range from cold critical to operational design conditions, the practical limit on the temperature response lag time between the three designs is approximately 25 seconds.

The following conclusions can be drawn from a comparison of outlet temperature response time between the three models:

a. If only engine power level control constraints are considered, the core outlet temperature response time variance is primarily a function of the neutronics response time constant

b. When considering the maximum variance in the heat transfer response time constant, outlet temperature response time over a 2500°K range is altered by only two seconds

c. Outlet temperature response time is primarily limited by transient thermal stress limits.

Figure 34 illustrates the turbopump outlet pressure response time from cold critical to within one percent of design conditions as a function of demand reactivity for each of the three reactor models. Recall from Sections 4.2.2 and 5.1 that the turbopump response time constant for the NERVA small engine and particle bed reactors was 1.0 second and 0.93 seconds for the wire core reactor. Thus the variance between the three models was only seven percent even though the turbopump outlet pressure requirement for the NERVA small engine model is approximately double that of the two folded flow reactors. As was the case for the core outlet temperature response time, it was found that the turbopump outlet pressure response time was not only a function of the turbopump response time constant but also the neutronics and heat transfer response time constants. From the derivation of the Smith-Stenning equations given in Appendix A, it is shown that the rate of change of shaft speed and the correspondent increase in turbopump outlet pressure is dependent upon the magnitude and rate of increase of core outlet temperature. Thus the wire core reactor exhibited the fastest turbopump outlet pressure response time of the three models. The outlet pressure lag time of the NERVA and particle bed models as compared to the wire core reactor increased as engine startup time increased.

Figure 34

Turbopump Outlet Pressure Response Time
Comparison for the Three Reactor Models

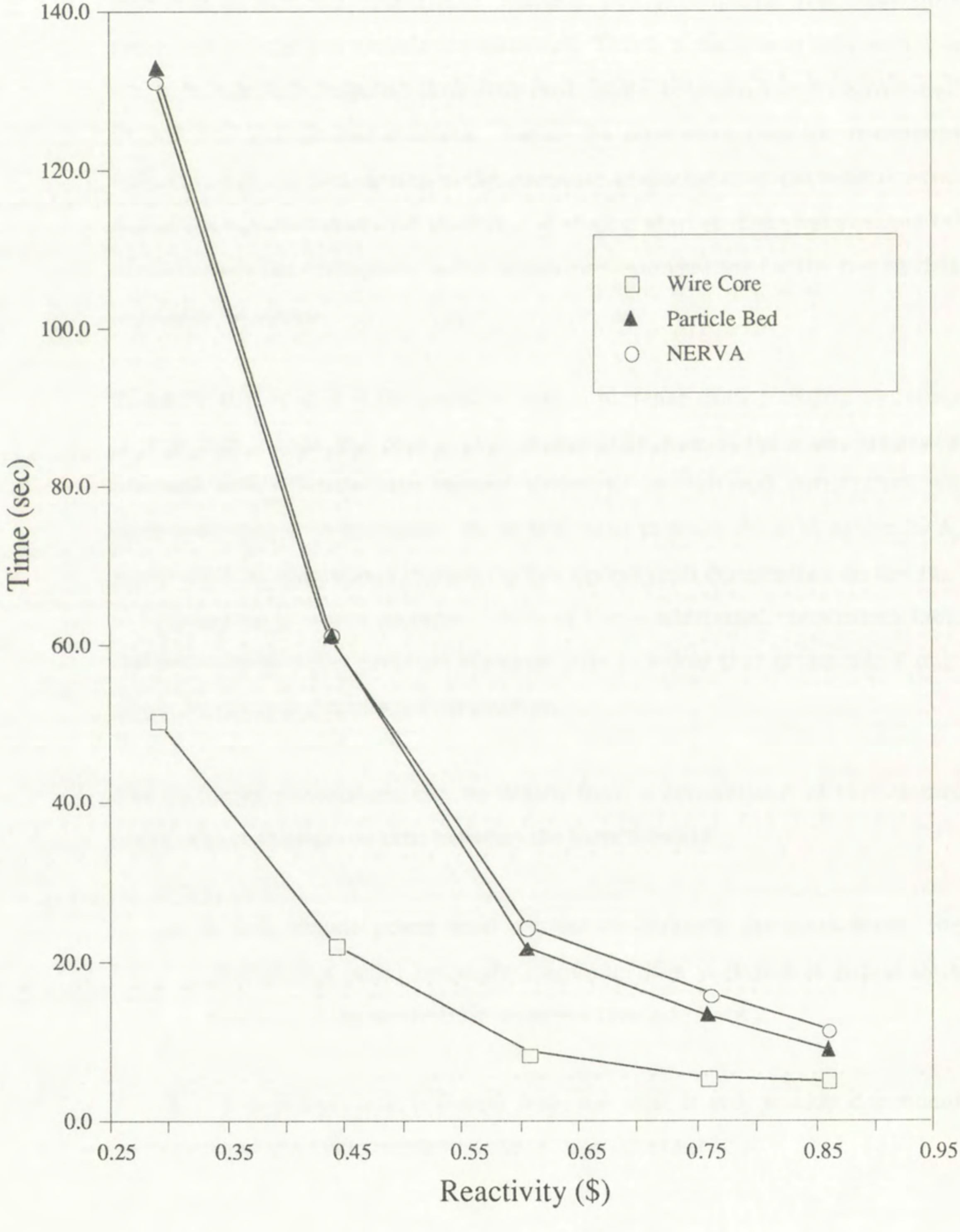

The NERVA small engine and particle bed models provide a basis for comparison which can be utilized to illustrate the limited dependence of the turbopump outlet pressure response time upon the heat transfer response time constant. First, the power level transit time to design conditions for the two models is nearly identical. Second, the turbopump response time constants for the two models are identical. Third, a maximum differential in the heat transfer response time constant exists between the NERVA small engine and particle bed reactors. Figure 34 illustrates that the maximum differential in the turbopump outlet pressure response time between the two models is approximately 20 percent. If engine startup time approaches 60 seconds then the turbopump outlet pressure response time for the two models is nearly identical.

Since the turbopump outlet pressure rate of increase during engine bootstrap is dependent upon the core outlet temperature rate of increase, transient thermal stress limits also impose practical operational constraints on turbopump pressure increases. As is discussed in more detail in Appendix A, pump stall considerations impose further operational constraints on the rate of turbopump pressure increase. Both of these additional constraints limit the turbopump outlet pressure response rate to below that attainable if only power level control limits are considered.

The following conclusions can be drawn from a comparison of turbopump outlet pressure response time between the three models:

a. If only engine power level control constraints are considered, the turbopump outlet pressure response time variance is primarily a function of the neutronics response time constant

b. Turbopump outlet pressure response time is only weakly dependent upon the heat transfer response time constant

c. Turbopump outlet pressure response is primarily limited by transient thermal stress limits and pump stall considerations.

The next area of comparison between the three reactor models to be discussed will be propellant reactivity feedback effects. Figure 35 illustrates the maximum propellant reactivity feedback differential as a function of demand reactivity for each of the three reactor designs. Recall from the discussion of propellant reactivity feedback effects in Sections 5.3, 5.4, and 5.5 that for the most rapid startup transient, propellant density can be less than its value at cold critical conditions during the first portion of the transient due to rapid increases in core outlet temperature and the lag time inherent in turbopump outlet pressure response. Therefore, the maximum propellant reactivity feedback differential will exceed the total positive propellant reactivity feedback when traversing from cold critical to design operating conditions during the most rapid transients.

The wire core reactor not only has the maximum positive propellant reactivity feedback but also the maximum differential in propellant reactivity feedback when compared with the other two designs. Wire core sensitivity studies which are described in Section 5.5 varied the maximum positive propellant feedback from approximately \$4.16 to \$1.0. Even with the maximum positive propellant feedback for the wire core set to \$1.0, the maximum propellant reactivity feedback differential was greater than that for either of the other two reactor designs for the most rapid startup transients. Therefore, the dominant contribution to the propellant reactivity feedback differential is not only from the ultimate value of positive reactivity added by traversing from cold critical to design operating conditions, but also from the relative speed of the reactor outlet temperature response and correspondent turbopump pressure increase lag time. The effect of the variance of the maximum propellant feedback differential and positive propellant feedback will be discussed later in this section when control drum span startup requirements and control drum reactivity insertion and removal rate requirements are compared for the three nuclear rockets.

Figure 35

Propellant Reactivity Feedback Differential
Comparison for the Three Reactor Models

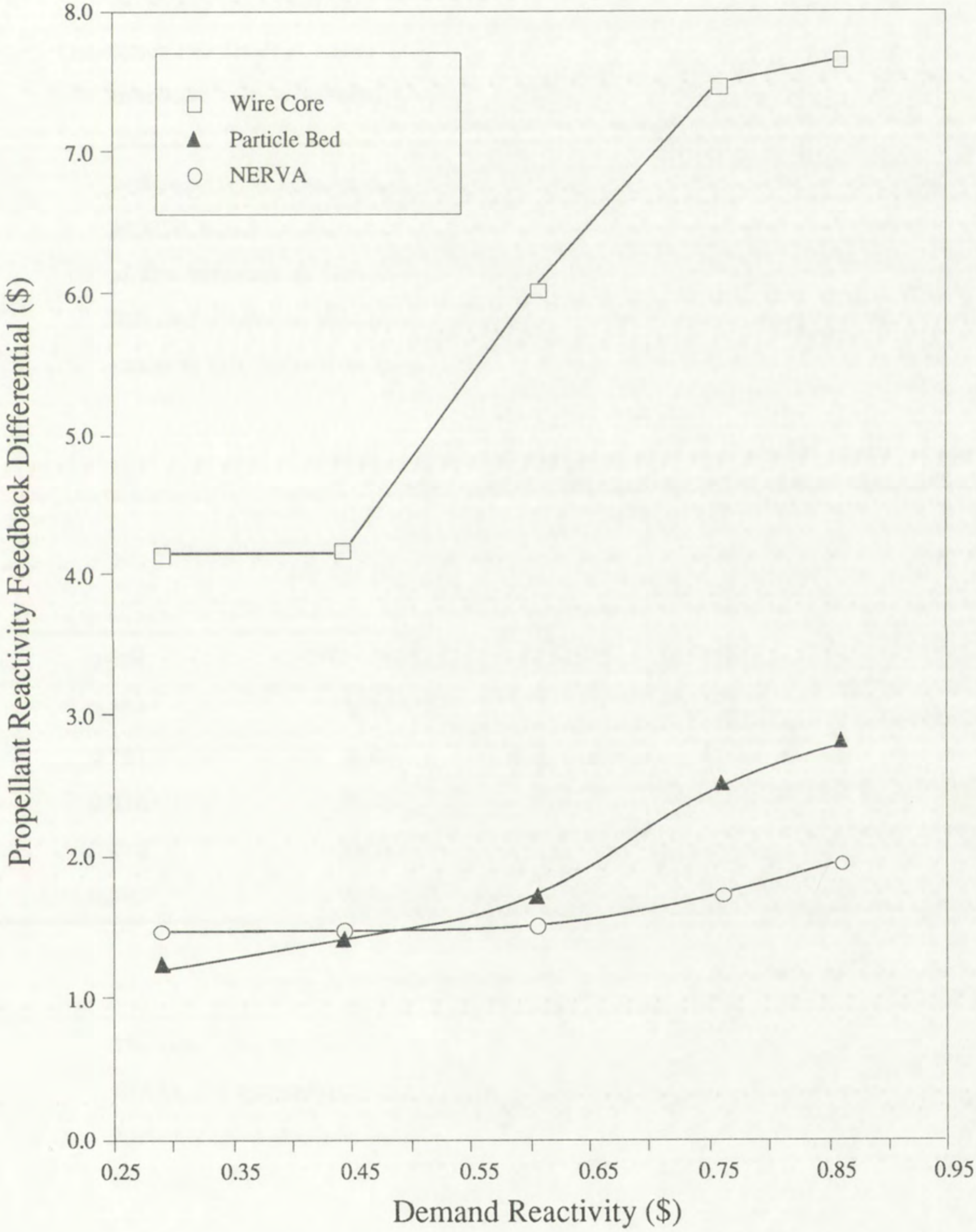

Another consequence of rapid startup transients with positive propellant reactivity feedback is rapid propellant reactivity insertion rates. Table 27 compares the maximum propellant reactivity insertion rate as a function of demand reactivity for each of the three reactor models. The propellant reactivity insertion rate for the wire core reactor is greater than that for the other two models. Also, the wire core reactor maximum propellant reactivity insertion rate is present until demand reactivity is decreased to 0.443 β. In contrast, the maximum propellant reactivity insertion rate for the particle bed reactor is present for the two most rapid startup transients and for the NERVA small engine for only the 0.864 β demand reactivity profile. The effect of the variance of the maximum propellant reactivity insertion rate will be discussed later in this section when the control drum reactivity insertion and removal rate requirements are compared for the three nuclear rocket engines.

Table 27

Maximum Propellant Reactivity Insertion Rate Comparison
for the Three Reactor Models ($/sec)

ρ_D($)	Wire Core	Particle Bed	NERVA
0.864	2.49	0.56	0.57
0.761	2.49	0.56	0.33
0.614	2.49	0.48	0.15
0.443	0.94	0.25	0.12
0.285	0.94	0.17	0.10

The next area of comparison between the three reactor models to be discussed will be the temperature reactivity feedback effects. Each of the three nuclear rocket engine designs exhibited the following similar temperature reactivity feedback effects:

a. In each of the five startup simulations temperature reactivity feedback was always negative

b. The total negative reactivity feedback contribution was within 38 percent

c. The temperature reactivity feedback differential was within 38 percent

d. In each of the five startup simulations temperature reactivity feedback profile shapes were nearly identical

e. The maximum temperature reactivity removal rate decreased as engine startup time increased.

Two of the initial conditions established for the startup simulations for each of the three reactor models were that engine chilldown was completed and that the reactor was at the cold critical operating point. Therefore, temperature reactivity feedback was always negative in each of the five startup simulations for the three rocket engines because chamber temperature during the startup transient was never below the cold critical temperature of 200°K.

In References 47 and 50 the total temperature reactivity feedback is given for the particle bed and NERVA small engine reactors, respectively. The total temperature reactivity feedback was within 38 percent for these two reactor models. The temperature reactivity feedback for the wire core of –\$1.0 was chosen based on values typical of fast spectrum reactors. Therefore, the total negative temperature reactivity feedback for the three reactor designs was similar.

The temperature reactivity feedback differential was within 38 percent for each of the three reactor models. This resulted as a consequence of the chamber temperature during all startup simulations never being below the cold critical temperature and similar total negative temperature reactivity feedback for the three designs. Therefore, when comparing the three designs the temperature reactivity feedback differential was identical to the difference in total negative temperature reactivity feedback contribution.

When Figures 21 through 23, 25 through 27, and 29 through 31 for NERVA small engine, particle bed, and wire core reactors are compared, similar temperature reactivity feedback profile shapes are observed. For the first portion of the startup transient temperature reactivity feedback is nearly zero. When chamber temperature begins to increase above 200°K and until the design operating temperature is approached, the temperature feedback profile shape is a negative reactivity addition at a decreasing rate. The differences between the temperature feedback profile shapes are mostly as a result of the variance of demand reactivity, not differences between the reactor models. As demand reactivity is decreased, the time when temperature reactivity feedback is nearly zero is increased and the time for the rocket chamber to transit from 200°K to 2700°K is also increased. The only difference in the temperature reactivity feedback profile shape attributable to differences between the three reactor models is the 38 percent variance in total reactivity feedback.

As was the case for propellant reactivity feedback, the maximum temperature reactivity change rate decreased as engine startup time increased. Table 28 provides a comparison of the maximum temperature reactivity removal rate as a function of demand reactivity for the three reactor models. Also, as was the case for propellant reactivity feedback, the maximum temperature reactivity change rate was dependent not only on the temperature response time constant but more importantly on the neutronics response time constant. Therefore, when comparing the wire core and particle bed models, the wire core temperature reactivity removal rate was always greater even though its temperature response time constant was a factor of 2.5 less.

Table 28

Maximum Temperature Reactivity Removal Rate Comparison
for the Three Reactor Models ($/sec)

ρ_D($)	Wire Core	Particle Bed	NERVA
0.864	–0.91	–0.60	–0.34
0.761	–0.88	–0.58	–0.31
0.614	–0.38	–0.20	–0.15
0.443	–0.19	–0.11	–0.08
0.285	–0.10	–0.05	–0.03

The next area of comparison between the three reactor models to be discussed will be the control drum span startup requirement. Figure 36 illustrates the control drum span startup requirement as a function of demand reactivity for each of the three reactor designs. The control drum span startup requirement is not only a function of demand reactivity (i.e., engine startup time) but also a function of reactivity feedback. The magnitude of propellant and temperature reactivity feedback as well as the lag time between outlet temperature and turbopump response both affect the magnitude of the control drum span startup requirement. The variance of the wire core reactor control drum span startup requirement will be utilized to illustrate the interrelationship between engine startup time and reactivity feedback effects.

For the wire core reactor, the control drum span startup requirement is approximately $4.4 at or below a demand reactivity of 0.285 β. The control drum span startup requirement is at a minimum when the demand reactivity is at 0.443 β. As engine startup time is further reduced, the control drum span startup requirement increases reaching a maximum of $7.9. Recall from the discussion in Section 5.5 that propellant reactivity feedback will be negative for some portion of the more rapid startup transients. Also, temperature feedback reactivity removal at or near its maximum rate coincides with the

Figure 36

Control Drum Span Startup Requirement Comparison
for the Three Reactor Models

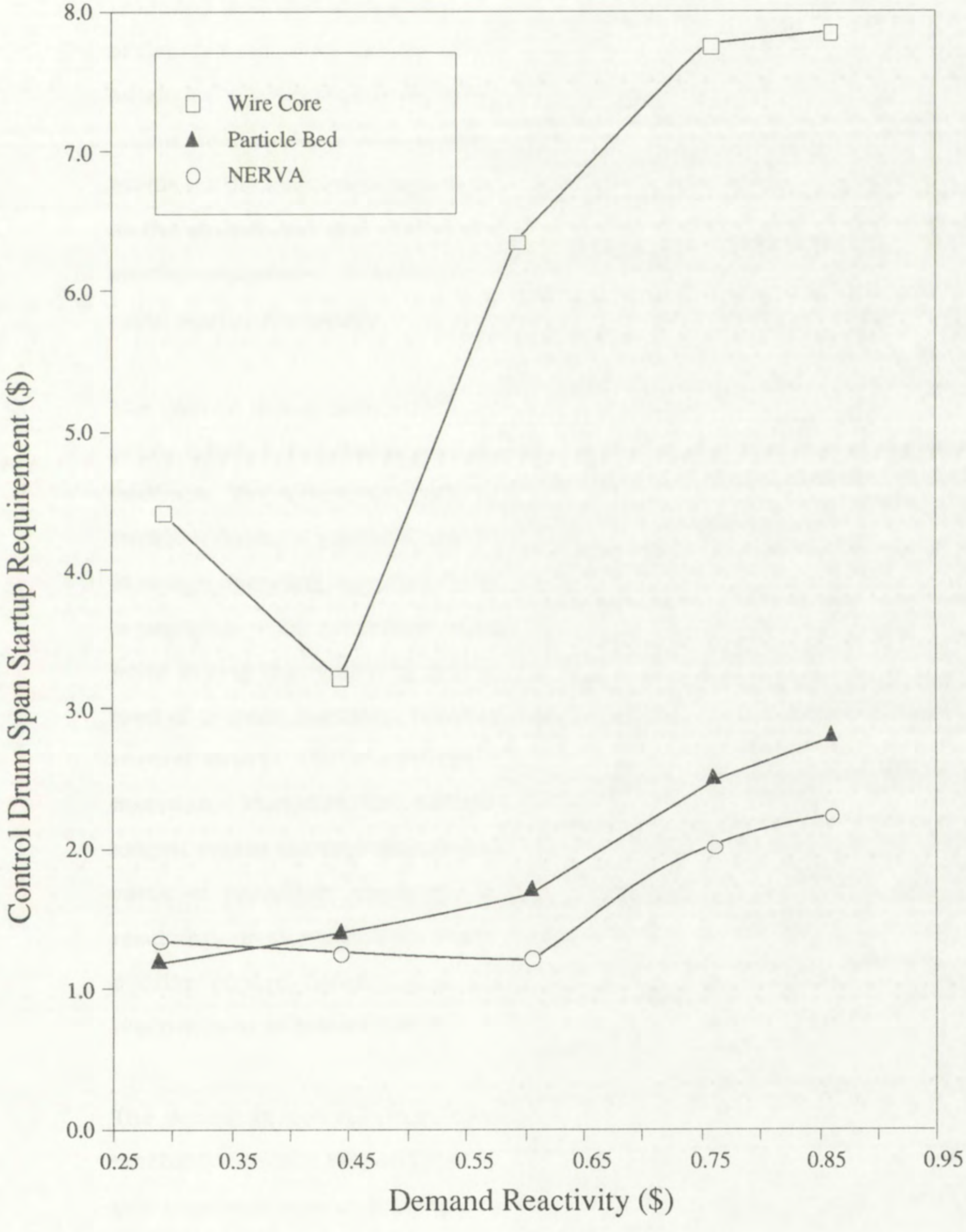

negative propellant reactivity feedback portion of the startup transient. Therefore, the control drums must compensate by reactivity insertion to counteract the negative reactivity feedback of both propellant density reduction and core temperature increase. The magnitude of the control drum reactivity insertion during this portion of the startup transient is a function of demand reactivity (the level of control drum reactivity insertion increases as engine startup time is reduced). Both the particle bed and NERVA small engine models also exhibit a similar control drum span startup requirement profile for the more rapid engine startups. Therefore, for the wire core as well as the particle bed and NERVA small engine reactors, the control drum span startup requirement increases as engine startup time is reduced for the more rapid startup transients.

The control drum span startup requirement for demand reactivities at or below 0.285 β is primarily a function of the level of propellant reactivity feedback. For a demand reactivity of 0.285 β, positive propellant reactivity feedback during a portion of the engine startup will exceed the total feedback at design operating conditions of $4.16. The temperature reactivity feedback is negligible when propellant reactivity feedback is at a maximum. At some point during the remaining portion of the engine startup depending on the level of demand reactivity, negative temperature feedback will occur and the control drums will counteract this temperature increase by reactivity insertion. Therefore, the control drum span startup requirement for the longest engine startup times is equal to the difference between the maximum value of propellant reactivity feedback and the magnitude of demand reactivity. Both the NERVA small engine and particle bed models exhibit a similar control drum span startup requirement profile at demand reactivities at or below 0.285 β.

The minimum control drum span startup requirement for the wire core reactor occurs at a demand reactivity of 0.443 β. The underlying reasons for this minimum control drum span startup requirement are as follows:

a. There is a relative lag time for turbopump response as compared to outlet temperature response. Physically, the core inlet pressure was at only one-third of its design value when the core outlet temperature reached 2700°K. Therefore, the negative temperature reactivity feedback counteracts the eventual buildup of positive propellant reactivity feedback.

b. As compared with the more rapid startup transients, propellant density throughout the entire transient was never less than that at the cold critical operating point. Therefore, propellant reactivity feedback was never negative which would have necessitated a greater control drum span startup requirement.

The NERVA small engine and particle bed models exhibit a similar minimum control drum span startup requirement at demand reactivities of 0.614 and 0.412 β, respectively.

Figure 36 demonstrates that the control drum span startup requirement can vary significantly based on differences in engine startup time, engine design, and reactivity feedback effects. A number of safety and design considerations arise as a consequence of this wide variance. The following is a summary of the major effects on design and safety considerations resultant from the difference in the control drum span startup requirement:

a. In the preceding discussion of engine startup time and reactivity feedback effects, a control system with a reactivity worth in excess of \$12.0 may well be required to provide an adequate safety margin throughout the operational lifetime of the ROTV for the most rapid engine startup transients if propellant feedback worth is approximately \$4.0. Therefore, the number of control drums may well have to be increased from the eighteen proposed for the NERVA small engine design. If control system reliability is to be maintained, the reliability of each control drum and its associated drive system and support hardware must be increased. Also, from a reactor physical construction standpoint, additional control drums may not be possible because of space constraints.

b. If individual control drum worth is increased from that proposed for the NERVA small engine design, then a stuck control drum poses an additional safety burden. As control drum worth is increased, the potential for localized temperatures in excess of design constraints (given a stuck drum) is increased.

c. For a high reactivity worth control system, safety margins are reduced when considering the potential for inadvertent inward rotation of a single control drum or a bank of control drums.

The final area of comparison between the three reactor models to be discussed will be the control drum speed (reactivity insertion and removal rate) requirement. For both the NERVA small engine and particle bed models, a control system reactivity removal rate of \$0.6/sec was sufficient to overcome the effects of positive propellant reactivity feedback even for the most rapid engine startups. For both models, safety margins were increased as engine startup time increased. For the wire core model even with a total propellant feedback worth of only \$1.0, the minimum control system reactivity removal rate where stable startup simulations would occur was \$1.5/sec. As propellant feedback worth increased to \$4.16 for the wire core model, the minimum control system reactivity removal rate where stable startup simulations would occur was \$2.5/sec. As compared to the particle bed and NERVA small engine models, the increased control system reactivity removal rate requirement for the wire core reactor poses the following additional design and safety burdens:

a. If a higher control drum speed is utilized in order to attain increased reactivity removal rates, the potential for reactivity overshoot due to control drum coasting is also increased. Therefore, the potential for unstable power oscillations is greater.

b. As was the case for a high reactivity worth control system, safety margins are reduced when considering the potential for inadvertent inward rotation of a single control drum or a bank of control drums.

6.0 SUMMARY AND CONCLUSIONS

Conventional chemical rockets are a very tightly coupled system compared to nuclear thermal rockets. The energy release from the chemical reaction determines the peak temperature that can be obtained in the combustion chamber. The nature of the chemical reaction also determines the startup and shutdown times for the engine. Also, engine sizing is optimized for one thrust level. In a nuclear thermal rocket engine, the propellant gas can be varied independent of the peak chamber temperature. Startup and shutdown times can be varied over a wide range due to this uncoupling of the energy source from the working fluid. It appears at this time that nuclear rockets can also be throttled over a much wider range than chemical rockets. Therefore, in the early stages of development, a study of the impact of the engine design on control strategies and systems was conducted.

Based on the chemical experience base, one might conclude that very short startup and shutdown times are essential. This may not really be the case, and it appears to be impossible for a prismatic core nuclear thermal rocket like the NERVA design. Nominal startup times for that design were in the tens of seconds range (approximately 80 seconds). It may be possible to speed up the startup sequence used for that engine, but it is not clear how much. The major problem with slow startup sequences is the ineffective use of coolant (hence a mass penalty) during the low power portion of the transient. If the required burn at full thrust is of the order of 10 seconds, then an 80 second startup sequence may well be very inefficient.

In order to define what is required in terms of engine thrusting times, this study focused on the thrust requirements for a Reusable Orbital Transfer Vehicle. The following scenario was considered. A ROTV designed to move nominal payloads from low earth orbit to geosynchronous earth orbit must burn four times to complete a circuit. The third and fourth burns are the shortest ones. Thus inefficiencies in using the propellant on these burns will have the largest mass penalties.

To determine the impact of engine design on control strategies, a range of designs must be considered. To base all of the analysis on a NERVA design may give the wrong answer. NASA had considered no less than 10 designs for solid core nuclear thermal rockets. These designs have many similarities and some significant differences. In order to cover the main differences, three nuclear rocket designs typical of solid core rockets which had been considered by NASA for the Space Exploration Initiative were utilized to compare control strategies. The three designs were the NERVA small engine, wire core, and particle bed reactors.

Models exist in the literature for both the NERVA and particle bed reactors. Therefore, no additional modeling development for these reactor types was performed. A comparable model of the wire core reactor was unavailable. Therefore, prior to assessing the impact of nuclear rocket engine design on control strategies, modeling of the wire core reactor was performed.

Before the startup modeling process commenced a list of key rocket engine parameters for the particle bed reactor was compiled. Some of these parameters were applicable to the wire core and NERVA small engine reactors while others were not. In the case of the wire core reactor, very little information was available in the literature, therefore most of the parametric values were derived from the model which was constructed as part of this dissertation. The NERVA small engine reactor has a substantial amount of description in the literature which was primarily utilized in the comparison.

To compare startup strategies for the three reactor types, development of a computer code which modeled the physical phenomena of a nuclear rocket engine startup was required. The important time-dependent effects that occur in a fission reactor as a result of the physics of fission were modeled by the STRTUP computer code. Also, modeled by the code were the core heat transfer process and a turbopump which provided the required chamber pressure, as well as reactivity feedback effects.

The Smith-Stenning equations were coded into the STRTUP computer model. These equations model the physical phenomena of a nuclear rocket engine startup. In the derivation of the non-dimensional Smith-Stenning equations, time response constants were defined for reactor power, delayed neutron precursor density, core outlet temperature, and core inlet pressure. The neutronics and heat transfer response time constants exhibited the greatest variance between the three reactors. The turbopump response time constant differed by only seven percent between the models while the six delayed neutron precursor response time constants were identical for the three rocket engine models.

Equations which modeled the time dependent change of reactivity feedback due to reactor heatup and propellant density differences were derived directly from the Smith-Stenning equations and were implemented into the STRTUP computer code. Reactivity feedback due to temperature change varies inversely with a given temperature change since the temperature coefficient of reactivity is always negative. The time rate of reactivity change due to propellant density differences is not only dependent upon the current operating point (i.e., propellant density) but also upon the relative time rates of change of core inlet pressure and outlet temperature.

The time optimal control law model implemented in the STRTUP computer code not only accounted for reactivity feedback effects but also determined the reactivity demand by a comparison between measured power level and design power level. To minimize the potential for undesirable power overshoots, the control law commenced demand reactivity removal at a lower relative power level when the previous constant reactivity insertion rate was higher.

When analyzing the startup simulation results for the three reactors it was found that the variance of the neutronics, heat transfer, and turbopump response time constants between the three rocket engine models altered engine response time. When comparing the thermal particle bed reactor and the epithermal NERVA small engine reactor, the power level startup time varied by no more than six percent for any of the startup simulations. As expected, the wire core reactor exhibited the most rapid power level increase of any of the three models. For the five startup simulations, the power level transit time from cold critical conditions to within one percent of design power level for the wire core reactor was from a factor of 3.5 to 2.6 faster.

When comparing the core outlet temperature response time from cold critical to within one percent of design conditions for each of the three reactor models, it was found that the outlet temperature response time was not only a function of the heat transfer response time constant but more importantly a function of the neutronics response time constant. When comparing outlet temperature response time for the wire core and particle bed models, the wire core reactor was at a minimum twice as fast for all five startup simulations. As compared with the particle bed reactor, the NERVA small engine model exhibited an approximately two second temperature response lag time until engine startup time approached 60 seconds.

The turbopump outlet pressure response time comparison from cold critical to within one percent of design conditions for each of the three reactor models will now be summarized. As was the case for the core outlet temperature response time, it was found that the turbopump outlet pressure response time was not only a function of the turbopump response time constant but also the neutronics and heat transfer response time constants. The wire core reactor exhibited the fastest turbopump outlet pressure response time of the three models. The outlet pressure lag time of the NERVA and particle bed models as compared to the wire core reactor increased as engine startup time increased.

The propellant reactivity feedback effects comparison between the three reactor models will now be summarized. The wire core reactor not only had the maximum positive propellant reactivity feedback but also the maximum differential in propellant reactivity feedback when compared with the other two designs. The dominant contribution to the propellant reactivity feedback differential was not only the ultimate value of positive reactivity added by traversing from cold critical to design operating conditions but also the relative speed of reactor outlet temperature response and correspondent turbopump pressure increase lag time.

Each of the three nuclear rocket engine designs exhibited the following similar temperature reactivity feedback effects:

a. In each of the five startup simulations temperature reactivity feedback was always negative
b. The total negative reactivity feedback contribution was similar

c. The temperature reactivity feedback differential was similar

d. In each of the five startup simulations the temperature reactivity feedback profile shapes were nearly identical

e. The maximum temperature reactivity removal rate decreased as engine startup time increased.

The next area of comparison between the three reactor models to be summarized is the control drum span startup requirement. The control drum span startup requirement was not only a function of demand reactivity (i.e., engine startup time) but also a function of reactivity feedback. The magnitude of propellant and temperature reactivity feedback as well as the lag time between the outlet temperature and turbopump response both affected the magnitude of the control drum span startup requirement.

The final area of comparison between the three reactor models to be summarized is the control drum speed (reactivity insertion and removal rate) requirement. For both the NERVA small engine and particle bed models a control system reactivity removal rate of \$0.6/sec was sufficient to overcome the effects of positive propellant reactivity feedback even for the most rapid engine startups. For both models, safety margins were increased as engine startup time increased. For the wire core model even with a total propellant feedback worth of only \$1.0, the minimum control system reactivity removal rate where stable startup simulations would occur was \$1.5/sec. As propellant reactivity feedback worth increased to \$4.16 for the wire core model, the minimum control system reactivity removal rate where stable startup simulations would occur was \$2.5/sec.

From a control standpoint alone, all five startups for each of the rocket engine designs were feasible. However, transient thermal stress limits were not considered for the purpose of this analysis. The NERVA engine response time exhibits an approximately 25 second lag as compared with the particle bed model when considering temperature heatup rate limits. This additional limitation on the NERVA engine startup time further increases the differential in the amount of propellant expended to perform a reusable orbital transfer mission as compared with the two folded flow core designs.

By investigating the impact of nuclear rocket engine design on startup control strategies this research:

a. Developed a wire core reactor rocket engine model to a consistent level of detail with the NERVA small engine and particle bed models
b. Performed a deterministic comparison of key rocket engine parameters for the NERVA small engine, particle bed, and wire core rocket engine designs
c. Quantified rocket engine response time constants for a low thrust (72 kN) engine for each of the three reactors
d. Developed a nuclear rocket engine modeling code which incorporated models for (1) the time dependent effects in a fission reactor which result from the physics of fission, (2) delayed neutrons with six delayed groups, (3) delayed beta and gamma heating, (4) the core heat transfer process, (5) a turbopump, (6) reactivity feedback effects, and (7) a time optimal control law
e. Defined a quantitative basis for the impact of solid core nuclear design on usable control strategies
f. Defined a quantitative basis for the impact of reactivity feedback effects on control and safety margins
g. Determined that even with substantial variance between the neutronics and heat transfer response time constants, one common time optimal startup control strategy could be employed for each of three rocket engine designs.

When comparing the startup simulation results between the three reactor models, it was found that the following parameters varied significantly as a result of differences in engine design and control strategies:

a. Startup response time for power level, reactor outlet temperature, and turbopump outlet pressure
b. Propellant reactivity feedback effects
c. Temperature reactivity feedback effects
d. Control drum span startup requirement
e. Control drum reactivity insertion and removal rate requirement.

However, from a reactor kinetics and engine controllability standpoint there was only a small difference found between the NERVA and particle bed reactors. The wire core exhibited a substantial difference with the other two designs primarily due to variance in the startup response time for power level and propellant reactivity feedback effects.

7.0 RECOMMENDATIONS FOR FUTURE WORK

This research developed a one-dimensional model for a wire core nuclear rocket engine. Also an investigation and comparison of optimal reactor startups for a NERVA small engine, particle bed, and wire core nuclear rocket engine were performed. To broaden the knowledge in this field, the following recommendations are made for future investigators:

a. This research conducted an investigation of the effects of nuclear rocket engine design differences on control strategies for reactor startups. Three reactor designs were chosen to represent the potential spectrum of designs which were considered by NASA for the Space Exploration Initiative. To expand the knowledge in this area of research it is recommended that additional reactor designs are investigated utilizing the methods and techniques developed in this work.

b. When a ROTV mission is considered, four separate burns are required to perform a Hohmann transfer ellipse which ferries payloads from low earth orbit to geosynchronous orbit. This mission necessitates that the rocket engine undergoes four reactor startups, at power burns, and reactor shutdowns. This research was limited to an investigation of reactor startups. Therefore, to fully understand the effects of the differences of rocket engine design on control strategies for a ROTV, it is recommended that the at power burn and reactor shutdown phases of rocket engine operation also be investigated.

c. Two potential thrust level engines could be developed for a ROTV. This dissertation chose to investigate a lower thrust engine like the NERVA small engine. However, a higher thrust engine which would be developed for a manned Mars mission could be tested through utilization as a ROTV. Therefore, it is recommended that the effect of throttled higher thrust engines on usable control strategies be investigated.

d. When rapid engine startup transients (10 seconds or less) are considered, a control system reactivity insertion rate of greater than \$1.0/sec may well be required to provide for adequate control margin. For any reactor model being considered for use as a ROTV, a detailed investigation of the effect of increasing the control system reactivity insertion rate on safety margins and reactor design is recommended.

8.0 REFERENCES

1. Grey, J., Nuclear rocket, Nucleonics 16, pp. 62-63, 1958.

2. Levoy, M., and Newgard, J., Rocket-reactor design, Nucleonics 10, pp. 66-68, 1958.

3. Newgard, J., and Levoy, M., Consideration in the design of a nuclear rocket, Nuclear Science Engineering 7, No. 4, p. 377, 1960.

4. Sutton, G., Rocket propulsion elements - an introduction to the engineering of rockets, Sixth edition, Wiley-Interscience, 1992.

5. Koenig, D., Experience gained from the space nuclear rocket program (Rover), LA-10062-H, May, 1986.

6. Spence, R., and Durham, F., The Los Alamos nuclear-rocket program, Astronaut, Aeron 3, pp. 42-46, 1965.

7. Bussard, R., and DeLauer, R., Fundamentals of nuclear flights, Chapter 1, McGraw-Hill, New York, NY, 1965.

8. McDaniel P., Do reusable orbital transfer vehicles make sense, Phillips Laboratory, Albuquerque, NM.

9. Searle, R., and Marcy, R., An approach to startup control of a nuclear rocket engine, TID-7653, pp. 546-557, 1952.

10. NERVA engineering and design concepts, reactor design configuration, Volume 1, Westinghouse Electric Co., Pittsburg, PA, June, 1968.

11. Trade study for NERVA support plate and plena design concepts, Westinghouse Electric Co., Pittsburg, PA, December, 1969.

12. Trade study for NERVA fuel element design concepts, Westinghouse Electric Co., Pittsburg, PA, December, 1969.

13. Trade study for NERVA core periphery design concepts, Westinghouse Electric Co., Pittsburg, PA, February, 1970.

14. TRW space log, TRW Space and Technology Group, Redondo Beach, CA, 1988.

15. Powell, J., and Botts, T., Particle bed reactors for space power and propulsion, Brookhaven National Lab, Upton, NY, 1984.

16. Feddersen, R., and Coiner, J., Conceptual design of a category III multimegawatt space nuclear power system, 24th Intersociety Energy Conversion Engineering Conference, Washington, DC, August, 1989.

17. Horn, F., et al., The use of nuclear energy for bimodal applications in space, 21st Intersociety Energy Conversion Engineering Conference, San Diego, CA, August, 1986.

18. Malloy, J., and Potekhen, D., A conceptual study of the use of a particle bed reactor nuclear propulsion module for the orbital maneuvering vehicle, 24th Intersociety Energy Conversion Engineering Conference, Washington, DC, August, 1989.

19. Powell, J., et al., Nuclear propulsion systems for orbit transfer based on the particle bed reactor, 4th Symposium on Space Nuclear Power Systems, Albuquerque, NM, January, 1987.

20. Horn, F., et al., Particle bed reactor propulsion vehicle performance and characteristics as an orbital transfer rocket, 3rd Symposium on Space Nuclear Power Systems, Albuquerque, NM, January, 1986.

21. Ludewig, H., et al., Small propulsion reactor design based on particle bed reactor concept, 6th Symposium on Space Nuclear Power Systems, Albuquerque, NM, January, 1989.

22. Walton, L., and Ma, P., Particle-frit interactions in PBR fuel elements, 7th Symposium on Space Nuclear Power Systems, Albuquerque, NM, January, 1990.

23. Charmchi, M., et al., Thermo-hydraulic characteristics of gas-cooled particle bed reactors, 4th International Topical Meeting on Nuclear Reactor Thermal-Hydraulics, Karlsruhe, Germany, October, 1989.

24. Araj, K., and Nourbakhsh, H., Thermal-hydraulic modeling of porous bed reactors, 1987 Winter Meeting of the American Nuclear Society, Los Angeles, CA, November, 1987.

25. Casey, W., Thermal-hydraulic transient analysis of a packed particle-bed reactor fuel element, Master's thesis, M.I.T., Cambridge, MA, June, 1990.

26. Horn, F., et al., Transient thermal hydraulic measurements on the particle bed reactor fuel element, 7th Symposium on space nuclear power systems, Albuquerque, NM, January, 1990.

27. Benenati, R., et al., Thermal-hydraulic considerations for particle bed reactors, 4th Symposium on Space Nuclear Power Systems, Albuquerque, NM, January, 1987.

28. Horn, F., and Powell, J., High temperature zirconium carbide coatings for use in particle bed reactors, 15th International Conference on Metallurgical Coatings, San Diego, CA, April, 1988.

29. Marshall, A., A review of gas-cooled reactor concepts for SDI applications, SAND87-0558, Sandia National Laboratories, Albuquerque, NM, August, 1989.

30. Mohler, R., and Perry, J., Nuclear rocket engine control, Nucleonics 19, pp. 80-84, 1961.

31. Mohler, R., Optimal control of nuclear reactor systems, Trans. Am. Nucl. Sci. 7, pp. 58-59, 1964.

32. Mohler, R., Stability and control of nuclear rocket propulsion, IRE Transactions Automatic Control AC-7, pp. 86-96, 1963.

33. Mohler, R., Optimal control of nuclear reactor processes, Los Alamos Scientific Laboratory Report, LA-3257-MS, Los Alamos Scientific Laboratory, Los Alamos, NM, 1965.

34. Mohler, R., Optimal nuclear rocket engine control, "Neutron Dynamics and Control," AEC Symposium Ser. 7, pp. 137-163, 1966.

35. Janson, W., and Buckner, J., Starting and control characteristics of nuclear rocket engines, AIAA-J. 1, No. 3, p. 563, 1963.

36. Mohler, R., Optimal control of nuclear reactors, Academic Press, New York, NY, 1970.

37. Shen, C., and Haag, F., Optimum nuclear rocket start-up to develop full power at exact time with consideration of noise, Proceedings International Instrumentation Measurement Conference 6th, (Special Sect. on Autom. Control), Stockholm, Sweden, September, 1964.

38. Smith, H., and Stenning, A., Open loop stability and response of nuclear rocket engines, Nuclear Science and Engineering, 11, 1961.

39. Smith, H., Closed-loop dynamics of nuclear rocket engines with topping turbine drive, Nuclear Science and Engineering, 18, 1964.

40. Stenning, A., Rapid approximate method for analyzing nuclear rocket performance, ARS Journal, pp. 169-172, February, 1960.

41. Smith, H., Closed loop dynamics of nuclear rocket engines, Nuclear Science and Engineering, 14, 1962.

42. Huzel, D., and Huang, G., Design of liquid propellant rocket engines, NASA SP-125, 1967.

43. Touloukian, Y., and Ho, C., Thermophysical properties of matter, the TPRC data series (13 volumes), Plenum Press, New York, 1970-1977.

44. Dulong, P., and Petit, A., Ann. Chim., Vol. 10, pp. 395-413, 1819.

45. Einstein, A., The Plank's theory of radiation and the theory of specific heat, Ann. Physik, Vol. 22, pp. 180-190, 1907.

46. Debye, P., The theory of specific heat, Ann. Physick, Vol. 39, pp. 789-839, 1912.

47. Powell, J., et al., Summary of particle bed reactor designs for the space nuclear thermal propulsion program, Brookhaven National Laboratory, Upton, NY, September 1993.

48. LaMarsh, J., Introduction to nuclear engineering, Second edition, Addison-Wesley, 1983.

49. Kreyszig, E., Advanced engineering mathematics, Fifth edition, Wiley, 1983.

50. Reactor controls concept trade study. Trade study No. 701, Westinghouse Electric Co., Pittsburg, PA, September, 1970.

51. Severson, W., Reactor controls concepts, Trade Study No. 713, Westinghouse Electric Co., Pittsburg, PA, September, 1970.

52. Hill, P., and Peterson, C., Mechanics and thermodynamics of propulsion, Addison-Wesley, 1965.

53. Dixon, S., Fluid mechanics, thermodynamics of turbomachinery, University of Liverpool, 1979.

54. Hanson, G., et al., Beryllium-reflected, graphite-moderated critical assemblies, AEC Report, LA-2141, 1957.

55. Schreiber, R., Los Alamos' Project Rover, Nucleonics, Volume 16, No. 7, pp. 70-72, July, 1958.

56. Wiberg, D., and Wayski, J., Stability of nuclear rocket engine dynamics, Nuclear Applications, Vol. 5, July, 1968.

57. Shen, C., and Liu, T., The control of absorption cross-section for a nuclear rocket, "Neutron Dynamics and Control," AEC Symposium Serial No. 7, p. 182, 1966.

58. Ma, C., Application of ion exchange for control of nuclear rocket reactors, Nuclear Science and Engineering, 11, pp. 19-25, 1961.

59. Crews, R., and Hohmann, G., Nuclear subsystem controls for the NERVA experimental engine, Nuclear Applications, Vol. 3, November, 1967.

60. Hohmann, G., and Walsh, J., Limiters in NERVA reactor control, Nuclear Applications, Vol. 3, November, 1967.

61. Smith, H., Divergence of the mean power level during an oscillation experiment, Nuclear Science and Engineering, 22, 1965.

62. Lindsey, R., Upcoming tests may determine nuclear rocket reactor design, Missiles/Rockets 10, p. 38, 1963.

63. Felix, B. and Bohl, R., Dynamics analysis of a nuclear rocket engine system, ARS J. 19, pp. 853-862, 1959.

64. Mills, R., Thermal and reactor analysis of nuclear rocket transients, North Carolina State University, 1973.

65. Walton, L., and Malloy, J., Nuclear propulsion tradeoffs for manned Mars missions, 8th Symposium on Space Nuclear Power Systems, Albuquerque, NM, January, 1991.

66. Brandes, D., High-temperature nuclear closed Brayton cycle power conversion system for the Space Exploration Initiative, 8th Symposium on Space Nuclear Power Systems, Albuquerque, NM, January, 1991.

67. Dobranich, D., and El-Genk, M., Heat transfer and thermal stress analyses of a multilayered fuel particle, 7th Symposium on Space Nuclear Power Systems, Albuquerque, NM, January, 1990.

68. Guerin, Y., and Mottet, P., Material studies for the ERATO space reactor project, 7th Symposium on Space Nuclear Power Systems, Albuquerque, NM, January, 1990.

69. Vrillon, B., et al., Space nuclear power studies in France - a new concept of particle bed reactor, 23rd Intersociety Energy Conversion Engineering Conference, Denver, CO, August, 1988.

70. Powell, J., et al., High flux research reactors based on particulate fuel, Advanced Steady-State Neutron Facility Conference, Gaithersburg, MD, December, 1985.

71. Lazareth, O., et al., Ultra high temperature particle bed reactor design, Vision-21 Space Travel Conference, Cleveland, OH, April, 1990.

72. Horn, F., et al., Compact nuclear power systems based on particle bed reactors, 4th International Conference on Emerging Nuclear Energy Systems, Madrid, Spain, January, 1986.

73. Slovik, G., et al., Particle bed reactor scaling relationships, 4th Symposium on Space Nuclear Power Systems, Albuquerque, NM, January 1987.

74. Horn, F., et al., Tests of candidate materials for particle bed reactors, 4th Symposium on Space Nuclear Power Systems, Albuquerque, NM, January, 1987.

75. Lazareth, O., et al., Analysis of the start-up and control of a particle bed reactor, 4th Symposium on Space Nuclear Power Systems, Albuquerque, NM, January, 1987.

76. Powell, J., et al., SNUG: A compact particle bed reactor for the 400 to 600 KWt power range, Symposium on Space Nuclear Power Systems, Albuquerque, NM, January, 1984.

77. Asker, J., Particle bed reactor central to SDI nuclear rocket project, Aviation Week and Space Technology, Vol. 134, April, 1991.

78. Coiner, J., and Short, B., Small particle bed reactors: Sensitivity to Brayton cycle parameters, 5th Symposium on Space Nuclear Power Systems, Albuquerque, NM, January, 1988.

79. El-Genk, M., et al., Pellet bed reactor for nuclear thermal propelled vehicles, 8th Symposium on Space Nuclear Power Systems, Albuquerque, NM, January, 1991.

80. El-Genk, M., et al., System design optimization for multimegawatt space nuclear power applications, Journal of Propulsion and Power, March, 1990.

81. Buden, D., et al., Pellet bed reactor for multi-modal space power, 3rd Symposium on Space Nuclear Power Systems, Albuquerque, NM, January, 1986.

82. El-Genk, M., Pellet bed reactor design for space power, 22nd Intersociety Energy Conversion Engineering Conference, Philadelphia, PA, August, 1987.

83. Preliminary definition of the structure/configuration of nuclear upper stage for Europa 3 launch vehicle, Bremen, Germany, June, 1972.

84. Walsh, J., Nerva reactor control system design criteria, Westinghouse Electric Co., Pittsburg, PA, August, 1966.

85. Spezialetti, I., Failure mode analysis summary. Nerva control drum actuator proposed by Bendix, Westinghouse Electric Co., Pittsburg, PA, January, 1963.

86. Spezialetti, I., Failure mode analysis summary. Nerva control drum actuator proposed by General Electric (Model Ag-14), Westinghouse Electric Co., Pittsburg, PA, January, 1963.

87. Zorn, J., Radiation test of a Nerva reactor control vane segment (WANL Test 15/W002), Westinghouse Electric Co., Pittsburgh, PA, November, 1964.

88. Roesmer, J., Neutron transmission measurements on Nerva reactor control vanes, Westinghouse Electric Co., Pittsburg, PA, September, 1969.

89. Mayer, J., et al., Nerva control drum actuator irradiation test program, NASA, Cleveland, OH, July, 1969.

90. Charmatz, A., Rover reactor control element worth calculations, Proceedings of nuclear propulsion conference, Los Alamos Scientific Laboratory, Los Alamos, NM, 1967.

91. Stiles, C., Interaction of liquid hydrogen with the Kiwi-B reactor, Los Alamos Scientific Laboratory, Los Alamos, NM, January, 1962.

92. Brown, E., et al., Accident and transient characteristics of Kiwi-B reactors, Los Alamos Scientific Laboratory, Los Alamos, NM, April, 1961.

93. Remshaw, R., and Weaver, L., State variable feedback design of a control system for a coupled-core reactor, Arizona University, Tucson, AZ, June, 1968.

94. Kennison, R., Development of the Rover computer program for flow-induced, self-excited vibration of a blade in a flow channel, Knolls Atomic Power Laboratory, Schenectady, NY, 1968.

95. Strait, B., and Lang, R., An integrated circuit control system for the Pewee reactor, Los Alamos Scientific Laboratory, Los Alamos, NM.

96. Kendrick, L., On-line digital computer control of the Nerva nuclear rocket engine, Thesis, 1972.

97. Stefanko, J., and Mowrey, A., One-dimensional calculations of Nerva reactor control spans, 13th American Nuclear Society Meeting, San Diego, CA, June, 1967.

98. Hohmann, G., et al., Limiters in Nerva Reactor Control, Westinghouse Astronuclear Lab, Pittsburg, PA, November, 1967.

99. Dynamic analysis and analog computer simulation of the Nerva engine, Aerojet-General Co., Azusa, CA, May, 1962.

100. Elminger, R., NRX-A1 and A2 control system, Final Report: Cy 63, Battelle Pacific Northwest Laboratories, Richland, WA, September, 1963.

101. Hafer, J., et al., Nerva engine reactor control system: preliminary synthesis and analysis, Westinghouse Electric Co., Pittsburg, PA, February, 1963.

102. Steiner, G., Preliminary study of the effects of the velocity limits of control drum actuators upon reactor control system stability in the power range, Westinghouse Electric Co., Pittsburg, PA, May, 1963.

103. Controls analysis presentation to Snpo-C, Aerojet-General Co., Azusa, CA, March, 1964.

104. Control components research and development, Aerojet-General Co., Sacramento, CA, June, 1962.

105. Morris, W., Estimated power requirements of the reactor control system, Westinghouse Electric Co., Pittsburg, PA, October, 1962.

106. Reactor control components, Phase I. Nerva nuclear subsystem, Westinghouse Electric Co., Pittsburg, PA, March, 1962.

107. Location of Nerva instrumentation and control components, Aerojet- General Co.

108. Walsh, J., Proposed drum actuator and control system for the NRX-A7 reactor, Westinghouse Electric Co., Pittsburg, PA, July, 1965.

109. Salaja, J., Cooldown controls functional design, Aerojet Nuclear Systems Co., Sacramento, CA, January, 1972.

110. Dowling, E., Engineering operations report: Nerva digital controller/actuator driver interface study, Aerojet Nuclear Systems Co., Sacramento, CA, April, 1972.

111. Kirschbaum, H., Actuation system for ganged drums, Westinghouse Electric Co., Pittsburg, PA, April, 1967.

112. Gilmour, G., Preliminary Wanl evaluation of the nuclear instrumentation for the NRX-A control system, Westinghouse Electric Co., Pittsburg, PA, 1963.

113. Addendum program plan for the development of the instrumentation and control (I and C) system for the Nerva engine, Aerojet Nuclear Systems Co., Sacramento, CA, April, 1970.

114. Design study of engine controls and reactor instrumentation for a nuclear flight test engine. Final report, Bendix Co., Southfield, MI, April, 1961.

115. Schaffer, D., Design study of engine controls and reactor instrumentation for a nuclear flight test engine, Final Data Report, Bendix Co., Southfield, MI, February, 1961.

116. Sheridan, E., Alternate methods of engine control, Aerojet-General C., Sacramento, CA, March, 1964.

117. Control drum actuator. Trade Study No. 754, Westinghouse Electric Co., Pittsburg, PA, January, 1970.

118. Instrumentation and controls requirements, Aerojet-General Co., Sacramento, CA, August, 1969.

119. Program plan for development of the instrumentation and control (I and C) system for the Nerva engine, Volume II. Appendices. Aerojet-General Co., January, 1970.

120. Kaluja, J., I and C analysis report on engine controllability (Njd- 0026), Aerojet Nuclear Systems Co., Sacramento, CA, December, 1970.

121. Instrumentation-and-control subsystem, Aerojet-General Co., Sacramento, CA, December, 1969.

122. NSCS acceptance test procedure for Nerva engine. Ets-1 engine control system, Issue 5, Aerojet-General Co., Sacramento, CA, March, 1967.

123. Performance/design and qualification requirements for instrumentation and control subsystem, Aerojet-General Co., Sacramento, CA, December, 1969.

124. Performance/design and qualification requirements for electronic, power, instrumentation, and control, Aerojet-General Co., Sacramento, CA, December, 1969.

125. Handbook of operating and maintenance instructions for XE-1 engine control system, Volume I. Aerojet-General Co., Sacramento, CA, August, 1968.

126. Presentation material from joint AGC-Wanl symposium on Nerva instrumentation and control, Aerojet-General Co., Sacramento, CA, December, 1969.

127. Porcelli, G., Summary report of work to date on the Nerva digital control system design, Aerojet-General Co., Sacramento, CA, September, 1970.

128. Control drum actuator design concepts, Westinghouse Electric Co., Pittsburg, PA, April, 1970.

129. Bervard, D., et al., Optimization of peripheral reactivity control in the Nerva reactor, Westinghouse Astronuclear Lab, Pittsburg, PA, 1969.

130. Schenz, R., Modal feedback control design, Aerojet Nuclear Systems Co., Sacramento, CA, August, 1970.

131. Reid, R., Ricatta feedback design technique, Aerojet Nuclear Systems Co., Sacramento, CA, August, 1970.

132. Reid, R., The application of the solution to the state regulator problem to the fourth order Smith-Stenning model, Aerojet Nuclear Systems Co., Sacramento, California, September, 1970.

133. Parziale, E., et al., Discussion of Nerva control design techniques, Aerojet Nuclear Systems Co., Sacramento, CA, August, 1970.

134. Parziale, E., and Porcelli, G., On the analysis and design of the Nerva engine control system, Aerojet Nuclear Systems Co., Sacramento, CA, August, 1970.

135. Parziale, E., A computer program for calculating the state transition matrix and the G matrix, Aerojet Nuclear Systems Co., Sacramento, CA, August, 1970.

136. Honka, E., and Josephson, J., Analysis and simulation feasibility study for NRX-A-on-off controller, Westinghouse Astronuclear Lab, Pittsburg, PA, May, 1965.

137. Finger, H., The Rover program, Nuclear Propulsion Conference, Monterey, CA, August, 1962.

138. Charmatz, A., Rover reactor control element worth calculations, Nuclear Propulsion Conference, Monterey, CA, August, 1962.

139. Balcomb, J., Startup studies of nuclear rocket reactor, Part 3, startup philosophy, Nuclear Propulsion Conference, Monterey, CA, August, 1962.

140. Blake, P., et al., Control systems for a liquid-hydrogen-cooled KIWI- B reactor, Nuclear Propulsion Conference, August, 1962.

141. Brown, E., et al., KIWI-B-1A power and temperature control systems, Nuclear Propulsion Conference, Monterey, CA, August, 1962.

142. Dix, G., Nuclear rockets - safety problems and safety programs, Nuclear Propulsion Conference, Monterey, CA, August, 1962.

143. Watts, G., et al., Startup studies of a nuclear rocket reactor- cryogenic cooldown experiments, Nuclear Propulsion Conference, Monterey, CA, August, 1962.

144. Parziale, E., Results of the Melsa design technique applied to the nonlinear Smith-Stenning nuclear engine model, Aerojet Nuclear Systems Co., Sacramento, CA, August, 1970.

145. Preliminary control and analysis of the dynamics of malfunctions of the AJ30-5 NERVA engine, Aeorjet-General Co., Sacramento, CA, October, 1963.

146. Angelo, J., and Buden, D., Space nuclear power, 1985.

APPENDIX A

NUCLEAR ROCKET STARTUP MODELING EQUATIONS, CONTROL TECHNIQUES, AND SAFETY IMPLICATIONS

In this appendix, a derivation of the Smith-Stenning equations (Refs. A1, A2, A3, A4) as they apply to nuclear rocket control is given in Section A.1. These equations were coded into the STRTUP computer program which is described in Chapter 4.

NERVA controller design was an ongoing and evolving process from the late 1950s until the program was terminated in the early 1970s. Section A.2 gives a description of the control design that was in place just prior to program termination. In Section A.3, a description of current control methodology for accomplishing a time optimal startup is given. Finally, Section A.4 describes safety issues pertaining to a time optimal startup.

A.1 Smith-Stenning Equations

The open loop dynamic performance of a nuclear rocket engine with either a bleed turbine or topping turbine drive can be accurately described by a system of ordinary, nonlinear differential equations (Refs. A1, A2, A3, A4). A linear approximation to these yields a stability criterion that is a function of (a) the rate of change of reactivity with temperature at constant propellant density, (b) the rate of change of reactivity with propellant density at constant core temperature, and (c) the relation between states of zero time rate of change of core inlet pressure.

A lumped parameter model was proposed. The standard lumped parameter neutron kinetic and precursor equations are as follows:

$$\frac{dP}{dt} = \frac{\rho - \beta}{\ell} P + \lambda z \tag{A.1}$$

$$\frac{dz}{dt} = \frac{\beta}{\ell} P - \lambda z \tag{A.2}$$

where,

P = reactor power

z = neutron precursor density

ρ = reactivity

β = effective delayed neutron fraction

ℓ = neutron generation time

λ = precursor decay constant.

The derivation of the non-dimensional time rate of change equations for reactor power and delayed neutron precursor density will be presented after discussion of core heat transfer and turbopump modeling. First, a description of the derivation of the non-dimensional time rate of change equation for reactor outlet temperature will be presented.

The core heat transfer process can be modeled by (Ref. A2):

$$M_c C_{p_c} \frac{T_c}{T_2} \frac{dT_2}{dt} = P - \dot{m} C_p (T_2 - T_1) \tag{A.3}$$

where,

M_c = fuel mass

C_{p_c} = fuel specific heat

T_c = mean core temperature

T_2 = propellant outlet temperature

$\dot{m}$ = propellant mass flow rate

C_p = propellant specific heat capacity

T_1 = propellant inlet temperature

and all other terms have been previously defined.

A key assumption in this derivation of the non-dimensional time rate of change equation for core outlet temperature is that choked flow conditions are present at the rocket nozzle throat. Choked flow is defined as a unique velocity at the nozzle throat because it is not possible to increase the throat velocity or flow rate by lowering the exit pressure or evacuating the exhaust section. All three nuclear rockets modeled in this dissertation will have choked flow due to their relatively high chamber pressure.

With choked flow conditions present at the nozzle throat Equations (A.4) and (A.5) can be derived:

$$\dot{m} \; \alpha \; \frac{P_2}{\sqrt{T_2}} \tag{A.4}$$

and,

$$\frac{P_2}{P_1} = \text{constant} \tag{A.5}$$

where,

P_2 = core outlet pressure
P_1 = core inlet pressure
and all other terms have been previously defined.

With $T_2 >> T_1$, as will be the case for all three reactor types, Equation (A.3) simplifies to:

$$M_c C_{p_c} \frac{T_c}{T_2} \frac{dT_2}{dt} = P - \dot{m} C_p T_2 \quad . \tag{A.6}$$

To solve for the time rate of change of core outlet temperature with respect to the design outlet temperature, Equation (A.6) must be converted into a non-dimensional form. Therefore, the following non-dimensional parameters are defined as:

$$T_2' = \frac{T_2}{T_{2d}} \tag{A.7}$$

$$P' = \frac{P}{P_d} \tag{A.8}$$

$$\dot{m}' = \frac{\dot{m}}{\dot{m}_d} \tag{A.9}$$

where,

T_2' = ratio of actual outlet temperature to design outlet temperature
T_{2d} = design outlet temperature
P' = ratio of actual power level to design power level
P_d = design power level
$\dot{m}'$ = ratio of actual propellant mass flow rate to design mass flow rate
$\dot{m}_d$ = design propellant mass flow rate
and all other terms have been previously defined.

To further simplify Equation (A.6), a temperature response time constant is defined as follows:

$$\tau_c = \frac{M_c C_{p_c} T_c}{\dot{m}_d C_p T_2} \tag{A.10}$$

where,

T_c/T_2 = constant.

By dividing each term in Equation (A.6) by its design value, a non-dimensional equation is derived which expresses the time rate of change of outlet temperature with respect to its design point. This relationship is as follows:

$$\frac{M_c C p_c T_c}{\dot{m}_d C_p T_2} \frac{d}{dt}\left(\frac{T_2}{T_{2d}}\right) = \frac{P}{P_d} - \frac{\dot{m} C_p T_2}{\dot{m}_d C_p T_{2_d}} \tag{A.11}$$

By substitution of the defined parameters from Equations (A.7) through (A.10) into Equation (A.11), the time rate of change of core outlet temperature with respect to its design point can be expressed as:

$$\tau_c \frac{dT_2'}{dt} = P' - \dot{m}' T_2' \quad . \tag{A.12}$$

Once again when considering choked flow conditions are present at the nozzle throat, a constant ratio exists between propellant mass flow rate and outlet temperature and pressure, and this ratio is independent of the operating state between initial startup conditions and full power. Equation (A.13) expresses this relationship:

$$\frac{\dot{m}\sqrt{T_2}}{P_2} = \frac{\dot{m}_d\sqrt{T_{2_d}}}{P_{2_d}} \quad . \tag{A.13}$$

Equations (A.14) through (A.17) can be directly derived from Equation (A.13). As is shown, the ratio between the actual core inlet and outlet pressures and their respective design values is equal and independent of the actual operating point. Equations (A.14) through (A.17) are now given:

$$\frac{\dot{m}'\sqrt{T_2'}}{P_2'} = 1.0 \tag{A.14}$$

$$\dot{m}' = \frac{P_2'}{\sqrt{T_2'}} \tag{A.15}$$

$$\frac{P_2}{P_1} = \frac{P_{2_d}}{P_{1_d}} \tag{A.16}$$

$$P_2' = P_1' \quad . \tag{A.17}$$

Therefore, Equation (A.12) can be modified by expressing non-dimensional propellant flow in terms of non-dimensional inlet pressure and outlet temperature:

$$\tau_c \frac{dT_2'}{dt} = P' - \frac{P_1'}{\sqrt{T_2'}} T_2' \quad . \tag{A.18}$$

The time rate of change of the ratio between actual core outlet temperature and its design value can, therefore, be characterized by:

$$\tau_c \frac{dT_2'}{dt} = P' - P_1' \sqrt{T_2'} \quad . \tag{A.19}$$

A brief derivation for the relationship between total reactivity of the reactor and the ratio of outlet temperature and inlet pressure to their respective design values will now be given. As was the case for the derivation of the time rate of change of core outlet temperature, a non-dimensional equation is derived.

The reactivity equation for the nuclear rocket reactor system is as follows:

$$\rho = \rho_o + \alpha_F \sqrt{T_2'} + \alpha_c \rho_c \tag{A.20}$$

where,

ρ = total reactivity
ρ_o = control device reactivity
α_F = negative fuel temperature coefficient
ρ_c = coolant density
α_c = positive propellant density coefficient
and all other terms have been previously defined.

With substitution from Equations (A.7) and (A.8):

$$\rho = \rho_o + \alpha_F \sqrt{T_2'} + \alpha_c \frac{P_1'}{T_2'} \quad . \qquad (A.21)$$

The relationship between total reactivity and the ratio between outlet temperature and inlet pressure and their respective design values can, therefore, be expressed as follows:

$$\rho = \rho_o + \alpha_F \sqrt{T_2'} + \alpha_H \frac{P_1'}{T_2'} \quad . \qquad (A.22)$$

The derivation for the time rate of change of the ratio between actual core inlet pressure and its design value will now be given. For all three reactor types, a turbopump is modeled. A turbopump was the design choice in preference to a high pressure propellant tank. This design choice minimized the overall vehicle structural weight, and therefore allowed for more payload for the ROTV for same total vehicle weight.

The turbopump is assumed to operate on a flat portion of its characteristic operational curve so that:

$$P_1 - P_p = k_p \, w^2 \qquad (A.23)$$

where,

P_p = pump inlet pressure
k_p = known constant
w = shaft speed in radians/sec
and all other terms have been previously defined.

To derive the time rate of change of reactor inlet pressure, pump and turbine power relationships must first be defined.

The pump power requirement is as follows:

$$P_{pump} = \dot{m}\left(P_1 - P_p\right)/\eta_p \rho_{HL} \qquad (A.24)$$

where,

P_{pump} = pump power
η_p = pump efficiency
ρ_{HL} = propellant density in the pump
and all other terms have been previously defined.

The turbine power requirement is:

$$P_{Turb} = \eta_T C_p T_2 \dot{m}_T \left\{ 1 - \left(\frac{1}{PR}\right)^{\frac{\gamma-1}{\gamma}} \right\} \qquad (A.25)$$

where,

η_t = turbine efficiency
$\dot{m}_T$ = turbine mass flow rate
T_2 = turbine inlet stagnation temperature
PR = turbine pressure ratio
γ = ratio of specific heats
and all other terms have been previously defined.

The change in turbopump shaft speed can be equated to the difference between turbine and pump power. Equation (A.26) expresses this relationship:

$$\frac{d}{dt}\left[Iw^2\right] = \eta_T C_p T_2 \dot{m}_T \left\{ 1 - \left(\frac{1}{PR}\right)^{\frac{\gamma-1}{\gamma}} \right\} - \dot{m}\left(P_1 - P_p\right)/\eta_p \rho_{HL} \qquad (A.26)$$

where,

I = rotational moment of inertia
and all other terms have been previously defined.

Since $P_1 >> P_p$ for all three reactor types, the shaft speed is proportional to the square root of inlet pressure:

$$w^2 = \frac{P_1 - P_p}{k_p} \cong \frac{P_1}{k_p} \quad . \tag{A.27}$$

To derive a non-dimensional form of Equation (A.26), a similar technique as was employed in the temperature derivation is utilized. First, Equation (A.27) is substituted into Equation (A.26). Next, all terms in Equation (A.26) are divided by their design values and the variable of turbine power at the design point (ϕ_p) is defined. These steps yield the following relationship:

$$\frac{I}{2\phi_p}\frac{P_{1d}}{k_p}\frac{d}{dt}\left(\frac{P_1}{P_{1d}}\right) = \frac{T_2}{T_{2d}}\frac{\dot{m}_T}{\dot{m}_{Td}} - \frac{\dot{m}}{\dot{m}_d}\frac{P_1}{P_{1d}} \tag{A.28}$$

where,

$$\phi_p = \eta_T C_p T_{2d} \dot{m}_{Td}\left\{1 - \left(\frac{1}{PR}\right)^{\frac{\gamma-1}{\gamma}}\right\} = \dot{m}_d \frac{P_{1d}}{\eta_p \ \rho_{HL}} \tag{A.29}$$

and,

$\dot{m}_{Td}$ = turbine design mass flow rate
and all other terms have been previously defined.

To simplify Equation (A.28), an inlet pressure response time constant is defined as follows:

$$\tau_p = \frac{I \, P_{1_d}}{2 \, \phi_p \, k_p} \qquad \text{(A.30)}$$

and substituting into Equation (A.28) yields,

$$\tau_p \frac{dP_1'}{dt} = T_2' \dot{m}_T' - \dot{m}' \; P_1' \quad . \qquad \text{(A.31)}$$

As is the case for the main thrust chamber which exhausts propellant into a convergent-divergent De Laval type nozzle to maximize the conversion of thermal energy into specific impulse, the inlet to a turbopump turbine also typically employs a De Laval nozzle. The increased flow velocity of the hydrogen monopropellant allows the turbine to extract more work from the increased kinetic energy of the gas. As another consequence of the turbine inlet nozzle arrangement, choked flow conditions exist at the inlet nozzle throat. Equations (A.32) and (A.33) express this relationship:

$$\dot{m}' = \frac{P_2'}{\sqrt{T_2'}} = \frac{P_1'}{\sqrt{T_2'}} \qquad \text{(A.32)}$$

and,

$$\dot{m}_T' = \frac{P_3'}{\sqrt{T_3'}} = \frac{P_2'}{\sqrt{T_2'}} = \frac{P_1'}{\sqrt{T_2'}} \quad . \qquad \text{(A.33)}$$

It can be seen from Equations (A.32) and (A.33) that the ratio between the actual mass flow rate through both the turbine and pump and their respective design values is equal and independent of the actual operating point. Also due to choked flow conditions either of these mass flow rate ratios can be equated to non-dimensional inlet pressure and outlet temperature ratios. Therefore, both the non-dimensional ratios of turbine and pump mass flow rate can be eliminated from Equation (A.31) by substitution of Equations (A.32) and (A.33).

The relationship between the time rate of change of the ratio between core inlet pressure and its design value can therefore be expressed as:

$$\tau_p \frac{dP_1'}{dt} = P_1' \sqrt{T_2'} - P_1'^2/\sqrt{T_2'} \ . \tag{A.34}$$

The derivation for the time rate of change between actual core power level and delayed neutron precursor density and their respective design values will now be given.

Equations (A.1) and (A.2) can be restated as:

$$\frac{\ell}{\beta}\frac{dP}{dt} = \left(\frac{\rho}{\beta} - 1\right)P + \frac{\lambda\ell}{\beta}z \tag{A.35}$$

$$\frac{1}{\lambda}\frac{\ell\lambda}{\beta}\frac{dz}{dt} = P - \frac{\lambda\ell}{\beta}z \quad . \tag{A.36}$$

To derive the non-dimensional relationships for both reactor power and delayed neutron precursor density, it is required to divide both parameters by their respective design points. Equations (A.37) and (A.38) define these relationships as follows:

$$z' = \frac{\ell\lambda}{\beta}\frac{z}{z_d} \tag{A.37}$$

$$P' = \frac{P}{P_d} \tag{A.38}$$

where,

z' = ratio between actual delayed neutron precursor density and its design value

z_d = design neutron precursor density

and all other terms have been previously defined.

As was the case for the derivation of the core outlet temperature and inlet pressure relationships, defining response time constants for reactor power and delayed neutron precursor density is required. Equations (A.39) and (A.40) define these parameters as follows:

$$\tau_m = \frac{\ell}{\beta} \tag{A.39}$$

$$\tau_D = \frac{1}{\lambda} \tag{A.40}$$

where,

τ_m = reactor power response time constant

τ_D = delayed neutron precursor density response time constant

and all other terms have been previously defined.

Straightforward substitution of Equations (A.37) through (A.40) into Equations (A.35) and (A.36) yields Equations (A.41) and (A.42):

$$\tau_m \frac{dP'}{dt} = \left(\frac{\rho}{\beta} - 1\right) P' + z' \tag{A.41}$$

$$\tau_D \frac{dz'}{dt} = P' - z' \quad . \tag{A.42}$$

Equations (A.19) and (A.34) which model core outlet temperature and inlet pressure, respectively, will now be restated here for convenience:

$$\tau_c \frac{dT_2'}{dt} = P' - P_1' \sqrt{T_2'} \tag{A.43}$$

$$\tau_p \frac{dP_1'}{dt} = \sqrt{T_2'}\,P_1' - P_1'^2 / \sqrt{T_2'} \ . \qquad \text{(A.44)}$$

Equations (A.41) through (A.44) form the complete set of coupled, ordinary nonlinear differential equations which model a nuclear rocket reactor. Equations (A.41) through (A.44) were used to model each of the three reactor types and were coded into the STRTUP computer program.

A.2 NERVA Controller Description and Design Methodology

The NERVA engine was a highly cross-coupled system in that all of the control inputs had a strong effect on all the controlled variables (Refs. A5, A6, A7). This cross-coupled nature made the design of controls on the basis of multiple loops, each loop using one control input to control one engine variable, an undesirable, iterative process (Refs. A8, A9). Multivariable control design, based on the use of state variable feedback, provided a one-pass design process. A digital computer was included within the control system to provide a compact, flexible means of implementing multivariable control. In this section the techniques that were developed during the NERVA program to automate the multivariable controller design process will be discussed. These techniques emphasized automation of the procedure through use of digital computer programs wherever possible.

The multivariable controller design process was divided into three distinct phases; system modeling, controller design, and controller simulation and checkout (Refs. A10, A11, A12). The basis for controller design and evaluation was the engine system as described by a set of nonlinear, first order differential equations, which for the normal operating range was the E-1 CAM (Common Analog Model) (Refs. A13, A14, A15).

The E-1 CAM, while providing the basis for controller design, was not in itself in a form to be used directly in the design of a controller feedback matrix. A set of linear, first order differential equations in the form:

$$\dot{\underline{X}} = A\underline{X} + B\underline{U} \qquad (A.45)$$

where,

$\underline{X}$ = vector of state variables
$\underline{U}$ = input vector
A,B = constant coefficient matrices
$\dot{\underline{X}} = \frac{d(\underline{X})}{dt}$

was required for the feedback matrix design.

Furthermore, this linear model was of low order, containing equations for only those states desired for control and required for a good approximation to the low frequency characteristics of the full model.

A technique had been developed to obtain low order, linear models from the high order, nonlinear E-1 CAM as mechanized with the TAF (Time and Frequency) digital program. The technique was based on dividing the states (variables defined by first order differential equations) in the E-1 CAM data into two groups. The first group ($\underline{X}_1$) contained those state variables dominated by low frequency dynamics. This group was retained as the state variables of the reduced order model. In general, these variables defined the engine feedback measurements to be used for control. The second group ($\underline{X}_2$) contained states dominated by high frequency dynamics. These states were treated as algebraic variables and were eliminated from the reduced model. The steps in the procedure were:

a. Linearization of the full model to get

$$\dot{\underline{X}} = A\underline{X} + B\underline{U} \tag{A.46}$$

b. Rearranging and subdividing the full linear model

$$\begin{bmatrix} \dot{\underline{X}}_1 \\ \dot{\underline{X}}_2 \end{bmatrix} = \begin{bmatrix} A_{11} & A_{12} \\ A_{21} & A_{22} \end{bmatrix} \begin{bmatrix} \underline{X}_1 \\ \underline{X}_2 \end{bmatrix} + \begin{bmatrix} B_1 \\ B_2 \end{bmatrix} \quad \underline{U} \tag{A.47}$$

c. Setting $\dot{\underline{X}}_2 = 0$ (treating the variables, $\underline{X}_2$, as algebraic) and solving for $\underline{X}_2$ in terms of $\underline{X}_1$ and $\underline{U}$

$$\underline{X}_2 = -A_{22}^{-1} (A_{21}\, \underline{X}_1 + B_2\underline{U}) \tag{A.48}$$

d. Eliminating $\underline{X}_2$ from the equations for $\dot{\underline{X}}_1$ to get the reduced model

$$\dot{\underline{X}}_1 = (A_{11} - A_{12}\, A_{22}^{-1}\, A_{21})\, \underline{X}_1 + (B_1 - A_{12}\, A_{22}^{-1}\, B_2)\, \underline{U} \quad .\text{(A.49)}$$

Advantages of producing reduced models in this fashion included:

a. The dc gains between the inputs ($\underline{U}$) and the retained states ($\underline{X}_1$) exactly matched those of the full model. This implied that control designed on the reduced model would exhibit the same degree of low frequency stability and performance when used with the full model as when used with the reduced model.

b. No internal relationships between variables were arbitrarily eliminated. Non-intuitive cross-coupling effects present in the full model automatically were retained in the reduced model as low frequency approximations.

The disadvantages of producing reduced models were as follows:

a. Since a unique set of variables to be retained in the reduced model did not exist, some degree of engineering judgment was needed in the selection of these variables. This had the advantage, however, of allowing other factors, such as the feasibility or the reliability of a particular measurement, to affect the selection of the model variables.

b. The higher the bandwidth desired for the controlled system, the higher must be the frequency to which the reduced model frequency response matched that of the full model. Extending the bandwidth of model agreement required the addition of more variables to the reduced model, and thus increased complexity.

For nominal engine control (non-malfunction) the controller consisted of four main elements; demand generator, feedback matrix, state estimation and supervisor (Refs. A16, A17, A18, A19). This configuration is shown in Figure A1.

The demand generator provided reference trajectories for the feedback states and nominal actuator position demand profiles. The nominal actuator demand profiles were chosen on the basis of engine controllability studies to provide the desired chamber condition sequencing while keeping engine operation within constraints. The state reference trajectories were calculated to be consistent with the nominal actuator demand profiles. Actuator trim signals were produced by the feedback matrix to minimize deviation of the engine states from the reference trajectories.

The key feature that distinguished the multivariable controller from multiple loop control was the feedback matrix. The feedback matrix trimmed each actuator demand based on all state errors. This integrated control concept was ideally suited to control of a highly cross-coupled system, such as the NERVA engine. The feedback gain matrix was calculated using a digital program employing an optimal control design technique based on quadratic optimization (Refs. A20, A21). The constant gain matrix was calculated, as

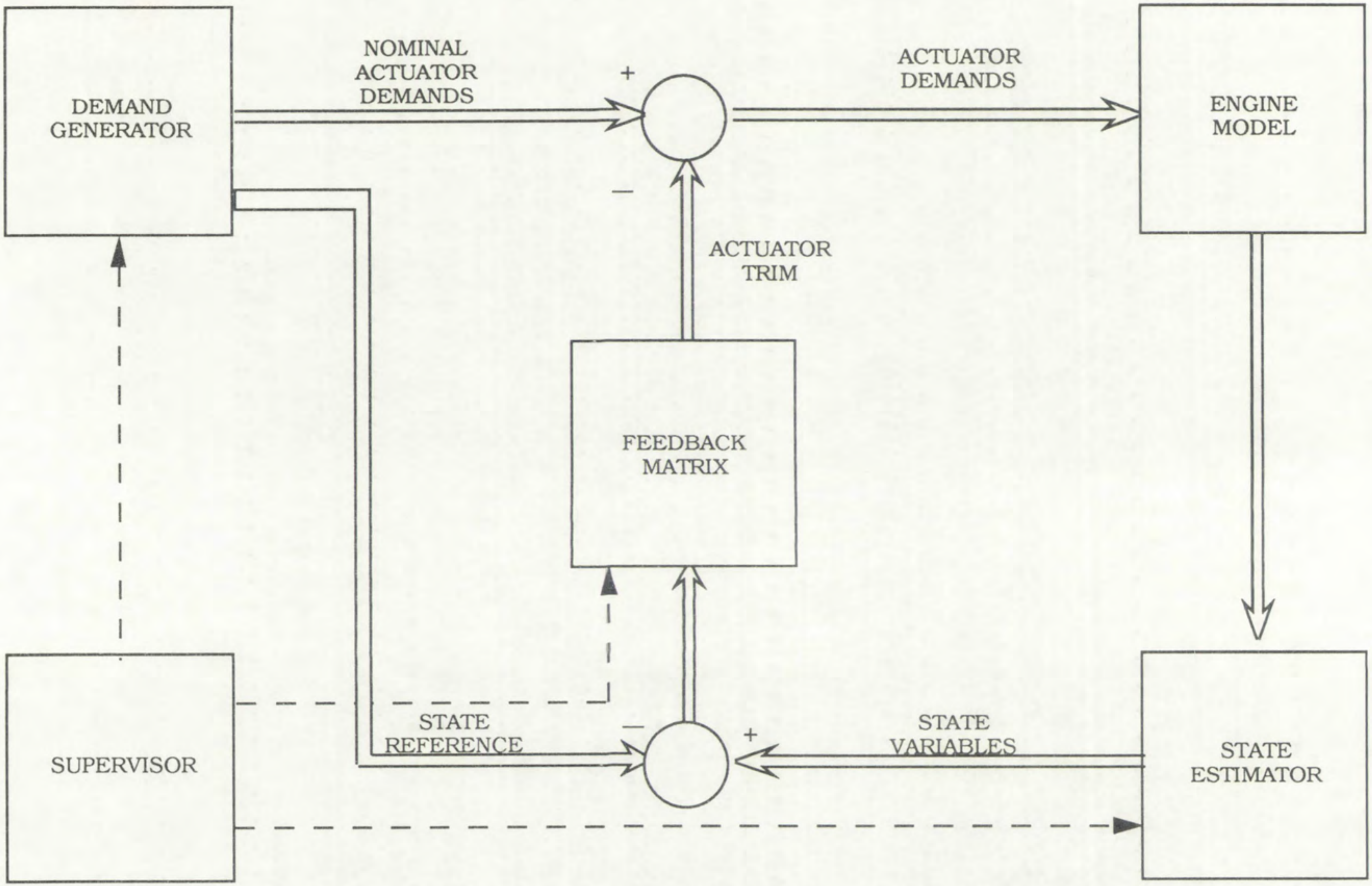

Figure A1 NERVA Multivariable Controller the asymptotic solution of the Matrix Riccati equation, to minimize deviation of state and control input variables from desired reference values. The digital program consisted of the coefficient matrices for the linear engine model and the weighting matrices which determined relative penalties associated with state and control input deviations (Ref. A22).

The state estimates were designed to estimate, from available engine measurements, the variables desired for control but not directly measurable (Refs. A23, A24, A25). Although techniques existed for estimating states from noisy measurement signals, state estimation design had been approached more simply by implementing the applicable CAM equations to obtain unmeasurable states from engine measurements.

The supervisor monitored engine and controller states and modified controller configuration and constants to be compatible with desired engine operation and present engine states. The multivariable design effort had been concentrated in one region of engine operation (the throttle line) so that no supervisory function had been required. Extension of the design effort to all regions of engine operation would have entailed design of a suitable supervisor.

The final steps in the controller design process were simulation of the controller in conjunction with the full, nonlinear engine model and evaluation of the controlled system performance. A hybrid computer was utilized to simulate and evaluate the complete controller. For this controller design the demand generator and feedback matrix were implemented on the digital portion of the hybrid computer, while the state estimator (two algebraic and one differential equation) were simulated on the analog portion. The hybrid computer simulation allowed parametric studies to be carried out to obtain feedback of design information. Primary feedback of information from the simulation was data to help determine the choice of penalty functions used in calculating the feedback matrix and to help shape the open loop actuator profiles.

To summarize, the controller design procedure had three distinct phases; system modeling, controller design, and controller simulation and checkout. System models were produced from the reference model (E-1 CAM) which were linear and low order. These models were used to calculate the feedback matrix using a quadratic optimization technique. Results of engine controllability studies were used to design nominal actuator profiles and the corresponding state reference trajectories. State estimation was provided through use of specific E-1 CAM equations. For design work upon termination of the NERVA project, requirements for a supervisor function had been minimal. However, this function would have assumed greater importance if controls for different engine operating modes and regions were integrated. The controller elements; demand generator, feedback matrix, and state estimator were mechanized with the E-1 CAM on a hybrid computer and the performance of the controlled system was evaluated against control requirements. Information from the controller evaluation was fedback to modify and improve the controller design.

The following digital programs were used in the design of the multivariable controller.

Program	Input	Output
TAF	E-1 CAM Equations	Steady state data Transient data Frequency response data Linear model coefficients
Model	Linear model coefficients State variables to be retained	Reduced linear model coefficients
Quad Op	Reduced linear model coefficients State and control use penalty coefficients	Feedback gain matrix

A.3 Current Control Methodology for Accomplishing a Time Optimal Startup

Several criteria influence the choice of operating methods during a time optimal reactor startup. The most important of these criteria are (Ref. A26):

a. Reactor criticality must be attained
b. Reactor flux level must be increased several decades in the shortest practical time
c. At the end of the reactor startup phase, engine system conditions must be suitable for initiation of propellant flow.

Three general methods were found in the literature for performing a time optimal reactor startup. These reactor startup control methods will be summarized in this section.

The first method to be discussed is adjustment of power level using closed-loop digital control. Refer to Reference A27 for more detail on this control technique. Closed-loop control is similar to manual control except that a given system output is used directly in the determination of the control signal. The control signal is a function of measured rather than actual output.

Proportional-integral-differential (PID) control is the most commonly used method for this type of automated operation (Ref. A27). The control signal is determined solely by comparison of measured and reference outputs. Information on system dynamics even if available is not used. Figure A2 depicts a simplified block diagram of a PID controller. The integral action of the controller is used to minimize instability which could be caused by small perturbations in the control signal. Derivate action is anticipatory and is used to reduce system oscillations. A drawback to the derivative action is that it may also amplify signal noise. The advantages of PID control are that it can be applied without regard to system dynamics and that its basic

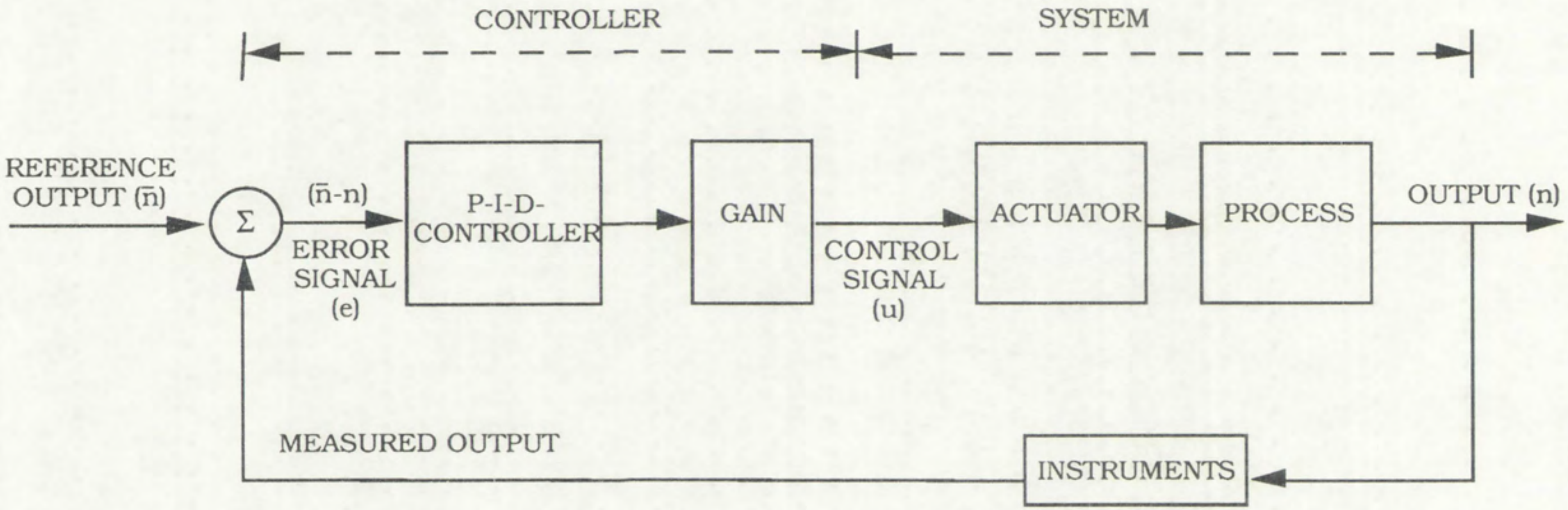

Figure A2 Simplified P-I-D Controller

concepts are readily understood. Its major disadvantage is in the selection of the control parameters which are empirical and only valid for one transient.

Most PID controllers which were either constructed as part of the NERVA program or proposed in the literature since the NERVA program was terminated utilized reactivity as the control mechanism. While controlling on reactivity is intuitively appealing, it is not possible in this case to achieve all of the theoretical advantages associated with the proportional controller which has been just described. Also, reactivity is not a directly measurable parameter. Therefore, new methods of PID control have proposed other alternative control mechanisms.

Relative to the control of a nuclear reactor, typical constraints as discussed in more detail in Section 1.4 are allowed reactor period, available rate of reactivity change, and permitted rates of change of temperature. The following state of the art control technique which is described next is for a limitation on reactor period. A description of the basic equations utilized for reactor period control and their derivation will follow in the subsequent discussion.

Reactors which have close-coupled cores may be described by the following space independent kinetics equations (Ref. A27). These are:

$$\frac{dP(t)}{dt} = \frac{\left(\rho(t) - \overline{\beta}\right)}{\ell} P(t) + \sum_{i=1}^{N} \lambda_i z_i(t) \qquad \text{(A.50)}$$

$$\frac{dz_i(t)}{dt} = \frac{\overline{\beta}_i}{\ell} P(t) - \lambda_i z_i(t) \quad \text{for } i = 1, N \qquad \text{(A.51)}$$

where,

$P(t)$ = reactor power
$\rho(t)$ = reactivity
$\overline{\beta}$ = effective delayed neutron fraction

λ_i = decay constant for the i^{th} precursor group

$z_i(t)$ = concentration of the i^{th} precursor group normalized to the initial power

ℓ = neutron generation time

$\bar{\beta}_i$ = effective fractional yield of the i^{th} group of delayed neutrons

N = number of groups of delayed neutrons including photoneutrons.

By defining an effective multigroup decay parameter as:

$$\lambda_e(t) = \Sigma\ \lambda_i\ \ z_i(t) / \Sigma\ \ z_i(t) \tag{A.52}$$

and differentiating Equation (A.50), the expression for instantaneous reactor period can be found. This expression is as follows:

$$\tau(t) = \frac{\bar{\beta} - \rho(t) + \ell\left(\dfrac{\dot{w}(t)}{w(t)} + w(t) + \lambda_e(t) - \dfrac{\dot{\lambda}_e(t)}{\lambda_e(t)}\right)}{\dot{\rho}(t) + \lambda_e(t)\ \ \rho(t) + \dfrac{\dot{\lambda}_e(t)}{\lambda_e(t)}\left(\bar{\beta} - \rho(t)\right)} \tag{A.53}$$

where,

$$w(t) \quad = \quad 1/\tau\ (t) \tag{A.54}$$

and,

$\tau(t)$ = instantaneous reactor period

$\dot{\lambda}_{e(t)}$ = time rate of change of the effective multigroup decay parameter

$\dot{\rho}(t)$ = time rate of change of reactivity

and all other terms have been previously defined.

Noting that the neutron generation time is extremely small, terms containing (ℓ) can be deleted. Equation (A.53) then reduces to:

$$\tau(t) = \frac{\overline{\beta} - \rho(t)}{\dot{\rho}(t) + \lambda_e(t)\rho(t) + \frac{\dot{\lambda}_e(t)}{\lambda_e(t)}\left(\overline{\beta} - \rho(t)\right)} \quad . \tag{A.55}$$

This relationship will accurately predict instantaneous reactor period associated with any reactivity pattern provided that the prompt critical value is not approached. An alternate form of this equation can be similarly be derived. For this alternate form of the equation, the effective multigroup decay parameter is defined as follows:

$$\lambda'_e(t) = \Sigma\lambda_i^2 \; z_i(t) / \Sigma\lambda_i \; z_i(t) \quad . \tag{A.56}$$

As was the case in the derivation of Equation (A.55), deleting terms containing (ℓ) yields:

$$\tau(t) = \frac{\overline{\beta} - \rho(t)}{\dot{\rho}(t) + \lambda'_e(t)\rho(t) + \Sigma\overline{\beta_i}\left(\lambda_i - \lambda'_e(t)\right)} \quad . \tag{A.57}$$

Figures A3 and A4 (Ref. A27) illustrate the behavior of the various terms in the standard and alternate equations for dynamic reactor period, respectively, for a given reactivity pattern. The physical meaning of the terms in the standard period equation will now be discussed. The rate of change of reactivity ($\dot{\rho}$) corresponds to the effect of changing the prompt neutron population. The quantities $(\lambda_e\rho)$ and $\left(\dot{\lambda}_e / \lambda_e\right)\left(\overline{\beta} - \rho\right)$ correspond respectively to changing the delayed neutron precursor population and the distribution of the delayed neutron precursors. These observations have practical consequences. Precursor populations are a function of power history and therefore cannot be altered on demand. Hence the terms $(\lambda_e\rho)$ and $\left(\dot{\lambda}_e / \lambda_e\right)\left(\overline{\beta} - \rho\right)$ cannot be directly manipulated and are not subject to direct control. However, prompt neutron population is essentially a function of only the current power level and it is therefore immediately controllable. If an immediate change in reactor period is required, then adjustment should be made in the rate of change of reactivity rather than in reactivity itself.

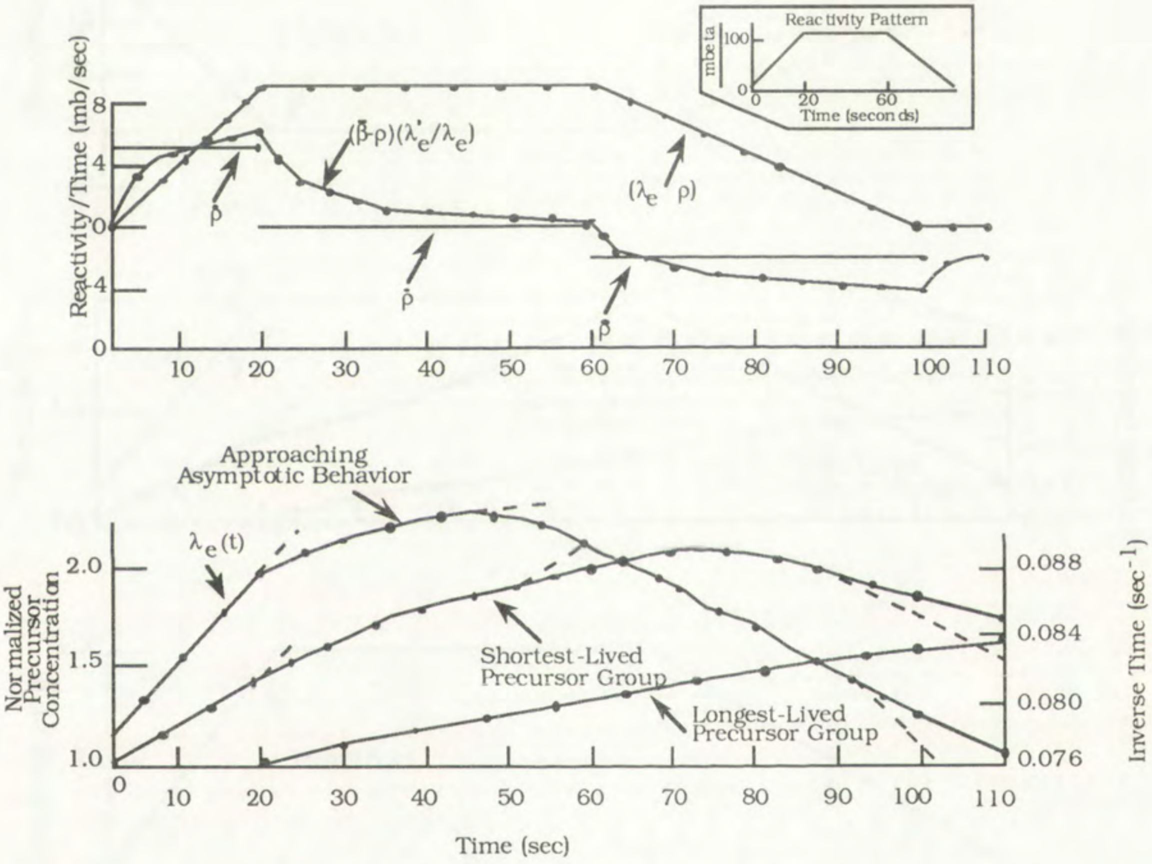

Figure A3 Behavior of Component Terms - Standard Equation

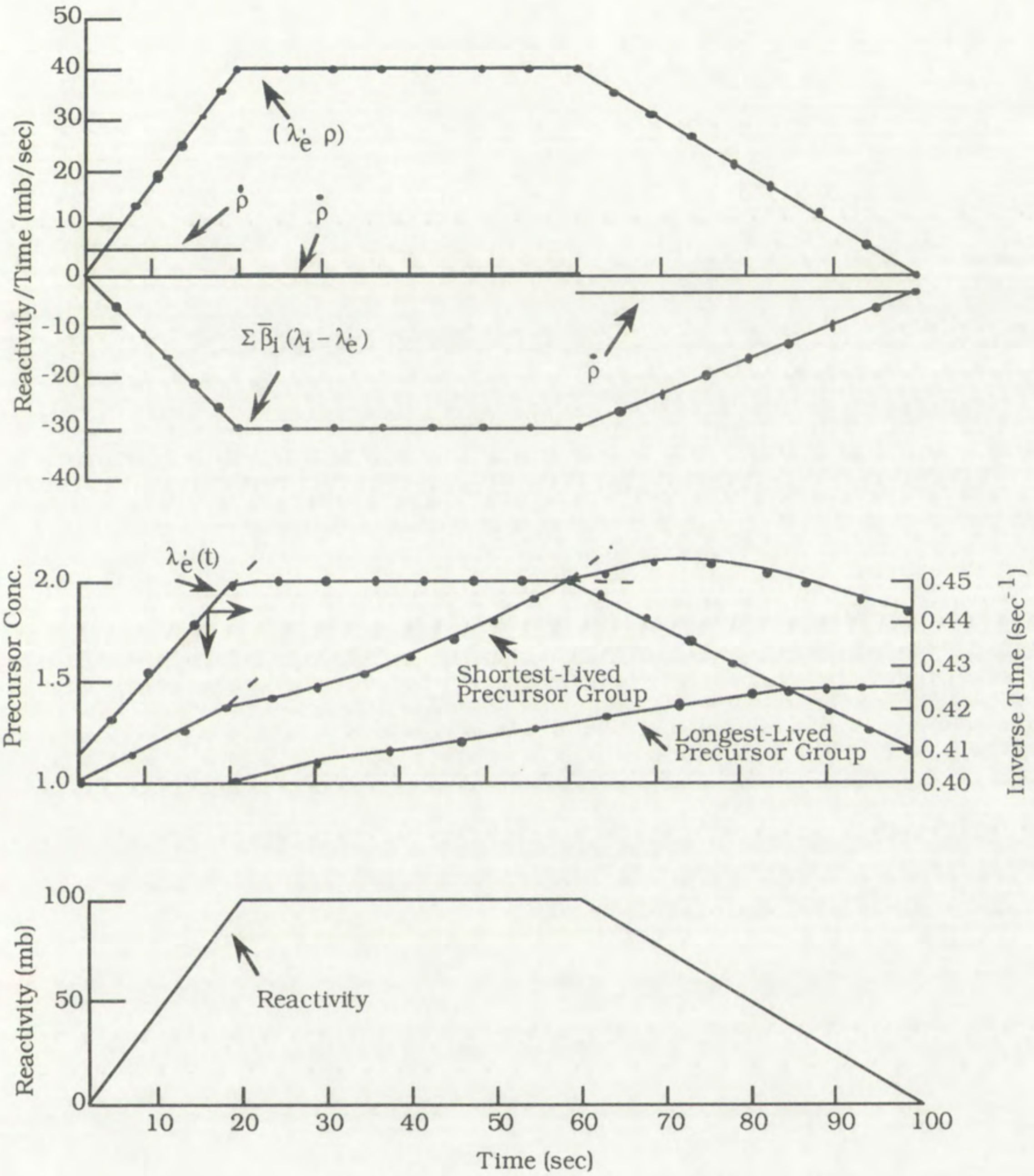

Figure A4 Behavior of Component Terms - Alternate Equation

A physical example of the preceding argument is that actuation of a control device will immediately alter the rate of change of reactivity but movement must be sustained for some finite period of time to alter reactivity itself.

Figure A3 illustrates a rapid insertion of reactivity, followed by an extended hold, and finally a gradual removal of reactivity. Also shown are the corresponding changes in the standard effective multigroup decay parameter and two of the precursor groups. Three features stand out relative to the quantity $\left(\dot{\lambda}_e / \lambda_e\right)\left(\bar{\beta} - \rho\right)$. First, it rises as reactivity is inserted. This behavior is in response to the shift of the effective multigroup decay parameter toward the decay constants of the shorter lived precursor groups that dominate during power increases because they remain near equilibrium levels. Offsetting factors are the decreasing value of the term $\left(\bar{\beta} - \rho\right)$ and the rising magnitude of the decay parameter. Second, this quantity tends to zero once the reactivity is held constant. This occurs because in the absence of varying reactivity, the precursor groups approach an asymptotic state. Third, once reactivity removal is begun, the value of this quantity becomes negative. Physically, there is an immediate decrease in the prompt neutron population, which in turn causes first the rate of rise of the total neutron population and then that of the short lived precursors to decline. The longer lived precursors are not immediately affected and therefore become more significant. The net result is that the effective multigroup decay parameter decreases. The significant feature depicted in Figure A3 is that the transient is being driven by changes in the prompt neutron population.

In Figure A4, which illustrates the behavior of the component terms of the alternate dynamic period equation, reactivity is added at the rate of five millibeta per second for twenty seconds. This reactivity addition is followed by a hold period of forty seconds, and then a gradual removal of reactivity for forty seconds at the rate of 2.5 millibeta per second. The middle portion of Figure A4 shows the behavior of effective alternate multigroup decay parameter and the normalized concentrations of the shortest and longest lived delayed neutron precursor groups. As is shown, the short lived group responds rapidly to changes in the reactivity insertion rate while the long lived group in comparison responds sluggishly. The behavior of the decay parameter is dominated by that of the short lived precursor groups and therefore conforms to the reactivity pattern. The decay parameter is defined in terms of the square of the precursor decay constants and is therefore quite sensitive to changes in concentrations of the short lived groups which have the largest decay constants. The upper portion of Figure A4 depicts the behavior of the three terms that form the denominator of the alternate formulation of the dynamic period equation. The quantity $\left(\dot{\lambda}_e \;\; \rho\right)$ conforms to the pattern of reactivity with some slight curvature resulting from the non-linearity of the decay parameter. The term $\left(\Sigma\bar{\beta}_i\left(\lambda_i - \dot{\lambda}_e\right)\right)$ is the most interesting. Its behavior follows that of $\left(\dot{\lambda}_e\right)$ except that it is of opposite sign. Thus, this term goes rapidly negative, remains almost constant, and then goes slowly to zero. As was the case for the behavior of the standard dynamic period equation illustrated in Figure A3, it should be noted that most significant feature of the reactivity transient shown in Figure A4 is that this transient is being driven by changes in the prompt neutron population.

As was demonstrated in Figures A3 and A4, the rate of change of reactivity has another critical attribute which is that an immediate change in instantaneous reactor period will result in a time-optimal control strategy for reactor power. Therefore, one current method available for time optimal control would be use of PID control using rate of change of reactivity as the measured control parameter.

Logarithmic power control is another potential method for accomplishing an optimal reactor startup (Refs. A28, A29, A30). In fact, a logarithmic power control system was developed at Los Alamos National Laboratories for use on the KIWI-A reactors (Ref. A31).

The primary engine parameters of interest in the KIWI-A reactors were core and exit gas temperatures and their rates of change, power, mass flow rate, and reactor period. The control philosophy adopted was that of the direct control of power and mass flow rate. Core and exit gas temperatures and their rates of change were controlled indirectly by programming power and flow rate to achieve the desired temperature-versus-time profile. During a nuclear rocket engine startup, power level will be increased by many decades. Therefore, the designers of the control system for the KIWI-A reactors defined a logarithmic power variable which made it possible to conveniently analyze startup problems as quasi-linear systems. A description of the basic equations utilized for logarithmic power control and their derivation will follow in the subsequent discussion.

For convenience of the following derivation Equations (A.50) and (A.51) will be restated as:

$$\frac{1}{n}\frac{dn}{dt} = \frac{\rho - \beta}{\ell} + \sum_{i} \lambda_i \frac{z_i}{n} \qquad \text{(A.58)}$$

and,

$$\frac{1}{n}\frac{dz_i}{dt} = \frac{\beta_i}{\ell} - \lambda_i \frac{z_i}{n} \qquad \text{(A.59)}$$

$$i = 1,\ 2,\ \dots,\ 6$$

where,

n = neutron density

ℓ = neutron generation time

ρ = reactivity

β = effective delayed neutron fraction

λ_i = decay constant for the i^{th} group of delayed neutron precursors

z_i = concentration of the i^{th} group of delayed neutron precursors

β_i = production factor for the i^{th} group of delayed neutron precursors.

To convert Equations (A.58) and (A.59) to a logarithmic form, a dimensionless logarithmic power variable $Q(t)$ will be defined as follows:

$$n(t) = n_o \exp Q(t) \tag{A.60}$$

where,

$n(t)$ = time rate of change of neutron density
n_o = initial neutron density
$Q(t)$ = logarithmic power variable.

If the variable $P_i(t)$ is introduced where:

$$P_i(t) = z_i(t)/n(t) = P_{i_o} + \Delta P_i(t) \tag{A.61}$$

then with substitution of this variable into Equation (A.59),

$$\lambda_i P_i(t) = \frac{\beta_i}{\ell} + \lambda_i \Delta P_i(t) \tag{A.62}$$

where,

$\Delta P_i(t)$ = variation of $P_i(t)$.

Equations (A.58) and (A.62) can be combined to obtain:

$$\frac{d}{dt} Q(t) = \frac{\rho(t)}{\ell} + \sum_i \lambda_i \Delta P_i(t) \tag{A.63}$$

and with substitution into Equation (2.59),

$$\lambda_i \frac{d}{dt} \Delta P_i(t) + \frac{d}{dt} Q(t) \left\{ \frac{\beta_i}{\ell} + \lambda_i \Delta P_i(t) \right\} + \lambda_i \left\{ \lambda_i \Delta P_i(t) \right\} = 0 \ . \tag{A.64}$$

Equations (A.64) and (A.63) can be considered fundamental to logarithmic power control optimization of a reactor startup. Typically, these equations were coupled with some absolute maximum reactivity limit such as $0.9\ \beta$ to insure prompt criticality was never reached (Refs. A30, A32).

A third proposed method in the literature for a time optimal reactor startup is open loop control. The control devices are simultaneously positioned by a programmed signal. The devices are positioned to be for a predetermined supercritical reactivity, then a ramp power increase occurs at a given reactivity rate. Reactor startup proceeds on an open loop or precalibrated basis and reactor power is not measured (Ref. A33). When reactor power reaches approximately 0.1 percent of full power closed-loop control can be initiated. Then either of the other two methods of logarithmic or rate of reactivity control of reactor power could be employed. Also, PID control with reactivity as the control parameter has been proposed in the literature.

Many variations of the three methods for control of reactor power level alteration which have just been described were found during a review of the literature. However, these variations did not significantly alter the fundamental control equations. Therefore, separate categorization and description in this section was not warranted.

The key for each of the previously discussed methods for control of time optimal reactor startups is the ability of the control to maintain neutron density essentially constant once design power level is reached, while the precursor level is not near steady state. As was discussed in Section 1.4, a time optimal startup also requires coupling between reactor startup, system heatup, and coolant flow increase. One proposed method for making this coupling between engine startup phases time optimal will be discussed in the remainder of this section.

A nuclear rocket is coupled between these three phases of overall system startup through core temperature reactivity and coolant density reactivity (Refs. A1, A2). Also, refer to Equation (A.20). In a time optimal process consumption of coolant is minimized which has the advantage of pounds of propellant saved which will allow less bulky propellant tanks and more payload.

Besides the transient stress constraints already discussed, additional flow rate increase constraints exist in this final step of rocket startup (Refs. A2, A4, A34, A35). The pump flow rate is also constrained by the velocity of the flow control valve, mechanical stresses, and certain regions of pump performance. The first two of these constraints are probably negligible compared to the third.

A hypothetical pump performance map is shown in Figure A5. This figure plots pressure rise across the pump versus pump flow rate. Specific speed is defined as:

$$N_s = NQ^{0.5} / H^{0.75} \tag{A.65}$$

where,

N_s = specific speed
N = pump speed
Q = flow rate
H = pump pressure head.

The importance of specific speed is that at the upper limit a pump stalls while at the lower limit cavitation occurs. A typical flow increase as illustrated in Figure A5 constrained by only thermal stress limits (shown by trajectory o-d-e-c) violates a pump constraint. The optimal flow rate increase process must therefore consider both thermal stress limitations as well as pump stall constraints.

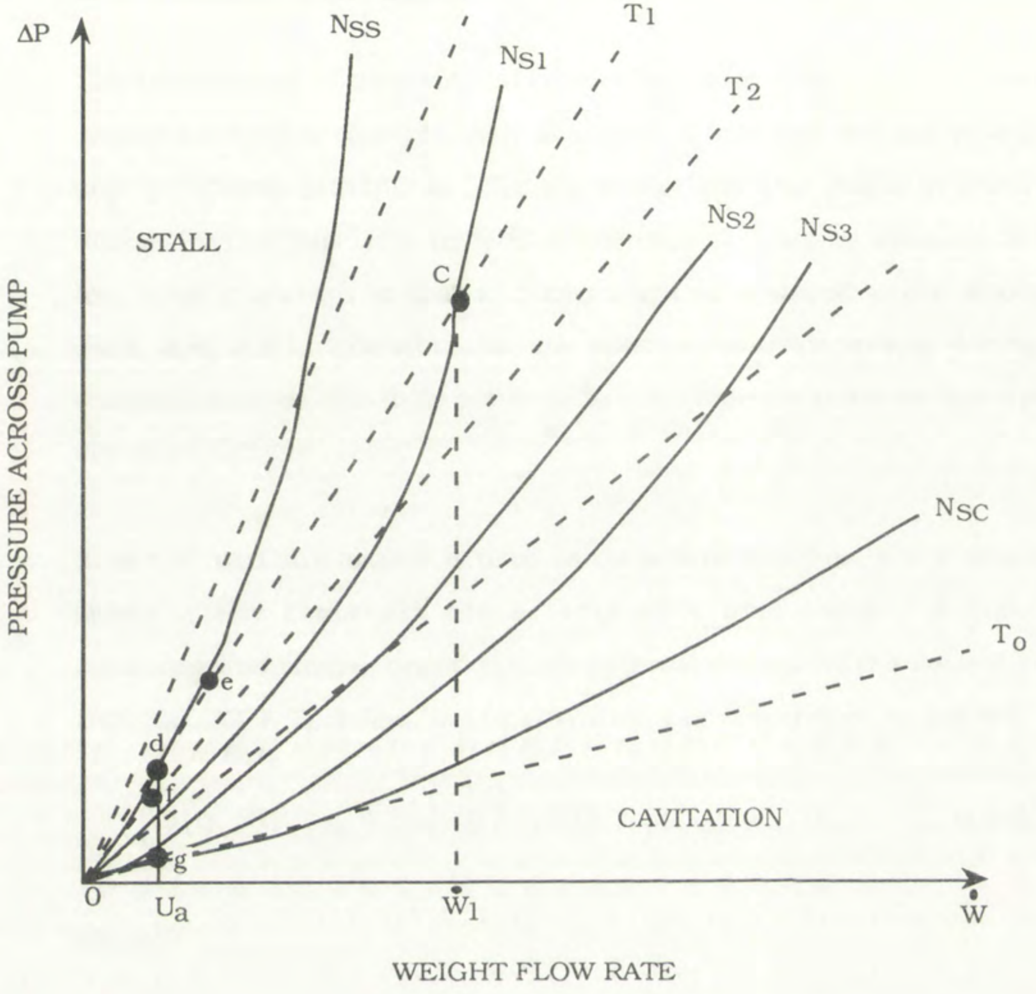

N_S = SPECIFIC SPEED

T_1 = TERMINAL TEMPERATURE

T_o = INITIAL TERMPERATURE

Figure A5 Pump Performance Map

A.4 Safety Implications Pertaining to Time Optimal Startups

The achievement of time optimal control in reactor startup implies that the system's output is changed both in minimum time and without violation of any operational constraints. For any control law that might be used, it is imperative that reactivity removal at the requisite rate be available to limit any power overshoot so that an independent safety scram is not demanded (Refs. A36, A37). Therefore, the net positive reactivity present during any transient must be able to be overcome by control device action so that a power overshoot will not occur.

If rate of reactivity change is used as the control function, the avoidance of safety system challenges can be achieved if it is possible to make the instantaneous reactor period infinite upon attainment of the desired power level (Ref. A27) Therefore, net reactivity must be constrained as follows:

$$\left[\lambda_e(t)\ \rho(t) + \left(\dot{\lambda}_e(t)/\lambda_e(t)\right)\left(\overline{\beta} - \rho(t)\right) + \dot{\rho}_f\right] \le \left|\dot{\rho}_c\right| \qquad \text{(A.66)}$$

where,

$\lambda_e(t)$ = effective multigroup decay parameter

$\dot{\lambda}_e(t)$ = rate of change of effective multigroup decay parameter

$\rho(t)$ = reactivity

$\overline{\beta}$ = effective delayed neutron fraction

$\dot{\rho}_f$ = rate of change of reactivity due to thermal-hydraulic feedback effects

$\dot{\rho}_c$ = maximum available rate of change of reactivity due to the control mechanism.

If the above inequality is always maintained then it will be always possible to drive reactor period to infinity. For time optimal control Equation (A.66) is unnecessarily restrictive. A less stringent constraint is that there should be sufficient time to eliminate whatever reactivity is present beyond the amount that can be immediately negated by the control mechanism before the desired power level is obtained (Ref. A27). This requirement can be written as:

$$\left(\rho(t) - |\dot{\rho}_c| / \lambda_e(t)\right) / |\dot{\rho}_c| \leq \tau(t) \ln\left(P_F / P(t)\right) \qquad \text{(A.67)}$$

where,

τ (t) = instantaneous reactor period
P_F = desired power level
P(t) = current power level
and all other terms have been previously defined.

The quantities on the left side of Equation (A.67) represent the time that is required to reduce net reactivity to the amount which can be offset by continuous removal of reactivity by the control mechanism. The terms on the right side of the equation represent the time remaining to attain a designated power level. If the inequality represented by the constraint is not satisfied, then the control device must remove reactivity. A major advantage of this constraint is that it determines if a change should be made in the present control signal to avoid an overshoot in power at some time in the future. Not all states are allowable intermediates through which the system may pass while transiting from some initial to final power. Excluded are both those states that represent actual overshoots as well as those from which overshoots could not be averted by manipulation of the control device.

Power changes can only be halted if the rate of rise of delayed neutrons can be offset by making the rate of change of prompt neutrons negative. Physically this means that it must be possible to counter positive reactivity by the negative reactivity insertion rate.

Along with control of rate of change of reactor power to insure no power overshoots, the rate of flow increase of hydrogen coolant must be controlled to insure that thermal limits are not exceeded (Refs. A3, A38). Computation of thermal stresses in a nuclear rocket is of importance from the standpoint of ensuring the necessary strength during operation. Whenever there is a rapid increase of hydrogen flow at rated power input, a large increase of thermal stresses in the fuel element will result (Ref. A39).

In order to evaluate the most critical thermal stresses of a nuclear rocket, it is necessary to know the thermal transients leading to the largest temperature gradients. An increase in hydrogen is desirable from the standpoint that it will eventually lower the steady state temperature. However, an increase in coolant flow also introduces a higher temperature gradient in the fuel elements. Thus excessive flow at rated power conditions yields transient stresses above steady state stresses. Necessarily the ratio of maximum transient to steady state stress at full power should be limited to ensure that the design of the reactor is within the margin of safety.

In summary, control of engine startup must ensure that both power level and thermal stress limits are not exceeded. However, since the startup must be as rapid as possible, these limits must be approached as closely as possible without exceedence.

A.5 REFERENCES

A1. Smith, H., and Stenning, A., Open loop stability and response of nuclear rocket engines, Nuclear Science and Engineering, 11, 1961.

A2. Smith, H., Closed-loop dynamics of nuclear rocket engines with topping turbine drive, Nuclear Science and Engineering, 18, 1964.

A3. Stenning, A., Rapid approximate method for analyzing nuclear rocket performance, ARS Journal, pp. 169-172, February, 1960.

A4 . Smith, H., Closed loop dynamics of nuclear rocket engines, Nuclear Science and Engineering, 14, 1962.

A5. Norman, H., et al., Nerva flight engine control system design, Westinghouse Electric Co., Sacramento, CA, September, 1972.

A6. Walsh, J., Nuclear reactor controls for Nerva rocket engine, American Nuclear Society Meeting, Los Angeles, CA, July, 1970.

A7. Nuclear subsystem control and its integration into engine control, Westinghouse Electric Co., Pittsburgh, PA, May, 1963.

A8. Bell, R., et al., Preliminary reactor system analysis for Nerva, Westinghouse Electric Co., Pittsburg, PA, October, 1967.

A9. Reactor control system, Nerva Phase I, Westinghouse Electric Co., Pittsburg, PA, March, 1962.

A10. Reactor controls concept trade study. Trade study No. 701, Westinghouse Electric Co., Pittsburg, PA, September, 1970.

A11. Buker, J., Feasibility of using core inlet pressure as a control variable for the Nerva engine, Westinghouse Electric Co., Pittsburg, PA, November, 1964.

A12. Dowling, E., Multivariable control design process, Aerojet-Nuclear Systems Co., Sacramento, CA, April, 1971.

A13. Parziale, E., and Porcelli, G., Analysis and design of the Nerva engine control system, Aerojet Nuclear System Co., Sacramento, CA, August, 1970.

A14. Openshaw, F., and Parziale, E., Startup controls design, Aerojet Nuclear Systems Co., Sacramento, CA, October, 1971.

A15. Parziale, E., and Schenz, R., Certain performance characteristics of the E-1 cam state variable feedback control system, Aerojet Nuclear Systems Co., Sacramento, CA, May, 1971.

A16. Openshaw, F., Direct iterative decoupling procedure for multivariable control system design, 1972.

A17. Nerva detail specification. Part I. Performance/design and qualification requirements for instrumentation and control subsystem, Aerojet Nuclear Systems Co., Sacramento, CA, July, 1970.

A18. Design requirement sheets for the instrumentation-and-control subsystem, Aerojet Nuclear Systems Co., Sacramento, CA, April, 1970.

A19. Porcelli, G., Linear programming design of multivariable feedback controllers for the Nerva nuclear engine, Fairchild Space and Electron Co., Germantown, MD, October, 1974.

A20. Rostoczy, Z., et al., Application of Pomtryagin's maximum principle to flux-state changes in nuclear reactors, "Reactor Kinetics and Control", AEC Symposium Ser. No. 2, pp. 265-277, 1964.

A21. Secker Jr., P., and Weaver, L., Synthesis of optimal reactor feedback control using the first variation, Trans. Am. Nucl. Soc. 8, p. 234, 1965.

A22. Wittler, M., Optimal nuclear rocket control subject to integro-differential constraints, P.H.D. Thesis, Rensselaer Polytechnic Institute, Troy, NY, 1968.

A23. Johnson, M., Precomputed state dependent digital control of a nuclear rocket engine (Semiannual report), Arizona University, Tucson, AZ, June, 1972.

A24. Johnson, M., Precomputed state dependent digital control of a nuclear rocket engine, Arizona University, Tucson, AZ, 1972.

A25. Johnson, M., Precomputed state dependent digital control of a nuclear rocket engine, PhD thesis, Arizona University, Tucson, AZ, 1972.

A26. Searle, R., and Marcy, R., An approach to startup control of a nuclear rocket engine, TID-7653, pp. 546-557, 1952.

A27. Bernard, J., Formulation and experimental evaluation of closed-form control laws for the rapid maneuvering of reactor neutrontic power, MITNRL-030, September, 1989.

A28. Brown, E., Logarithmic power control in KIWI-A reactors, IRE Transactions Nuclear Science, NS-9, No. 1, p. 145, 1962.

A29. Kagayama, T., Dynamic analysis of start-up of a nuclear reactor, Proceedings United Nations International Conference Peaceful Uses Atomic Energy 2nd, Geneva, Switzerland, 1958.

A30. Mohler, R., et al., Kiwi-B system dynamics, Los Alamos Scientific Laboratory Report, LAMS 2539, Los Alamos Scientific Laboratory, Los Alamos, NM, 1961.

A31. Rappaport, E., KIWI-B-1B control systems, LAMS-2966, Los Alamos Scientific Laboratory, Los Alamos, NM, November, 1963.

A32. Shen, C., and Haag, F., Adaptive control for nuclear reactor start-up and regulation, Transactions American Nuclear Society 6, No. 1, p. 109, 1963.

A33. Shen, C., and Haag, F., Application of optimum control to nuclear reactor start-up, IEEE Transactions Nuclear Science NS-11, No. 2, p. 1, 1964.

A34. Mohler, R., Optimal control of nuclear reactor systems, Trans. Am. Nucl. Sci. 7, pp. 58-59, 1964.

A35. Phelan, J., et al., Modern control aspects of nuclear reactors, Eng. Res. Rept. EE-157, Univ. of New Mexico, Albuquerque, NM, 1968.

A36. Briggs, D., and Shen, C., Distributed parameter optimum control of a nuclear rocket with thermal stress constraints, Journal of Basic Engineering 89, No. 2, pp. 300-306, 1967.

A37. Price, H., and Mohler, R., Computation of optimal controls for a nuclear rocket reactor, IEEE Transactions Nuclear Science, NS-15, pp. 64-73, 1968.

A38. Mohler, R., and Wheatley, E., A mathematical model to represent the basic dynamics of a nuclear rocket system, Transactions American Nuclear Society 3, No. 2, p. 386, 1960.

A39. Shen, C., and Liu, T., Distributed parameter type of control for a bilinear system with reference to control of a nuclear reactor, Proceedings International Federation Automated Control, 3rd, London, England, June, 1966.

APPENDIX B

WIRE CORE REACTOR MODELING

Models exist in the literature for both the NERVA small engine and particle bed reactors, therefore no additional modeling development for these reactors types was performed. In the case of the wire core reactor, a comparable model to the other reactor types was unavailable. Therefore, prior to assessing the impact of nuclear rocket engine design on control strategies, modeling of the wire core reactor was performed. This appenedix will describe this modeling process and the final wire core reactor configuration which was utilized as comparison with the NERVA small engine and particle bed designs.

B.1 Initial Configuration Assessment

To aid in the compatibility of the results, when startup strategy comparisons were performed as described in Chapters 4 and 5, key rocket engine parameters were matched between the NERVA small engine design (Ref. B1) and the wire core design. These parameters are given in Table B1.

Table B1

Engine Parameters of the NERVA Small Engine Design

Parameter	Design Value
Thrust	72 kN
Chamber Temperature (T_c)	2695°K
Chamber Pressure (P_c)	3.1 MPa
Engine Flow Rate ($\dot{w}$)	8.5 kg/s
Core Exit Velocity (V_e)	0.25 Ma

A brief description of the wire core and its coolant flow path will now be given. Coolant is discharged from a turbopump into a central hole in the wire core (refer to Figure 12). After entering this center hole, coolant flows radially outward through a cold frit and then into the active fuel region. Figure 10 gives an illustration of the configuration within the fuel region.

The fuel region is composed of fuel wires clad with tungsten, tungsten spacer wires, and void space for the coolant. Coolant continues flowing radially outward from the fuel region into the exit duct. Encircling the exit duct is a carbon steel liner. The next region of the core in the radially outward direction contains the reflector and the control drums. Finally, a stainless steel pressure shell provides for structural integrity.

After the coolant leaves the exit duct it enters the nozzle. This De Laval nozzle attains supersonic velocity in the divergent section of the nozzle and chocked flow in the throat of the nozzle. The chocked flow condition is present because the chamber pressure is sufficiently greater than the critical pressure for the throat. Ideal rocket assumptions were utilized for the wire core model. In most rockets the measured performance is within one to six percent of calculated ideal values (Ref. B2). The ideal rocket assumptions which were utilized are as follows:

a. All the species of the working fluid are *gaseous*. Any condensed phases (liquid) have negligible mass.

b. The working substance obeys the *perfect gas laws*.

c. There is *no heat transfer* across the rocket walls; therefore, the flow is adiabatic.

d. The expansion of the working fluid takes place in a uniform and steady manner *without vibration*. Transient effects (start, stop) are of very short duration and can be neglected.

e. All the exhaust gases leaving the rocket nozzle have an *axially directed velocity*.

f. The *gas velocity, pressure, temperature*, and *density* are *uniform* across any section normal to the nozzle axis.

g. There is *no friction* and *boundary layer effects* are neglected.

h. There are no *shock waves* or *discontinuities* in the nozzle flow.

The first step employed in determination of the wire core rocket engine dimensions was to find the throat area (A_t) in the rocket nozzle. The throat area must be determined first before the core exit duct area is calculated.

The area ratio for an isentropic nozzle can be expressed in terms of Mach numbers for any points X and Y within the nozzle (Ref. B2). This relation is as follows:

$$\frac{A_y}{A_x} = \frac{M_x}{M_y}\sqrt{\left\{\frac{1+[(k-1)/2]M_y^2}{1+[(k-1)/2]M_x^2}\right\}^{(k+1)/(k-1)}} \tag{B.1}$$

where,

A_y/A_x = ratio of area for any two points within the nozzle

M_x/M_y = ratio of Mach numbers for any two points within the nozzle

k = specific heat ratio.

The Mach number is a dimensionless flow parameter and is defined as the ratio of the flow velocity to the local acoustic velocity. Equation (B.2) expresses this relation:

$$M = v/a = v/\sqrt{kRT} \tag{B.2}$$

where,

M = Mach number

v = coolant flow velocity

a = local acoustic velocity

k = specific heat ratio

R = gas constant

T = fluid or free-stream temperature.

An illustration of the relationship between core exit area to throat area and also to nozzle exit area is given for different specific heat ratios in Figure B1.

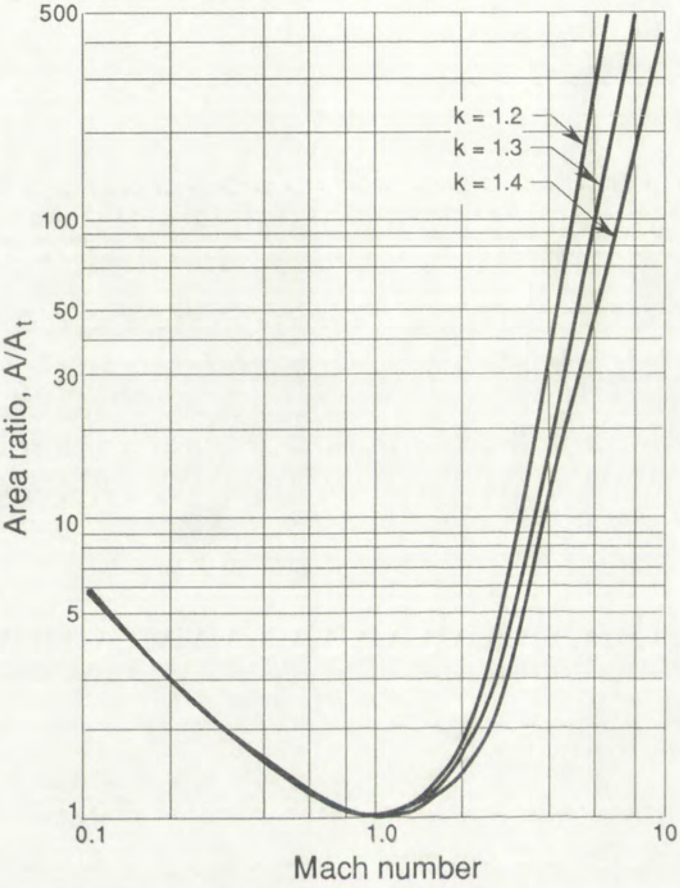

Figure B1 Relation of Area Ratio to Mach Number for Isentropic Flow in a De Laval Nozzle

After making the design choice of hydrogen propellant, the throat area can be determined from a manipulation of the following equation:

$$\dot{m} = \frac{A_t v_t}{V_t} = A_t P_1 \frac{k\sqrt{[2/(k+1)]^{(k+1)/(k-1)}}}{\sqrt{kRT_1}} \tag{B.3}$$

where,

$\dot{m}$ = coolant mass flow rate

P_1 = core exit pressure

T_1 = core exit temperature

V_t = coolant specific volume at the nozzle throat

v_t = coolant velocity at the nozzle throat

A_t = nozzle throat area

and all other terms have been previously defined.

Employing the core design parameters given in Table B1, the nozzle throat area was found to be 146.8 cm^2. Once the nozzle throat area was known, the core exit duct area could be determined by either Equation (B.1) or Figure B1. The results of this calculation yielded a core exit duct area of 352.7 cm^2.

The calculation of the area of the central hole for the wire core will now be described. To determine the dimensions of the central hole, the coolant properties of liquid hydrogen at 100°K were utilized with a flow velocity of 18 m/s. The propellant velocity and temperature initial design choices were assigned to be consistent with typical values found in the literature when hydrogen was employed as the propellant (Refs. B1, B3, B4, B5, B6). Once these parametric values were chosen the diameter could be determined from:

$$D_{\substack{\text{central}\\ \text{hole}}} = 2\left(\frac{\dot{m}}{\pi\rho v}\right)^{1/2} \tag{B.4}$$

where,

$D_{\substack{\text{central}\\ \text{hole}}}$ = diameter central hole

ρ = hydrogen density

v = hydrogen coolant velocity

and all other terms have been previously defined.

The central hole diameter was found to be 9.0 cm.

Next an approximation for the material composition and dimensions of the fuel region was performed. Figures 10 and 11 were used as a first cut approximation of the relative structural dimensions of the fuel region. To calculate the volume fractions, a unit area was constructed from Figure 10. This unit area consisted of four partial and one complete fuel wire. Using the dimensions given in Figure 10, each unit area was found to be 3.76 mm^2. To determine what percentage of this area was occupied by fuel wires, it was known that each unit area consisted of four partial (one-quarter) fuel wires and one whole fuel wire. Therefore, the total area of fuel wires can be found from:

$$A_{\substack{\text{fuel}\\ \text{wires}}} = 2\left(\frac{\pi}{4} D^2\right) \tag{B.5}$$

where,

$A_{\substack{\text{fuel}\\ \text{wires}}}$ = area of fuel wires within the unit cell

D = diameter of fuel wire given in Figure 12.

The fuel wire area was determined to be 1.24 mm^2 (32.9 percent of the total area). Next a determination of what portion of the fuel wire is cladding was made. There were two values of cladding thickness (0.076 and 0.18 mm) given in Figure 10. An average value of 0.128 mm was assumed. The area of the cladding can be determined from the following equation:

$$A_{clad} = \frac{\pi}{4}\left(D_o^2 - D_i^2\right) \tag{B.6}$$

where,

A_{clad} = area of cladding for a fuel wire

D_o = diameter of the fuel wire

D_i = diameter of the fueled region within the fuel wire.

The total cladding area within the unit cell can be found by doubling the area from Equation (B.6). Thus, the total clad area was determined to be 0.613 mm^2 (16.3 percent of the total area of the unit cell).

Next the area of the spacer wires was approximated. It was assumed based on Figures 10 and 11 that there are two spacer wires which traverse the entire length of the unit cell and that they are approximately 0.5 mm in thickness. The area of the spacer wires for this initial approximation was found to be 1.94 mm^2 (51.6 percent of the total cell area).

Finally, the remainder of the area (15.5 percent of the total unit cell area) was void space for passage of the radially outward flowing hydrogen propellant. It was realized that this initial approximation based on Figures 10 and 11 contained cladding and spacer wires dimensions which were much greater than practicable. Therefore, both of their percentages of total unit cell area were decreased based upon typical values for structure and cladding found in the literature for the particle bed and NERVA reactors (Refs. B1, B3, B4, B5, B6). Table B2 gives the final approximations which were to be used as the initial input into the criticality calculations which are described later in this chapter.

Table B2

Unit Area Composition

Constituent	Percent Area	Area (mm^2)
Fuel Region	27.9	1.05
Cladding	5.2	0.19
Spacer Wires	10.0	0.38
Void Space	56.9	2.14

Figure 12 was utilized to approximate the total fuel region area. By employing Equation (B.6) and the radial dimensions given in Figure 12 the total fuel area initial approximation was calculated to be 3,297.49 cm^2. Using the percentage of area contributions from Table B2 yielded the total area contributions within the fuel region given in Table B3. Composition of materials in the fuel region is also given in Table B3.

Table B3

Fuel Region Area Contributions by Constituent

Constituent	Material	Total Area (cm^2)
Fuel	UN	920.0
Clad	W	171.5
Spacer Wires	W	329.7
Void Space	H_2	1,876.2

Once the areas were determined for the exit duct and fuel region, the outer diameter for each of these regions was calculated. Recall that the diameter for the central inlet hole was found to be 9.0 cm. An aluminum cold frit (0.5 cm in thickness) was modeled to distribute hydrogen coolant flow to the fuel region. Next a calculation of the outer diameter of the fuel region was performed. Equation (B.6) was modified to obtain:

$$D_o = \left(\frac{4}{\pi} A_{fuel} + D_i^2\right)^{1/2} \tag{B.7}$$

where,

D_o = outer diameter of the fuel region
A_{fuel} = area of the fuel region
D_i = inner diameter of the fuel region.

This calculation yielded an outer diameter for the fuel region of 66.42 cm. A similar calculation for the exit duct found its outer diameter to be 69.77 cm.

The next concentric region of the core is a carbon steel liner. This liner was initially approximated to be 1.0 cm in thickness and therefore had an outer diameter of 71.77 cm.

A reflector region containing control drums was the next modeled region of the core in a radially outward direction. For an initial approximation the beryllium reflector was assumed to have a thickness of three mean free paths. A mean free path is defined by the average distance that a neutron moves between collisions. Equation (B.8) expresses this relationship:

$$\lambda = 1/\Sigma_t \tag{B.8}$$

where,

λ = mean free path
Σ_t = total macroscopic cross section.

By making the simplification for the beryllium reflector that the microscopic absorption cross section ($\sigma_{a_{Be}}$) was negligible compared with the scattering cross section, Equation (B.8) can be approximated by:

$$\lambda = 1/\Sigma_s \tag{B.9}$$

where,

Σ_s = macroscopic scattering cross section
and all other terms have been previously defined.

Reference B7 gives a value for ($\Sigma_{s_{Be}}$) of 0.7589 cm^{-1}. Therefore, the thickness of this reflector region was approximated to be 28.56 cm with an outer diameter of 128.89 cm.

To allow for the control drums the reflector region was subdivided into three subregions. Two subregions, one of which was an innermost concentric circle and one an outermost concentric circle, both with a thickness of 0.5 cm modeled the control drum. The concentration of B_4C was varied in these two regions to simulate positioning of the control drum.

The outermost region of the wire core model is the pressure vessel. This pressure shell composed of stainless steel was taken to be 2.0 cm thick. Therefore, the initial approximation for the outer diameter of the wire core was 132.89 cm. Table B4 gives the relative dimensions as well as the material constituents by region for the model.

Table B4

Wire Core Regions - Material Constituents and Dimensions

Region	Material Constituents	Area (cm^2)	Outer Diameter (cm)
Inlet Hole	Hydrogen	63.6	9.0
Inlet Frit	Aluminum Hydrogen	14.9	10.0
Fuel Region	UN Tungsten Hydrogen	3,297.4	66.42
Exit Duct	Hydrogen	352.7	69.77
Liner	Carbon Steel	219.2	71.77
Reflector with Control Drums	Beryllium B_4C	8,912.3	128.89
Pressure Shell	Stainless Steel	816.1	132.89

After these two dimensional calculations were performed, the next step was to calculate the overall mass of the materials by extending the results in the axial direction. Also, two hemispherical ends were added to the pressure vessel to consider it in its entirety. As an initial approximation all material constituents in each of the regions were considered to be uniformly distributed in the axial direction.

In the calculation of pressure vessel mass, the volume of a hemisphere can be found from:

$$V = 1/6 \ \pi h\left(3a^2 + h^2\right) \qquad (B.10)$$

where,

V = total volume of hemisphere
a = radius of the base
h = height from the center of the base.

Figure B2 depicts the modeled geometry for the hemispherical ends. The surface area was determined as follows:

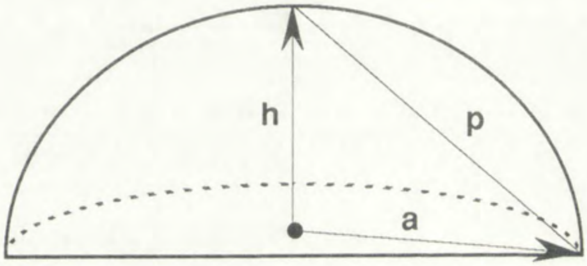

Figure B2 Wire Core Pressure Vessel Hemispherical Ends

$$S=\pi\ p^2 \tag{B.11}$$

where,

S = surface area of a hemisphere
p = is as depicted in Figure B2.

Equation (B.10) was modified to obtain the following:

$$V=\frac{1}{6}\pi\left[3a^2(h_o-h_i)+h_o{}^3-h_i{}^3\right] \tag{B.12}$$

where,

V = volume of one hemispherical end
a = radius of the wire core

h_o = height to the outer surface of the hemispherical end
h_i = height to the inner surface of the hemispherical end.

The thickness of the pressure vessel was assumed to be uniform. Therefore, the total volume of hemispherical ends was determined to be 34,496 cm^3.

The volume of all regions within the cylindrical portion of the reactor was calculated as follows:

$$V = \pi h \left(r_o^2 - r_i^2\right) \qquad \text{(B.13)}$$

where,

V = volume of a given core region
h = height of the cylindrical portion of the core
r_o = outer radius of a given core region
r_i = inner radius of a given core region.

Table B5 gives the volume of each of the regions for the wire core. The mass by constituent is shown in Table B6.

Table B5

Wire Core Regions - Volume

Zone	Area Description	Volume (cm^3)
1	Inlet Hole	6,731
2	Inlet Frit	1,579
3	Fuel	358,274
4	Exit Duct	38,028
5	Liner	23,525
6	Reflector (Drums In)	12,012
7	Reflector	403,816
8	Reflector (Drums Out)	16,832
9	Pressure Vessel	86,237

Table B6

Wire Core Mass by Constituent

Zone	Material	Mass (kg)
Frit	Aluminum	10.45
Fuel	UN	612.75
	Tungsten	1,045.59
Liner	Carbon Steel	37.64
Reflector	Beryllium	769.28
	B_4C	
Pressure Vessel	Stainless Steel -304	42.42

This initial configuration served as the starting point for the computer-based criticality and dimension determination analysis which will be described in Section B.2.

B.2 Criticality, Safety Margin, and Configuration Analysis

This computer-aided analysis utilized the FEMP1D code (Ref. B8). FEMP1D stands for **F**inite **E**lement, **M**ulti-Group, **P_N**, **1-D**imensional code. The code approximates the Boltzmann transport equation in one dimension using a spherical harmonic basis for the angular variable and a linear finite element (hat function) basis for the spatial variable. The energy variable is dealt with by the fairly standard multigroup approximation. In rectangular and spherical coordinates, the spherical harmonic basis reduces to the Legendre polynomials.

FEMP1D solves a number of steady state neutral particle radiation transport problems based on the Boltzmann model for the energy dependent, angular flux density conservation equation. The steady state Boltzmann transport equation for the multi-dimensional energy and angular dependent angular flux density is given by:

$$\begin{aligned}&\nabla \bullet \Omega\Psi(\bar{r},E,\Omega) + \Sigma_T(\bar{r},E,\Omega)\Psi(\bar{r},E,\Omega) = S(\bar{r},E,\Omega)\\ &\quad + \int_{E'}\int_{\Omega'}\Sigma_S(\bar{r},E',\Omega' > E,\Omega)\Psi(\bar{r},E',\Omega')dE'\,d\Omega' \qquad \text{(B.14)}\\ &\quad + \int_{E'}\int_{\Omega'}\frac{\chi(E)}{4\pi}\upsilon\Sigma_f(\bar{r},E)\Psi(\bar{r},E',\Omega')dE'\,d\Omega'\end{aligned}$$

where,

$\psi(\hat{r},E,\Omega)$ = neutron angular flux density

$\Sigma_T(\hat{r},E)$ = total interaction cross section

$\Sigma_S(\hat{r},E',\Omega' > E,\Omega)$ = scattering cross section for transfer from energy E' and angle Ω', to energy E and angle Ω

$\chi(E)\upsilon\Sigma_f(\hat{r},E')$ = number of neutrons produced per fission at energy E times the fission cross section for a neutron of energy E'

$S(\hat{r},E,\Omega)$ = the time independent source of neutrons at position r, with energy E, and moving in direction Ω.

The spatial, energy and angle discretized equations can be written in the following symbolic matrix equation:

$$[M]\{\phi\} = \{S\} + (1/k)[F]\{\phi\} \qquad \text{(B.15)}$$

where **M** is the migration matrix that considers the effects of transfers between groups and transport in the spatial dimension. The **S** vector is the inhomogeneous source. The **F** matrix is the fission source matrix and corresponds to the generation of neutrons as a result of fission. The eigenvalue **k** must be introduced if a solution is desired for the pure eigenvalue problem, where {**S**} equals zero. It should be kept in mind that though the set of equations solved only considers one spatial dimension, the equations are actually the solution to a three dimensional problem in space, angle, and energy.

After completing the determination of initial dimensions, material constituents, mass, and volume for the wire core, the FEMP1D code was utilized to calculate the core and fuel region dimensions necessary to attain a critical configuration.

As well as the initial dimensions given in Section B.1, a calculation of number density for all materials was required. Since this calculation was rather straightforward no details will be given. The uranium enrichment was assumed to 93 percent. Table B7 gives the results of this calculation. The initial input deck was now assembled from both Tables B4 and B7.

Table B7

Wire Core Constituent Number Densities by Region

Core Region	Material	Number Density $\left(\frac{\text{atom}}{\text{barn} \bullet \text{cm}}\right)$
Inlet Hole	Hydrogen (H_2)	4.96E–3
Inlet Frit	H_2	3.42E–4
	Aluminum (Al)	3.92E–2
Fuel Region	UN (U^{28})	6.13E–4
	(U^{25})	8.15E–3
	(N)	8.76E–3
	Tungsten (W^{182})	2.52E–3
	(W^{183})	1.38E–3
	(W^{184})	2.93E–3
	(W^{186})	2.72E–3
	H_2	1.95E–4
Exit Duct	H_2	1.65E–4
Liner	Carbon Steel (C)	8.02E–2
Reflector	Beryllium (Be)	1.24E–1
	B_4C (B^{10})	2.17E–2
	(B^{11})	8.81E–2
	(C)	2.75E–2
Pressure Shell	Stainless Steel (Fe-74%, Cr-18%, Ni-8%) (Fe)	6.27E–2
	(Ni)	7.30E–3
	(Cr)	1.48E–2

To account for differences in diffusion of neutrons between regions containing only relatively low density hydrogen (e.g., inlet hole and exit duct) and other regions of the reactor, a buckling height correction calculation was performed. The following equation expresses the relationship between diffusion length and buckling:

$$L_f \;\alpha\; D \; B_{tr}^2 \qquad \text{(B.16)}$$

where,

L_f = diffusion length

D = diffusion coefficient

B_{tr}^2 = buckling.

Buckling is defined as a measure of curvature of the flux profile. The diffusion coefficient D is defined as follows:

$$D = \frac{1}{3\Sigma_{tr}} \qquad \text{(B.17)}$$

where,

Σ_{tr} = macroscopic transport equation.

For an infinite cylindrical core:

$$B_{tr}^2 \cong \left(\frac{\pi}{H}\right)^2 \qquad \text{(B.18)}$$

where,

H = height of the core region.

Equations (B.16) through (B.18) can be combined to obtain:

$$N_f H_f^2 = N_H \, H_H^2 \qquad \text{(B.19)}$$

where,

N_f = number density of the fuel
H_f = height of fuel region
N_H = number density of hydrogen in either the inlet hole or exit duct
H_H = height of either the inlet hole or exit duct.

Rearranging Equation (B.19) yields:

$$H_H = H_f \left(\frac{N_f}{N_H} \right)^2 \quad . \qquad \text{(B.20)}$$

Now calculating the buckling height correction factor was a relatively simple process. Utilizing the number densities given in Table B4 yielded a buckling height correction factor of 3.16. For FEMP1D this is input into the 35 $ array. As an initial estimate of core height for the 35 $ array, the radius of the core was doubled.

The cross section library employed in the criticality analysis had a 47 energy group structure for neutrons and a 20 energy group structure for gammas. The mesh points for each of the regions were set to be less than one mean free path in separation. A sample input deck is provided in Appendix E. For further details on input deck construction refer to Reference B8.

An initial criticality computation was now performed. This calculation was a seven zone problem deleting the control drum regions. Also, the initial buckling correction factor employed was 100. This preliminary computation did not converge to a K_{eff} of 1.0. The actual K_{eff} found was 1.49.

In the next computation, the thickness of the beryllium reflector was reduced to 15.0 cm. Also, the number of mesh points in the reflector were doubled and a buckling height correction of 3.16 was employed. Modification of the dimensions of the reflector also reduced the core diameter to 105.78 cm. The height of core was decreased as well but still kept as two times the radius. These modifications resulted in a K_{eff} of 1.17.

For the third computer run, two additional regions were added. As described in Section B.1, control drums were considered. For this computation naturally occurring concentrations of B^{10} and B^{11} were employed in the B_4C control drums. To simulate the control drums being turned outward, B_4C was only allowed in the zone on the outside of the reflector. With these modifications K_{eff} was determined to be 1.16.

In the next analysis, 100 percent B^{10} was utilized in the B_4C control drums. As in the third run B_4C was modeled only in the zone on the outside of the reflector. This sensitivity analysis also yielded a K_{eff} of 1.16. Therefore, whether naturally occurring or enriched B_4C control drums were utilized, it had only a marginal effect on this wire core configuration.

For the fifth run, the control drums were still assumed to contain 100 percent B^{10}. However, the B_4C was now positioned inside the reflector to simulate the control drums turned fully inward. This configuration yielded a K_{eff} of 1.06.

An additional sensitivity analysis on boron concentration was now performed. This analysis modeled control drums rotated inward with naturally occurring boron. K_{eff} was found to be approximately 1.10. Therefore, whether the control drums were rotated inward or outward determined whether increasing B^{10} concentration from 19.8 percent to 100 percent had any effect on K_{eff}. In the outward direction only a negligibly small change occurred, while in the inward direction a 3.6 percent difference in K_{eff} was calculated.

Since a subcritical configuration could not be obtained with the control drums rotated in the inward direction, a sensitivity analysis was performed by varying hydrogen concentration in the inlet hole, inlet frit, fuel, and exit duct regions. For this sensitivity analysis, the modeled configuration was naturally occurring boron control drums rotated in the outward direction. Table B8 presents the results obtained by varying hydrogen concentration. This analysis was used to determine by what factor hydrogen concentration would have to be reduced to obtain a K_{eff} of approximately 1.05 with the control drums rotated in the outward direction. As can be seen from Table B8 the hydrogen concentration reduction factor obtained was 2.2.

Table B8

Sensitivity Analysis - Varying H_2 Concentration
With Control Drums Rotated Outward

Run #	Hydrogen Concentration Reduction Factor	K_{eff}
1	20.0	0.879
2	4.0	0.985
3	2.0	1.072
4	2.5	1.031
5	2.25	1.047
6	2.2	1.050

Next, the control drums were modeled as being rotated inward. This model employed the hydrogen concentration reduction factor of 2.2 that was obtained from the previous sensitivity analysis. Also, as in the sensitivity analysis a naturally occurring concentration of B^{10} was modeled for the control drums. This computer run resulted in a K_{eff} of 1.02. Once again a subcritical configuration was not obtained.

Another sensitivity analysis was now performed. In this analysis and all other computer runs which are described subsequently, only natural concentrations of B^{10} in the B_4C control drums were modeled. For the base case analysis, the hydrogen concentration reduction factor was not utilized.

Therefore, hydrogen concentrations for the inlet hole, inlet frit, fuel, and exit duct regions were set to the values initially modeled. Buckling height correction factors for the inlet hole and exit duct regions were set to 0.0. Also, the control drums were modeled as being rotated in the outward direction. Hydrogen concentrations were now varied in the inlet hole, inlet frit, fuel, and exit duct regions to determine the effect of this modification on K_{eff}. Table B9 presents the results of this sensitivity study. As can be seen from Table B9 even relatively large reductions in hydrogen concentration had only a minimal effect on K_{eff} with control drums modeled as being rotated radially outward. The results of both sensitivity analyses which varied hydrogen concentration indicated that core as modeled to this point contained too much fuel. Therefore, FEMP1D was employed in the dimension search mode.

Table B9

Sensitivity Analysis – Varying H_2 Concentration with Control Drums Rotated Outward and Buckling Height Correction Factor Set to 0.0

Run #	Hydrogen Concentration Reduction Factor	K_{eff}
1	1.0	1.354
2	20.0	1.353
3	2,000.0	1.337

A material outer dimension search was now conducted. This search is an order of magnitude estimate for the amount of fissile material required for a critical assembly. It is simply an expansion of all boundaries by a constant factor to obtain a desired K_{eff}. An example input deck for the material outer dimension search is provided in Appendix E. For the base case run, the model employed was from the third computer run which was previously described in this appendix. To summarize, the reflector thickness was taken to be 15.0 cm and the buckling height correction factor was set to 3.16. The control drums were modeled as being rotated outward. Also, mesh points within the reflector region were doubled and no hydrogen concentration reduction was employed. This initial dimension search and all other iterations were seeking to obtain the area reduction factor for the fuel region which would yield a K_{eff} of 1.05 with the control drums modeled as rotated radially outward. A fuel region reduction factor of 0.755 was found in this initial dimension search.

Four computer-aided iterations were required to obtain a final reduction factor for the fuel region. As previously discussed, FEMP1D calculates a modification of dimensions factor that is applicable for all regions. However, it was obvious from the reduction of hydrogen concentration sensitivity studies, that only the amount of fissile material needed to be reduced. In fact to obtain the required thrust as specified in Section B.1, the exit duct and inlet hole areas should remain constant. Also, structural portions of the core such as the inlet frit, liner, control drums, and pressure vessel should not have their dimensions reduced as well. Therefore, the relative dimensions of all other regions except for the fuel were kept constant throughout this iterative process. The diameter of core varied from iteration to iteration. Therefore, the core height was also modified to keep it at a constant factor of two greater than the radius. Table B10 gives the results of this fuel region dimension search process. After four iterations, it appeared that the dimension search was converging to 0.86 of the initial fuel region dimensions. Therefore, to expedite this process a reduction factor of 0.86 was chosen and another computer run was performed. This resulted in a reduction multiplier from this approximation of 0.99. Convergence was so close that this new fuel region size of 86.0 percent of the initial area was utilized to determine a value for K_{eff} with the control rods rotated fully inward. This computation yielded a K_{eff} of 0.993 and was the first model which resulted in a subcritical configuration with the control drums fully inward.

Table B10

Fuel Region Dimension Search

Run #	Reduction Factor	Cumulative Reduction Factor
1	0.755	0.755
2	1.241	0.937
3	0.853	0.799
4	1.145	0.915

Now other modifications to wire core model were undertaken. First and most importantly, the UN fuel density was increased from 13.0 g/cm^3 to 14.32 g/cm^3 based on Reference B9. The pressure vessel was now taken to be constructed of aluminum to reduce the overall structural weight. Also, a 2.0 cm thick beryllium top reflector and 5.0 cm thick carbon steel bottom reflector were modeled. The core inlet temperature was also increased to 200°K to be consistent with the NERVA small engine and particle bed models.

Due to these modifications, a dimension search once again needed to be performed. However, as initial conditions for this fuel region adjustment, the 14 percent reduction already calculated was utilized as the computational starting configuration. The correspondent reduction in core height was also employed. As was the case in the previous dimension search analysis only the fuel area and core height were varied while all other regions were kept constant. Table B11 presents the results of this analysis. With the four iterations as illustrated in Table B11, K_{eff} converged to 1.017.

Now as in the previous dimension search, K_{eff} with the control drums modeled as rotated fully inward was determined. The fuel area reduction factors from the two sets of dimension searches were combined. This combined reduction factor was 0.756 of the initial base case analysis from computer run number three. K_{eff} was found to be 0.959.

Table B11

Fuel Region Dimension Search – Fuel Density Increased by 10 Percent

Run #	Reduction Factor	Cumulative Reduction Factor
1	0.871	0.871
2	1.072	0.930
3	0.961	0.894
4	0.984	0.879

Therefore, some final adjustments to fuel region dimensions were undertaken to still insure adequate shutdown margin, but also to allow enough positive reactivity with the control drums fully outward for rapid startup capability. Six additional calculations were performed which ultimately added another 0.6 cm in the radial dimension to the fuel region.

Once these computer–aided computations were completed, a recalculation of the wire core mass was performed. Table 9 in Chapter 3 gives the final dimensions and masses by region for the wire core model. These dimensions were utilized in the startup strategy comparison analysis which was described in Chapters 4 and 5. As can be seen from Table 9, if aluminum is utilized for the pressure vessel, the mass for total assembly is reduced by 18.8 percent to 1809 kg. As a comparison, the NERVA small engine mass is 2550 kg (Ref. B1).

The wire core model obtained by analytical and computer–aided analysis was used to calculate the response time constants employed in the startup comparison for the Reusable Orbital Transfer Vehicle. Response time constants for the particle bed and NERVA reactors were derived primarily from the literature review that was described in Chapter 1 and Appendix A.

B.3 REFERENCES

B1. Koenig, D., Experience gained from the space nuclear rocket program (Rover), LA-10062-H, May, 1986.

B2. Sutton, G., Rocket propulsion elements - an introduction to the engineering of rockets, Sixth edition, Wiley-Interscience, 1992.

B3. NERVA engineering and design concepts, reactor design configuration, Volume 1, Westinghouse Electric Co., Pittsburg, PA, June, 1968.

B4. Trade study for NERVA support plate and plena design concepts, Westinghouse Electric Co., Pittsburg, PA, December, 1969.

B5. Powell, J., and Botts, T., Particle bed reactors for space power and propulsion, Brookhaven National Lab, Upton, NY, 1984.

B6. Feddersen, R., and Coiner, J., Conceptual design of a category III multimegawatt space nuclear power system, 24th Intersociety Energy Conversion Engineering Conference, Washington, DC, August, 1989.

B7. LaMarsh, J., Introduction to nuclear engineering, Second edition, Addison-Wesley, 1983.

B8. McDaniel P., FEMP1D user's manual, PL/WSA, February, 1993.

B9. Ross, S., Uranium nitride swelling and thermal conductivity correlations, Master's thesis, University of New Mexico, December, 1985.

APPENDIX C

LISTING OF THE
STRTUP
COMPUTER
PROGRAM

```
      PROGRAM DKCOOL
C
C  TITLE CARD
C
C   'POWR'
C
C     P0,BEFF,GTIM,DT0,NP
C     T20,PR0,POWD,T2D,PRD,TC,TPT,TM,TD(1)-TD(6)
C     WDOT,CPH,T1
C
C       P0=Initial Power in Watts
C       T20=Initial Temperature
C       PR0=Initial Pressure
C       POWD=Design Power
C       T2D=Design Temperature
C       PRD=Design Pressure
C       TC=Temperature Time Constant
C       TPT=Turbopump Time Constant
C       TM=Neutron Kinetics Time Constant
C       TD(1)-TD(6)=Delayed Neutron Time Constants
C       WDOT=Coolant Weight Flow Rate
C       CPH=Coolant Specific Heat Capacity
C       T1=Core Inlet Temperature
C       BEFF=Beta Effective For the Reactor
C       GTIM=Generation Time For The Reactor
C       DT0=Integration Time Step In Seconds
C       NP=Number of Print Intervals
C
C     P(1),RO(1,1),RO(2,1),T(1),TP(1)
C     P(2),RO(1,2),RO(2,2),T(2),TP(2)
C       .    .    .
C       .    .    .
C       .    .    .
C       .    .    .
C     P(NP),RO(1,NP),RO(2,NP),T(NP),TP(NP)
C
C       P(K)=Desired Power For The Kth Interval
C       RO(1,K)=Minimum Reactivity For The Kth Interval
C       RO(2,K)=Maximum Reactivity For The Kth Interval
C       T(K)=Time In Seconds That The Kth Interval Lasts
C       TP(K)=Time Between Print Outs During Kth Interval
C
C   'NEUT'
C
C     NN,(AN(I),TIN(I),I=1,NN)
C
C       NN=Number Of Delay Neutron Families
C       AN(I)=Delayed Fission Yield For Ith Family
C       TIN(I)=Decay Constant For Ith Delalyed Family
C       (If This Block Is Not Entered, Default Data Used)
C
C   'GAMM'
C
C     NG,(AG(I),TIG(I),I=1,NG)
C
```

```
C       NG=Number Of Delay Gamma Families
C       AG(I)=Delayed Fission Yield For Ith Family
C       TIG(I)=Decay Constant For Ith Delalyed Family
C       (If This Block Is Not Entered, Default Data Used)
C
C    'BETA'
C
C     NB,(AB(I),TIB(I),I=1,NB)
C
C       NB=Number Of Delay Beta Families
C       AB(I)=Delayed Fission Yield For Ith Family
C       TIB(I)=Decay Constant For Ith Delalyed Family
C       (If This Block Is Not Entered, Default Data Used)
C
C    'STAR'
C
C     Begin the computation
C
C
C
C
      COMMON/LU/LU1,LU2,LU3,LU4,LU5,LU6,LU7,LU8
      COMMON/POWR/P0,BEFF,GTIM,DT0,TMINPR,NP,
     1 P(20),RO(2,20),RM(20),T(20),TP(20),ENK(20),
     2 T20,PR0,POWD,T2D,PRD,TC,TPT,TM,WDOT,CPH,T1
      COMMON/NEUT/NN,AN(10),TIN(10),YN(10),TD(6)
      COMMON/GAMM/NG,AG(20),TIG(20),YG(20)
      COMMON/BETA/NB,AB(20),TIB(20),YB(20)
      COMMON/SYST/K,DT,TF,LPP,LDGP,LDBP,LY1,LY2,LDY,LW,
     1 YNU,PPC,DPC,LIM
      COMMON/TITL/TITLE(80)
      CHARACTER*1 TITLE
      DIMENSION BC(2000)
      LIMIT=2000
      LU1=1
      LU2=2
      LU3=3
      LU4=4
      LU5=5
      LU6=6
    1 CONTINUE
      READ(LU5,1000,END=2) TITLE
 1000 FORMAT(80A1)
      WRITE(LU6,2000) TITLE
 2000 FORMAT(//,1X,80A1)
      CALL INPUT(BC,NEQ)
      CALL SOLVER(BC,NEQ)
      GO TO 1
    2 CONTINUE
      END
C
C
C
      SUBROUTINE INPUT(BC,NEQ)
C
C  READS THE INPUT DATA FOR THIS CASE
```

```
C
C
C
      COMMON/LU/LU1,LU2,LU3,LU4,LU5,LU6,LU7,LU8
      COMMON/POWR/P0,BEFF,GTIM,DT0,TMINPR,NP,
     1 P(20),RO(2,20),RM(20),T(20),TP(20),ENK(20),
     2 T20,PR0,POWD,T2D,PRD,TC,TPT,TM,WDOT,CPH,T1
      COMMON/NEUT/NN,AN(10),TIN(10),YN(10),TD(6)
      COMMON/GAMM/NG,AG(20),TIG(20),YG(20)
      COMMON/BETA/NB,AB(20),TIB(20),YB(20)
      COMMON/SYST/K,DT,TF,LPP,LDGP,LDBP,LY1,LY2,LDY,LW,
     1 YNU,PPC,DPC,LIM
      COMMON/TITL/TITLE(80)
      CHARACTER*1 TITLE
      CHARACTER*4 DATA,POWR,NEUT,GAMM,BETA,STAR
      DATA POWR,NEUT,GAMM,BETA,STAR
     1 /'POWR','NEUT','GAMM','BETA','STAR'/
C
C  INITIALIZE WITH DEFAULT VALUES
C
      CALL DEFALT
    1 CONTINUE
      READ(LU5,1000) DATA
 1000 FORMAT(A4)
C
C  READ THE POWER AND REACTIVITY DATA
C
      IF(DATA.EQ.POWR) THEN
        READ(LU5,*) P0,BEFF,GTIM,DT0,NP
        WRITE(LU6,2000) P0,BEFF,GTIM,DT0,NP
 2000   FORMAT(/,5X,1PE12.4,' P0   INITIAL POWER LEVEL(W)',/,
     1  5X,E12.4,' BEFF  BETA EFFECTIVE FOR REACTOR',/,
     2  5X,E12.4,' GTIM  GENERATION TIME FOR THE REACTOR(SEC)',/,
     3  5X,E12.4,' DT0   INTEGRATION STEP SIZE(SEC)',/,
     4  5X,  I12,' NP    NUMBER OF DIFFERENT POWER INTERVALS',/)
        READ(LU5,*) T20,PR0,POWD,T2D,PRD,TC,TPT,TM,WDOT,CPH,T1
        WRITE(6,2002) T20,PR0,POWD,T2D,PRD,TC,TPT,TM,WDOT,CPH,T1
 2002   FORMAT(/,5X,1PE12.4,'T20  INITIAL TEMPERATURE(K)',/,
     1  5X,E12.4,'PR0  INITIAL PRESSURE(PA)',/,
     2  5X,E12.4,'POWD   DESIGN POWER(W)',/,
     3  5X,E12.4,'T2D   DESIGN TEMPERATURE(K)',/,
     4  5X,E12.4,'PRD   DESIGN PRESSURE(PA)',/,
     5  5X,E12.4,'TC   TEMP TIME CONSTANT(S)',/,
     6  5X,E12.4,'TPT   PUMP TIME CONSTANT(S)',/,
     7  5X,E12.4,'TM   NEUT TIME CONSTANT(S)',/,
     8  5X,E12.4,'WDOT   WEIGHT FLOW RATE(KG/S)',/,
     9  5X,E12.4,'CPH   COOL SPEC HEAT(J/KG*K)',/,
     10 5X,E12.4,'T1   INLET TEMPERATURE(K)',/)
        DO 10 K=1,NP
          READ(LU5,*) P(K),RO(1,K),RO(2,K),RM(K),T(K),TP(K)
          WRITE(LU6,2001) K,P(K),RO(1,K),RO(2,K),RM(K),T(K),TP(K)
 2001     FORMAT(6X,I5,1P6E12.4)
   10   CONTINUE
C
C  READ THE NEUTRON PARAMETERS
C
```

```
      ELSE IF(DATA.EQ.NEUT) THEN
        READ(LU5,*) NN,(AN(I),TIN(I),I=1,NN)
C
C  READ THE GAMMA DECAY PARAMETERS
C
      ELSE IF(DATA.EQ.GAMM) THEN
        READ(LU5,*) NG,(AG(I),TIG(I),I=1,NG)
C
C  READ THE BETA DECAY PARAMETERS
C
      ELSE IF(DATA.EQ.BETA) THEN
        READ(LU5,*) NB,(AB(I),TIB(I),I=1,NB)
      ELSE IF(DATA.EQ.STAR) THEN
        GO TO 2
      ENDIF
      GO TO 1
C
C  ALLOCATE STORAGE
C
    2 CONTINUE
      NEQ=1+NN+NG+1+NB+1+2
      LPP=1
      LDGP=LPP+NN+NG+1
      LDBP=LDGP+NB+1
      LY1=1
      LY2=LY1+NEQ
      LDY=LY2+NEQ
      LW=LDY+NEQ
      LIM=LW+6*NEQ
      RETURN
      END
C
C
C
      SUBROUTINE SOLVER(BC,NEQ)
C
C  SOLVES THE SYSTEM EQUATIONS IN TIME
C
C
      COMMON/LU/LU1,LU2,LU3,LU4,LU5,LU6,LU7,LU8
      COMMON/POWR/P0,BEFF,GTIM,DT0,TMINPR,NP,
     1 P(20),RO(2,20),RM(20),T(20),TP(20),ENK(20),
     2 T20,PR0,POWD,T2D,PRD,TC,TPT,TM,WDOT,CPH,T1
      COMMON/NEUT/NN,AN(10),TIN(10),YN(10),TD(6)
      COMMON/GAMM/NG,AG(20),TIG(20),YG(20)
      COMMON/BETA/NB,AB(20),TIB(20),YB(20)
      COMMON/SYST/K,DT,TF,LPP,LDGP,LDBP,LY1,LY2,LDY,LW,
     1 YNU,PPC,DPC,LIM
      COMMON/TITL/TITLE(80)
      CHARACTER*1 TITLE
      DIMENSION BC(1)
      N=0
      TT=0.0
      DT=GTIM/(AMAX1(ABS(RO(1,1)-1.0),ABS(RO(2,1)-1.0))*BEFF)
      TPRT=TT+TP(1)
      TF=TT+T(1)
```

```
     CALL INIT(TT,BC(LY1),BC(LDY),NEQ)
     WRITE(6,3000)
3000 FORMAT(1H1,//,5X,'TIME',3X,'REACTIVITY',1X,'TOT. POWER',1X,
    1 'PROMPT PWR',2X,'ENERGY(K)',2X,'DKGAM PWR',2X,'DKBET PWR',
    2 2X,'OUTL TEMP',2X,'INP PRESS')
     PPWR=PPC*BC(LY1)/GTIM/YNU
     DGPWR=DPC*BC(LDGP)
     DBPWR=DPC*BC(LDBP)
     DKPWR=DGPWR+DBPWR
     PWR=PPWR+DKPWR
     P1=PWR
     ENK(1)=0.0
     RHO=0.0
     T2=T20
     PR=PR0
     WRITE(LU6,2000) TT,RHO,PWR,PPWR,ENK(K),DGPWR,DBPWR,T2,PR
2000 FORMAT(F11.2,1P8E11.3)
   1 CONTINUE
       IF(PPWR.GE.0.01*DKPWR) THEN
         CALL RKF34M(BC(LY1),BC(LY2),BC(LDY),BC(LW),NEQ,TT,DT,ERR)
       ELSE
         CALL DIS(BC(LY1),BC(LY2))
       ENDIF
       N=N+1
       IF(N.GT.10000000) GO TO 2
       TT=TT+DT
       IF(TT.GE.TPRT) THEN
         PPWR=PPC*BC(LY1)/GTIM/YNU
         DGPWR=DPC*BC(LDGP)
         DBPWR=DPC*BC(LDBP)
         DKPWR=DGPWR+DBPWR
         PWR=PPWR+DKPWR
         T2=BC(32)
         PR=BC(33)
         ENK(K)=ENK(K)+0.5*TP(K)*(P1+PWR)
         P1=PWR
         RHO=RHOF(PWR,P(K),RO(1,K),RO(2,K),RM(K))
         WRITE(LU6,2000) TT,RHO,PWR,PPWR,ENK(K),DGPWR,DBPWR,T2,PR
         TPRT=TPRT+TP(K)
         IF(PPWR.LE.0.01*DKPWR) DT=TP(K)
       ENDIF
       CALL SCOPY(NEQ,BC(LY2),1,BC(LY1),1)
       IF(TT.GE.TF) THEN
         K=K+1
         IF(K.GT.NP) GO TO 2
         ENK(K)=0.0
         P1=PWR
         DT=GTIM/(AMAX1(ABS(RO(1,K)-1.0),ABS(RO(2,K)-1.0))*BEFF)
         TPRT=TF+TP(K)
         TF=TT+T(K)
         IF(PPWR.GE.0.01*DKPWR) CALL SYSEQ(TT,BC(LY1),BC(LDY),NEQ)
       ENDIF
       GO TO 1
   2 CONTINUE
      WRITE(LU6,2002) (K,ENK(K),K=1,NP)
2002 FORMAT(/,5X,'INTERVAL ENERGY CALCULATION',//,
```

```
     1 (10X,'INT= ',I3,1PE12.4,' JOULES'))
      RETURN
      END
C
C
C
      SUBROUTINE INIT(TZ,Y,DY,NEQ)
C
C  INITIALIZES THE STATE VARIABLES AND CALCULATES THE FIRST DERIVATIVES
C
      COMMON/LU/LU1,LU2,LU3,LU4,LU5,LU6,LU7,LU8
      COMMON/POWR/P0,BEFF,GTIM,DT0,TMINPR,NP,
     1 P(20),RO(2,20),RM(20),T(20),TP(20),ENK(20),
     2 T20,PR0,POWD,T2D,PRD,TC,TPT,TM,WDOT,CPH,T1
      COMMON/NEUT/NN,AN(10),TIN(10),YN(10),TD(6)
      COMMON/GAMM/NG,AG(20),TIG(20),YG(20)
      COMMON/BETA/NB,AB(20),TIB(20),YB(20)
      COMMON/SYST/K,DT,TF,LPP,LDGP,LDBP,LY1,LY2,LDY,LW,
     1 YNU,PPC,DPC,LIM
      COMMON/TITL/TITLE(80)
      CHARACTER*1 TITLE
      DIMENSION Y(*),DY(*)
      DATA YNU,PPC,DPC/2.5,28.8E-12,1.602E-13/
      K=1
      DT=DT0
      L=1
      Y(L)=GTIM*YNU*P0/PPC
C
C  CALCULATE NEUTRON DECAY PARAMETER AVERAGES
C
      TNAV=0.0
      TINAV=0.0
      DO 10 I=1,NN
        L=L+1
        TNAV=TNAV+AN(I)/TIN(I)
        TINAV=TINAV+AN(I)*TIN(I)
        YN(I)=BEFF*AN(I)/GTIM
        Y(L)=YN(I)*Y(1)/TIN(I)
   10 CONTINUE
C
C  CALCULATE GAMMA DECAY PARAMETER AVERAGES
C
      EGFAV=0.0
      SUMG=0.0
      DO 11 I=1,NG
        L=L+1
        EGFAV=EGFAV+AG(I)/TIG(I)
        YG(I)=AG(I)/GTIM/YNU/TIG(I)
        Y(L)=AG(I)*P0/PPC/TIG(I)/TIG(I)
        SUMG=SUMG+TIG(I)*Y(L)
   11 CONTINUE
C
C  CALCULATE BETA DECAY PARAMETER AVERAGES
C
      L=L+1
      Y(L)=SUMG
```

```
      LDGP=L
      EBFAV=0.0
      SUMB=0.0
      DO 12 I=1,NB
        L=L+1
        EBFAV=EBFAV+AB(I)/TIB(I)
        YB(I)=AB(I)/GTIM/YNU/TIB(I)
        Y(L)=AB(I)*P0/PPC/TIB(I)/TIB(I)
        SUMB=SUMB+TIB(I)*Y(L)
   12 CONTINUE
      L=L+1
      Y(L)=SUMB
      LDBP=L
      TINAV=1.0/TINAV
      EGFAV=EGFAV*DPC/PPC
      EBFAV=EBFAV*DPC/PPC
      WRITE(6,2000) BEFF,GTIM,TNAV,TINAV,EGFAV,EBFAV
 2000 FORMAT(//,
     1 5X,1PE12.4,' BEFF  EFFECTIVE DELAYED NEUTRON FRACTION',/,
     1 5X,E12.4,' GTIM  GENERATION TIME(SEC)',/,
     2 5X,E12.4,' TNAV  AVERAGE NEUTRON DECAY TIME(SEC)',/,
     3 5X,E12.4,' TINAV AVERAGE INVERSE NEUTRON DECAY TIME(SEC)',/,
     4 5X,E12.4,' EGFAV DECAY GAMMA ENERGY FRACTION',/,
     5 5X,E12.4,' EBFAV DECAY BETA ENERGY FRACTION')
C
C  ESTIMATE INITIAL OUTLET TEMPERATURE
C
      L=L+1
      T2=T20
      Y(L)=T2
C
C  ESTIMATE INITIAL INLET PRESSURE
C
      L=L+1
      PR=PR0
      Y(L)=PR
C
C  ESTIMATE INITIAL POWER
C
      PPWR=PPC*Y(1)/GTIM/YNU
      DGPWR=DPC*Y(LDGP)
      DBPWR=DPC*Y(LDBP)
      PWR=PPWR+DGPWR+DBPWR
C
C  RENORMALIZE TO INITIAL POWER
C
      FAC=P0/PWR
      DO 5 L=1,NEQ
        Y(L)=Y(L)*FAC
    5 CONTINUE
C
C  CALCULATE INITIAL DERIVATIVES
C
      CALL SYSEQ(TZ,Y,DY,NEQ)
      RETURN
      END
```

```
C
C
C
      SUBROUTINE SYSEQ(TT,Y,DY,NEQ)
C
C EVALUATES THE SYSTEM EQUATIONS FOR THE DECAY MODEL
C
C
      COMMON/LU/LU1,LU2,LU3,LU4,LU5,LU6,LU7,LU8
      COMMON/POWR/P0,BEFF,GTIM,DT0,TMINPR,NP,
     1 P(20),RO(2,20),RM(20),T(20),TP(20),ENK(20),
     2 T20,PR0,POWD,T2D,PRD,TC,TPT,TM,WDOT,CPH,T1
      COMMON/NEUT/NN,AN(10),TIN(10),YN(10),TD(6)
      COMMON/GAMM/NG,AG(20),TIG(20),YG(20)
      COMMON/BETA/NB,AB(20),TIB(20),YB(20)
      COMMON/SYST/K,DT,TF,LPP,LDGP,LDBP,LY1,LY2,LDY,LW,
     1 YNU,PPC,DPC,LIM
      COMMON/TITL/TITLE(80)
      CHARACTER*1 TITLE
      DIMENSION Y(*),DY(*)
      L=1
C
C DELAYED NEUTRON GROUPS
C
      SUMN=0.0
      DO 10 I=1,NN
        L=L+1
        SUMN=SUMN+TIN(I)*Y(L)
        DY(L)=YN(I)*Y(1)-Y(L)/TD(I)
   10 CONTINUE
C
C DELAYED GAMMA GROUPS
C
      SUMG=0.0
      DO 11 I=1,NG
        L=L+1
        SUMG=SUMG+TIG(I)*Y(L)
        DY(L)=YG(I)*Y(1)-TIG(I)*Y(L)
   11 CONTINUE
      L=L+1
      DY(L)=0.0
      Y(L)=SUMG
C
C DELAYED BETA GROUPS
C
      SUMB=0.0
      DO 12 I=1,NB
        L=L+1
        SUMB=SUMB+TIB(I)*Y(L)
        DY(L)=YB(I)*Y(1)-TIB(I)*Y(L)
   12 CONTINUE
      L=L+1
      DY(L)=0.0
      Y(L)=SUMB
C
C PROMPT POWER
```

```
C
      PWR=PPC*Y(1)/YNU/GTIM+DPC*(SUMG+SUMB)
      RHO=RHOF(PWR,P(K),RO(1,K),RO(2,K),RM(K))
      DY(1)=((RHO-1.0)*Y(1))/TM+SUMN
C
C  TEMPERATURE RESPONSE
C
      L=L+1
      PPWR=PPC*Y(1)/GTIM/YNU
      DY(L)=(PPWR/(WDOT*CPH*TC))+((T1-Y(L))/TC)
C
C  PRESSURE RESPONSE
C
      L=L+1
      DY(L)=Y(L)*(SQRT(Y(L-1)/T2D))/TPT-((Y(L)**2.0/PRD)
     1  /(SQRT(Y(L-1)/T2D))*TPT)
      RETURN
      END
C
C
C
      SUBROUTINE DEFALT
C
C  Resets All Major Variables To Their Default Values
C
C
      COMMON/LU/LU1,LU2,LU3,LU4,LU5,LU6,LU7,LU8
      COMMON/POWR/P0,BEFF,GTIM,DT0,TMINPR,NP,
     1 P(20),RO(2,20),RM(20),T(20),TP(20),ENK(20),
     2 T20,PR0,POWD,T2D,PRD,TC,TPT,TM,WDOT,CPH,T1
      COMMON/NEUT/NN,AN(10),TIN(10),YN(10),TD(6)
      COMMON/GAMM/NG,AG(20),TIG(20),YG(20)
      COMMON/BETA/NB,AB(20),TIB(20),YB(20)
      COMMON/SYST/K,DT,TF,LPP,LDGP,LDBP,LY1,LY2,LDY,LW,
     1 YNU,PPC,DPC,LIM
      COMMON/TITL/TITLE(80)
      CHARACTER*1 TITLE
      DIMENSION AND(6),TIND(6),AGD(11),TIGD(11),ABD(11),
     1 TIBD(11),TDD(6)
      DATA AND/0.037,0.221,0.211,0.381,0.108,0.042/
      DATA TIND/0.0127,0.0317,0.115,0.311,1.40,3.87/
      DATA AGD/2.808E-11,6.038E-10,3.227E-8,4.055E-7,8.439E-6,
     1 2.421E-4,1.792E-3,2.810E-2,0.1516,0.4162,0.1053/
      DATA TIGD/7.332E-10,4.335E-8,1.932E-7,1.658E-6,2.147E-5,
     1 2.128E-4,1.915E-3,1.769E-2,1.652E-1,1.266,5.222/
      DATA ABD/6.169E-11,2.249E-9,2.365E-8,2.194E-7,1.140E-5,
     1 1.549E-4,1.991E-3,3.256E-2,0.2227,0.5381,0.1282/
      DATA TIBD/7.953E-10,2.758E-8,2.082E-7,1.846E-6,2.404E-5,
     1 2.337E-4,1.897E-3,1.926E-2,0.1573,1.264,5.196/
      DATA TDD/80.65,32.79,9.01,3.32,0.88,0.33/
C
C
C  Reset problem initial conditions and step sizes
C
      P0=1000.0
      BEFF=0.007
```

```
      GTIM=5.0E-5
      DT0=0.01
      TMINPR=1.0
      T20=200.0
      PR0=100.0
      POWD=3.0E+8
      T2D=2700.0
      PRD=1.2E+7
      TC=0.5
      TPT=1.02
      TM=0.014
      WDOT=8.5
      CPH=1.58E+4
      T1=200.0
C
C  Reset power interval parameters
C
      NP=2
      CALL CLEAR(P,20)
      CALL CLEAR(RO,40)
      CALL CLEAR(T,20)
      CALL CLEAR(TP,20)
      P(1)=1.0E+6
      RO(1,1)=-0.50
      RO(2,1)=0.95
      T(1)=200.0
      TP(1)=TMINPR
      P(2)=0.0
      RO(1,2)=-10.0
      RO(2,2)=0.0
      T(2)=250.0
      TP(2)=TMINPR
C
C  Reset neutron decay parameters
C
      CALL CLEAR(AN,10)
      CALL CLEAR(TIN,10)
      NN=6
      DO 10 I=1,NN
        AN(I)=AND(I)
        TIN(I)=TIND(I)
   10 CONTINUE
C
C  Reset gamma decay parameters
C
      CALL CLEAR(AG,20)
      CALL CLEAR(TIG,20)
      NG=11
      DO 20 I=1,NG
        AG(I)=AGD(I)
        TIG(I)=TIGD(I)
   20 CONTINUE
C
C  Reset beta decay parameters
C
      NB=11
```

```
      CALL CLEAR(AB,20)
      CALL CLEAR(TIB,20)
      DO 30 I=1,NB
       AB(I)=ABD(I)
       TIB(I)=TIBD(I)
   30 CONTINUE
C
C Reset delayed neutron time constants
C
      CALL CLEAR(TD,6)
      ND=6
      DO 40 I=1,ND
       TD(I)=TDD(I)
   40 CONTINUE
      RETURN
      END
C
C
C
      FUNCTION RHOF(PWR,P,ROMIN,ROMAX,RM)
C
C  PROVIDES CONTROL REACTIVITY PROFILE
C
      IF(PWR.LE.P) THEN
       RHOF=AMIN1(ROMAX,RM*(1.0-PWR/P))
      ELSE
       RHOF=AMAX1(ROMIN,RM*(1.0-PWR/P))
      ENDIF
      RETURN
      END
C
C
C
      SUBROUTINE SCOPY(N,A,NA,B,NB)
      DIMENSION A(NA,1),B(NB,1)
      DO 10 I=1,N
       B(1,I)=A(1,I)
   10 CONTINUE
      RETURN
      END
C
C
C
      SUBROUTINE CLEAR(A,N)
      DIMENSION A(N)
      DO 10 I=1,N
       A(I)=0.0
   10 CONTINUE
      RETURN
      END
C
C
C
      SUBROUTINE ET2M(Y1,Y2,DY,W,NEQ,TOLD,DT,EPS)
C
C  EULER-TRAPEZOIDAL INTEGRATION RULE FOR
```

```
C   ORDINARY DIFFERENTIAL EQUATIONS WITH ERROR ESTIMATE
C
      DIMENSION Y1(*),Y2(*),DY(*),W(NEQ,*)
      EPS=0.0
C
C  APPLY EULER RULE
C
      DO 10 I=1,NEQ
        W(I,1)=DY(I)
        Y2(I)=Y1(I)+DT*W(I,1)
        W(I,2)=Y2(I)
   10 CONTINUE
C
C  CONVERGE TRAPEZOIDAL RULE
C
      T=TOLD+DT
      DO 20 J=1,10
        CALL SYSEQ(T,Y2,DY,NEQ)
        DO 21 I=1,NEQ
          W(I,3)=Y2(I)
          Y2(I)=Y1(I)+0.5*DT*(W(I,1)+DY(I))
   21   CONTINUE
        IF(J.GT.1) THEN
          DELY=0.0
          DO 22 I=1,NEQ
            DEL=Y2(I)-W(I,3)
            IF(Y2(I).NE.0.0) DEL=DEL/Y2(I)
            DELY=AMAX1(ABS(DEL),DELY)
   22     CONTINUE
          IF(DELY.LT.0.001) GO TO 25
        ENDIF
   20 CONTINUE
   25 CONTINUE
C
C  ERROR ESTIMATE
C
      DO 30 I=1,NEQ
        W(I,1)=0.1428*(W(I,2)-Y2(I))
        EP=W(I,1)
        IF(Y2(I).NE.0.0) EP=EP/Y2(I)
        EPS=AMAX1(EPS,ABS(EP))
   30 CONTINUE
      EPS=DT*EPS
      RETURN
      END
C
C
C
      SUBROUTINE DIS(Y1,Y2)
C
C  EVALUATES THE SYSTEM EQUATIONS FOR THE DECAY MODEL
C
      COMMON/LU/LU1,LU2,LU3,LU4,LU5,LU6,LU7,LU8
      COMMON/POWR/P0,BEFF,GTIM,DT0,TMINPR,NP,
     1 P(20),RO(2,20),RM(20),T(20),TP(20),ENK(20),
     2 T20,PR0,POWD,T2D,PRD,TC,TPT,TM,WDOT,CPH,T1
```

```
      COMMON/NEUT/NN,AN(10),TIN(10),YN(10),TD(6)
      COMMON/GAMM/NG,AG(20),TIG(20),YG(20)
      COMMON/BETA/NB,AB(20),TIB(20),YB(20)
      COMMON/SYST/K,DT,TF,LPP,LDGP,LDBP,LY1,LY2,LDY,LW,
     1 YNU,PPC,DPC,LIM
      COMMON/TITL/TITLE(80)
      CHARACTER*1 TITLE
      DIMENSION Y1(*),Y2(*)
      L=1
      Y2(L)=0.0
C
C  DELAYED NEUTRON GROUPS
C
      DO 10 I=1,NN
        L=L+1
        Y2(L)=0.0
   10 CONTINUE
C
C  DELAYED GAMMA GROUPS
C
      SUMG=0.0
      DO 11 I=1,NG
        L=L+1
        Y2(L)=Y1(L)*EXP(-TIG(I)*DT)
        SUMG=SUMG+TIG(I)*Y2(L)
   11 CONTINUE
      L=L+1
      Y2(L)=SUMG
C
C  DELAYED BETA GROUPS
C
      SUMB=0.0
      DO 12 I=1,NB
        L=L+1
        Y2(L)=Y1(L)*EXP(-TIB(I)*DT)
        SUMB=SUMB+TIB(I)*Y2(L)
   12 CONTINUE
      L=L+1
      Y2(L)=SUMB
      RETURN
      END
C
C
C
      SUBROUTINE RKF12M(Y1,Y2,DY,W,NEQ,TOLD,DT,EPS)
C
C  FIRST ORDER RUNGE-KUTTA INTEGRATION RULE FOR
C   ORDINARY DIFFERENTIAL EQUATIONS WITH ERROR ESTIMATE
C
      DIMENSION Y1(*),Y2(*),DY(*),W(NEQ,*),B1(2)
      DATA B0/0.5/
      DATA B1/3.90625E-3,9.9609375E-1/
      DATA C1/1.953125E-3/
      EPS=0.0
C
C  FIRST FUNCTION EVALUATION
```

```
C
      BDT=B0*DT
      DO 10 I=1,NEQ
        W(I,1)=DY(I)
        Y2(I)=Y1(I)+BDT*W(I,1)
   10 CONTINUE
      T=TOLD+0.5*DT
      CALL SYSEQ(T,Y2,W(1,2),NEQ)
C
C  SECOND FUNCTION EVALUATION
C
      DO 20 I=1,NEQ
        Y2(I)=Y1(I)+DT*(B1(1)*W(I,1)+B1(2)*W(I,2))
   20 CONTINUE
      T=TOLD+DT
      CALL SYSEQ(T,Y2,DY,NEQ)
C
C  ERROR ESTIMATE
C
      DO 30 I=1,NEQ
        EP=C1*(W(I,1)-DY(I))
        IF(Y2(I).NE.0.0) EP=EP/Y2(I)
        EPS=AMAX1(EPS,ABS(EP))
   30 CONTINUE
      EPS=DT*EPS
      RETURN
      END
C
C
C
      SUBROUTINE RKF23M(Y1,Y2,DY,W,NEQ,TOLD,DT,EPS)
C
C  SECOND ORDER RUNGE-KUTTA INTEGRATION RULE FOR
C   ORDINARY DIFFERENTIAL EQUATIONS WITH ERROR ESTIMATE
C
      DIMENSION Y1(*),Y2(*),DY(*),W(NEQ,*),
     1 A(2),B1(2),B2(3),TE(4)
      DATA A/0.25,0.675/
      DATA B0,B1/0.25,-0.23625,0.91125/
      DATA B2/0.240179574,0.03030303,0.729517396/
      DATA TE/-0.012906846,0.03030303,-0.030216697,0.012820513/
      EPS=0.0
C
C  FIRST FUNCTION EVALUATION
C
      BDT=B0*DT
      DO 10 I=1,NEQ
        W(I,1)=DY(I)
        Y2(I)=Y1(I)+BDT*W(I,1)
   10 CONTINUE
      T=TOLD+A(1)*DT
      CALL SYSEQ(T,Y2,W(1,2),NEQ)
C
C  SECOND FUNCTION EVALUATION
C
      DO 20 I=1,NEQ
```

```
        Y2(I)=Y1(I)+DT*(B1(1)*W(I,1)+B1(2)*W(I,2))
   20 CONTINUE
      T=TOLD+A(2)*DT
      CALL SYSEQ(T,Y2,W(1,3),NEQ)
C
C  THIRD FUNCTION EVALUATION
C
      DO 21 I=1,NEQ
        Y2(I)=Y1(I)+DT*(B2(1)*W(I,1)+B2(2)*W(I,2)+B2(3)*W(I,3))
   21 CONTINUE
      T=TOLD+DT
      CALL SYSEQ(T,Y2,DY,NEQ)
C
C  ERROR ESTIMATE
C
      DO 30 I=1,NEQ
        W(I,1)=TE(1)*W(I,1)+TE(2)*W(I,2)+TE(3)*W(I,3)+TE(4)*DY(I)
        EP=W(I,1)
        IF(Y2(I).NE.0) EP=EP/Y2(I)
        EPS=AMAX1(EPS,ABS(EP))
   30 CONTINUE
      EPS=DT*EPS
      RETURN
      END
C
C
C
      SUBROUTINE RKF34M(Y1,Y2,DY,W,NEQ,TOLD,DT,EPS)
C
C  THIRD ORDER RUNGE-KUTTA INTEGRATION RULE FOR
C   ORDINARY DIFFERENTIAL EQUATIONS WITH ERROR ESTIMATE
C
      DIMENSION Y1(*),Y2(*),DY(*),W(NEQ,*),
     1 A(3),B2(2),B3(3),B4(4),TE(5)
      DATA A/0.285714286,0.4666666667,0.921052632/
      DATA B1,B2/0.285714286,0.0855555556,0.381111111/
      DATA B3/0.557479224,-1.406455023,1.77002843/
      DATA B4/0.16122449,0.0,0.599834528,0.238940982/
      DATA TE/0.005442177,0.0,-0.020683949,0.070797328,-0.0555555556/
      EPS=0.0
C
C  FIRST FUNCTION EVALUATION
C
      BDT=B1*DT
      DO 10 I=1,NEQ
        W(I,1)=DY(I)
        Y2(I)=Y1(I)+BDT*W(I,1)
   10 CONTINUE
      T=TOLD+A(1)*DT
      CALL SYSEQ(T,Y2,W(1,2),NEQ)
C
C  SECOND FUNCTION EVALUATION
C
      DO 20 I=1,NEQ
        Y2(I)=Y1(I)+DT*(B2(1)*W(I,1)+B2(2)*W(I,2))
   20 CONTINUE
```

```
      T=TOLD+A(2)*DT
      CALL SYSEQ(T,Y2,W(1,3),NEQ)
C
C  THIRD FUNCTION EVALUATION
C
      DO 21 I=1,NEQ
        Y2(I)=Y1(I)+DT*(B3(1)*W(I,1)+B3(2)*W(I,2)+B3(3)*W(I,3))
   21 CONTINUE
      T=TOLD+A(3)*DT
      CALL SYSEQ(T,Y2,W(1,4),NEQ)
C
C  FOURTH FUNCTION EVALUATION
C
      DO 22 I=1,NEQ
        Y2(I)=Y1(I)+DT*(B4(1)*W(I,1)+B4(3)*W(I,3)+B4(4)*W(I,4))
   22 CONTINUE
      T=TOLD+DT
      CALL SYSEQ(T,Y2,DY,NEQ)
C
C  ERROR ESTIMATE
C
      DO 30 I=1,NEQ
        W(I,1)=TE(1)*W(I,1)+TE(3)*W(I,3)+TE(4)*W(I,4)+TE(5)*DY(I)
        EP=W(I,1)
        IF(Y2(I).NE.0) EP=EP/Y2(I)
        EPS=AMAX1(EPS,ABS(EP))
   30 CONTINUE
      EPS=DT*EPS
      RETURN
      END
C
C
C
      SUBROUTINE RKF45M(Y1,Y2,DY,W,NEQ,TOLD,DT,EPS)
C
C  FOURTH ORDER RUNGE-KUTTA INTEGRATION RULE FOR
C   ORDINARY DIFFERENTIAL EQUATIONS WITH ERROR ESTIMATE
C
      DIMENSION Y1(*),Y2(*),DY(*),W(NEQ,*),
     1 A(5),B2(2),B3(3),B4(4),B5(5),C(6),TE(6)
      DATA A/0.25,0.375,0.9230769231,1.0,0.5/
      DATA B1,B2/0.25,9.375E-2,2.8125E-1/
      DATA B3/8.79380974E-1,-3.277196177,3.320892126/
      DATA B4/2.032407407,-8.0,7.173489279,-0.2058966862/
      DATA B5/-0.296296296,2.0,-1.381676413,0.4529727096,-0.275/
      DATA C/0.118518519,0.0,0.518986355,0.50613149,-0.18,0.036363636/
      DATA TE/-2.777777778E-3,0.0,2.994152047E-2,2.919989367E-2,
     1 -0.02,-3.636363636E-2/
      EPS=0.0
      BDT=B1*DT
      DO 10 I=1,NEQ
        W(I,1)=DY(I)
        Y2(I)=Y1(I)+BDT*W(I,1)
   10 CONTINUE
C
C  FIRST FUNCTION EVALUATION
```

```
C
     T=TOLD+A(1)*DT
     CALL SYSEQ(T,Y2,W(1,2),NEQ)
     DO 20 I=1,NEQ
       Y2(I)=Y1(I)+DT*(B2(1)*W(I,1)+B2(2)*W(I,2))
  20 CONTINUE
C
C  SECOND FUNCTION EVALUATION
C
     T=TOLD+A(2)*DT
     CALL SYSEQ(T,Y2,W(1,3),NEQ)
     DO 21 I=1,NEQ
       Y2(I)=Y1(I)+DT*(B3(1)*W(I,1)+B3(2)*W(I,2)+B3(3)*W(I,3))
  21 CONTINUE
C
C  THIRD FUNCTION EVALUATION
C
     T=TOLD+A(3)*DT
     CALL SYSEQ(T,Y2,W(1,4),NEQ)
     DO 22 I=1,NEQ
       Y2(I)=Y1(I)+DT*(B4(1)*W(I,1)+B4(2)*W(I,2)
    1               +B4(3)*W(I,3)+B4(4)*W(I,4))
  22 CONTINUE
C
C  FOURTH FUNCTION EVALUATION
C
     T=TOLD+A(4)*DT
     CALL SYSEQ(T,Y2,DY,NEQ)
     DO 23 I=1,NEQ
       Y2(I)=Y1(I)+DT*(B5(1)*W(I,1)+B5(2)*W(I,2)
    1  +B5(3)*W(I,3)+B5(4)*W(I,4)+B5(5)*DY(I))
  23 CONTINUE
C
C  FIFTH FUNCTION EVALUATION
C
     T=TOLD+A(5)*DT
     CALL SYSEQ(T,Y2,W(1,6),NEQ)
     DO 24 I=1,NEQ
       Y2(I)=Y1(I)+DT*(C(1)*W(I,1)+C(3)*W(I,3)+C(4)*W(I,4)
    1               +C(5)*DY(I)+C(6)*W(I,6))
  24 CONTINUE
C
C  ERROR ESTIMATE
C
     DO 30 I=1,NEQ
       W(I,1)=TE(1)*W(I,1)+TE(3)*W(I,3)+TE(4)*W(I,4)
    1                 +TE(5)*W(I,5)+TE(6)*W(I,6)
       EP=W(I,1)
       IF(Y2(I).NE.0.0) EP=EP/Y2(I)
       EPS=AMAX1(EPS,ABS(EP))
  30 CONTINUE
     EPS=DT*EPS
     RETURN
     END
```

APPENDIX D

INPUT DECKS FOR THE STRTUP COMPUTER PROGRAM

NERVA Small Engine Sample Input Deck – Startup Analysis

```
RUN STRTCD.EXE
STARTUP TEST CASE
POWR
 1000.0 0.007 1.0E-4  0.001  1 -9.79E-3  9.24E-4 0.6
 200.0 1.2E+5 3.45E+8 2.7E+3 6.0E+6 0.978 1.0 1.43E-2 8.5 1.58E+4 200.0
 3.45E+8   -0.05  0.285  50.0  140.0   0.1
STAR
```

Particle Bed Sample Input Deck – Startup Analysis

```
RUN STRTCD.EXE
DKCOOL TEST CASE
POWR
 1000.0 0.00758 3.92E-5  0.0001  1 -1.57E-2 2.0E-3 0.6
 200.0 1.2E+5 3.45E+8 2.7E+3 3.41E+6 0.141 1.0 5.17E-3 8.5 1.58E+4 200.0
 3.45E+8   -0.05  0.285  50.0  140.0  0.1
STAR
```

Wire Core Sample Input Deck – Startup Analysis

```
RUN STRTCD.EXE
DKCOOL TEST CASE
POWR
 1000.0 0.0065 1.0E-7  3.5E-6   1 -1.31E-2 2.0E-3 1.5
 200.0 1.2E+5 3.45E+8 2.7E+3 3.41E+6 0.357 0.97 1.54E-5 8.5 1.58E+4 200.0
 3.45E+8   -0.05  0.285  50.0  80.0   0.1
STAR
```

APPENDIX E

INPUT DECKS FOR
THE FEMP1D
COMPUTER PROGRAM

Wire Core Sample Input Deck – Criticalilty and Control Margin Analysis

```
RUN FEMP1D.EXE
 FEMP1D MODEL(RADIAL) OF THE WIRE CORE REACTOR
1$$ 2 3 0 1 9 47 20 1 3R0 20 0 0 20 63 9 1 0 2 0 10 40 0 10 0 0 -1 19 F0
2** 1.0E-5 1.0 1.0 T
10$$ 1 2 3 3 3 3 3 3 3 3 4 5 6 7 8 8 8 9 9 9
11$$ 1269 1193 1261 1262 1275 1128 1129 1130 1131 1269 1269 1274
    1289 1289 1273 1160 1274 1190 1191 1192
12** 0.005 0.06 0.009 0.00067 0.0097 0.0025 0.0014 0.0029 0.0027
    0.00019 0.00017 0.08 0.12 0.12 0.022 0.088 0.028 0.0073 0.015
    0.063 T
30** 1I0.0 1I4.5 24I5.0 1I26.63 1I28.31 1I29.31 19I29.81 1I43.81
    4I44.31 46.31
33$$ 1 2 3 4 5 6 7 8 9
34$$ 2R1 2R2 25R3 2R4 2R5 2R6 20R7 2R8 5R9
35** 292.89 92.62 92.62 292.89 92.62 92.62 92.62 92.62 92.62
36** 0.0 4.5 3I5.0 1I26.63 28.31 29.31 2I29.81 43.81 1I44.31 46.31 T
```

Wire Core Sample Input Deck – Dimension Search Analysis

```
RUN FEMP1D.EXE
 FEMP1D MODEL(RADIAL) OF THE WIRE CORE REACTOR
1$$ 2 4 0 1 9 47 20 1 3R0 20 0 0 20 63 9 1 0 2 0 10 40 0 10 0 0 -1 19 F0
2** 1.0E-5 1.0 1.0
3$$ 2 0 0 0 0
4** 1.05 0.0 0.0 0.0 T
10$$ 1 2 3 3 3 3 3 3 3 3 4 5 6 7 8 8 8 9 9 9
11$$ 1269 1193 1261 1262 1275 1128 1129 1130 1131 1269 1269 1274
   1289 1289 1273 1160 1274 1190 1191 1192
12** 0.005 0.06 0.009 0.00067 0.0097 0.0025 0.0014 0.0029 0.0027
   0.00019 0.00017 0.08 0.12 0.12 0.022 0.088 0.028 0.0073 0.015
   0.063 T
30** 1I0.0 1I4.5 24I5.0 1I26.33 1I28.01 1I29.01 19I29.51 1I43.51
   4I44.01 46.01
33$$ 1 2 3 4 5 6 7 8 9
34$$ 2R1 2R2 25R3 2R4 2R5 2R6 20R7 2R8 5R9
35** 309.52 97.88 97.88 309.52 97.88 97.88 97.88 97.88 97.88
36** 0.0 4.5 3I5.0 1I26.33 28.01 29.01 2I29.51 43.51 1I44.01 46.01 T
```